SYNERGISTIC ACTION OF ORGANIC INHIBITORS TO MITIGATE CORROSION OF ALUMINIUM, COPPER AND ALUMINIUM-COPPER ALLOY IN CHLORIDE SOLUTION

Dževad Kozlica

Doctoral Dissertation
Jožef Stefan International Postgraduate School
Ljubljana, Slovenia

Supervisor: Prof. Dr. Ingrid Milošev, Jožef Stefan International Postgraduate School and Jožef Stefan Institute, Ljubljana, Slovenia

Evaluation Board:

Asst. Prof. Dr. Peter Rodič, Chair, Jožef Stefan International Postgraduate School and Jožef Stefan Institute, Ljubljana, Slovenia

Prof. Dr. Miran Gaberšček, Member, National Institute of Chemistry and Faculty of Chemistry and Chemical Technology, Ljubljana, Slovenia

Prof. Dr. Ricardo M. Souto, Member, University of La Laguna, Tenerife, Spain

MEDNARODNA PODIPLOMSKA ŠOLA JOŽEFA STEFANA
JOŽEF STEFAN INTERNATIONAL POSTGRADUATE SCHOOL

Dževad Kozlica

SYNERGISTIC ACTION OF ORGANIC INHIBITORS TO MITIGATE CORROSION OF ALUMINIUM, COPPER AND ALUMINIUM-COPPER ALLOY IN CHLORIDE SOLUTION

Doctoral Dissertation

SINERGIJSKI UČINEK ORGANSKIH ZAVIRALCEV KOROZIJE ALUMINIJA, BAKRA IN ZLITINE ALUMINIJ-BAKER V KLORIDNI RAZTOPINI

Doktorska disertacija

Supervisor: Prof. Dr. Ingrid Milošev

Ljubljana, Slovenia, May 2022

To my beloved family

Acknowledgments

On the way to achieving the title of Doctor of Science, I owe my gratitude to many people, so let's start chronologically.

First, a big thank you goes to my family who have always been my biggest support. Then, to my friend and former mentor from Sarajevo Asst. Prof. Dr. Sanjin Gutić who persuaded me to come to Ljubljana for a doctoral study.

I express my gratitude to the Ad futura for providing the PhD scholarship through the Public scholarship, development, disability and maintenance fund of Republic of Slovenia (grant no. 11011-116/2017-13), which mostly covered the three-year costs of staying in Ljubljana, as well as the costs of studying at the International Postgraduate School of Jožef Stefan.

I owe the greatest thanks to my supervisor Prof. Dr. Ingrid Milošev who made me feel at home and provided me with additional financial support. However, as my greatest merits, I would like to emphasize her dedication, availability and time invested in my PhD journey.

I would also like to thank Asst. Prof. Dr. Anton Kokalj, Prof. Dr. Stojan Stavber and Asst. Prof. Dr. Janez Kovač for their many tips and fruitful discussion. In addition, great thanks go to Dolores Zimerl, MSc for her valuable technical assistance and Barbara Kapun, BSc for her valuable contribution by performing numerous SEM/FIB/EDS analyses.

Special thanks go to the Erasmus+ scholarship to finance a three-month stay at the University of La Laguna, Chemistry Department, Tenerife, Spain. Here I would like to thank Prof. Dr. Ricardo M. Souto who mentored and motivated me on that short visit. I would also like to mention the contribution of Asst. Prof. Dr. Javier Izquierdo which reflected in many adviced, availability and help in the laboratory.

Finally, I would like to thank all my colleagues from the department who helped me in any way and made my days spent at the institute more fun.

Abstract

The inhibitory action of organic compounds, 2-mercaptobenzimidazole (MBI), octylphosphonic acid (OPA) and their binary combinations was studied on aluminium, copper and aluminium alloy (AA) 2024 in chloride environments by *ex-situ* conventional electrochemical methods and surface-analytical techniques. In addition, the influence of pre-treatment of the metal surface and the choice of solvent for liquid-phase deposition on adsorption of MBI and OPA was studied on individual metals, aluminium and copper. Although OPA is not an inhibitor of copper, it can synergistically boost corrosion inhibition of copper when added to MBI. It is believed that the porous straw-like morphology of the $[\text{Cu-Cl-MBI}]_n$ overlayer together with the formed Cu_2O underlayer was responsible for the excellent corrosion protection of copper. Unambiguous evidence is presented that the chloride ions act simultaneously as a promoter of polymerized $[\text{Cu-Cl-MBI}]_n$ film formation and a reactant incorporated in the film. In contrast, a synergistic effect between MBI and OPA as corrosion inhibitors was not observed for AA2024.
Localized electrochemical methods such as SVET and SECM were employed to study *in-situ* electrochemical activity on Al/Cu galvanic couple and AA2024. Anodic and cathodic reactions of Al/Cu were significantly suppressed when the copper surface was treated with an MBI inhibitor associated with the isolation of copper metal from aluminium due to the inhibitory effect of MBI on copper. Treatment of Al/Cu with OPA was not as effective as with MBI. SECM imaging in substrate generation-tip collection mode revealed the local concentrations of hydrogen gas over Al metal which is associated with the pitting corrosion. Immersion of AA2024 in an OPA-containing solution caused significant localized corrosion, while no local electrochemical activity on AA2024 was detected in an MBI-containing solution, indicating that the MBI inhibitor was very effective against pitting corrosion. Furthermore, the chemical analysis employed at the cross-section of the Al_2CuMg revealed the MBI layer on the porous copper surface which together with the remaining Mg indicates that MBI reduces the dissolution rate of dealloying of this phase, but also the rate of oxygen reduction on the copper remnant sites.

The novel approach used in the present work involves investigating the corrosion protection properties of mixed inhibitors for copper and aluminium substrates in chloride-containing solutions, which will serve as a benchmark for further investigation of the aluminium alloys with intermetallic particles containing Cu being the main culprits for localized corrosion.

Povzetek

V disertaciji smo raziskali organski spojini, 2-merkaptobenzimidazol (MBI) in oktilfosfonsko kislino (OPA) ter njuni binarni kombinaciji kot inhibitorje korozije aluminija, bakra in aluminijeve zlitine (AA) 2024 v kloridni raztopini. Pri tem smo uporabili ex-situ konvencionalne elektrokemijske metode in površinsko-analitične tehnike. Na posameznih kovinah, Al in Cu, smo proučevali tudi vpliv pred-obdelave kovinske površine in izbire topila na adsorpcijo MBI in OPA. Čeprav OPA ne zavira korozijo Cu, sinergijsko prispeva k le-tej, če ga dodamo v kombinaciji z MBI. Ugotovili smo, da se v prisotnosti obeh spojih v raztopini na površini Cu_2O tvori vrhnja plast $[Cu\text{-}Cl\text{-}MBI]_n$, ki ima značilno porozno, slamici-podobno morfologijo. Nastali film s strukturo $Cu_2O/[Cu\text{-}Cl\text{-}MBI]_n$ je odgovoren za odlično korozijsko zaščito bakra. Kloridni ioni hkrati delujejo kot spodbujevalec tvorbe polimerizirane plasti $[Cu\text{-}Cl\text{-}MBI]_n$ in kot reaktant, vgrajen v plast. Pri AA2024 nismo opazili sinergijskega učinka med MBI in OPA kot je to bilo ugotovljeno pri kovini Cu.

Lokalne elektrokemijske metode, kot sta SVET in SECM, smo uporabili za in situ preučevanje elektrokemijske aktivnosti na galvanskem paru Al/Cu in AA2024. Anodne in katodne reakcije Al/Cu so bile znatno zavirane, ko je bila bakrena površina obdelana z inhibitorjem MBI. Ta pojav je povezan z izolacijo kovine bakra od aluminija zaradi zaviralnih učinkov MBI na baker. Zaščita Al/Cu z OPA ni bila tako učinkovita kot z MBI. SECM tehnika je razkrila lokalne koncentracije vodikovega plina nad kovino Al, kar je povezano z jamičasto korozijo. Potopitev AA2024 v raztopino, ki vsebuje OPA, je povzročila znatno lokalno korozijo, medtem ko v raztopini, ki vsebuje MBI, ni bila zaznana nobena lokalna elektrokemijska aktivnost na AA2024, kar kaže, da MBI deluje kot zelo učinkovit inhibitor korozije. Poleg tega je kemijska analiza prečnega prereza Al_2CuMg, razkrila plast MBI na porozni bakreni površini, kar skupaj s preostalim Mg kaže, da MBI zmanjša hitrost selektivnega raztapljanja te faze, pa tudi hitrost redukcije kisika na mestih, kjer je prišlo do redepozicije bakra.

Nov pristop, uporabljen v pričujočem delu, ki vključuje raziskavo protikorozijskih lastnosti mešanice inhibitorjev za bakrene in aluminijeve podlage v kloridnih raztopinah, predstavlja nov mejnik za nadaljnje raziskave aluminijevih zlitin z intermetalnimi delci, ki vsebujejo Cu kot glavni vzrok za lokalno korozijo.

Contents

List of Figures

List of Tables

Chapter 1

Introduction

1.1 Description of the Problem

The lightweight aluminium alloy (AA) 2024 is a paramount material in the aerospace industry due to its high strength-to-weight ratio. However, the heterogeneous nature of the surface microstructure, which consists of alloying elements such as Cu, Mg, Fe, Mn, etc., decreases the alloy's intrinsic corrosion resistance and makes it susceptible to localized corrosion, especially in chloride (Cl^-) containing aqueous solutions. The corrosion initiation was reported to be mainly related to the electrochemical activity of Cu-containing intermetallic particles (IMPs), such as S-phase (Al_2CuMg), θ-phase (Al_2Cu), Al_7Cu_2Fe and the surrounding Al matrix.

One of the methodologies to mitigate corrosion of metals and alloys is the use of corrosion inhibitors. Introducing new inhibitors requires screening, synthesis, up-scaling and rigorous testing, complying with the REACH directive [1], [2]. Therefore, it is of great interest to investigate the synergism of already registered compounds that could achieve greater efficiency when used together. This would avoid or reduce the need to synthesise new chemicals, which should go through a new registration process. Of course, the toxicity of the compounds should be avoided or minimized. In that context, it is worth mentioning the example of chromate compounds. Chromates, which have been used as pigment additives or conversion coatings to mitigate corrosion in the aerospace industry to date [3], are mainly being replaced due to their carcinogenic nature [4], [5]. Therefore, numerous studies have been conducted to find chromate replacements with more environmentally acceptable compounds, among them being various inorganic and organic coatings or pigments [6].

The approach used in the present work involves investigating the corrosion protection properties of mixed inhibitors for copper and aluminium substrates in chloride-containing solutions, which will serve as a benchmark for further studies of alloy AA2024, with Cu and Al being the main culprits for localized corrosion. A synergistic mixture of inhibitors could find potential applications in novel blending combinations to be added, for example, in cooling water as an inhibitor in closed systems or incorporated in various protective coatings as additives, nano-containers, etc. If possible, the protective inhibitor film should show irreversibility of inhibition which can be defined as the ability to, once formed, retains its protective properties when the concentration of the corrosion inhibitor decreases [7]. This irreversibility of the protective properties is essential for long-term protection. Usually, the active protective process, known as leaching, is initiated by the ingress of water via a defect or crack in the coating, enabling the dissolution and transport of the corrosion inhibitor to the defect to inhibit the corrosion process [3], [8].

From the mechanistic point of view, much effort has been put into the adsorption configurations of these inhibitors, but data on the general mechanism of degradation of metal-inhibitors films are lacking. We believe that it would be of great importance to fill this gap. In addition, regarding the role of chlorine in the inhibitor film, several authors have reported that the Cl^- may be an essential factor in the formation of metal-inhibitor films [9]–[11]. However, there is no consensus on the validity of these allegations, and therefore a systematic study, including an unambiguous identification, is necessary.

Another point of interest is the influence of surface pre-treatment before applying corrosion inhibitors. Surface pre-treatments of metal surfaces, either mechanical and/or chemical, usually target improved bonding ability with inhibitor molecules, conversion coatings, primers or paints and increased corrosion resistance in corrosive environments [12]–[17].

The corrosion phenomena in the alloys or single metal materials are related to nanometer- to micrometre-sized defects where the onset and the initial stages of the corrosion processes occur within such spatial range. The conventional direct current (DC) electrochemical methods, such as potentiodynamic polarization curves, voltammetry, or alternating current (AC) methods, such as electrochemical impedance spectroscopy (EIS), lack spatial resolution and provide little information on behaviour at sites of corrosion initiation or defects. Thus, there is a need for techniques that provide laterally resolved information, preferably under real-time and under in-situ corrosion conditions. Such techniques are scanning electrochemical microscopy (SECM) [18]–[20] and scanning vibrating electrode technique (SVET) [21], [22]. These techniques have been previously employed to study the localized dissolution of metals and alloys [23]–[26] and metal-inhibitor systems [9], [27]–[30].

1.2 Common Forms of Corrosion

Davis [31] has summarized all the basic corrosion impact forms, classifying them into uniform and localized corrosion phenomena. But the dominant type depends on the medium and conditions to which aluminium and its alloys are exposed.

1.2.1 Uniform corrosion

This type of corrosion includes the commonly recognized rusting of iron or tarnishing of silver. The corrosive environment must have the same access to all parts of the metal surface, and the metal itself must be metallurgically and compositionally uniform. Atmospheric corrosion is probably the most prevalent example of uniform corrosion at a visually apparent rate [32].

1.2.2 Localized corrosion

Among the most common types of localized corrosion of aluminium are galvanic, pitting and dealloying corrosion.

1.2.2.1 Galvanic corrosion

Galvanic corrosion occurs when a potential difference exists between two dissimilar metals immersed in a corrosive solution (Fig. 1.1a). The potential difference between more and less noble metals results in the flow of electrons. Galvanic corrosion is generally more prominent at the junction of two dissimilar metals, and the severity of attack decreases with increasing distance from the junction [33].

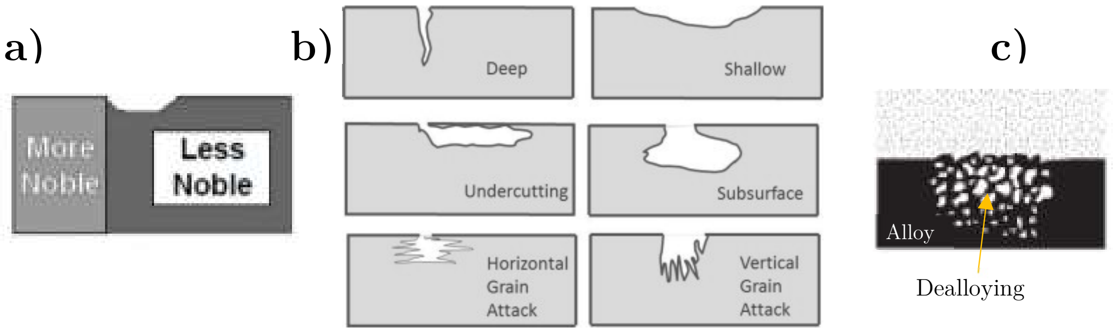

Figure 1.1: Common forms of corrosion: (a) galvanic, (b) pitting and (c) dealloying [33].

1.2.2.2 Pitting corrosion

Pitting corrosion is the most dangerous type of corrosion for aluminium and copper, which can lead to other types of corrosion, e.g. intergranular corrosion, and subsequently to structural degradation. It occurs as holes and pits of irregular shapes on the surface of the metal (Fig. 1.1b). The diameter and depth of the pits are dependent on the type of aluminium alloy, the corrosive medium, surface passivation and the properties of the environment that the metals are exposed to. Pitting corrosion often occurs in aerated chloride solutions [34]–[36].

1.2.2.3 Dealloying - Selective leaching

Dealloying is the selective removal of an element from an alloy by corrosion (Fig. 1.1c). An alloying element such as magnesium that is active (negative electrochemically) to the major solvent element such as aluminium is likely to be preferentially corroded by dealloying [32].

1.3 The Mechanisms of Corrosion of Aluminium, Copper and AA2024-T3 in Chloride-containing Solutions

1.3.1 Pitting corrosion of aluminium

The dissolution-precipitation mechanism of corrosion of aluminium at anodic sites in aqueous chloride solutions occurs through several steps [35], [37]–[39]. According to the Pourbaix diagram [40], aluminium is passive (protected by its oxide film) in the pH range of 4–8.5 in aqueous solutions at 25 °C. Beyond this range, e.g., in mildly acidic aqueous solutions, the naturally existing oxyhydroxide passive layer undergoes dissolution yielding Al^{3+}.

$$\mathrm{Al} \longrightarrow \mathrm{Al}^{3+} + 3\mathrm{e}^{-} \tag{1.1}$$

The aluminium cations may diffuse to another area where they hydrolyse and precipitate from the solution as a gelatinous hydroxide (Fig. 1.2), leading to acidification, Eq. (1.2). Note that these hydrolysis products are more complex with an idealized formula $Al[O_x(OH)_y(H_2O)_z]$.

$$Al^{3+} + 3H_2O \longrightarrow Al(OH)_3 + 3H^+ \tag{1.2}$$

The presence of aggressive chloride ions prevents the formation of the passive film and accelerates the process of anodic dissolution. The pitting corrosion of Al is due to the migration of chloride ions through the oxide film forming the oxide-chloride complexes, or simply $AlCl_3$ [38].

$$Al + 3Cl^- \longrightarrow AlCl_3 + 3e^- \tag{1.3}$$

The formed $AlCl_3$ within the pits further reacts with chloride ions forming very soluble $AlCl_4^-$ complexes that diffuse into the bulk of the solution leaving the space for pitting to continue.

$$Al^{3+} + 4Cl^- \longrightarrow AlCl_4^- \tag{1.4}$$

Also, chloride clusters form around the aluminium cations and then, after diffusion and reaction with water or hydroxyls, precipitate out as aluminium hydroxide [39].

$$AlCl_3 + 3OH^- \longrightarrow Al(OH)_3 + 3Cl^- \tag{1.5}$$

Finally, the chloride anions are released from the cluster and return to the pit to continue the dissolution-precipitation reaction, leading to the autocatalytic nature of this process.

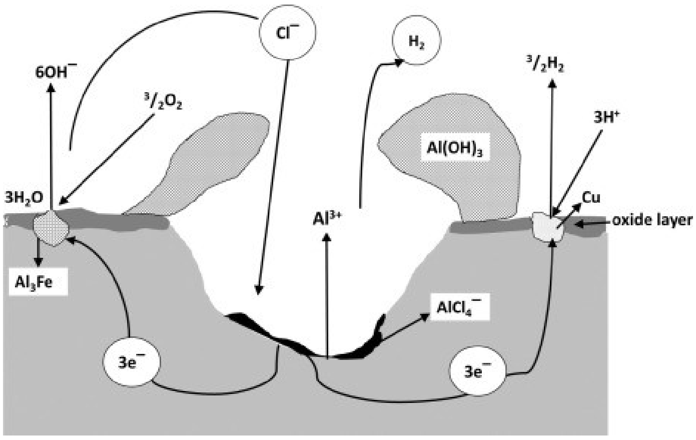

Figure 1.2: Cone-shaped accumulations of corrosion products are formed at the mouth of the pits due to the precipitation of aluminium hydroxide outside the pits [35].

Possible cathodic reactions on the aluminium surface are the reduction of H^+ protons in acidic and/or near-neutral media, Eq. (1.6), and the reduction of oxygen dissolved in alkaline or near-neutral solution, Eq. (1.7).

$$2H^+ + 2e^- \longrightarrow H_2 \tag{1.6}$$

$$O_2 + 2H_2O + 4e^- \longrightarrow 4OH^- \tag{1.7}$$

1.3.2 Electrodissolution of copper

The mechanism of copper dissolution in near-neutral NaCl solution has been explained in the literature in three stages [41]–[44]. The initial step is considered to be the oxidation of Cu to Cu(I) in the presence of Cl^- ions, forming a loose and insoluble film (i.e., a white precipitate) of cuprous chloride, CuCl, Eq. (1.8).

$$Cu + Cl^- \longrightarrow CuCl_{(s)} + e^- \tag{1.8}$$

Then, the porous CuCl film is further attacked by excess Cl^-, transforming into a stable and soluble dichlorocuprous complex anion, $[CuCl_2]^-$, Eq. (1.9). The formed $[CuCl_2]^-$ diffuses away from the copper surface, i.e., from the Helmholtz plane, into a diffuse layer extended to a bulk solution [45].

$$CuCl_{(s)} + Cl^- \longrightarrow [CuCl_2]^- \tag{1.9}$$

Finally, the resultant $[CuCl_2]^-$ is oxidized to Cu(II), Eq. (1.10), after which the process reverse of copper disproportionation (i.e. comproportionation) takes place in the presence of metallic copper (fraction of the active surface, i.e., not covered by CuCl) and chloride ions, Eq. (1.11) [11], [46], leading to an equilibrium between the formation of CuCl and dissolution of $[CuCl_2]^-$. It was reported that at equilibrium, on average, 50 % of the surface is active (i.e., free of CuCl), and 50 % is covered by CuCl [47].

$$[CuCl_2]^- \longrightarrow Cu^{2+} + 2Cl^- + e^- \tag{1.10}$$

$$Cu^{2+} + Cu + 2Cl^- \longrightarrow 2CuCl_{(s)} \tag{1.11}$$

In an aerated chloride solution, the cathodic process for the corrosion of copper involves an irreversible oxygen reduction reaction (ORR), which is initially controlled by charge transfer and then by mass transport, Eq. (1.7). The fact that anodic and cathodic reactions can exist at different sites at the same metal surface is due to the physical and chemical heterogeneity of the metal surface [45].

Due to the increase in pH, it is reported that the formation of a protective Cu(I) oxide film takes place on the Cu surface via Eq. (1.12) [48].

$$2CuCl + 2OH^- \longrightarrow Cu_2O + H_2O + 2Cl^- \tag{1.12}$$

When the concentration of $[CuCl_2]^-$ reaches the saturation limit, it precipitates back into CuCl, which leads to the formation of Cu_2O film via Eq. (1.12). That is why the overall method of Cu_2O production in the presence of the chloride ion is usually taken as a precipitation reaction, Eq. (1.13), rather than a direct electrochemical or chemical formation from the base metal or cuprous chloride [49], [50]. Liu and Li [51] performed the *real-time* Raman spectroscopy measurements along with electrochemical tests. They found out that the chlorides are formed at OCP during the initial 2 h, after which the formation of Cu_2O was accelerated by the increased concentration of $CuCl_2^-$ at the interface between copper and solution. Moreover, the potential-dependent spectra demonstrated that the formation of chlorides can be accelerated by anodic polarization.

$$2[CuCl_2]^- + 2OH^- \longrightarrow Cu_2O + H_2O + 4Cl^- \tag{1.13}$$

Although the ORR is controlled by mass transport, the diffusion of $[CuCl_2]^-$ is what limits the mass transfer process for the oxidative Cu dissolution at the OCP [52].

1.3.3 Pitting corrosion of copper

The dissolution of Cu at lower NaCl concentrations is relatively uniform, Eqs. (1.8 and 1.9), and in higher concentrations of chloride ions ($10^{-2} - 5 \times 10^{-1}$ M), the pitting of copper occurs. In dilute chloride solutions, the predominant species in the surface film is Cu_2O, whereas, in a higher concentration of NaCl, the surface film is mainly CuCl.

The pitting corrosion of copper occurs when a protective film of Cu_2O exists on its surface via Eq. (1.12) in contact with higher concentrations of chloride ions [48], [53], [54]. The initiation of the pits was believed to occur at sites where CuCl was trapped by a thin layer of Cu_2O. The chloride then dissolves at micro-pits to form soluble $[CuCl_2]^-$ via, Eq. (1.9) (Fig. 1.3).

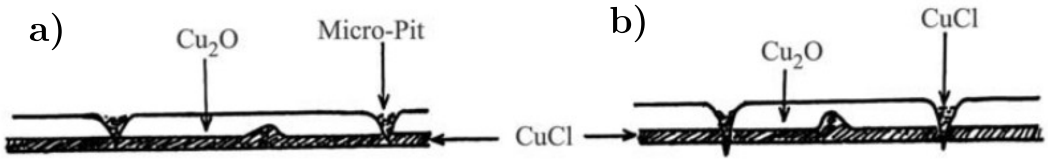

Figure 1.3: Schematic representation of the mechanism of pitting corrosion of copper in NaCl solutions [48]: (a) the initiation of the pits was found to occur at sites where CuCl was trapped, resulting in the formation of micro-pits, (b) propagation of the pit.

1.3.4 Pitting corrosion of AA2024

The localized corrosion of wrought aluminium alloys in chloride enriched media is a major issue in the aeronautics and automobile industry. Probably the most famous member is the AA2024-T3 belonging to a class of precipitation-hardened aluminium alloys with a high strength-to-weight ratio [55]. AA2024 is selected in this work because it is the main structural alloy used for wings and fuselage structures of the aircraft and parts in the military and other vehicles [56]. The elemental composition of AA2024 is shown in Table 1.1.

Table 1.1: Chemical composition of AA2024 [57].

AA2024	Mg	Cu	Fe	Mn	Si	Cr	Zn	Ti	Al
wt.%	1.2–1.8	3.8–4.9	max. 0.5	0.3–0.9	max. 0.5	max. 0.1	max. 0.25	max. 0.15	90.7–94.7

The susceptibility of high-strength aluminium alloy 2024-T3 to localized corrosion (for example, in Cl^- electrolyte) is generally attributed to the presence of local galvanic cells that form between the precipitated Cu-rich intermetallic particles such as θ-phase (Al_2Cu), S-phase (Al_2CuMg), $Al_7Cu_2Fe(Mn)$ and the Al matrix, but also to the rate of oxygen reduction over the intermetallic particles. Although the overall behaviour of dealloying and trenching had been proposed for S-phase, a recent study reported a dealloying-driven local corrosion initiation at the studied IMPs that have been considered as cathodic phases traditionally (such as $Al_7Cu_2Fe(Mn)$), thus suggesting a possible initial (local) anodic character in most IMs due to local compositional variations [58], [59].

The dominant and most active intermetallic compound (IMC) is the S-phase precipitate with Al_2CuMg composition and an average size of 7.6 ± 5.2 μm [60]. Initially, the S-phase particle is anodically polarized by the surrounding Al matrix (S-phase particles have corrosion potentials negative to that of the matrix). The particle dealloys under anodic polarization, i.e., it undergoes preferential dissolution of Mg and Al, leaving behind a very high surface area porous Cu sponge structure (Fig. 1.4). This leads to the polarity switching from anodic to cathodic as the copper remnant (i.e., dealloyed S-phase), which serves as a cathode active to oxygen reduction, promotes the anodic dissolution of the adjacent Al matrix, causing trenching. As long as the remnant Cu sponge remains mechanically and electrically connected to the Al matrix, the corrosion potential is too low to allow copper to dissolve electrochemically. If the particles of the Cu sponge are mechanically separated from the matrix, direct oxidation of copper particles at its corrosion potential becomes possible, which leads to a subsequent reduction of Cu ions on the nearby surface of the alloy, known as copper redistribution. It has been shown that copper redistribution also occurs from the solid solution due to the matrix dealloying process [60]–[63]. The new cathodic sites support even greater oxygen reduction that leads to both raised local potentials and local alkalinity due to the production of OH^- ions, causing further localized attacks near IMCs. Therefore, an effective way to increase the corrosion resistance of AA2024 is to suppress the dissolution of S-phase particles.

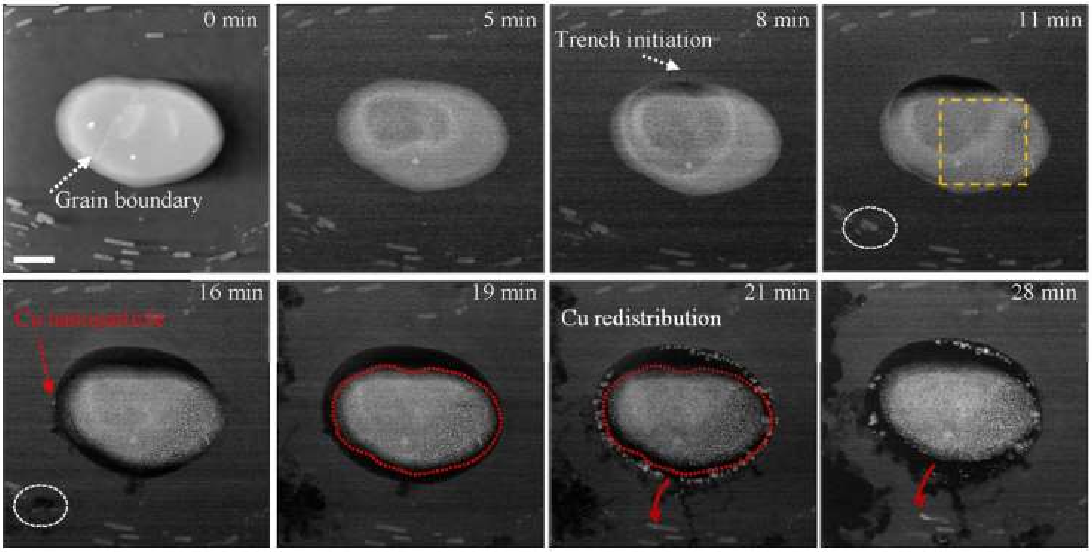

Figure 1.4: *In-situ* top-view observations of local corrosion by S-phase (Al_2CuMg) from AA2024 [64]. Images were recorded in time-resolved top-view HAADF-STEM mode showing morphological evolutions of the particle and its adjacent matrix in 0.01 M NaCl electrolyte. The image taken at 0 min is in the absence of the electrolyte. The red-dashed lines border the particle area before and after the detachment from the alloy matrix. The red solid arrows indicate the redistribution of Cu particles. The scale bar is 500 nm.

1.4 Corrosion Inhibition

1.4.1 Problem-solving strategy

A corrosion inhibitor is a chemical compound that, when added to a liquid or gas, decreases the corrosion rate of a material, typically a metal or an alloy, that comes into contact with the fluid. Organic compounds acting like corrosion inhibitors possess functional group(s) with heteroatom(s) (N, P, O, or S) containing a lone pair of electrons and/or delocalized π electrons due to the presence of multiple bonds or aromatic rings [33], [65].

In this dissertation, we are dealing with organic compounds as corrosion inhibitors for Al, Cu and Cu-containing Al alloy (2024) in slightly acidic and near-neutral chloride environments. Under such conditions, an efficient organic inhibitor should be able to adsorb on the bare or oxide-covered metal surface and form a protective layer. Moreover, the synergistic effect of a mixture of organic inhibitors is investigated. Synergy (Greek „working together“) is an interaction or cooperation giving rise to a whole that is greater than the simple sum of its parts. To understand the corrosion processes of Cu-containing aluminium alloys such as 2024 it is important to study separately the corrosion processes taking place on individual metals, aluminium and copper.

1.4.2 Classification of corrosion inhibitors

There are two main classifications of inhibitors; environment modifiers and adsorption inhibitors.

1.4.2.1 Environment modifiers

In the case of environmental modifiers, the action and mechanism of inhibition is a simple interaction with the corrosive species in the environment, thereby preventing the attack of the metal by the aggressive species. This is exemplified by oxygen scavengers such as hydrazine. In the case of corrosion in neutral and alkaline solutions, oxygen reduction is the cathodic reaction, which the oxygen scavengers can mitigate and thus inhibit the corrosion like in conventional heating systems [33].

1.4.2.2 Adsorption inhibitors

Adsorption of inhibitors on the metal surface leading to inhibition of corrosion processes consists of two steps [33]:

i. Transport of inhibitor to the metal surface and
ii. Metal–inhibitor interactions

Depending on whether the corrosion inhibitor suppresses the cathodic or anodic reaction, the inhibitors are further classified into cathodic, anodic and mixed inhibitors.

Cathodic inhibitors inhibit the hydrogen evolution in acidic solutions or the oxygen reduction in neutral or alkaline solutions. Substances with high overpotential for hydrogen in acidic solutions and those that form insoluble products in alkaline solutions are, in general, effective cathodic inhibitors, such as inorganic phosphates, silicates, or borates in alkaline solutions inhibiting the oxygen reduction at the cathodic sites [33].

The E_{corr} shifts to more negative values when the cathodic reaction is affected, and the current decreases (Fig. 1.5).

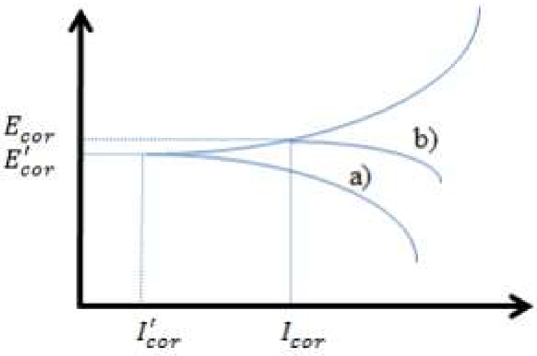

Figure 1.5: Potentiostatic polarization diagram: electrochemical behaviour of the metal in (a) electrolyte containing cathodic inhibitor, (b) electrolyte without inhibitor [66].

Anodic inhibitors (known as passivation inhibitors) block the anodic reaction and support the natural passivation reaction (protective layer of oxide film) on the metal surface. Oxyanions such as chromates are quite effective anodic inhibitors repairing the defects in the passive oxide films [33].

When the anodic reaction is affected by corrosion inhibitors, the E_{corr} of the metal shifts to more positive values along with a decrease in the current (Fig. 1.6).

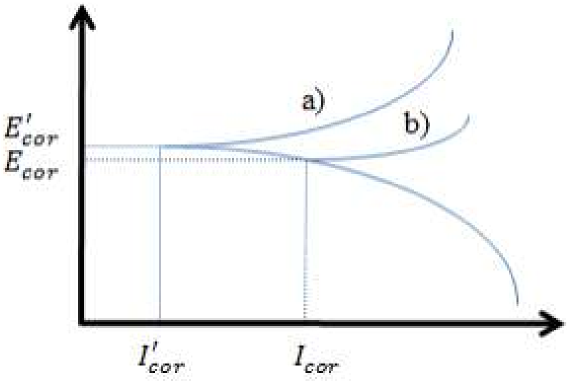

Figure 1.6: Potentiostatic polarization diagram: electrochemical behaviour of a metal in (a) electrolyte containing anodic inhibitor, (b) electrolyte without inhibitor [66].

Mixed-type inhibitors occasionally act as cathodic, anodic, or together as cathodic and anodic inhibitors; nevertheless, as a general rule, they act through a surface adsorption process termed film formation.

Fig. 1.7 shows a theoretical potentiostatic polarization curve showing the effect of the presence of organic inhibitor in solution on the anodic and cathodic behaviour of metal. After adding the inhibitor, the corrosion potential remains the same, but the current decreases from I_{corr} to I'_{corr} [66].

Generally, to estimate the effect of the different inhibitors on the anodic and cathodic partial electrode reaction, potentiodynamic polarization measurements were carried out.

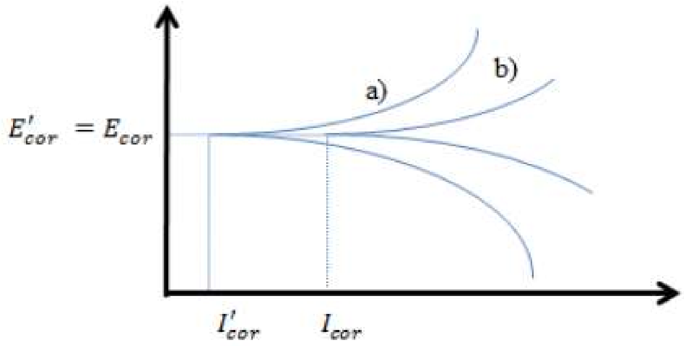

Figure 1.7: Theoretical potentiostatic polarization diagram: electrochemical behaviour of a metal in (a) electrolyte containing cathodic and anodic inhibitor, (b) electrolyte without inhibitor [33], [66].

1.5 Surface Pre-treatment

Another point of interest is the influence of surface pre-treatment before applying corrosion inhibitors. Surface pretreatments of metal surfaces, either mechanical and/or chemical, usually target improved bonding ability with inhibitor molecules, conversion coatings, primers or paints and increased corrosion resistance in corrosive environments [12]–[17]. The mechanical pre-treatment, including grinding and/or polishing, is usually based on SiC sandpaper and produces a macro-rough surface [67], [68]. The chemical pretreatment typically involves several steps: (i) degreasing, (ii) etching and (iii) desmutting. Effective cleaning produces a contaminant-free surface. Main surface contaminants that require removal with degreasers (acetone) come from the processing and shaping of the metals and alloys (lubrication oils). Alkaline etching, usually performed using sodium hydroxide, generates complex oxides and hydroxides of aluminium, removes any organic residue and also removes several micrometres of the metal/alloy. Some of these reaction products, including intermetallic compounds, are insoluble in the etch solution. These remain on the surface of the aluminium parts in the form of "smut". The etching step is followed by applying acid deoxidizer (also called desmutting or pickling), such as nitric acid, to remove any residue, i.e., dissolve the surface oxide or smut, from – or caused by – the previous alkaline step [13], [68].

1.6 Purpose of the Dissertation

The primary purpose of this dissertation is to investigate three different inhibitor systems (2-mercaptobenzimidazole, MBI, octylphosphonic acid, OPA and their mixture, MBI+OPA) on individual metals Al and Cu, Al/Cu galvanic couple and finally on Al-Cu containing alloy 2024 to bring some new fundamental insights related to the mechanism of formation and breakdown of metal-organic passive films. The final goal is to demonstrate an improved efficiency of a novel binary inhibitor mixture due to the synergy and stability between mercapto and phosphono groups. The inhibitor synergy has potential applications in novel blending mixtures incorporated in protective coatings or as an additive to open or closed industrial/supply cooling systems.

1.7 Objectives of the Dissertation

1. To find the optimal chemical surface pre-treatment conditions for improved adsorption of 2-mercaptobenzimidazole and octylphosphonic acid on Cu and Al substrates.
2. To examine the possible synergy and stability of a novel binary inhibitor mixture MBI+OPA on AA2024 and possibly Cu and Al in a chloride environment. The synergistic effect should be demonstrated in terms of irreversibility, i.e. in the absence of an inhibitor reservoir.
3. To reveal the polymerized nature of Cu-MBI protective inhibitor film on Cu and the role of chloride ions in its formation.
4. To investigate the mechanism of degradation of Cu-MBI film.
5. To analyse the local surface properties, electrochemical phenomena and mechanisms on Al/Cu galvanic couple and aluminium alloy 2024 during the early stages of corrosion and corrosion protection processes by MBI and OPA.

1.8 Hypothesis

1. The chemical surface pre-treatment improves the adsorption of organic inhibitors on Cu and Al.
2. The binary mixture MBI+OPA acts synergistically in corrosion inhibition of AA2024, but shows no synergy on individual metals Al and Cu. The possible synergistic effect will be irreversible under optimal conditions.
3. Formed Cu-MBI layer(s) in NaCl medium possess a polymerized structure. The chloride ions have multiple roles: as catalysts of layer formation and as integral components of the layer's structure.
4. The degradation of the Cu-MBI layer results in the formation of dimers.
5. SECM analyses can detect local reactive sites of the hydrogen evolution reaction (HER), as well as the oxygen evolution reaction (OER) on the surface of Al/Cu substrate.
6. SVET can distinguish between cathodic and anodic sites on the Al/Cu galvanic couple and AA2024 and define the effectiveness of MBI and OPA inhibitors.

1.9 Methodology

The methodology covers the use of a wide range of instruments. They are classified as:

i. Methods for surface characterization of the substrate and surface layers: X-ray photoelectron spectroscopy (XPS), attenuated total reflectance Fourier transform infrared spectroscopy (ATR-FTIR), optical microscopy, scanning electron microscopy combined with energy-dispersive X-ray spectroscopy (SEM-EDS), focused ion beam microscopy (FIB) SEM-EDS, time-of-flight secondary mass spectrometry (ToF-SIMS) and contact angle goniometer.

ii. Conventional (macro) electrochemical methods for the evaluation of corrosion protection performance: open circuit potential (OCP), linear polarization resistance (LPR), potentiodynamic polarization curves (PD), and cyclic voltammetry (CV).

iii. *In-situ* local electrochemical methods for revealing the mechanism of early stages of corrosion and corrosion protection: scanning electrochemical microscopy (SECM) and scanning vibrating electrode technique (SVET).

Chapter 2

Corrosion Inhibition of Copper and Aluminium by 2-Mercaptobenzimidazole and Octylphosphonic Acid: Influence of the Solvent and Surface Pre-Treatment

2.1 Literature Review

Triazoles, thiazoles, imidazoles and their derivatives are some common effective organic inhibitors that have been frequently used for copper protection [28], [41], [42], [69]–[71]. Among these, the 2-mercaptobenzimidazole (MBI) has received significant attention in the past few decades. It possesses nitrogen and sulphur heteroatoms together with the aromatic ring and can form bonds with various metal substrates. The high corrosion inhibition efficiency of MBI for copper in 3 wt.% NaCl aqueous solution and its bonding mechanism was reported by Finšgar [70], [72] and Milošev et al. [41], [73]. Furthermore, Žerjav and Milošev investigated the combined action of benzotriazole (BTA), MBI and stearic acid in a simulated urban rain solution (pH = 5) [74]. The results revealed that BTA is an inefficient inhibitor under such acidic conditions unless combined with stearic acid, indicating a synergistic effect between the two compounds.

In contrast, the MBI was able to inhibit the corrosion of Cu and gave even better results in combination with stearic acid [74]. In addition, other compounds such as carboxylic acids [75]–[79] and alkylphosphonic acids [79]–[84] have been used to form well-ordered self-assembled monolayers (SAMs) on oxide-covered metal surfaces. Such SAMs increase hydrophobicity [75] of metal surfaces and exhibit the advantages of high coverage, few defects, and high inhibition efficiency [85], [86]. Hoque et al. [80] investigated the influence of chain length of alkylphosphonic acids on the formation of SAMs on copper oxide surfaces and reported denser packing and better orientation of the molecules with longer chain lengths. The presence of metal surface oxide was crucial for the chemisorption of phosphonates on copper [80] and aluminium by liquid deposition in ethanol solution [12], [87], [88].

The group from the University of La Laguna investigated metal—inhibitor interactions using localized scanning micro-electrochemical techniques [9], [28] and demonstrated that the combination of spatial resolution and chemical sensitivity was indispensable to determining the inhibition mechanism of MBI and BTA. In addition, computational studies based on density functional theory (DFT) [73], [75], [89], as complementary to the experimental findings, provide mechanistic information about the bonding of inhibitors to the metal substrates.

The studies showed that the aluminium (hydr)oxides with large amounts of active surface sites (high surface area and low-crystalline) are more active than the well-crystalline (hydr)oxides with a lower surface area [12], [75]. On the other hand, it was revealed that the lupine extract is more effective as an inhibitor for non-etched compared to etched aluminium [15]. The adsorption of carboxylic acids and, consequently, the effect on corrosion protection was more efficient on the acid-etched copper surface [90] than on the ground surface. Similar behaviour was observed for alkaline-etched aluminium, where the adsorption of carboxylic acids and other organic inhibitors required a micrometre-level rough surface [75]. On the ground Al surface, the adsorption was unsuccessful. To test this issue further, we investigated the influence of surface pre-treatment of Al and Cu on the adsorption of MBI and OPA. Organic layers were prepared by simple liquid-phase depositions, i.e., by immersion of individual Al and Cu samples either directly in chloride-containing inhibitor aqueous solution or prepared by immersion in a non-aqueous inhibitor solution [74], [75], [91]. The ultimate aim was to achieve long-lasting protection.

2.2 Experimental

2.2.1 Materials, substrate preparation and chemicals

Working electrodes were prepared from a 2 mm thick copper and aluminium sheet (Goodfellow, Cambridge, UK, purity of 99.9 % and 99.0 %, respectively) and cut out in the form of discs, 15 mm in diameter.

The surface of the samples was either mechanically or chemically pre-treated. First, using a rotating plate polisher, the samples were successively water-ground with P1000 and P2400-grit SiC emery papers (provided by Struers, Ballerup, Denmark), followed by polishing with a polish nap (MD, Mol, Struers, Ballerup, Denmark) using water diamond suspension up to 3 µm (DiaDuo, Struers, Ballerup, Denmark) to obtain a uniform, mirror-like surface appearance. These samples were denoted as mechanically (mc) pre-treated. Then, another set of aluminium and copper samples was chemically (ch) pre-treated, i.e., aluminium was etched in 0.01 M NaOH for 10 min at 60 °C followed by desmutting in 10 % HNO_3 for 3 min at room temperature, while copper was slightly etched in 10 % HNO_3 for 3 min at room temperature. After any pre-treatment, the surfaces were subject to ultrasonic cleaning in absolute ethanol (Panreac AppliChem, Germany, purity of 99.8 %) for 3 min, double-rinsed with Mili-Q water (Millipore, Billerica, MA, USA, resistivity 18.2 MΩ cm at 25 °C) and blown dry with nitrogen gas.

The chemicals utilized for Cu and Al modification were sodium chloride (NaCl, purity 99.5 %, supplied by Fisher Scientific), 2-mercaptobenzimidazole (MBI, purity 98 %, supplied by Sigma Aldrich) and octylphosphonic acid (OPA, purity of 98 %, supplied by Ark Pharm, Inc.); molecular skeletal structures of MBI and OPA are shown in Fig. 2.1. All the reagents were used as received without further modification.

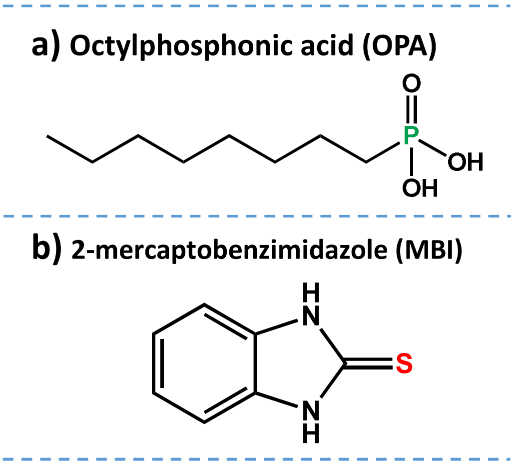

Figure 2.1: Skeletal chemical structures of (a) octylphosphonic acid (OPA) and (b) 2-mercaptobenzimidazole (MBI).

2.2.2 Preparation of organic films

Organic films for both types of pre-treated samples were prepared by liquid-phase deposition either from ethanol (et) or aqueous (aq) solution containing MBI (S) and OPA (P).

1) Liquid-phase deposition from EtOH inhibitor solution: Mechanically or chemically pretreated copper and aluminium samples were immersed for 30 min in an ethanol medium at a concentration of 1 mM. After immersion, samples were rinsed with water, dried in the stream of nitrogen and then subject to electrochemical and surface characterization. Electrochemical measurements were conducted in 3 wt.% NaCl solution.
2) Liquid-phase deposition from aqueous NaCl + inhibitor solution: Mechanically or chemically pre-treated copper and aluminium samples were immersed for 24 h in an aqueous aggressive chloride medium (i.e. 3 wt.% NaCl) with the addition of individual MBI or OPA organic compounds (Fig. 2.1) at a concentration of 1 mM. After denoted immersion period (24 h), the samples were removed from the solution, double rinsed gently with deionized water, dried in the stream of nitrogen and then subject to electrochemical and surface characterization. Electrochemical measurements were conducted in 3 wt.% NaCl solution containing 1 mM inhibitor MBI or OPA.

All the utilized solutions and their as-prepared pH and shorthand labels are summarized in Table 2.1. The pH values of the solutions used for immersion of Cu and Al samples were not adjusted to match that of NaCl but used as-prepared. The pH values of solutions used for surface modification of Al samples were adjusted to 7 since aluminium undergoes dissolution in aqueous solutions below about pH 4.

Table 2.1: List of solutions, their pH values (as-prepared), and shorthand designations. The total concentration of individual inhibitors is 1 mM.

Solution	**pH (as-prepared)**	**designation**
NaCl	5.5	bl
NaCl + MBI	5.6	100S
NaCl + OPA	3.0	100P

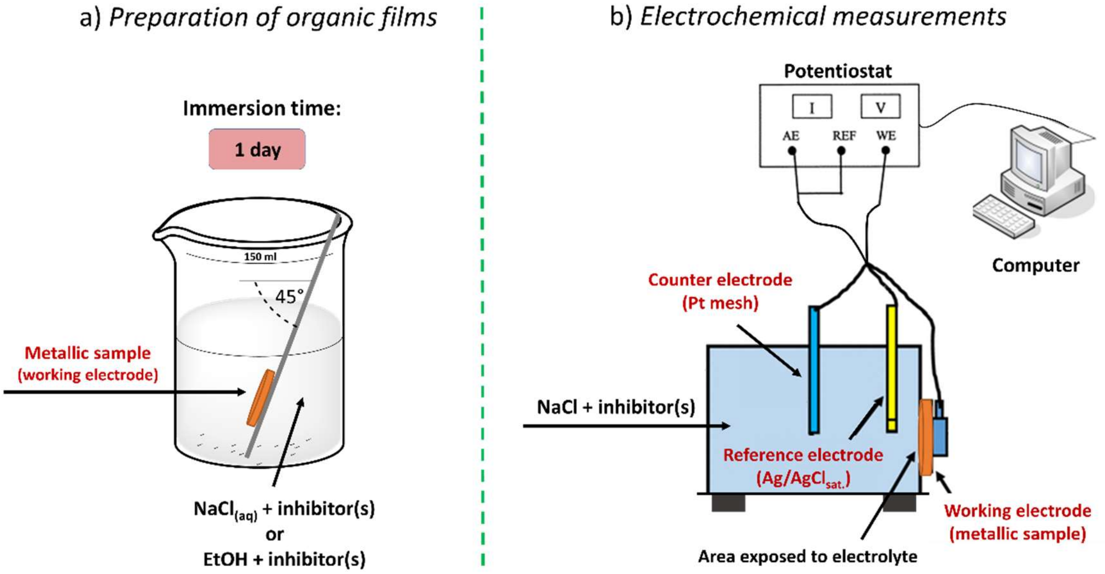

Figure 2.2: Scheme of (a) preparation of organic films and (b) set-up for the electrochemical measurements (three-electrode electrochemical corrosion cell coupled with a potentiostat.

2.2.3 Electrochemical measurements

Electrochemical measurements were carried out in an open-to-air conventional three-electrode cell assembly using PGSTAT M204 Autolab (Metrohm Autolab, Utrecht, Netherlands) multichannel potentiostat/galvanostat controlled by NOVA software (version 2.1.4) (Fig. 2.2.b). The working electrodes (WE) were copper and aluminium discs pressed against a Teflon o-ring with a 1 cm^2 exposed surface area. A Pt mesh and an Ag/AgCl/KCl$_{\text{sat.}}$ (0.197 V vs. standard hydrogen electrode) were employed as the counter electrode and the reference electrode, respectively. The latter was used with a Luggin capillary to minimize IR drops at the WE surface. In the text, potentials are given with respect to Ag/AgCl/KCl$_{\text{sat}}$ electrode.

Once the measurement started, specimens were allowed to rest for approximately 1 h until a near steady-state of open circuit potential (OCP), denoted as E_{OCP}, was established. A steady-state is assumed to be reached when the E_{OCP} changes less than 5 mV over 10 minutes [92]. Electrochemical measurements for organic films prepared by aqueous-phase deposition were carried out in NaCl solution containing inhibitor, except the blank solution contained only 3 wt. % NaCl. In contrast, measurements for the films obtained by ethanol-phase deposition were performed only in NaCl solution. Reported results were based on at least three experiments to ensure reproducibility. Measurements were carried out at ambient temperature (23 °C).

2.2.3.1 Potentiodynamic polarization curves

Through the DC polarization technique, information on the corrosion rate, pitting susceptibility, passivity, and cathodic behaviour of an electrochemical system may be obtained [93]. The potentiodynamic polarization curves were recorded starting in the cathodic range 250 mV below E_{OCP} and increasing the potential in the anodic direction up to 1 V at a scan rate of 1 mV s^{-1}.

Through the DC polarization technique, information on the corrosion rate, pitting susceptibility, passivity, and cathodic behaviour of an electrochemical system may be obtained [93]. The potentiodynamic polarization curves were recorded starting in the cathodic range 250 mV below E_{OCP} and increasing the potential in the anodic direction up to 1 V at a scan rate of 1 mV s^{-1}.

2.2.4 Surface characterization

2.2.4.1 X-ray photoelectron spectroscopy

X-ray photoelectron spectroscopy (XPS) was used to determine the presence of the oxide and organic layers and the elemental composition in the first few nanometres of a surface [81]. XPS analysis was performed on a TFA Physical Electronics Inc. spectrometer equipped with a hemispherical analyser. All the spectra were acquired utilizing a monochromatic Al K_{α} X-ray source (1486.6 eV) with an analysed area of 400 μm in diameter. Survey scan spectra were obtained at a pass energy of 187.9 eV, while the core level single peaks were measured at pass energy of 29.4 eV with an energy step of 0.1 eV. The take-off angle, defined as the emission angle normal to a sample surface, was 45°. The binding energies (E_b) were calibrated by reference to the C 1s photoelectron peak at 284.8 eV. The uncertainty in the binding energy scale is estimated to be 0.2 eV. The linear method was used for the Cu 2p line and the iterative Shirley method for the Cu LMM, followed by smoothing using a Savitzky-Golay algorithm [94]. The quantitative analysis of the species at the surface was derived from the peak area intensities. Quantification was carried out using the MultiPak processing software (Version 8.1). The estimated relative error for all XPS data used for elemental quantification is ± 2 %.

2.2.4.2 Scanning electron microscopy coupled with energy-dispersive X-ray spectroscopy

Scanning electron microscopy combined with energy-dispersive X-ray spectroscopy (SEM-EDS) was applied to reveal the morphology and semi-quantitative composition of the surface at areas of interest, with an analysis depth of about 1 μm. SEM images were recorded in secondary electron (SE) and back-scattered electron (BSE) imaging modes at beam energies of 5 keV and 15 keV, respectively, using a field emission (FE) SEM JSM 7600F, JEOL, Japan, equipped with EDS (Inca Oxford 350 EDS SDD). Before analysis, Al and Cu samples were coated with a thin carbon layer to reduce the charging effect.

2.3 Results and Discussion

2.3.1 Copper

2.3.1.1 Potentiodynamic polarization curves

Fig 2.3. shows the potentiodynamic polarization curves for mechanically (mc) and chemically (ch) pre-treated copper samples without inhibitor (i.e., control samples) in 3 wt.% NaCl solution open to the air. Utilizing the Pourbaix (*E* vs. pH) diagram of copper in chloride-containing aqueous solution [44], it can be assumed that at the mean E_{corr} (−250 mV) and more positive potentials (to approximately 1000 mV (Ag/AgCl$_{sat'd}$)), Cu reacts to form chloride species such as CuCl and $CuCl_2^-$, and Cu^{2+} ions. It is generally accepted that the anodic dissolution of copper in neutral NaCl solutions is a mass transfer rather than activation controlled process in which the diffusion of soluble $CuCl_2^-$ species from copper to the bulk of the solution is the rate-determining step [44], [95], [96]. As long as the salt film is present, the dissolution process is governed by diffusion kinetics [97].

The related anodic polarization curve recorded for the control sample (mc) after 1 h at OCP demonstrates apparent Tafel behaviour with a slope of 61 mV/dec, which corresponds to 2.3 RT/F, i.e., 59 mV/dec (Fig. 2.4a) [44], [95]. In addition, it should be noted that the ch curve shows similar electrochemical characteristics as mc.

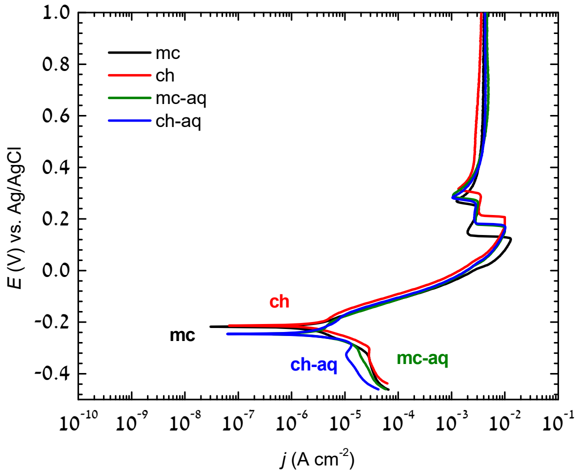

Figure 2.3: Potentiodynamic polarization curves recorded for copper samples in 3 wt.% NaCl solution. The copper surface before measurements implies (a) mechanical pre-treatment and (b) chemical pre-treatment. The samples differ only in immersion time; mc and ch samples were immersed in a chloride solution for 1 h and mc-aq and ch-aq for 24 h.

Considering the potentiodynamic polarization response of Cu measured after 24 h immersion in chloride solution (mc-aq) (Fig. 2.4c), a small passivity at lower overpotentials was noticed that is barely observed for mc (Fig. 2.4a). This makes the determination of the anodic Tafel slope difficult, and it is more appropriate to determine it from the cathodic branch and intersection with E_{corr}. The mc-aq sample was immersed in chloride solution for 24 h at OCP before the polarization measurements, while mc was immersed for 1 h at OCP before PD testing in 3 wt.% NaCl. Prolonged exposure to NaCl solution may indicate a thicker barrier layer of Cu_2O on the porous and poorly protective CuCl layer [48], [51], [95]. Moreover, the appearance of the passivation region, due to the existence of a $CuCl/Cu_2O$ film and its corresponding pitting potential (E_{pit}), may suggest the occurrence of pitting corrosion [48]. The pitting behaviour is caused by the ease of penetration of chloride ions at some insufficiently protected sites on the surface of Cu, which are weak spots where the localized attack begins.

Although anodic behaviour is the area of primary interest, it is necessary to note a few observations regarding cathodic polarization behaviour. The only oxidants (i.e., reducible species) in near-neutral chloride solutions open to the air (pH = 5.5) were dissolved oxygen and hydrogen ions. Examination of the cathodic polarization curve for mc-aq (Fig. 2.4c) shows that the E_{corr} is higher than the equilibrium potential of H^+/H_2, i.e., $E_{H^+/H_2} = -0.0591$ (pH) vs. V_{SHE} at 25 °C (Eq. 1.6); therefore, at potentials immediately below the E_{corr}, cathodic behaviour is governed by the oxygen reduction reaction (ORR) [44]. In practice, the limit of (Eq. 1.6) has been moved towards more negative values because the cathodic polarization, initiated 250 mV below the E_{corr} and then gradually increased towards more positive values, caused the rise of pH in local regions. If the solution is stationary and/or when the pH is higher in the presence of dissolved O_2, diffusion of H^+ ions will be slow, and concentration polarisation can act to shorten the linear Tafel region in the cathodic branch. For a scenario like the mc-aq case, linearity disappears altogether, with the cathodic reaction now under combined activation and diffusion control at E_{corr}; the contribution of mass transport is predominant based on the high cathodic slope [44], [98]. Also, at higher cathodic overpotentials (i.e., at lower potentials, near the region of polarization initiation), the activation polarization and concentration polarization co-occur; the O_2 reduction is under diffusion control, and the H^+ reduction is under activation control [99]. All of the results taken together lead to the conclusion that at $E_{corr,}$ the ORR is under mixed kinetic control.

Another interesting feature is that at a potential of −0.33 V, a cathodic current peak was observed (especially for the ch-aq), which may be attributed to the reduction of Cu_2O film. The surface composition of the ch-aq (see below, Table 2.4) revealed the presence of Cu_2O, so it is reasonable to expect its reduction during cathodic polarization. This conclusion is consistent with the results of Benzbiria et al. [98], obtained by rotating disk electrode (RDE), where the cathodic peak at −0.29 V independent of the electrode rotation rate was reported. Given that anodic and cathodic curves (mc-aq and ch-aq) do not show a clear Tafel region, we suggest that the most appropriate procedure to determine the corrosion current of the system would be the extrapolation of the cathodic pseudo-limited-current density (p-j_L) back to the zero overvoltage (Figs. 2.4c and 2.4d). The term „pseudo“ was introduced to denote a deviation from the conditions of pure mass transfer. The p-j_L was determined as the halfway point of the potential limits of the linear cathodic region and was estimated to be 25 µA cm^{-2} under stagnant electrolyte conditions, which is close to the literature value of 20-30 µA cm^{-2} in neutral solution, as reported by Vukmirovic et al. [100] using RDE set-up. The more accurate j_L or the contribution of charge transfer could be derived from the Koutecky-Levich equation [101] in the RDE measurements. Because the net rate of the anodic reaction (i.e., copper corrosion) must equal the net rate of the cathodic reaction (i.e., mainly oxygen reduction), and given that the slowest reaction controls the rate of corrosion, it can be concluded that ORR kinetics determine the general corrosion rate of copper at the OCP because the ORR is slower than the anodic dissolution of copper [92], [99]. Since the corrosion of copper is under cathodic control (predominantly controlled by concentration polarization), it is, therefore, crucial for reducing the rate of ORR.

Organic films for both types of pre-treated samples were prepared by liquid-phase deposition either from ethanol (et) or aqueous (aq) solution containing MBI (S) and OPA (P) inhibitors. The current density responses of the mc-S-Et and mc-P-Et (Fig. 2.4a), but also the ch-S-Et and ch-P-Et (Fig. 2.4b), seem to be very similar to the control sample mc and ch (Table 2.2). The only difference is that the OCP of both samples modified with MBI, S-mc-Et and S-ch-Et, is shifted towards more positive values for ca. 40 mV. This could mean that the possibly pre-formed Cu-MBI layer in ethanol immediately falls off the electrode when immersed in NaCl solution. Moreover, the chemical composition (see below, Table 2.4) of the copper surface, derived from the XPS spectra, revealed the absence of sulphur and phosphorus, indicating that neither Cu-MBI nor Cu-OPA films were present after the functionalization step in the ethanolic solution of MBI and OPA followed by immersion in NaCl solution for 24 h, respectively (see below).

In contrast to the inhibitor deposition from the ethanol solution, mechanically (S-mc-aq) and chemically (S-ch-aq) pre-treated copper specimens were prepared by 24 h immersion in aqueous MBI+NaCl, followed by potentiodynamic measurements in NaCl+MBI solution.

Table 2.2: Electrochemical parameters – corrosion potential (E_{corr}), corrosion current density (j_{corr}), pitting potential (E_{pit}), passive range ($\Delta E_{\mathrm{pass}} = |E_{\mathrm{pit}} - E_{\mathrm{corr}}|$), passive current density (j_{pass}), anodic Tafel slope (b_a) and cathodic Tafel slope (b_c) – deduced for Cu from the potentiodynamic polarization curves (Fig. 2.3 and Fig. 2.4).

Cu samples	$\boldsymbol{E_{\mathrm{corr}}}$ **(mV$_{\mathrm{Ag/AgCl}}$)**	$\boldsymbol{j_{\mathrm{corr}}}$ **(A cm^{-2})**	$\boldsymbol{E_{\mathrm{pit}}}$ **(mV)**	$\boldsymbol{\Delta E_{\mathrm{pass}}}$ **(mV)**	$\boldsymbol{j_{\mathrm{pass}}}$ **(A cm^{-2})**	$\boldsymbol{b_a}$ **(mV/dec)**	$\boldsymbol{-b_c}$ **(mV/dec)**
mc-aq	−250	2.50×10^{-5}	−200	50	4.67×10^{-6}	64	384
mc-S-aq	−120	6.24×10^{-9}	160	280	3.86×10^{-7}	74	103
mc-P-aq	−192	2.26×10^{-6}	–	–	–	48	204
ch-aq	−245	1.58×10^{-5}	−172	70	8.98×10^{-6}	61	295
ch-S-aq	−92	3.25×10^{-8}	200	290	6.50×10^{-7}	105	120
ch-P-aq	−165	1.51×10^{-6}	–	–	–	31	164

For such prepared specimens, the current densities of both corrosion reactions are diminished together with the shift of E_{corr} more positive than the control sample (mc-aq) (Figs. 2.4c and 2.4d). This can be attributed to the Cu(I) complexation with MBI and subsequent adsorption of the complex formed on the copper surface. Because there is a significant reduction in the j_{corr} by almost four orders of magnitude, MBI is considered a very effective corrosion inhibitor for copper in an aqueous chloride-containing solution. In the Tafel region, only a small portion of the anodic Tafel slope is available, which is considered not well-defined. The linearity between E and log j is interrupted after E_{pp} is reached, whereby significant passivity occurs. The improved resistance to localized corrosion is reflected by increased pitting (breakdown) potential, as shown in the polarization curves of Fig. 2.4c.

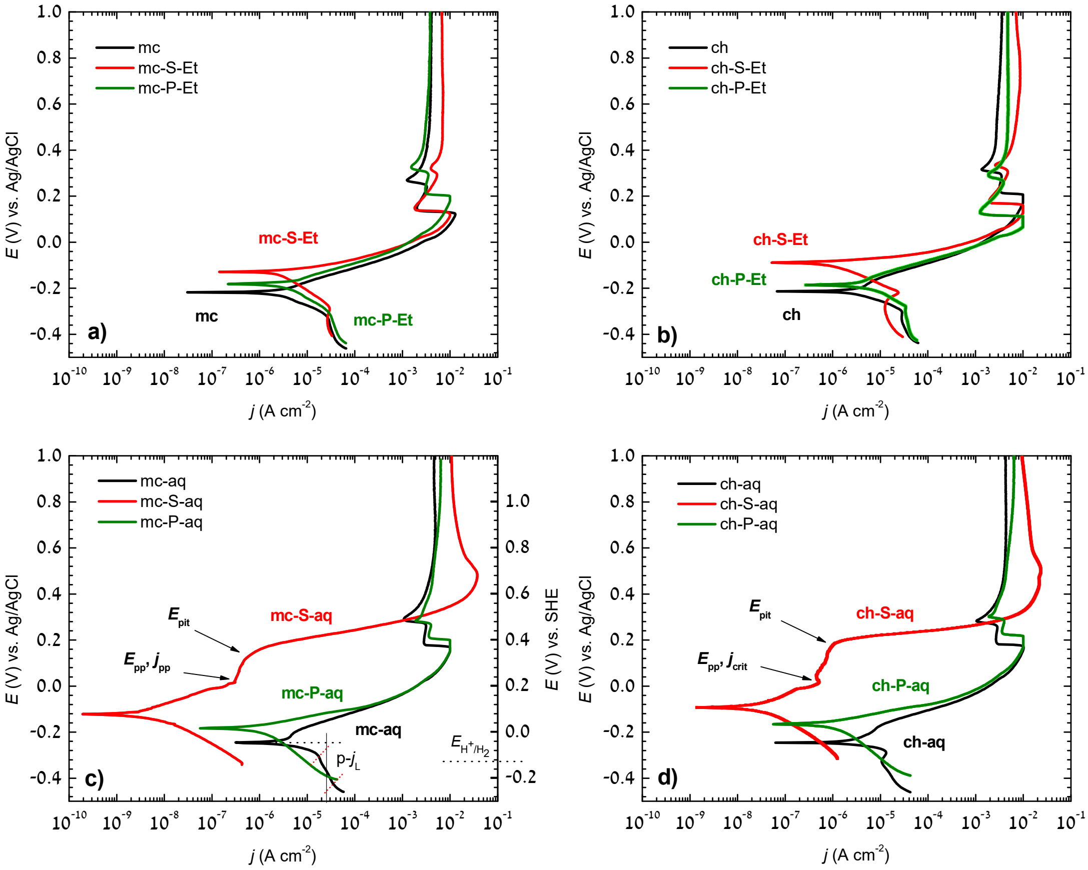

Figure 2.4: Potentiodynamic polarization curves recorded for copper in (a and b) 3 wt.% NaCl solution and (c and d) 3 wt.% NaCl with the addition of 1 mM OPA or MBI. The copper surface before measurements implies: (a) mechanical pre-treatment + deposition of inhibitors from ethanol solution, (b) chemical pre-treatment + deposition from ethanol solution, (c) mechanical pre-treatment + deposition from aqueous solution, and (d) chemical pre-treatment + deposition from aqueous solution.

Regarding the cathodic polarization curve for mc-S-aq, an evident change in kinetics relative to the control sample was observed. The Tafel region with a corresponding slope of approx. 100 mV/dec was established together with a significant decrease in current density, indicating a charge-transfer controlled process, i.e., the rate of oxygen reduction is controlled by the potential across the interface, not by the rate at which dissolved oxygen diffuses to the metal surface. It is believed that the adsorption of MBI molecules on the surface of copper minimizes the number of active sites where oxygen is expected to adsorb.

The same is true for the ch-S-aq. The anodic current density increases as an exponential function of potential until reaching a critical passivating current density, j_{crit}, at a potential E_{pp}, at which point a large decrease in current density is observed in an upward scan (Fig. 2.4d). Moreover, ch-S-aq shows somewhat more positive E_{corr} and broader ΔE_{pass}, but larger j_{corr} by factor of 5 with respect to mc-S-aq. It is difficult to decide which of these two samples has an advantage in corrosion protection because their electrochemical parameters are comparable (Table 2.2). In summarizing, the polarization curves in Figs. 2.4c and 2.4d (red curves) clearly showed that MBI is a mixed-type inhibitor for copper in aqueous chloride solutions. It reduces the rate of the anodic reaction more strongly than the cathodic reaction rate and makes the OCP of copper more positive. Unlike MBI, the OPA induce only a slight reduction of charge transfer on Cu (Figs. 2.4c and 2.4d). Interestingly, the contribution of mass transfer for the cathodic reaction is significantly smaller than the control sample.

Moreover, the i_{corr} for mc-P-aq is smaller than for mc-aq by 5 times, but without any significant impact since pitting occurs immediately (i.e., at the OCP). Generally, at E_{pit}, the current density rises due to the active dissolution within developing corrosion pits. The same is true for the ch-P-aq relative to the control ch-aq Cu sample. Inferior inhibitory properties of OPA have been confirmed by the absence of phosphorus content on the copper surface for both samples, mc-P-aq and ch-P-aq (see below, Table 2.4).

2.3.1.2 Cyclic voltammetry

Fig. 2.5 shows cyclic voltammograms for copper-based samples: mc-aq, mc-S-aq, mc-P-aq, ch-aq, ch-S-aq and ch-P-aq, recorded in 3 wt.% NaCl solution with and without added MBI and OPA inhibitors after 24 h of immersion, at a scan rate of 10 mV s^{-1}. For mechanically pre-treated copper sample immersed in 3 wt.% NaCl solution (mc-aq), two anodic peaks, at 0.29 V (peak A_1) and 0.52 V (peak A_2) in the forward scan, and a single cathodic peak at −0.31 V (peak C_1) in the reverse scan, are observed (Fig. 2.5a). Peak A_1 can be attributed to the formation of CuCl salt via (Eq. 1.8). The shoulder peak A_2 accounts for the electro-oxidation of Cu(I) to soluble Cu^{2+} followed by a limiting current in the plateau region, the equilibrium between CuCl and $CuCl_2^-$ (Eq. 1.9). The intensity of the limiting current indicates a poorly protective and porous film. The only cathodic peak, C_1, is ascribed to the reduction of Cu(I) to Cu(0), i.e., CuCl to Cu.

Chemisorbed MBI on the Cu substrate, mc-S-aq, retard electron transfer across the electrode interface so that the peak A_1 disappears completely, which suggests an excellent inhibition efficiency (Fig. 2.5a). Such behaviour coincides with the existence of passivation observed in polarization curves measurements (vide supra, Fig. 2.4a). The current suddenly rose sharply at potentials above 0.4 V, reaching the maximum at 0.82 V (peak A*). The position of this prominent peak is at more positive potential than expected to be attributed to a simple transition from Cu(I) to Cu(II). We reported previously [102] that the enlarged current densities of the peak A* could be assigned to the film degradation caused by oxidative dimerization of Cu(I)-MBI according to:

$$2\mathrm{Cu\text{-}MBI} \longrightarrow 2\mathrm{Cu}^{2+} + (\mathrm{MBI})_2 + 4\mathrm{e}^- \tag{2.1}$$

The overall oxidation reaction consists of the two competing half-cell reactions:

$$\mathrm{Cu}^+ \longrightarrow \mathrm{Cu}^{2+} + 2\mathrm{e}^- \tag{2.2}$$

$$2\mathrm{MBI}^- \longrightarrow (\mathrm{MBI})_2 + 2\mathrm{e}^- \tag{2.3}$$

It is striking to note that, indeed, the peak A*(inset of Fig. 2.5a) may be deconvoluted into two Gaussian peaks: (a) the smaller peak labelled A_2, which could be attributed to the anodic oxidation of Cu(I) to Cu (II) ions (Eq. 2.2), and (b) a broader and larger peak labelled A_3, which could correspond to the oxidative dimerization of MBI^- (Eq. 2.3). The peak A_2 becomes noticeable at higher sweep rates such as 10 mV s^{-1}. This is why we did not noticed it earlier, where all measurements were performed at a scan rate of 1 mV s^{-1} [102]. The interpretation of observed phenomena coincides with the results of XPS and ToF-SIMS investigation of the products collected after cyclic voltammetry run, which is discussed in detail in *Chapter 4*.

Note that using the Gaussian peak function to fit the cyclic voltammogram does not provide information on the actual A_2/A_3 peak ratio but qualitatively shows the components comprising the larger A* peak.

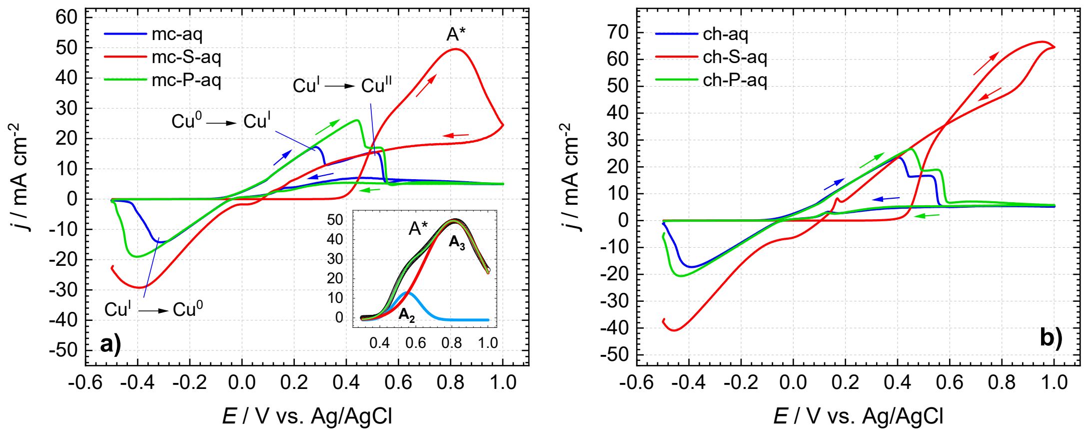

Figure 2.5: Cyclic voltammograms recorded for copper in 3 wt.% NaCl solution with and without the addition of 1 mM OPA or MBI at a scan rate of 10 mV s^{-1}. The copper surface prior to measurements implies: (a) mechanical pre-treatment + deposition of inhibitors from aqueous solution and (b) chemical pre-treatment + deposition of MBI from aqueous solution.

It is noteworthy that the oxidation of Cu(I) to Cu(II) is an irreversible process since the soluble Cu^{2+} species diffuse away from the electrode surface and thus cannot be reduced in the cathodic scan. On the other hand, the transition from Cu(0) to Cu(I) is a partially irreversible system, where the cathodic peak is not as pronounced as the anodic one ($I_{\mathrm{p,a}}/I_{\mathrm{p,c}} \neq 1$) and the peak-to-peak separation is greater than 59 mV at 25 °C ($\Delta E_\mathrm{p} > 0.059$ V). There is a high barrier to electron transfer, i.e. slow electron transfer at the electrode surface, so the more positive (negative) potentials are required to observe oxidation (reduction) reactions, giving rise to larger ΔE_p [103].

The voltammogram in Fig. 2.5b for the chemically pre-treated copper sample shows similar redox trends as mechanical pre-treatment. However, a few significant differences should be highlighted. First, the intensities of the peaks A_1 and A_2 for ch-aq in chloride solution are greater than for the mc-aq. This can be explained based on the SEM image

(Fig. 2.8), which suggests that the chemical treatment caused an increased surface roughness, increasing the surface area and thus current densities. Second, the $i_{\mathrm{p,a}}$ of the A* for ch-S-aq is also higher than the $i_{\mathrm{p,a}}$ for the mc-S-aq, indicating that more Cu-MBI film was degraded, which is a simple consequence of an immense amount of adsorbed inhibitor during the process of organic film formation. XPS surface analysis revealed (Fig. 2.7, Table 2.4) a higher elemental ratio between N and S for ch-S-aq compared to mc-S-aq (Table 2.4), which is consistent with a larger surface area caused by chemical etching (Fig. 2.8).

Another interesting feature of the copper samples protected with MBI (i.e., mc-S-aq and ch-S-aq) is that the cathodic peak $\mathrm{C_1}$ exists in the reverse scan, although the corresponding anodic peak $\mathrm{A_1}$ does not appear at all in the forward scan. This should come as no surprise given that Cu-MBI film formation was accompanied by the formation of $\mathrm{Cu_2O}$ underlayer during the preparation of samples mc-S-aq and ch-S-aq. Such finding was previously published by our group [102], and it is elaborated on further in Chapter *4*. When such a sample is anodically polarized, the $\mathrm{A_1}$ peak, corresponding to the oxidation of Cu(0) to Cu(I), is suppressed entirely due to the high inhibition efficiency of Cu-MBI layer. Furthermore, after the Cu-MBI film decomposes at higher potentials, the remaining $\mathrm{Cu_2O}$ and possibly $\mathrm{CuCl/CuCl_2^-}$, formed upon doping of cuprous oxide, could be reduced to metallic Cu at sufficient negative potentials during the reverse scan. Based on this, it can be assumed that the $\mathrm{C_1}$ peak would not appear if the degradation of the inhibitor did not occur. This is confirmed for the Cu substrate covered with the polymerized Cu-MBI film [12], shown in *Chapter 4*.

Another set of experiments, which includes the influence of the potential scanning rate (Fig. 2.6, Table 2.3), was performed over the 1-10 mV $\mathrm{s^{-1}}$ range. Peak $\mathrm{A_1}$ was well-defined, and peak $\mathrm{A_2}$ appeared like a shoulder, whatever the scan rate. The intensities of peaks $\mathrm{A_1}$, $\mathrm{A_2}$ and $\mathrm{A_3}$, and $\mathrm{C_1}$ fit a linear relationship vs square root of sweep rate ($\upsilon\nu^{1/2}$) for all samples (Figs. A.1-A.6), with a slight deviation of the intercept from the origin.

Such deviation may be related to electrode roughness or adsorbed species on the surface. The potential of peaks $\mathrm{A_1}$, $\mathrm{A_2}$, $\mathrm{A_3}$ and $\mathrm{C_1}$ also linearly increases with $\upsilon\nu^{1/2}$. Since both E_{p} and I_{p} change linearly with $\upsilon\nu^{1/2}$, we report that copper corrosion in 3 wt.% NaCl solution, but also the formation of the metal-inhibitor layer (Cu-MBI), obeys the Müller-Casandra passivation model [104]. This is very likely because Cu in chloride solutions forms a layer of insoluble CuCl salt (mc-aq), while MBI forms an insoluble complex with Cu(I) ions forming Cu-MBI (mc-S-aq). It should be noted that mc-P-aq also follows the passivation model, but compared to MBI, OPA does not mitigate copper corrosion but accelerates it, which can be inferred from the increased currents of peaks $\mathrm{A_1}$ and $\mathrm{A_2}$.

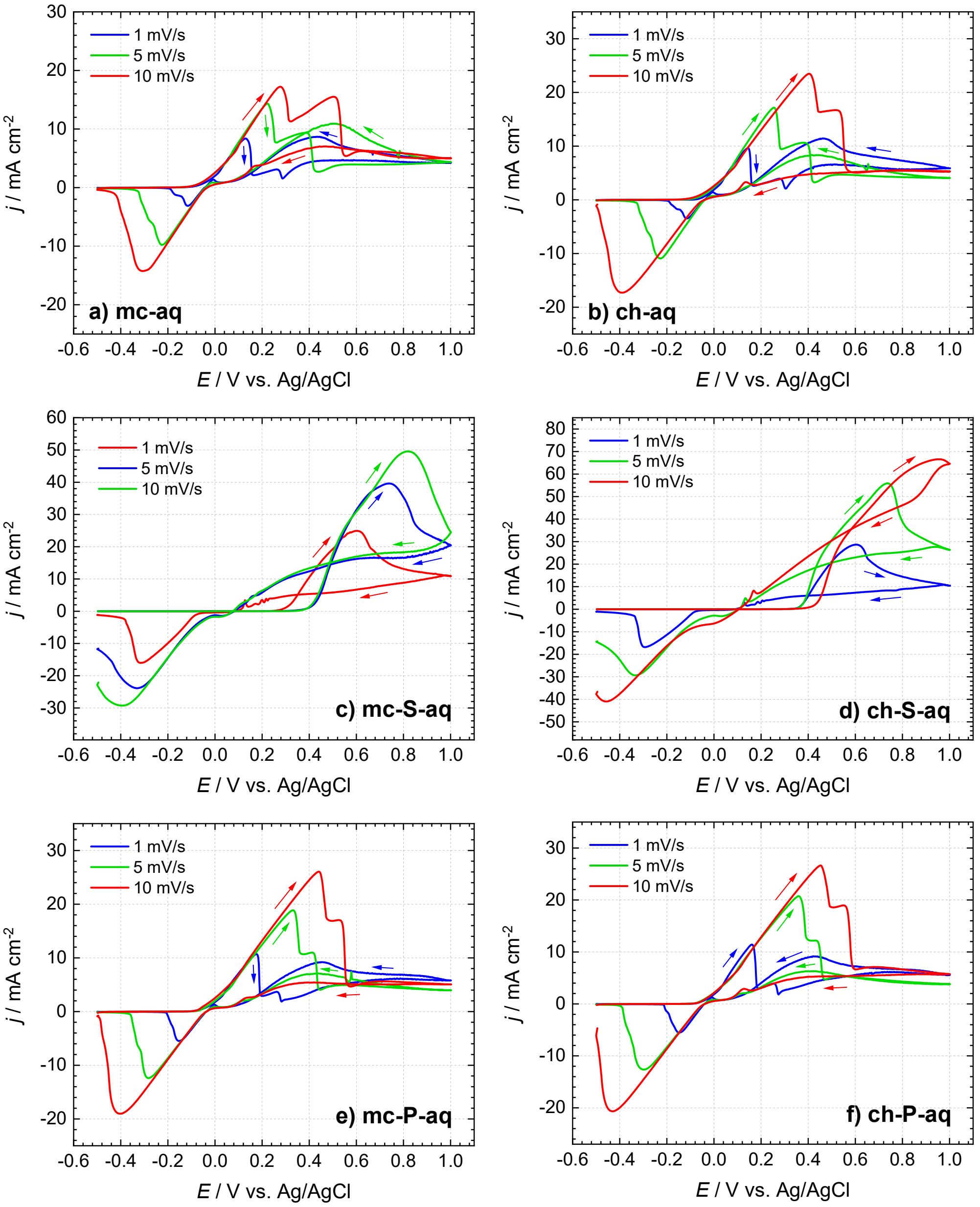

Figure 2.6: Cyclic voltammograms recorded for copper in 3 wt.% NaCl solution with and without the addition of 1 mM OPA or MBI at different scan rates; 1, 5 and 10 mV s^{-1}. The copper surface before measurements implies: (a) mechanical pre-treatment, control sample, (b) chemical pre-treatment, control sample, (c) mechanical pre-treatment + deposition of MBI from aqueous solution, and (d) chemical pre-treatment + deposition of MBI from aqueous solution, (e) mechanical pre-treatment + deposition of OPA from aqueous solution, and (f) chemical pre-treatment + deposition of OPA from aqueous solution.

Table 2.3: The relationships between the peak current (j_p), peak potential (E_p), and the square root of the scan rate ($\nu^{1/2}$) for redox reactions that obey the passivation model deduced from the cyclic voltammograms for Cu (Fig. 2.6).

Samples	**j(A$_1$) [mA cm^{-2}]**	**E(A$_1$) [mV]**	**j(A$_2$) [mA cm^{-2}]**	**E(A$_2$) [mV]**
	Passivation model			
	$j_\mathrm{p} = \mathrm{x} \cdot \nu^{1/2} + \mathrm{y}$	$E_\mathrm{p} = \mathrm{x'} \cdot \nu^{1/2} + \mathrm{y'}$	$j_\mathrm{p} = \mathrm{x} \cdot \nu^{1/2} + \mathrm{y}$	$E_\mathrm{p} = \mathrm{x'} \cdot \nu^{1/2} + \mathrm{y'}$
mc-aq	$j_\mathrm{p} = 4.18 \cdot \nu^{1/2} + 4.41$ ($\mathrm{R}^2 = 0.9889$)	$E_\mathrm{p} = 69.56 \cdot \nu^{1/2} + 61.65$ ($\mathrm{R}^2 = 0.9989$)	$j_\mathrm{p} = 5.70 \cdot \nu^{1/2} - 2.72$ ($\mathrm{R}^2 = 0.9946$)	$E_\mathrm{p} = 110.68 \cdot \nu^{1/2} + 147.28$ ($\mathrm{R}^2 = 0.9988$)
ch-aq	$j_\mathrm{p} = 6.41 \cdot \nu^{1/2} + 3.16$ ($\mathrm{R}^2 = 0.9986$)	$E_\mathrm{p} = 0.12 \cdot \nu^{1/2} + 0.01$ ($\mathrm{R}^2 = 0.971$)	$j_\mathrm{p} = 5.94 \cdot \nu^{1/2} - 2.23$ ($\mathrm{R}^2 = 0.9964$)	$E_\mathrm{p} = 0.11 \cdot \nu^{1/2} + 0.15$ ($\mathrm{R}^2 = 0.9615$)
mc-S-aq	$j_\mathrm{p} = 11.22 \cdot \nu^{1/2} + 13.37$ ($\mathrm{R}^2 = 0.9990$)	$E_\mathrm{p} = 102.37 \cdot \nu^{1/2} + 501.67$ ($\mathrm{R}^2 = 0.9946$)		
ch-S-aq	$j_\mathrm{p} = 17.76 \cdot \nu^{1/2} + 12.75$ ($\mathrm{R}^2 = 0.9752$)	$E_\mathrm{p} = 182.42 \cdot \nu^{1/2} + 360.95$ ($\mathrm{R}^2 = 0.9717$)		
mc-P-aq	$j_\mathrm{p} = 7.05 \cdot \nu^{1/2} + 3.57$ ($\mathrm{R}^2 = 0.9976$)	$E_\mathrm{p} = 125.12 \cdot \nu^{1/2} + 46.49$ ($\mathrm{R}^2 = 0.9994$)	$j_\mathrm{p} = 6.13 \cdot \nu^{1/2} - 2.47$ ($\mathrm{R}^2 = 0.9981$)	$E_\mathrm{p} = 125.12 \cdot \nu^{1/2} + 136.49$ ($\mathrm{R}^2 = 0.9994$)
ch-P-aq	$j_\mathrm{p} = 7.11 \cdot \nu^{1/2} + 4.53$ ($\mathrm{R}^2 = 0.9960$)	$E_\mathrm{p} = 140.00 \cdot \nu^{1/2} + 28.09$ ($\mathrm{R}^2 = 0.9885$)	$j_\mathrm{p} = 7.01 \cdot \nu^{1/2} - 3.25$ ($\mathrm{R}^2 = 0.9886$)	$E_\mathrm{p} = 139.55 \cdot \nu^{1/2} + 115.69$ ($\mathrm{R}^2 = 0.9951$)

2.3.1.3 X-ray photoelectron spectroscopy

The chemical composition (Table 2.4), deduced from the survey spectra, showed that control samples (mc-aq and ch-aq) contain high content of Cu and O, which can be attributed to the formation of the oxide layer. Upon exposure to MBI containing aqueous chloride solution (mc-S-aq and ch-S-aq), the concentration of Cu and O at the surface layer diminished together with the trend of increasing concentration of C, N and S. In contrast, phosphorus was not detected on the surface of mc-P-aq and ch-P-aq, which is in line with the electrochemical performance. Table 2.4 also reveals that the metal-inhibitor complexes did not form on the surface of samples modified with inhibitors in EtOH solution.

Fig. 2.7a displays high-resolution XPS spectra of the Cu 2p core level and the Cu LMM Auger transition for all ten non-inhibited and inhibited copper samples. Results reveal a general tendency for Cu_2O formation, following other reports where preferably Cu(I) oxide was produced on the surface of copper in the chloride solutions [41], [48], [105]. The $Cu2p_{3/2}$ peak at 932.5 eV could be assigned to Cu_2O as we expect, but it is essentially impossible to distinguish between Cu and Cu_2O based on $Cu2p_{3/2}$ photoelectron line measurements because the binding energy for the two is too close to be distinguished within the measured uncertainty [106]. To this end, the intense peak at 570.1 eV in the Auger Cu LMM bands (Fig. 2.7b) of all samples is an indication that Cu_2O is present on the surface, whereas the contribution of metallic Cu is well-separated by a shift in binding energy (E_b) of 2 eV, i.e., it is at 568.1 eV [107]–[109]. Copper(II) was not detected in any of the samples due to a lack of strong satellite peaks that would appear in the range 942-947 eV [106] (Fig. 2.7a). In the Auger spectra of mc-S-aq and ch-S-aq samples, the peaks are broadened, indicating an extra component at about 570.4 eV, probably arising from the formation of a complex between Cu(I) and MBI.

Furthermore, the presence of inhibitor film was corroborated by inspection of N 1s and S 2p spectra (Figs. 2.7c and 2.7d). Nitrogen was detected in all samples treated with the inhibitor (Fig. 2.7c) but with a significant amount only in mc-S-aq and ch-S-aq. This is consistent with the sulphur content detected only for these two samples. The atomic ratio of N/S is between 2.6 and 2.7 for mc-S-aq and ch-S-aq, which is greater than the stoichiometric ratio of N/S, being 2 for an MBI molecule. The N 1s spectra comprise pyridine (C=N—C) peak at 398.9 eV and pyrrole (C—NH—C) peak at 400.1 eV. The intensity ratio of $I_{\text{pyridine}}/I_{\text{pyrrole}}$ is almost 1:1 (with a slightly higher pyridine peak) for mc-S-aq, whereas the pyrrole peak is larger than the pyridine peak for ch-S-aq. Such a difference in the ratio between nitrogen components suggests that the MBI bond to copper surfaces differently.

Table 2.4: Chemical composition of the copper surface after 24 h of immersion in: 1) 3 wt.% NaCl with and without the addition of 1 mM 2-mercaptobenzimidazole (S), octylphosphonic acid (P), and 2) ethanolic solution containing S and P. The copper surface before measurements implies: (a) mechanical pre-treatment + deposition of inhibitors from ethanol solution, (b) chemical pre-treatment + deposition from ethanol solution, (c) mechanical pre-treatment + deposition from aqueous solution, and (d) chemical pre-treatment + deposition from aqueous solution.

Sample		mechanical pre-treatment					chemical pre-treatment				
Solution		NaCl	+MBIH (S)		+OPA (P)		NaCl	+MBIH (S)		+OPA (P)	
Inhibitor medium		aq	EtOH	aq	EtOH	aq	aq	EtOH	aq	EtOH	aq
Elements	Cu	45.3	35.8	7	30.8	43.4	40.2	28.2	6.4	28.9	35.1
	O	26.4	25.2	6.5	25.3	19.4	25.5	25.3	8.2	25.2	21.1
	C	27.8	36.2	69.7	40.3	35.4	29.6	42.7	68	42.8	41.5
	Cl	0.5	0.8	–	1.7	–	1.5	–	–	–	–
	N	–	2	12.1	1.9	1.8	3.2	3.8	12.7	3.1	2.3
	S	–	–	4.7	–	–	–	–	4.7	–	–
	P	–	–	–	–	–	–	–	–	–	–

In our previous publications [45], [73], we showed, by DFT calculations, that the MBI molecules adsorb on the copper surface either as thione or thiolate, with the preference between the two depending on surface details. Furthermore, our XPS results [45] suggested that when the ratio of $I_{\mathrm{pyridine}}/I_{\mathrm{pyrrole}} = 1$, the MBI molecules adsorb on the copper surface as deprotonated thiolates due to the equal peak contribution of the two chemical states.

On the other hand, when the pyrrole peak predominates over pyridine, it indicates that some MBI molecules, in addition to being adsorbed as thiolate, also adsorb as thione (see below Fig. 3.6) [45]. To conclude, in the mc-S-aq sample, the MBI was adsorbed on the copper surface as thiolate, whereas in ch-S-aq, MBI is adsorbed as thiolate and thione. It seems that chemical etching with HNO_3 altered the copper surface.

The sulphur 2p spectra consist of S $2p_{3/2}$ and S $2p_{1/2}$ spin-orbit components that differ by only 1.1 eV with $2p_{3/2}/2p_{1/2}$ intensity ratio of about 2. Both peaks, S $2p_{3/2}$ at 162.5 eV and S $2p_{1/2}$ at 163.6 eV, are attributed to a single chemical state of metal-mercapto compounds, i.e., Cu-S-C bonding [41], [72], [110].

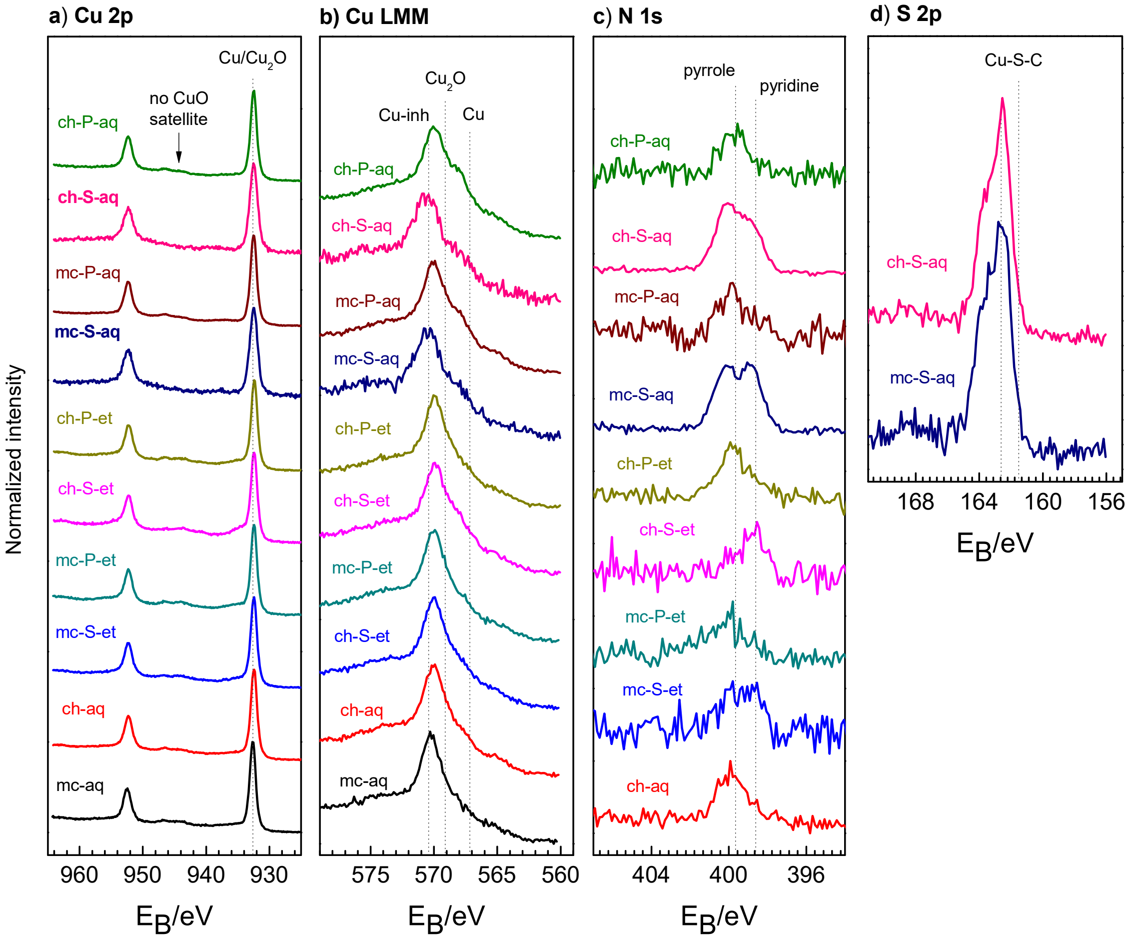

Figure 2.7: High-resolution XPS spectra of (a) Cu 2p, (b) Cu LMM, (c) N 1s, and (d) S 2p recorded after immersion of copper in: 1) 3 wt.% NaCl solution for 24 h with and without the addition of 1 mM OPA or MBI, and 2) ethanolic solution containing MBI and OPA. The modification of copper surface before XPS measurements implies: mechanical or chemical pre-treatment and deposition of MBI or OPA either from ethanol or aqueous solution.

2.3.1.4 Scanning electron microscopy coupled with energy-dispersive X-ray spectroscopy

The surfaces of mechanically and chemically pre-treated samples were examined by FE-SEM coupled with EDS to determine the morphology, structure and composition of the surface layers (Fig. 2.8). The surface of the mechanically abraded copper immersed in chloride solution (mc-aq) appears to have corroded uniformly (Fig. 2.8a). Moreover, large chloride-containing aggregates were observed along with the SiC inclusions originating from sandpaper. Deposition of MBI and OPA from ethanolic solution followed by immersion in chloride solution (mc-S-et and mc-P-et) caused significant damage to the copper surface (Fig. A.7). The compositional analysis showed the presence of chloride-containing corrosion products (Fig. 2.9a). The copper oxide layer was detected for all five samples that had been mechanically pre-treated (Fig. 2.9). The high carbon content is associated with the sputter coating of the samples before SEM imaging, which is necessary to increase the conductivity of organic surfaces and thus obtain a good-quality image.

In contrast, the deposition of MBI from an aqueous solution containing NaCl (mc-S-aq) leads to significant corrosion protection, which can be inferred from a smooth surface on which traces from the grinding process are still visible (Fig. 2.8b). In addition, some small clusters may be noticed at higher magnification (the inset in Fig. 2.8b) which at first glance can be attributed to corrosion products. However, the BSE image and EDS analysis revealed that the cluster originates from an inhibitor since it contains nitrogen and sulphur (Fig. 2.9b). Also, the cluster contains chlorine which correlates with the polymerized [Cu-Cl-MBI]$_n$ structure observed in our previous publication [102] for copper samples treated with an aqueous chloride solution containing a synergistic combination MBI and OPA. This study will be further elaborated on in the next chapter. Another inhibitor, OPA, dissolved in an aqueous solution (mc-P-aq), caused severe corrosion of copper (Fig. 2.8c). Interestingly, chlorine was not detected on the surface of this sample (Fig. 2.9c). On the other hand, the surface of copper chemically etched (ch-aq) seems to become much rougher (Fig. 2.8d) than mc-aq. The visible large aggregates marked with green arrows are attributed to the chloride corrosion products.

The chemically pre-treated copper surface after exposure to MBI and OPA solutions, either ethanolic (Figs. A.7 and A.9) or aqueous (Figs. 2.8 and 2.10), behave similarly to their counterparts, i.e., mechanically prepared copper samples treated with inhibitors (Figs. 2.8 and 2.9, Figs. A.7 and A.8). Only ch-S-aq showed the inhibition of corrosion in chloride solution.

The surface of ch-S-aq (Fig. 2.8e) was less rough than the surface of the control sample (ch-aq), with no visible corrosion products. However, the EDS detected clusters corresponding to MBI (Fig. 2.10b), as described in the case for mc-S-aq. Noteworthy is that the oxygen was not detected on the surface covered with the thin Cu-MBI film. Since the surface composition of ch-S-aq is the same as mc-S-aq, the somewhat more pronounced corrosion inhibition of ch-S-aq compared to mc-S-aq can be attributed to a more favourable morphology, i.e., ch-S-aq has a larger surface area. Such observations are consistent with XPS and electrochemical measurements.

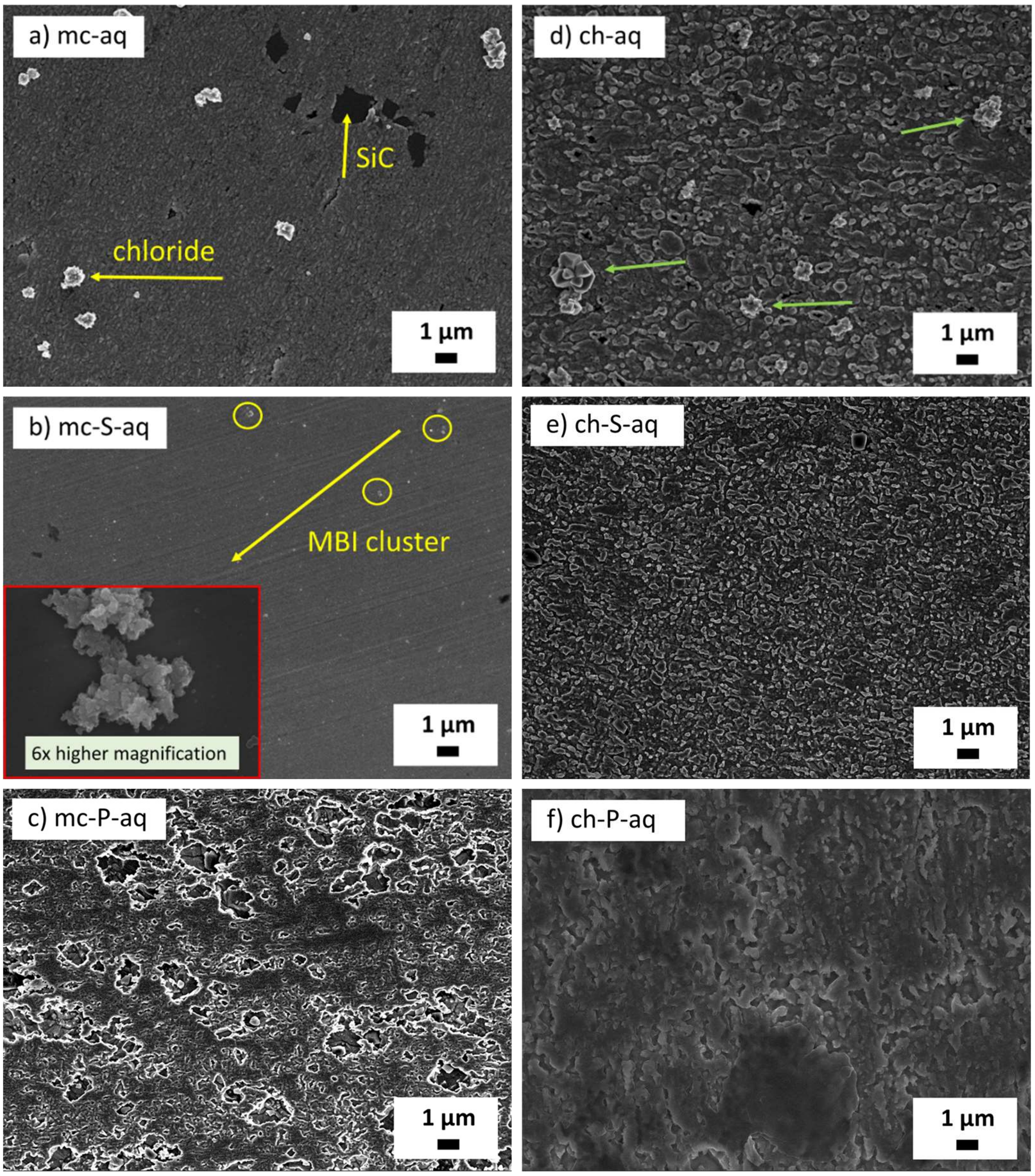

Figure 2.8: SEM secondary electron images for copper immersed in 3 wt.% NaCl solution for 24 h with and without the addition of 1 mM OPA or MBI. The copper surface before recording the images implies: (a) mechanical pre-treatment, (b) mechanical pre-treatment + MBI deposition from aqueous solution, (c) chemical pre-treatment + OPA deposition from aqueous solution, (d) chemical pre-treatment, (e) mechanical pre-treatment + MBI deposition from aqueous solution, (f) chemical pre-treatment + OPA deposition from aqueous solution.

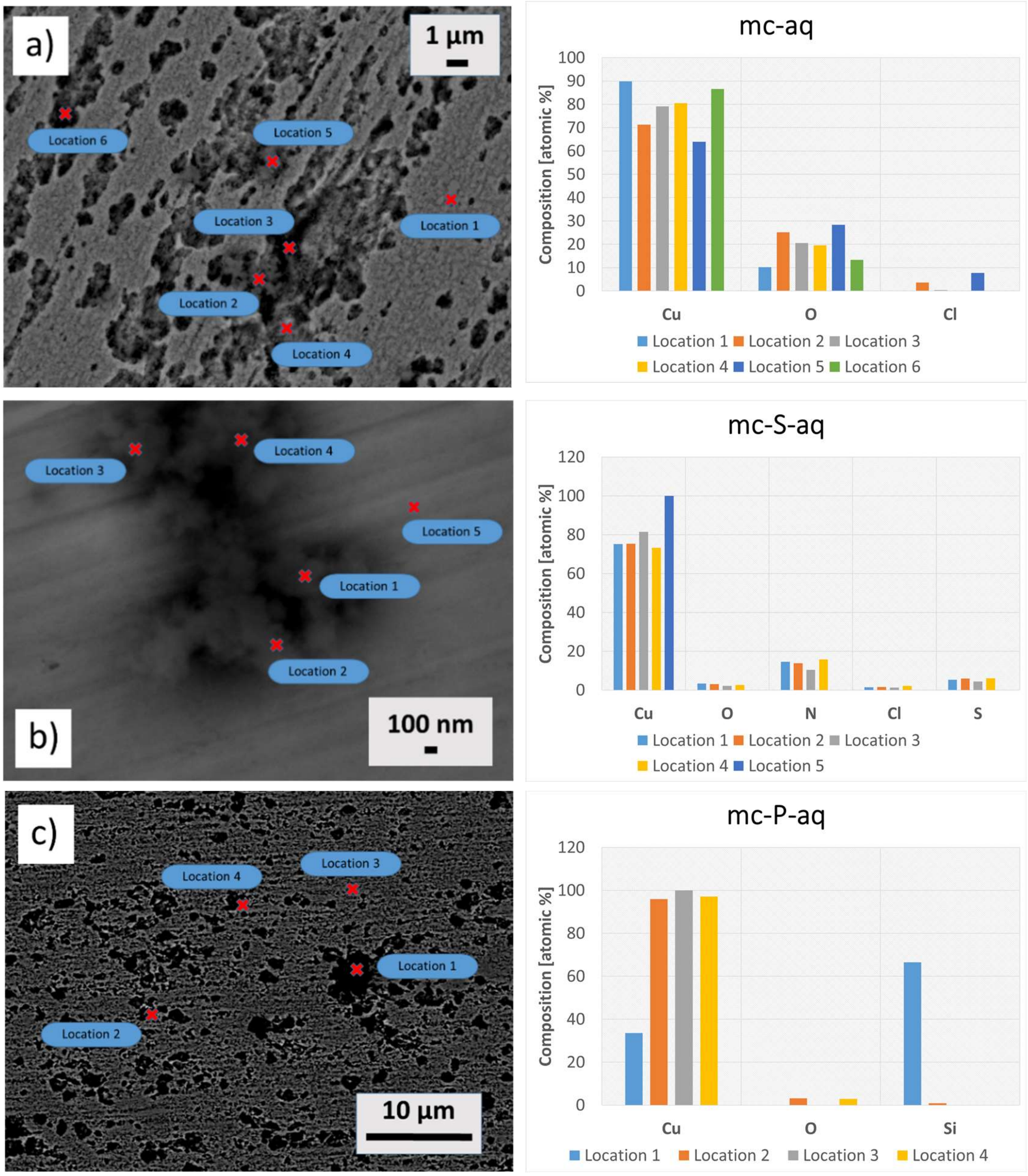

Figure 2.9: SEM images recorded in backscattered electron (BSE) mode for copper immersed in 3 wt.% NaCl solution with and without the addition of 1mM OPA or MBI. The copper surface before recording the images implies: (a) mechanical pre-treatment, (b) mechanical pre-treatment + MBI deposition from aqueous solution, (c) mechanical pre-treatment + OPA deposition from aqueous solution. Locations denoted by a cross mark indicate the spots where EDS analysis was conducted (charts to the right of the SEM images).

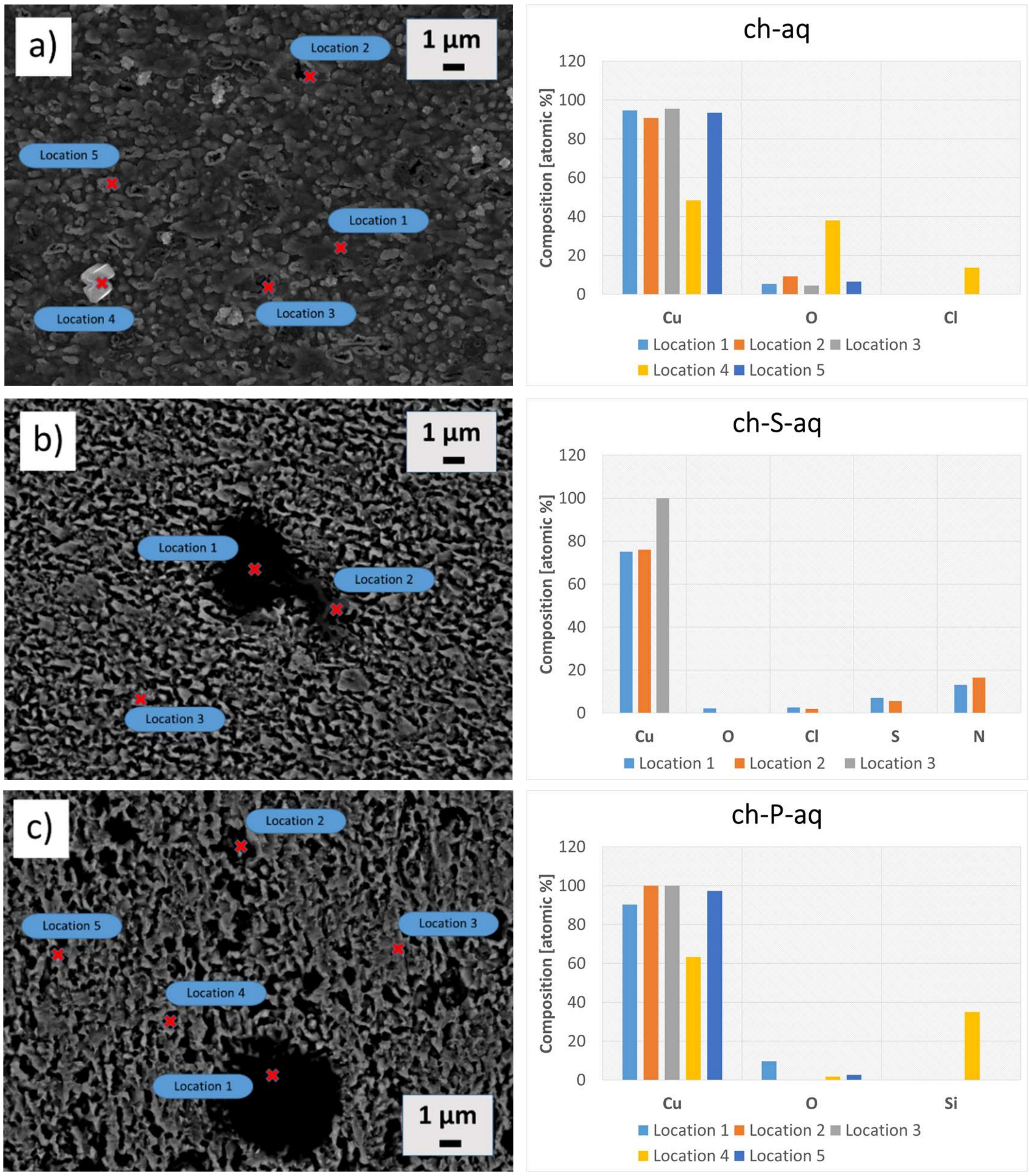

Figure 2.10: SEM images recorded in backscattered electron (BSE) mode for copper immersed in 3 wt.% NaCl solution with and without the addition of 1 mM OPA or MBI. The copper surface before recording the images implies: (a) chemical pre-treatment, (b) chemical pre-treatment + MBI deposition from aqueous solution, (c) chemical pre-treatment + OPA deposition from aqueous solution. Locations denoted by a cross mark indicate the spots where EDS analysis was conducted (charts to the right of the SEM images).

2.3.2 Aluminium

2.3.2.1 Potentiodynamic polarization curves

Fig. 2.11 shows the potentiodynamic curves recorded in 3 wt.% NaCl solution for mechanically and chemically pre-treated aluminium samples. Anodic dissolution of the control sample (mc) takes place without any sign of passivation. The pitting is likely near the E_{corr} (Table 2.5) due to the interaction of $\mathrm{Cl^-}$ with the oxide film [111]. Moreover, the constant perturbations in the anodic curve are probably due to the metastable pitting phenomena [112]. In contrast, a small pseudo-passive region ($\Delta E_{\mathrm{pass}} \approx 70$ mV) was observed for ch. The cathodic polarization curve of mc exhibits a higher contribution of mass transport than that of ch. Fig. 2.11 also shows the corrosion behaviour of a chemically etched Al sample immersed for 24 h in NaCl. The ch-aq underwent immediate pitting, but the cathodic currents were slightly decreased with no change in OCP compared to the mechanically pretreated sample, mc-aq (Table 2.5). These results strongly suggest that the surface morphology and composition of aluminium were modified after chemical pre-treatment by NaOH and $\mathrm{HNO_3}$, as presented by XPS and SEM-EDS results (see below).

Organic films for both pre-treated samples were pre-formed by liquid-phase deposition either from non-aqueous (ethanol) or an aqueous solution containing MBI and OPA. Polarization curves of the MBI and OPA-modified surfaces in the ethanol solution, mc-S-Et and mc-P-Et, show that both samples behave similarly, i.e., there is no decrease in the current densities compared to mc (Fig. 2.12a, Table 2.5).

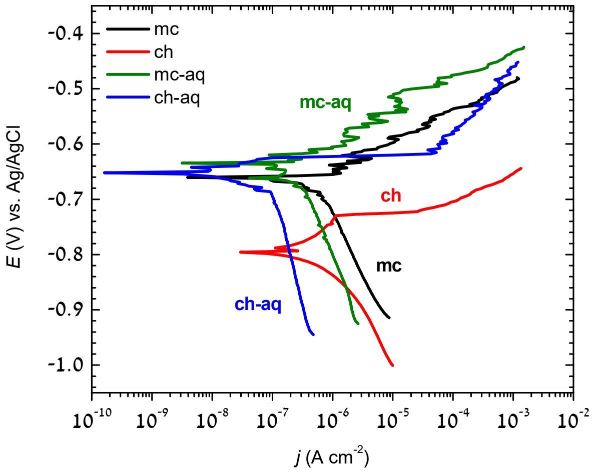

Figure 2.11: Potentiodynamic polarization curves recorded for aluminium samples in 3 wt.% NaCl solution. The aluminium surface prior to measurements implies: (a) mechanical pre-treatment and (b) chemical pre-treatment. Note that the difference between “mc” and “ch” and “mc-aq” and “ch-aq” samples is only in immersion time; the former were immersed for 1 h and the latter for 24 h in chloride solution.

Table 2.5: Electrochemical parameters – corrosion potential (E_{corr}), corrosion current density (j_{corr}), pitting potential (E_{pit}), passive range (ΔE_{pass}), passive current density (j_{pass}), anodic Tafel slope (b_{a}) and cathodic Tafel slope (b_{c}) – deduced for Al from the potentiodynamic polarization curves (Fig. 2.11 and Fig. 2.12).

Al samples	$\boldsymbol{E_{\mathrm{corr}}}$ **($\mathbf{mV_{Ag/AgCl}}$)**	$\boldsymbol{j_{\mathrm{corr}}}$ **($\mathbf{A\ cm^{-2}}$)**	$\boldsymbol{E_{\mathrm{pit}}}$ **(mV)**	$\boldsymbol{\Delta E_{\mathrm{pass}}}$ **(mV)**	$\boldsymbol{b_{\mathrm{a}}}$ **(mV/dec)**	$\boldsymbol{-b_{\mathrm{c}}}$ **(mV/dec)**
mc-aq	−665	2.18×10^{-7}	–	–	–	243
mc-S-aq	−670	4.57×10^{-8}	–	–	–	186
mc-P-aq	−544	2.03×10^{-8}	−220	330	134	188
ch-aq	−655	8.68×10^{-8}	–	–	–	295
ch-S-aq	−800	7.56×10^{-8}	–	–	–	137
ch-P-aq	−490	1.55×10^{-8}	−120	350	144	150

Such behaviour is explained by the fact that neither MBI nor OPA were adsorbed on the surface of the aluminium substrate, as confirmed by XPS (see below, XPS Table). This is in line with the study by Hauffman et al., who reported that ethanol was an unsuitable solvent for the deposition of n-octylphosphonic acid [113]. The authors suggested that the reaction of the phosphonic acids with the aluminium hydroxyls creates a local aqueous environment, which is, in combination with dissolved acids, hazardous to the oxide surface. However, only the ch-P-Et counterpart showed a slight decrease in the corrosion current rate (i.e., a pronounced decrease in the ORR rate) by order of magnitude compared to the control sample, ch (Fig. 2.12b, Table 2.5). It is not clear how the OPA affects the surface of an aluminium substrate because the chemical composition obtained from the XPS surface measurements showed no phosphorus content. Since neither OPA nor MBI induced passivity in any of the samples (mc-S-Et, mc-P-Et, ch-S-Et and ch-P-Et), they are considered ineffective inhibitors when ethanol is used to deposit the layers.

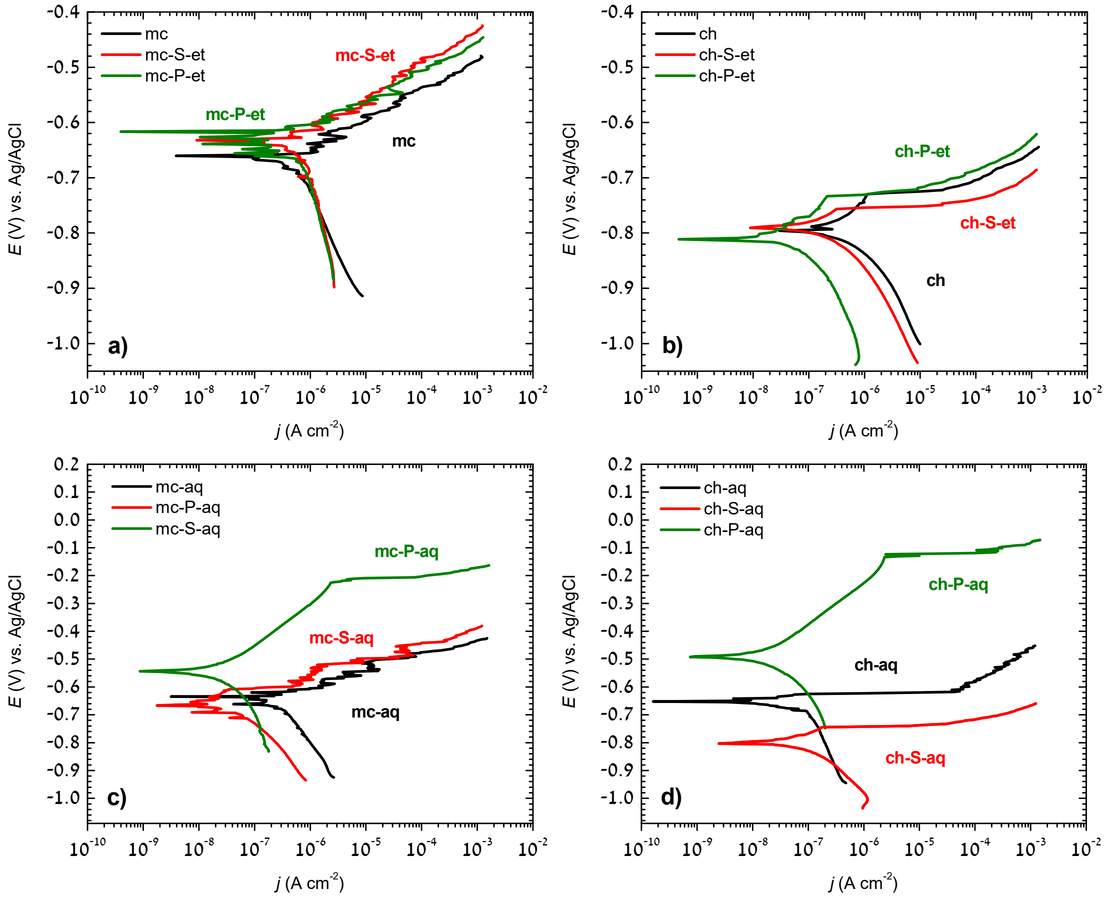

Figure 2.12: Potentiodynamic polarization curves recorded for aluminium in (a and b) 3 wt.% NaCl solution and (c and d) 3 wt.% NaCl with the addition of 1 mM OPA or MBI. The aluminium surface before measurements implies: (a) mechanical pre-treatment + deposition of inhibitors from ethanol solution, (b) chemical pre-treatment + deposition from ethanol solution, (c) mechanical pre-treatment + deposition from aqueous solution, and (d) chemical pre-treatment + deposition from aqueous solution.

On the other hand, functionalization of the Al surface with OPA+NaCl in an aqueous solution, mc-P-aq (Fig. 2.12c), shows a passivation response (i.e., pseudo-passivation because there is no sharp transition between the active-passive region) [45], [91], [114] consistent with the suppression of the anodic reaction and with the positive shift in E_{corr}, compared to the control sample, mc-aq. In contrast to mc-S-et, mc-S-aq adsorbed MBI on the Cu surface induced a two-fold reduction of corrosion rate (Fig. 2.12c, Table 2.5). Only the ORR was influenced by slight inhibition, whereas immediate pitting occurs already at E_{corr}, which is in line with the surface characterization results, XPS and EDS (see below). In the presence of MBI (ch-S-aq), the corrosion was accelerated. In contrast, the OPA induces a reduction of corrosion current density (ch-P-aq) relative to the control sample but has almost the same ΔE_{pass} range and the same slope of the pseudo-passive region as for the mc-P-aq (Table 2.5). The identifiable E_{pit} for ch-P-aq shifts to less active values (i.e., more noble potentials) compared to mc-P-aq. This result may indicate that the role of OPA in mitigating corrosion of aluminium is predominantly as a pitting corrosion inhibitor. It should be noted that although OPA is recognized as a potential corrosion inhibitor for aluminium, it offers only moderate inhibition efficiency due to its relatively short octyl chain, which can also be inferred from the pseudo-passive behaviour of the polarization curve. This observation agrees with the results of Milošev and co-workers [79], which showed that the backbone of the inhibitor molecules is responsible for lateral cohesive interactions, i.e., the elongation of the alkyl chain is beneficial and results in the establishment of a broader pseudo-passivity region.

2.3.2.2 X-ray photoelectron spectroscopy

Table 2.6 shows that the surface composition of mc-aq differs significantly from ch-aq; during chemical etching, a large portion of adventitious organic compounds is removed, i.e., the content of C is reduced from 39% to 26%, followed by an increase in the content of Al and O. The characteristic peak located at 72.6 eV was assigned to the metallic Al [75], [110]. This peak is much more pronounced and shifted by almost 1 eV (i.e., at 71.7 eV) for ch-aq, compared to mc-aq. The Al 2p core-level spectra also present a peak centred at 74.7 eV assigned to the aluminium oxide and/or hydroxide component [115], [116]. Aluminium oxides and hydroxides (Al_2O_3, $Al(OH)_3$ and AlOOH) are extremely difficult to differentiate by XPS because their corresponding E_b values overlap each other [117], [118]. However, different hydroxides formed by different pre-treatments could be deduced from the O/Al ratio. This assumption shows that some difference exists between mechanical and chemical pre-treatment. The O/Al ratio for mc-aq is 2.8, compared to the O/Al ratio of 2 for ch-aq. This may indicate that the surface after mechanical pre-treatment consists mainly of $Al(OH)_3$ and that the chemical pre-treatment modified the surface in a way that led to the formation of AlO(OH) or a combination of $Al(OH)_3$ and Al_2O_3. It can be seen from Fig. 2.13a that all spectra corresponding to the chemical pre-treatment were shifted towards higher E_b values.

After immersion of the pre-treated Al samples in an ethanol solution of OPA, no significant changes can be observed. The most important result is that phosphorus was detected only on the surfaces of the samples exposed to the OPA containing aqueous solution, i.e., mc-P-aq and ch-P-aq (Table 2.6). Moreover, the organic film of the ch-P-aq contained a higher amount of phosphorus (7.4 at.%) than mc-P-aq (6.2 at.%). The peak maximum at 133.6 eV (Fig. 2.13b) was related to the metal-phosphonate (P-O-Al) bonding as reported previously [45], [80], [116], [119].

The adsorption of OPA is confirmed by a significant decrease in Al and O content and an increase in the content of C. It is well-known that the presence of oxide/hydroxide on the Al surface is required for the condensation reaction; $\text{P-OH} + \text{OH-Al}^* \longrightarrow \text{P-O-Al}^* + H_2O$, where Al* stands for surface Al ion [79]. Apart from the recorded signal for phosphorus, no sulphur content was detected in any of the samples (Table 2.6). The adsorption of phosphonate was corroborated by the broadening of the O 1s core-level peaks for mc-P-aq and ch-P-aq (Fig. 2.13c), indicating the presence of the new component(s), as demonstrated by deconvolution of the high-resolution spectra in our previous work [45]. The peaks centred at 532 eV are ascribed to aluminium oxide/hydroxide species [84], [115], whereas the new component(s) between 533 eV and 534 eV correspond to Al-O-P and/or H-O-P [81], [116], [119].

Table 2.6: Chemical composition of the aluminium surface after 24 h of immersion in: 1) 3 wt.% NaCl with and without the addition of 1 mM 2-mercaptobenzimidazole (S), octylphosphonic acid (P), and 2) ethanolic solution containing S and P. The aluminium surface before measurements implies: (a) mechanical pre-treatment + deposition of inhibitors from ethanol solution, (b) chemical pre-treatment + deposition from ethanol solution, (c) mechanical pre-treatment + deposition from aqueous solution, and (d) chemical pre-treatment + deposition from aqueous solution.

Sample		mechanical pre-treatment					chemical pre-treatment				
Solution		NaCl	+MBIH (S)		+OPA (P)		NaCl	+MBIH (S)		+OPA (P)	
Inhibitor medium		aq	EtOH	aq	EtOH	aq	aq	EtOH	aq	EtOH	aq
Elements	Al	16	19.1	13.9	18.8	7.4	24.3	12.3	16.7	13.9	4
	O	44.4	60.5	43.8	59.2	28.6	49.7	46.2	47.4	47.3	25.6
	C	39.1	19.4	41.9	21.6	57.8	26	39.2	35.9	38.2	63
	Cl	–	1	0.4	0.4	–	–	0.4	–	0.5	–
	N	0.5	–	–	–	–	–	0.7	–	–	–
	S	–	–	–	–	–	–	–	–	–	–
	P	–	–	–	–	6.2	–	–	–	–	7.4
	Na	–	–	–	–	–	–	1.2	–	0.1	–

Fig. 2.13d shows the C 1s spectra with the peaks at 284.8 eV and around 289 eV attributed to C-H/C-C and C=O/O-C=O groups, respectively, which generally arise from airborne carbonaceous contaminants [84], [115], [120]. Upon adsorption of OPA inhibitor on Al substrate, the major peak corresponds to the methylene groups of OPA molecule,

whereby the signal for oxidized carbon contaminants wholly disappeared. The alkyl chain length has a strong influence on the molecular packing during film formation. The longer chains adsorb stronger due to an increase in van der Waals attractive forces; the strength of the van der Waals interactions increases with the number of methylene units in adsorbate. Hoque et al. [84] reported that longer chain molecules such as dodecylphosphonic acid (DP) and octadecylphosphonic acid (ODP) formed more densely packed phosphonate self-assembling monolayer (SAM) on Al surface, unlike octylphosphonic acid (OPA). This agrees with the electrochemical results where the mc-P-aq and ch-P-aq did not reach complete passivity or broad pseudo-passivity as in the work of Milošev et al. [79].

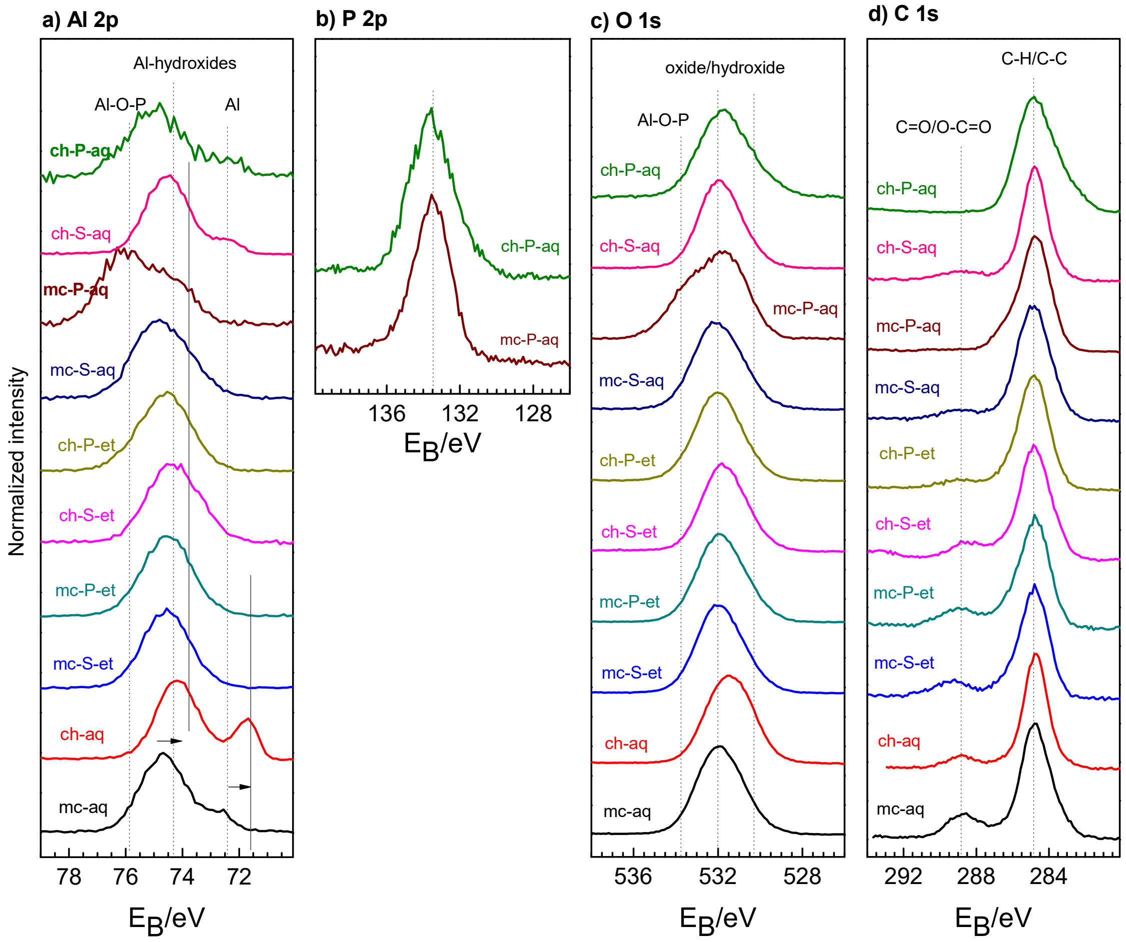

Figure 2.13: High-resolution XPS spectra of (a) Al 2p, (b) P 2p, (c) O 1s, and (d) C 1s recorded after immersion of aluminium in: 1) 3 wt.% NaCl solution with and without the addition of 1 mM OPA or MBI, and 2) ethanolic solution containing MBI and OPA. The modification of aluminium surface before XPS measurements implies: mechanical or chemical pre-treatment and deposition of MBI or OPA either from ethanol or aqueous solution.

Furthermore, Kokalj and Costa [121] analysed, with the aid of computational modelling, the mechanism by which organic self-assembled-monolayers hinder the penetration of Cl^- ions from aqueous solution toward the metal substrate. Their scheme describes the activation barrier for Cl^- penetration into SAM as a function of the electrode potential and shows that the activation barrier decreases as the electrode potential increases. Still, for thick SAMs, the barrier remains sizable, even at more positive potentials. The authors suggested that this might be one of the reasons why dense and sufficiently thick SAMs efficiently inhibit corrosion.

2.3.2.3 Scanning electron microscopy coupled with energy-dispersive X-ray spectroscopy

First, the ground (mechanically pre-treated, mc-aq) and etched (chemically pre-treated, ch-aq) surfaces are compared to get insight into the potential importance of mild surface preparation of aluminium. The surface of ch-aq (Fig. 2.14d) was characterised by large roughness with a hemisphere-like appearance compared to mc-aq, which was flat with visible inclusions of corrosion products (Fig. 2.14a). EDS analysis showed that both surfaces (Fig. 2.15a and Fig. 2.16a) contained aluminium oxide. In addition, impurities such as SiC and iron particles are distributed over the entire surface. The presence of carbon in all samples originates from the deposited layer before SEM imaging.

After immersion of the mechanically prepared Al sample in an ethanolic solution of MBI (mc-S-et, Fig. A.10a) and OPA (mc-P-et, Fig. A.10b), no significant changes were observed except that the particles belonging to the corrosion products were larger compared to the control sample (mc-aq). Also, when the chemically prepared Al samples were immersed in the ethanolic solution of MBI (ch-S-et, Fig. A.10c) and OPA (ch-P-et, Fig. A.10d), the shape and composition (Figs. A.11 and A.12) of the hemispheres did not change relative to the control sample (ch-aq), indicating no inhibition of the corrosion processes which is consistent with the electrochemical and XPS results.

In contrast, when instead of ethanol, an aqueous solution was used as a solvent of choice, events on the aluminium surface changed drastically. To this end, let us compare the SEM micrographs for mechanically and chemically pre-treated surfaces immersed in an aqueous solution of MBI and OPA containing chloride. The mc-S-aq surface is less damaged over the entire surface (Fig. 2.14b), but galvanic corrosion, as well as locally attacked sites, appear to occur at the edges of very large iron particles[1], as confirmed by EDS analysis (Fig. 2.15b). It is difficult to notice a difference in surface appearance between ch-S-aq (Fig. 2.14e) and the control sample (ch-aq) (Fig. 10d), while it is evident that ch-S-aq has fewer Fe particles (Fig. 2.16b) compared to its counterpart sample mc-S-aq (Fig. 2.16a). The corrosion inhibition effect was observed only for OPA inhibitor in aqueous solutions containing chlorides, such as mc-P-aq and ch-P-aq. The morphology of mc-P-aq shows that the scratches from the grinding process are not visible due to the coverage of almost the entire surface by inhibitor particles (Fig. 2.14c). In addition, large OPA clusters were observed, which was confirmed with EDS analysis where phosphorus was detected (Fig. 2.15c). It is imperative to highlight that the phosphorus signal was detected only at locations where the OPA agglomerates are formed but not at locations where the thin OPA film was formed. Such a result was expected because the sampling depth of EDS is within

---

[1] Iron particles represent metal impurities of low solubility in aluminium metal. It is the most pervasive impurity element in Al alloys, which stems from the bauxite ore and steel tools used during primary and secondary production [200]. In terms of galvanic series, iron is more noble to aluminium and thus these particles represent electrochemically different sites from Al matrix (sites of cathodic reaction).

the first few micrometres, while the XPS allows the measurement of surface composition within a few nanometres.

The surface of ch-P-aq (Fig. 2.14f) is even more densely covered with the OPA inhibitor compared to mc-P-aq, which led to a less rough surface compared to the control sample (ch-aq) (Fig. 2.14d). It appears that ch-P-aq (Fig. 2.16c) contains more OPA clusters than mc-P-aq (Fig. 2.15c), as shown by EDS results. The more densely packed OPA on the Al surface recorded with SEM-EDS is consistent with the higher phosphorus content detected by XPS and lower corrosion current rates of ch-P-aq compared to mc-P-aq.

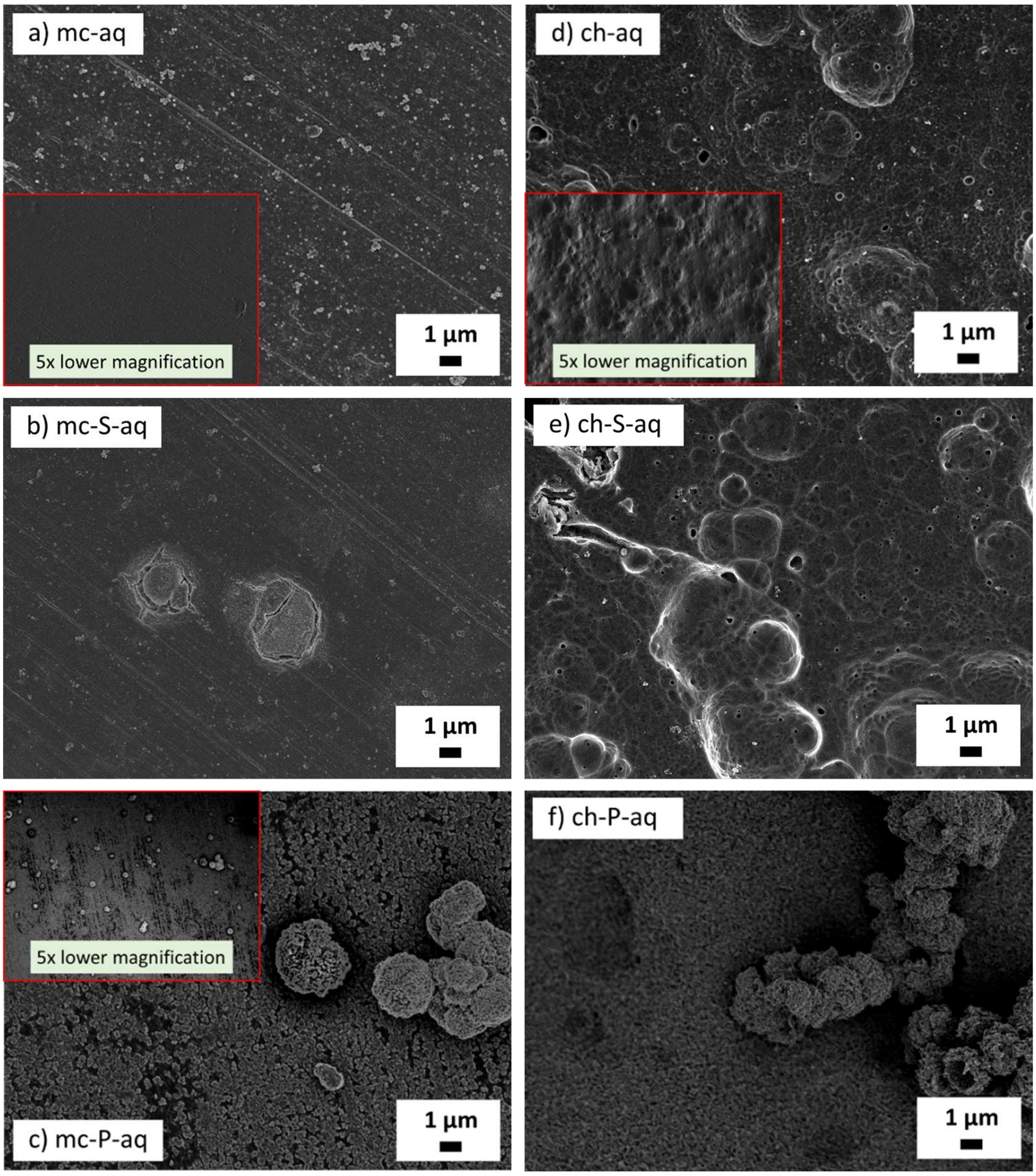

Figure 2.14: SEM secondary electron images for aluminium immersed in 3 wt.% NaCl solution with and without the addition of 1 mM OPA or MBI. The aluminium surface before recording the images implies: (a) mechanical pre-treatment, (b) mechanical pre-treatment + MBI deposition from aqueous solution, (c) chemical pre-treatment + OPA deposition from aqueous solution, (d) chemical pre-treatment, (e) mechanical pre-treatment + MBI deposition from aqueous solution, (f) chemical pre-treatment + OPA deposition from aqueous solution.

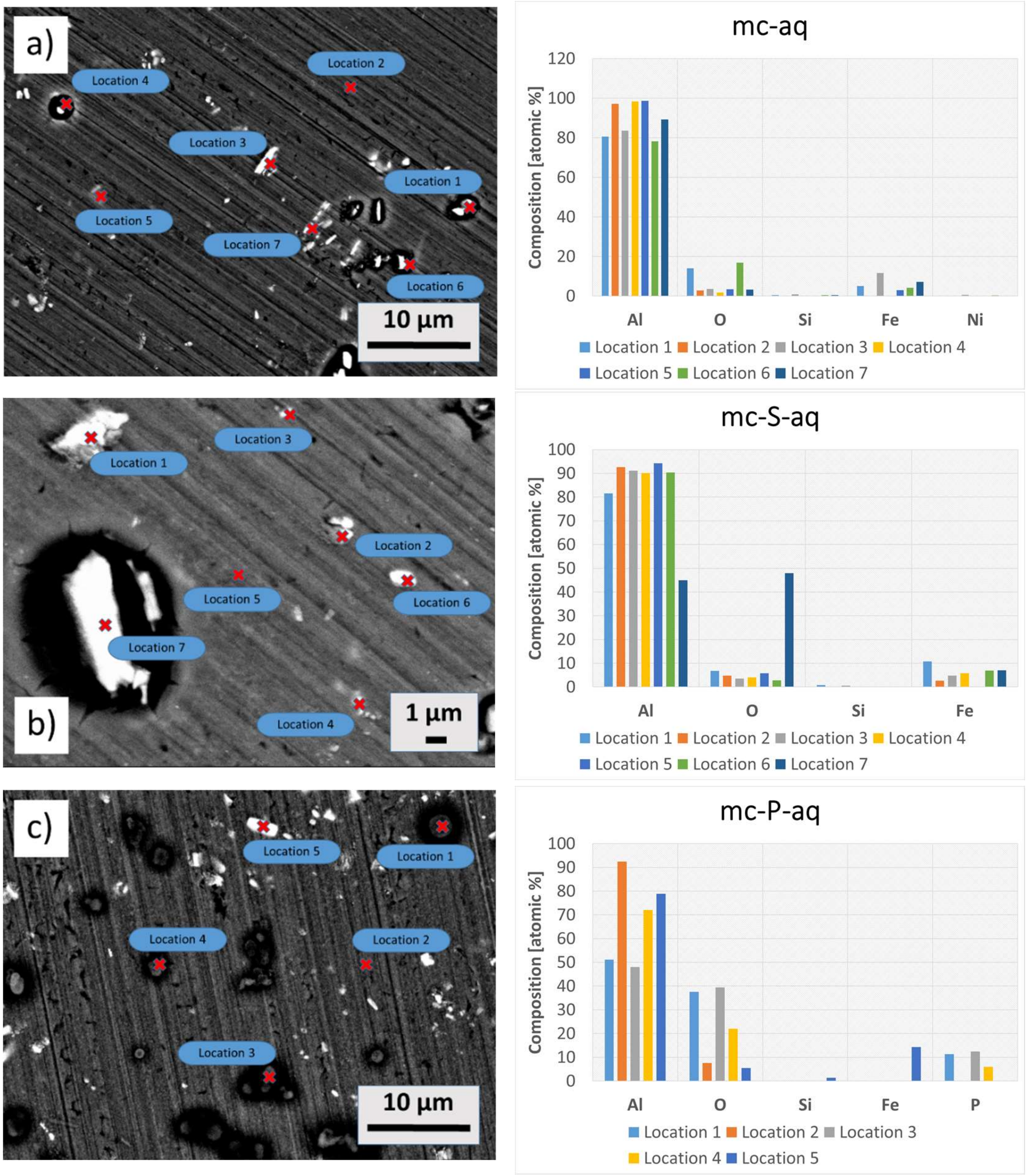

Figure 2.15: SEM images recorded in backscattered electron (BSE) mode for copper immersed in 3 wt.% NaCl solution with and without the addition of 1 mM OPA or MBI. The copper surface before recording the images implies: (a) mechanical pre-treatment, (b) mechanical pre-treatment + MBI deposition from aqueous solution, (c) mechanical pre-treatment + OPA deposition from aqueous solution. Locations denoted by a cross mark indicate the spots where EDS analysis was conducted (charts to the right of the SEM images).

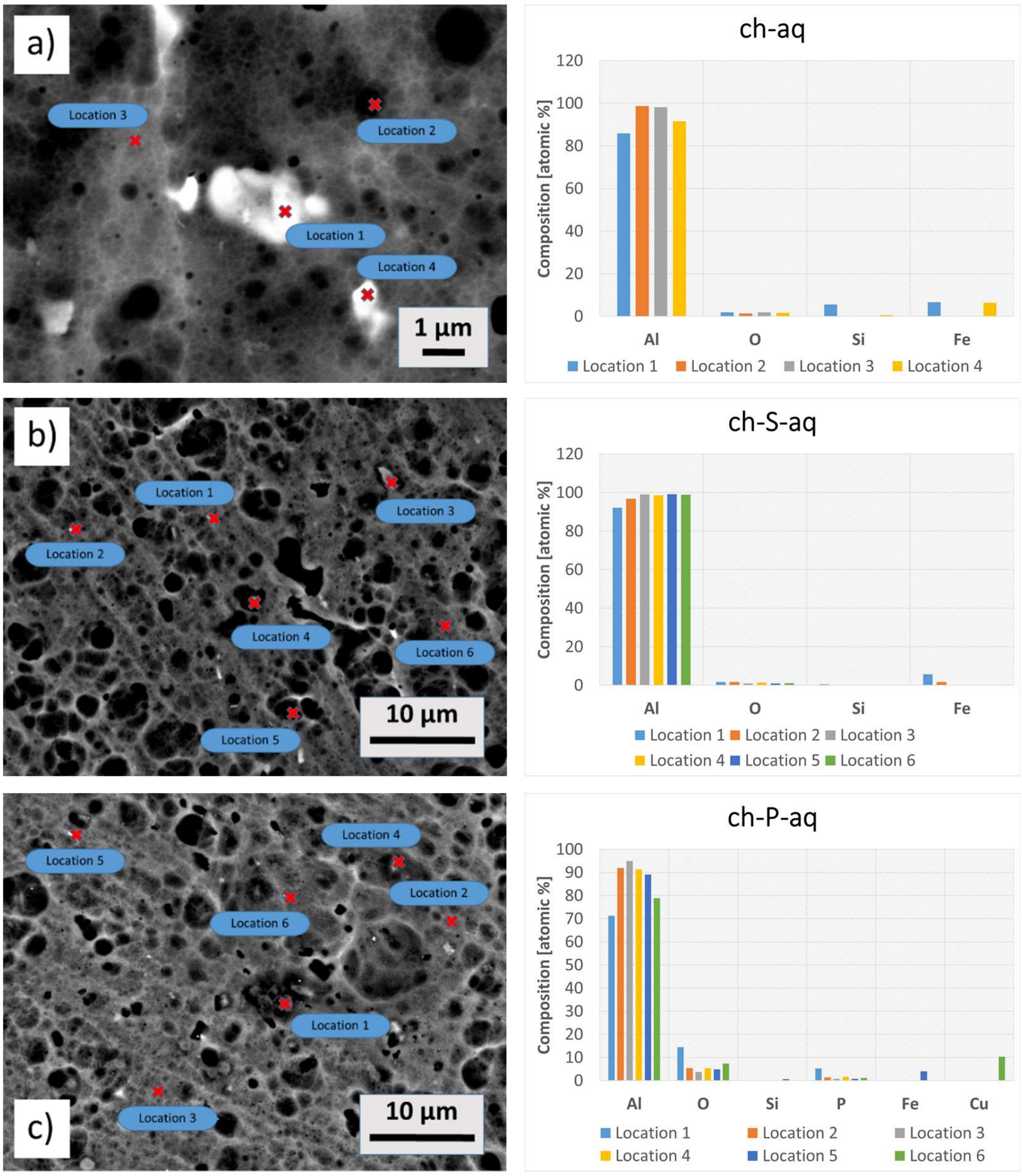

Figure 2.16: SEM images recorded in backscattered electron (BSE) mode for aluminium immersed in 3 wt.% NaCl solution with and without the addition of 1 mM OPA or MBI. The aluminium surface before recording the images implies: (a) chemical pre-treatment, (b) chemical pre-treatment + MBI deposition from aqueous solution, (c) chemical pre-treatment + OPA deposition from aqueous solution. Locations denoted by a cross mark indicate the spots where EDS analysis was conducted (charts to the right of the SEM images).

2.4 Conclusions

The corrosion behaviour of mechanically (mc) and chemically (ch) pre-treated copper and aluminium samples (i.e., control bare samples) was investigated by electrochemical and surface-analytical characterization means in 3 wt.% NaCl solution. The curves recorded for both control samples for Cu show similar electrochemical characteristics; therefore, the influence of the surface pre-treatment on the bare samples is neglected. On the other hand, the polarization curves for Al showed that the ORR was slightly inhibited on the chemically pretreated sample compared to the mechanically pretreated one.

Organic films for both types of pre-treated samples were prepared by liquid-phase deposition either from ethanol (et) or aqueous (aq) solution containing MBI (S) and OPA (P) inhibitors. The potentiodynamic measurements, measured in 3 wt.% NaCl, revealed that the current density responses on the Cu surface for the samples deposited from ethanol solutions (mc-S-Et and mc-P-Et, ch-S-Et and ch-P-Et) were similar to the control samples mc and ch. The XPS study confirmed that the inhibitor films were not formed in ethanolic solutions and that the Cu-MBI films were formed only after the deposition from an aqueous NaCl solution containing MBI inhibitor. The polarization curves for mc-S-aq and ch-S-aq showed a significant reduction in the i_{corr} by almost four orders of magnitude together with the shift of the E_{corr} more positive than the control samples mc-aq and ch-aq. Hence, MBI is considered an effective corrosion inhibitor for Cu in chloride environments. The degradation mechanism of Cu-MBI was resolved by the peaks fitting of the cyclic voltammogram of Cu-S-aq, revealing the two peaks within the enlarged peak corresponding to Cu^{2+} and $(MBI)_2$.

The inhibition chemistries of aluminium in aqueous solutions were opposite to those of copper; only the Cu-OPA layer was identified by XPS and confirmed by potentiodynamic polarization measurements. The polarization curves for mc-P-aq and ch-P-aq showed a pseudo-passivation response with the shift in E_{pit} to less active values and a positive shift in E_{corr} compared to the control sample. Admittedly, the E_{pit} was slightly higher for ch-P-aq than mc-P-aq. Although OPA is considered a potential corrosion inhibitor for aluminium, it offers only moderate inhibition efficiency due to its relatively short octyl chain.

Finally, the results showed that the surface pre-treatment did not significantly influence the chemistries of copper and aluminium. However, the solvent choice was crucial, i.e., the inhibitor film was only formed from inhibitor-containing aqueous solutions.

Chapter 3

Synergistic Effect Between 2-Mercaptobenzimidazole and Octylphosphonic Acid On Copper and Aluminium Substrates

3.1 Literature Review

In the context of novel corrosion protection strategies, the use of multicomponent systems (i.e., the mixture of two inhibitors) that could lead to a synergistic effect is being considered. Since AA2024 consists of ca. 4 wt.% of Cu, it is beneficial to explore the behaviour of individual metals, Al and Cu, in chloride-containing solutions of mixed inhibitors separately. Recent studies [122]–[125] evidenced that the combination of two or more inhibitors may result in improved corrosion protection of AA2024 due to synergistic effects. The multicomponent inhibitor is better than the single inhibitor since the former effectively protects multimetal systems; moreover, the mixture of inhibitors allows the use of lower concentrations [33].

The synergistic effect is when chemical substances interact, resulting in an overall effect greater than the sum of individual effects of any of them. This implies that it is necessary to test different molar ratios of the two inhibitors to establish the most efficient protection system.

MBI and OPA inhibitors are chosen in the present study based on their well-known inhibition efficiency, previously reported in the literature. The main idea was to combine two organic molecules, the one with a tendency to adsorb on copper and the other with a tendency to adsorb on aluminium. To this end, 2-mercaptobenzimidazole (MBI) has been widely recognized as a promising corrosion inhibitor for Cu [28], [41], [70], [72], [73], and octylphosphonic acid for Al [79], [81]–[84], [115], [126]. Based on the previous reports, we expected that MBI would not be an efficient inhibitor for Al [79]. However, the mixture might suit a heterogeneous system like Cu-containing aluminium alloy.

3.2 Experimental

3.2.1 Materials, substrate preparation and chemicals

Materials and chemicals have already been described in *Chapter 2*, the *Experimental section*. The Al and Cu samples were successively ground with P1000, P2400 and P4000-grit SiC emery papers (mechanical pre-treatment). Then the surface was subject to ultrasonic cleaning in absolute ethanol for 3 min, double-rinsed with Milli-Q water and blown dry with nitrogen gas.

3.2.2 Preparation of organic films

Organic layers on metallic surfaces were produced by liquid-phase deposition from an aqueous solution only. In the previous chapter, it was established that the deposition from ethanolic solution is not efficient. Polished copper and aluminium samples immersed in an aqueous aggressive chloride medium (i.e. 3 wt.% NaCl) were regarded as control samples (bl). Organic layers were prepared on polished copper and aluminium samples immersed in 3 wt.% NaCl with the addition of (i) individual MBI or OPA organic compounds at a concentration of 1 mM and (ii) both organic compounds at different molar ratios at a total concentration of 1 mM (Fig. 2.2). After denoted immersion period, the samples were removed from the solution, double rinsed gently with deionized water, dried in the stream of nitrogen and then subject to electrochemical and surface characterization.

All the utilized synergistic solutions and their as-prepared pH and shorthand labels are summarized in Table 3.1 (the data about blank and individual MBI and OPA samples are shown in Table 3.1). Binary mixtures are labelled as xS+yP, where x and y represent molar ratios in %-units, whereas individual MBI and OPA are 100S and 100P, respectively. Cu and Al samples were immersed individually into these solutions, and measurements were performed after 1 day, 3 days and 7 days of immersion. The pH values of the solutions used for immersion of Cu samples were not adjusted to match that of NaCl but used as-prepared. The pH values of solutions used for surface modification of Al samples were adjusted to 7 since aluminium undergoes dissolution in aqueous solutions below about pH 4.

Table 3.1: List of solutions, their pH values (as-prepared), and shorthand abbreviations. The total concentration of binary inhibitors is 1 mM. The MBI:OPA ratios are expressed as molar ratios.

Solution	**pH (as-prepared)**	**denotation**
NaCl + MBI + OPA (9:1)	4.0	90S+10P
NaCl + MBI + OPA (1:1)	3.3	50S+50P
NaCl + MBI + OPA (1:9)	3.0	10S+90P

3.2.3 Electrochemical measurements

3.2.3.1 Linear polarization resistance

The linear polarization resistance is a convenient method that can be used within 10 minutes to measure the corrosion rate rapidly. It makes it possible to reveal a high degree of corrosion at the early stages. To estimate the polarization resistance (R_p), the potential was scanned from 10 mV cathodic to 10 mV anodic relative to the E_OCP using a scan rate of 0.1 mV/s. R_p was then calculated from the slope of the linearly fitted potential vs. current density using NOVA software.

The inhibition efficiency (IE) given in % is estimated by the formula:

$$\mathrm{IE} = \frac{R_\mathrm{p}^\mathrm{inh} - R_\mathrm{p}^\mathrm{blank}}{R_\mathrm{p}^\mathrm{inh}} \times 100, \tag{3.1}$$

where $R_\mathrm{p}{}^\mathrm{inh}$ and $R_\mathrm{p}{}^\mathrm{blank}$ are the polarization resistance measured for metal substrate exposed to NaCl solution with or without inhibitor added, respectively.

3.2.3.2 Potentiodynamic polarization curves

The experimental procedure has already been explained in *Chapter 2*.

3.2.3.3 Synergistic effect

The synergistic parameter (S) was calculated as proposed by Aramaki and Hackerman [127]:

$$S = \frac{R_{12}}{R_{1+2}}, \quad \text{where} \tag{3.2}$$

$$R_{1+2} = \frac{R_1 R_2}{R_0}. \tag{3.3}$$

The parameters R_0, R_1 and R_2 are the measured polarization resistances of noninhibited and inhibited samples with individual inhibitors 1 and 2, respectively. R_{1+2} is the "threshold" polarization resistance for the mixture of inhibitors 1 and 2, calculated with (Eq. 3.3), whereas R_{12} is the measured polarization resistance of the binary inhibitor. The synergistic effect S is the relative comparison of polarization resistances R_{12} and R_{1+2}. Values of $S > 1$ indicate a synergistic effect of the inhibitor combination.

3.2.4 Surface characterization

3.2.4.1 X-ray photoelectron spectroscopy

The experimental procedure has already been explained in *Chapter 2*.

3.2.4.2 Attenuated total reflectance Fourier-transform infrared spectroscopy

The Fourier-transform infrared spectroscopy (FTIR) was applied to gain qualitative information about the presence and interaction between the organic molecules and metallic surfaces by detecting specific vibrational modes involving sulphur and phosphorus bonds. The samples were analysed using a Fourier-Transform Infrared Spectrometer (FTIR; Perkin Elmer Spectrum 100, Massachusetts, USA) in the attenuated total reflectance (ATR) mode (a diamond crystal/KRS-5 substrate). The FTIR spectra of the samples were recorded in the range 4000–400 cm^{-1} with a resolution of 4 cm^{-1} and presented as transmittance (%).

3.2.4.3 Water contact angle measurements

Water contact angle (WCA) measurements were used to investigate the wetting properties of unmodified and inhibitor modified copper and aluminium surfaces. Sessile drop static contact angle measurements were determined using a tensiometer Krüss DSA 20 (Krüss GmbH, Hamburg, Germany). WCA values reported are the average of three or more measurements at different locations on the same sample performed within a day of sample preparation. Deionized water droplets of 5–8 µL in the volume are gently deposited on the substrate surface in an ambient environment at 22 °C using a micro-syringe. The obtained images of droplets were analysed using Drop-shape-analysis software for the precise determination of the contact angle (θ). All water contact angles have an absolute error or uncertainty between ±1° to ±11°.

3.2.4.4 Digital microscope

The appearance of the surface of copper samples was captured by ZEISS Smartzoom 5 automated digital microscope (ZEISS GmbH, Oberkochen, Germany). The images of samples with the magnification of 34× and 200× were recorded.

3.3 Results and Discussion

3.3.1 Copper

3.3.1.1 Potentiodynamic polarization curves

The potentiodynamic polarization curve recorded for mechanically pretreated copper in 3 wt.% NaCl after 24 h rest at the open circuit potential is presented in Fig. 3.1a. The mechanism of anodic electro-dissolution of copper in near-neutral chloride media has already been well explained in *Chapter 1*.

After 1 day of immersion, the presence of MBI in the chloride solution induced a significant reduction in cathodic current density by two orders of magnitude, as shown in Fig. 3.1a and Table 3.2. The predominance of its effect on the anodic processes is reflected in a reduced current density of almost four orders of magnitude and a shift in E_{corr} more positive by 130 mV compared to the NaCl solution. Based on this, 100S showed a mixed-type inhibition behaviour on the copper surface (Table 3.2) with a stronger effect on the anodic side. This was corroborated by the establishment of a passive range extending from the primary passivation potential (E_{pp}) at 0.02 V when the anodic curve changed its slope and the increase in current density ceased up until E_{pit} was reached at 0.16 V. The corresponding passivity parameters are listed in Table 3.2. The formation of the passive range confirmed that in the presence of 100S, the Cu surface was covered with a protective layer. At potentials more positive than E_{pit}, the current density raised again up to 0.5 V when a diffusion-limited plateau is formed, similar to that in a blank solution. Surfaces modified by inhibitors to achieve passivity usually exhibit rather complex anodic polarization curves, i.e., there is no extensive and well-defined anodic Tafel region due to the existence of a dissolution reaction in conjunction with the onset of the passivation reaction (i.e. active-passive transition) [128]. Therefore, the nature and kinetics of cathodic reactions have become critical in determining their dissolution rates [92], [99].

For 100S, E_{pass} spanned 280 mV; hence 100S acts as a strong Cu corrosion inhibitor. Overall, the corrosion current density (j_{corr}) was reduced from 1.19×10^{-5} A cm^{-2} for blank (i.e., NaCl) to 6.24×10^{-9} A cm^{-2} for 100S (Table 3.2).

Unlike 100S, octylphosphonic acid (100P) showed a completely different tendency towards adsorption on copper (Fig. 3.1a). 100P did not induce any significant reduction in cathodic or anodic current densities, but the cathodic Tafel slope changed, indicating that the kinetics have been modified with a greater contribution of charge transfer. The E_{corr} shifted more positive by 80 mV, and j_{corr} decreased from 1.19×10^{-5} A cm^{-2} in NaCl to 2.26×10^{-6} A cm^{-2} in the presence of OPA. It can be stated that in this sense, 100P acts as a weak anodic inhibitor for Cu corrosion.

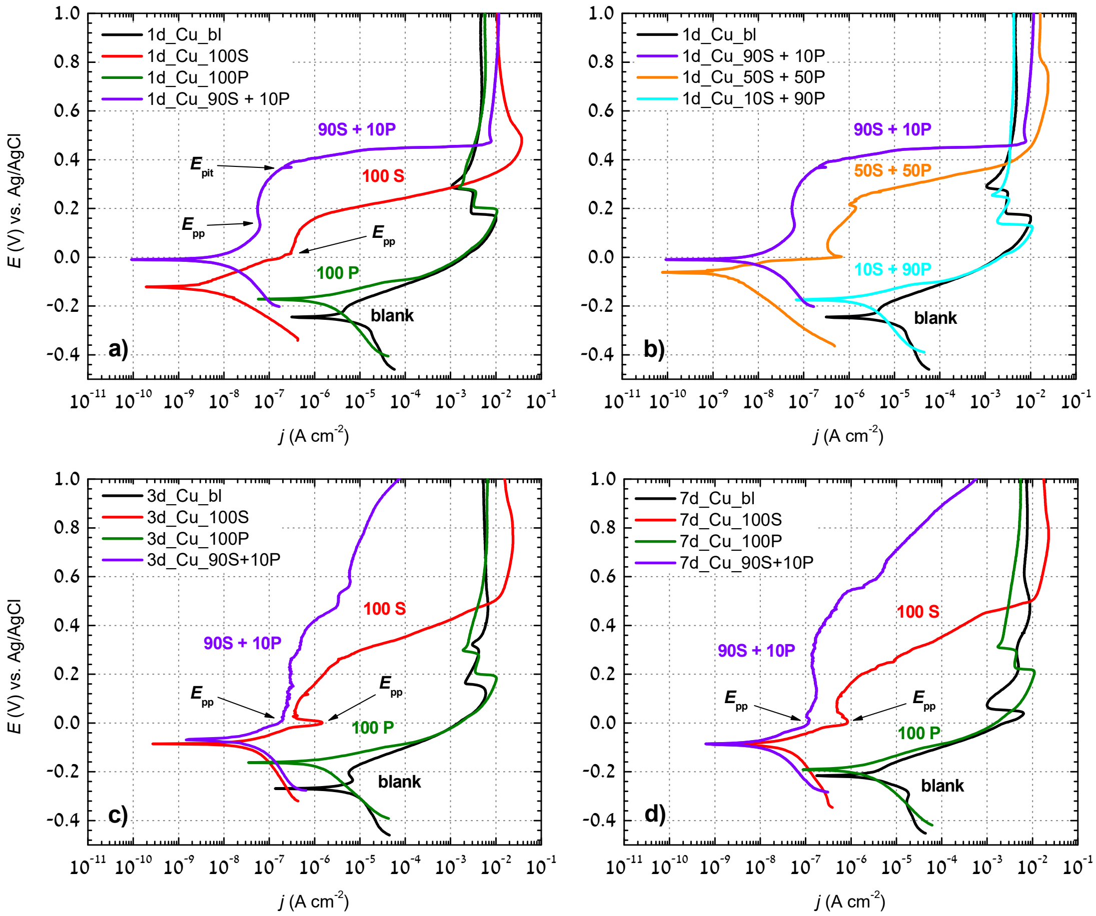

Figure 3.1: Potentiodynamic polarization curves recorded for copper in 3 wt.% NaCl solution with and without (bl) the addition of 1 mM of (a) 100S, 100P and binary 90S+10P after 1 day of immersion, (b) binary inhibitors 90S+10P, 50S+50P and 10S+90P after 1 day of immersion, (c) 100S, 100P and binary 90S+10P after 3 days of immersion, (d) 100S, 100P and binary 90S+10P after 7 days of immersion. The scan rate was 1 mV/s.

Table 3.2: Electrochemical parameters – corrosion potential (E_{corr}), corrosion current density (j_{corr}), pitting potential (E_{pit}), passive range ($\Delta E_{\mathrm{pass}} = |E_{\mathrm{pit}} - E_{\mathrm{corr}}|$), passive current density (j_{pass}), anodic Tafel slope (b_a) and cathodic Tafel slope (b_c) – deduced for Cu from the potentiodynamic polarization curves (Fig. 3.1.) after 1 day (1d), 3 days (3d) and 7 days (7d) of immersion in 3 wt.% NaCl with and without inhibitor.

Sample	E_{corr} ($\mathrm{mV_{Ag/AgCl}}$)	j_{corr} ($\mathrm{A\ cm^{-2}}$)	E_{pit} (mV)	ΔE_{pass} (mV)	j_{pass} ($\mathrm{A\ cm^{-2}}$)	b_a (mV/dec)	$-b_c$ (mV/dec)
1d_Cu_bl	−250	1.19×10^{-5}	−200	50	–	–[a]	384
1d_Cu_100S	−120	6.24×10^{-9}	160	280	7.50×10^{-7}	–[a]	103
1d_Cu_100P	−170	2.26×10^{-6}	–	0	–	48	204
1d_Cu_90S+10P	−10	9.33×10^{-9}	380	390	7.76×10^{-8}	–[a]	136
1d_Cu_50S+50P	−60	2.91×10^{-9}	250	310	8.48×10^{-7}	–[a]	153
1d_Cu_10S+90P	−170	2.33×10^{-6}	–	0	–	44	190
3d_Cu_bl	−270	7.95×10^{-6}	−180	90	–	–[a]	296
3d_Cu_100S	−80	5.06×10^{-8}	260	340	0.3×10^{-6}	–[a]	263
3d_Cu_100P	−160	1.24×10^{-6}	–	0	–	40	163
3d_Cu_90S+10P	−60	4.72×10^{-8}	400	460	4.58×10^{-7}	–[a]	207
7d_Cu_bl	−210	8.92×10^{-6}	−170	40	–	–[a]	430
7d_Cu_100S	−90	4.54×10^{-8}	150	240	8.66×10^{-7}	–[a]	254
7d_Cu_100P	−190	2.53×10^{-6}	–	0	–	–[a]	170
7d_Cu_90S+10P	−80	1.25×10^{-8}	540	620	2.28×10^{-7}	–[a]	136

[a] The polarization curves with not well defined anodic Tafel region were extrapolated by inspecting only a linear fit of the cathodic Tafel curve, which intersects E_{corr}.

The following potentiodynamic measurements aimed to explore the possibility of the synergistic effect of the inhibition system containing two organic molecules, with different chemisorption kinetics, mixed to protect the surface of copper metal from corrosion attack. Fig. 3.1b shows the polarization curve recorded after 1 day of immersion of copper samples in NaCl containing binary inhibitors with different molar ratios of S and P compounds, i.e., 90S+10P, 50S+50P and 10S+90P. Table 3.2 reveals that the S/P ratio affects the polarization curves and related electrochemical parameters. As the molar ratio of S/P increased, the E_{corr} values became more noble, and the current densities decreased for both the cathodic and anodic branches of the Tafel curves (Fig. 3.1b). These positive shifts reflect an increased barrier to dissolution with an increasing S/P ratio. Compared to the individual 100S and 100P curves (Fig. 3.1a), the binary mixture 10S+90P did not significantly improve the behaviour of 100P. In contrast, a significant improvement was found for the 50S+50P and, especially, 90S+10P, compared to individual 100S and 100P. The E_{corr} of 90S+10P was shifted more noble by 240 mV compared to blank. Even more significant is the shift of the E_{pit} to more noble values, being 580 mV more positive than the blank and 220 mV compared to 100S. Due to this strong noble shift in E_{pit}, the ΔE_{pass} values of 100S and 90S+10P differ significantly, being 280 mV and 390 mV, respectively. Also, the passive current density (j_{pass}) was reduced by almost one order of magnitude for the 90S+10P compared to 100S. This indicates a synergistic effect of the two inhibitors in molar ratios S:P = 90:10 and 50:50. The curves exhibited substantially low current densities, especially in the anodic region, showing great potential to compete with the most efficient inhibitory systems in terms of efficacy [71], [129], [130].

Our further intention was to examine whether the observed synergy phenomenon is stable with an immersion time of up to seven days or is it just due to a kinetic effect that causes ostensible synergism at the beginning (after 1-day immersion), then disappears at a more prolonged immersion. The results showed that the degree of synergism increased over time, which confirmed the phenomenon of synergy. Furthermore, prolonged immersion contributed to even better anti-corrosion properties of 90S+10P than 100S (Figs. 3.1c,d). Note that prolonged immersion herein refers to 7 days of immersion. In contrast, for 100P, negligible changes with immersion time were observed in the Tafel region, indicating that this molecule did not induce any appreciable inhibition effect with prolonged immersion time.

On the other hand, for the 100S and 90S+10P curves, the Tafel slope has a strong potential dependence (Figs. 3.1c,d): in the vicinity of E_{corr} (i.e. in the active region), the Tafel slope is governed by a linear relationship between the potential and log j. However, the Tafel slope increased tremendously near the E_{pp} and immediately after that, it became even negative for a short range of potential (active-passive transition) and then near infinite. This point is followed by the passive region in which the current density remained approximately constant despite a large increase in potential, which, therefore, did not cause a significant increase in the dissolution rate. The j_{corr} of 100S after 3 and 7 days of immersion was slightly higher than 1 day, but the degree of passivation was similar. Finally, a similar trend in j_{corr} could be observed for the 90S+10P samples for 3 days and 7 days, but with E_{pit} being significantly more positive (Table 3.2). After 3 days of immersion, a wide passive range was established for 90S+10P ($E_{\mathrm{pass}} = 460$ mV), indicating strong barrier properties of the film. After 7 days of immersion, the ΔE_{pass} of the 90S+10P was 620 mV versus 240 mV of 100S. It is noteworthy that the samples immersed in the inhibitor mixture were not susceptible to pit growth even at potentials above 1 V, indicating that the formed layer exceptionally protects the metal surface from localized chloride attack. The 90S+10P sample thus showed the most promising synergistic characteristics and was therefore used for further testing.

The morphology and consistency of the surface products formed in 90S+10P, 50S+50P and 10S+90P after 24 h of immersion varied greatly (Videos 1—4 in the Appendices). While in 90S+10P, a bluish-grey adherent and the insoluble film is formed, an abundant gelatinous layer was formed in 50S+50P and 10S+90P solution; this voluminous layer formed a soft shell around the sample that was readily detached by shaking the sample to bounce into the solution leaving only a portion of this poorly adherent layer on the surface. Therefore, among S+P formulations, only 90S+10P should be considered to form a compact, stable and protective barrier against corrosion.

3.3.1.2 Linear polarization resistance

The corrosion protection characteristics of copper systems were evaluated utilizing polarization resistance (R_p), inhibition efficiency (IE) and synergistic effect (S). These parameters are outlined in Table 3.3. Copper samples exposed to solutions containing 100S for 1 day showed very high R_p values of 4211 kΩ cm^2, compared to the bare sample of 12 kΩ cm^2. Unlike 100S, 100P induced slight corrosion activation, and the sample showed a lower R_p value of 7 kΩ cm^2. When these two organic compounds were mixed in a molar ratio of S:P = 90:10, their corrosion protection behaviour became superior to 100S. After 1 day of immersion, sample 90S+10P had an R_p value of 5117 kΩ cm^2 with a synergistic parameter of $S = 2.08$. With longer immersions, R_p and IE first decreased (after 3 days) and then increased slightly (after 7 days). After 7 days of immersion, the S parameter for 90S+10P is 5.79; hence the degree of synergism improved with prolonged exposure time, indicating that, in relative terms, the corrosion protection of 90S+10P became better with immersion time compared to 100S and 100P (Fig. A.13). Note that parameters S and IE from Table 3.3 are not correlated because increasing S does not necessarily mean that the absolute value of R_p and IE also increases (Fig. A.13); instead, it means that R_p increases relative to those of individual inhibitors according to (Eq. 3.2). The increase in R_p is consistent with the increase in j_{corr} derived from polarization curves (Fig. 3.1, Table 3.2). In contrast, 50S+50P showed an R_p value less than 100S, which is the first of the two reasons why the S parameter for 50S+50P is not given in Table 4; the second reason is due to the aforementioned formation of an unstable film.

Table 3.3: Electrochemical parameters – polarization resistance (R_p), inhibition efficiency (IE) and synergistic factor (S) – measured and calculated for Cu from linear polarization resistance curves after 1 day, 3 days and 7 days of immersion in 3 wt.% NaCl with and without inhibitor. Note that the S parameter was calculated only for the binary mixtures which possess R_p greater than that of 100S.

Sample		**1 day**			**3 days**			**7 days**	
	R_p (kΩ cm^2)	**IE (%)**	**S**	**R_p (kΩ cm^2)**	**IE (%)**	**S**	**R_p (kΩ cm^2)**	**IE (%)**	**S**
Cu_bl	12 ± 0.6	–		16 ± 1.5	–		12 ± 1.5	–	
Cu_100S	4211 ± 960	99.7 ± 0.1		270 ± 93	94.1 ± 2.6		278 ± 135	95.7 ± 3.0	
Cu_100P	7 ± 2.5	–[a]		7 ± 2.1	–[a]		12 ± 2.8	0	
Cu_90S + 10P	5117 ± 1908	99.8 ± 0.1	2.08 ± 1.18	400 ± 95	96.0 ± 1.3	3.39 ± 1.63	1611 ± 471	99.3 ± 0.4	5.79 ± 3.40
Cu_50S + 50P	3020 ± 374	99.6 ± 0.1							
Cu_10S + 90P	5 ± 0	–[a]	–						

[a] The calculated value of IE is negative

3.3.1.3 X-ray photoelectron spectroscopy

XPS analysis was performed on Cu samples immersed for 1 day in 3 wt.% NaCl solution with and without the addition of 1 mM MBI (100S), OPA (100P) and their binary mixtures (90S+10P, 50S+50P, 10S+10P). Therefore, these data can be compared with the electrochemical data obtained after 1 day of immersion (Figs. 3.1a,b).

3.3.1.3.1 Surface composition

The chemical composition of the copper surface derived from the survey spectra is summarized in Table 3.4. A blank sample, i.e. immersed in 3 wt.% NaCl solution, contained 47.6 at.% Cu and 25.4 at.% O, which is compatible with oxide layer formation. The presence of 26.6 at.% C and 0.5 at.% Cl is attributed to adventitious carbon and chlorine contamination, respectively. Upon exposure to inhibitors, the concentration of Cu and O at the surface diminishes together with the trend of increasing the concentration of C, N and S, especially for samples 100S, 90S+10P and 50S+50P. This is in accordance with electrochemical measurements, as already explained in detail in Sections 3.3.1.1. and 3.3.1.2. Decreased metal concentration, together with the presence of sulphur and nitrogen, indicates the adsorption of inhibitors on the metal surface. Samples immersed in synergized inhibitor solutions (50S+50P and 90S+10P) showed little or no oxygen content, suggesting that inhibitor layers were the thickest or that oxide formation beneath was suppressed.

Table 3.4: Chemical composition of the copper surface after 24 h of immersion in 3 wt.% NaCl with and without the addition of 1 mM 2-mercaptobenzimidazole (100S), octylphosphonic acid (100P) and the binary inhibitors with the molar ratio 90:10 (90S+10P), 50:50 (50S+50P) and 10:90 (10S+90P). The composition was derived from XPS survey spectra.

Element	**Surface composition (at.%)**					
	blank (NaCl)	**100S**	**100P**	**90S+10P**	**50S+50P**	**10S+90P**
Cu	47.6	15.4	45.9	14.4	14.3	38.6
O	25.4	5.1	20.5	0.7	–	15.1
C	26.5	64.1	33.6	60.2	58.2	46.3
N	–	10.8	–	14.7	14.6	–
S	–	4.6	–	7.9	7.5	–
Cl	0.5	–	–	2.1	5.4	–
P	–	–	–	–	–	–

As for the film thickness, samples 100S and 90S+10P can be compared with the naked eye (Fig. 3.1). First of all, compared to Cu immersed in inhibitor-free NaCl solution, the appearance of the resulting surface of the 100S sample shows an improvement in corrosion inhibition on the majority of the surface, but some corroded spots are also visible. On the other hand, the surface of sample 90S+10P is covered with a much thicker film which, according to electrochemical measurements (vide supra), exhibits pronounced anticorrosion performance. A noteworthy feature is that despite the non-uniform film thickness, the surface protection is remarkably enhanced (Fig. 3.1).

The elemental ratio of N and S for 2-mercaptobenzimidazole assembled monolayers on a copper substrate is close to 2, as expected from stoichiometry (Table 3.4). In addition, the absence of phosphorus content proves that the sample exposed to octylphosphonic acid (100P) solution does not contain OPA compound on the copper surface, which explains why there is no observed effect of corrosion inhibition. At the same time, the missing phosphorus on the copper surface of 50S+50P and 90S+10P is an enigma because these two samples show the best anti-corrosion properties, with 90S+10P exhibiting the strong synergistic inhibition effect, as demonstrated by electrochemical investigation (Fig. 3.1). The sulphur content in these samples increases almost twice compared to 100S. This may be important for understanding.

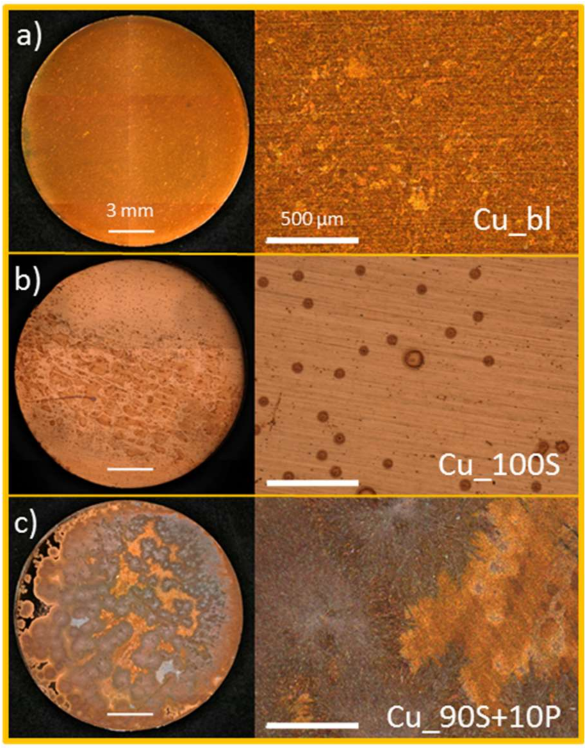

Figure 3.2: Optical microscope images of the surface appearance and localized corrosion sites on copper for (a) blank, (b) 100S and (c) 90S+10P samples after 24 h immersion: lower magnification (left) and higher magnification (right).

3.3.1.3.2 Evaluation of chemical states

To gain insight into the chemical environment of the elements and to address certain components to appropriate chemical states, high-resolution spectra were analysed in terms of chemical shifts and deconvolution of peaks (fitting) of selected spectra. Namely, the peak fitting in XPS is a valuable method for analysing complex spectra. Fitting parameters are summarized in Fig. A.14.

Fig. 3.3a shows the high-resolution Cu 2p XPS spectra for all six copper samples stacked one on the other. The centre of the Cu $2p_{3/2}$ peak at 932.5 eV can be assigned either to Cu(0) or/and Cu(I) species due to a negligibly small chemical shift among them and the absence of satellite peaks [106]. The shift in E_b by 1.1 ± 0.3 eV and 2.3 ± 0.3 eV above the main Cu $2p_{3/2}$ peak, followed by moderate peak broadening, would indicate the presence of Cu(II) compounds, probably, oxyhydroxides [106], [131], [132]. Furthermore, shake-up satellites in the range of 942 − 947 eV should exist in the spectra of samples containing $3d^9$ Cu(II) [106], [132]. In Fig. 3.3a, the samples do not show peak broadening, but only very weak satellite peaks are found in the spectra of blank and 100P samples indicating the possible occurrence of Cu(II). In other samples, especially the one with a synergistic effect, 90S+10P, the presence of a +2 oxidation state of Cu was not observed. To overcome the lack of differentiation between Cu(0) and Cu(I), X-ray induced Auger Cu peak LMM was analysed (Fig. 3.3b). For Cu(0) and Cu(I), the shift between the binding energies for the $L_3M_{4,5}M_{4,5}$ Auger lines is about 2.0 − 2.2 eV, which makes an obvious distinction between the two species. This shift, within 0.2 eV, is consistent with other studies [107]–[109]. In these overlapping high-resolution spectra, Cu(I) is pronounced on the surface of all samples except 10S+90P, in which the metallic peak predominates. Furthermore, the peak maxima of the 100S, 50S+50P and 90S+10P samples were shifted toward higher E_b along with peak broadening.

The spectra for blank, 100S and 90S+10P were further analysed by peak fitting. For the blank sample (Fig. 3.3c), the fitted Cu LMM band shows various contributions originating from different transition states, including admixtures of the final state and the occurrence of Coster-Kronig transition [132]–[134], observed at 572.4 eV, 574.5 eV and 565.8 eV, respectively. However, the spectrum displays a strong maximum at 570.2 eV associated with Cu_2O, whereas the contribution of metallic copper is located at 568.2 eV. In contrast, for the 100S and 90S+10P samples, the peaks were widened, indicating additional components at 571.5 eV and 571.9 eV, respectively, which are likely to result from a metal−inhibitor bond, i.e. the formation of a complex involving Cu(I) and MBI (Figs. 3.3d and e) [135]. In these samples, the naturally grown Cu_2O layer was so thin that the Auger feature of the underlying metal is still observed.

The C 1s core level high-resolution XPS spectra for all samples are shown in Fig. 3.4a. The appearance of a narrow main peak at a binding energy of 284.8 eV, which is attributed to the C−C/C−H groups [136]–[138], arises from adventitious organic compounds.

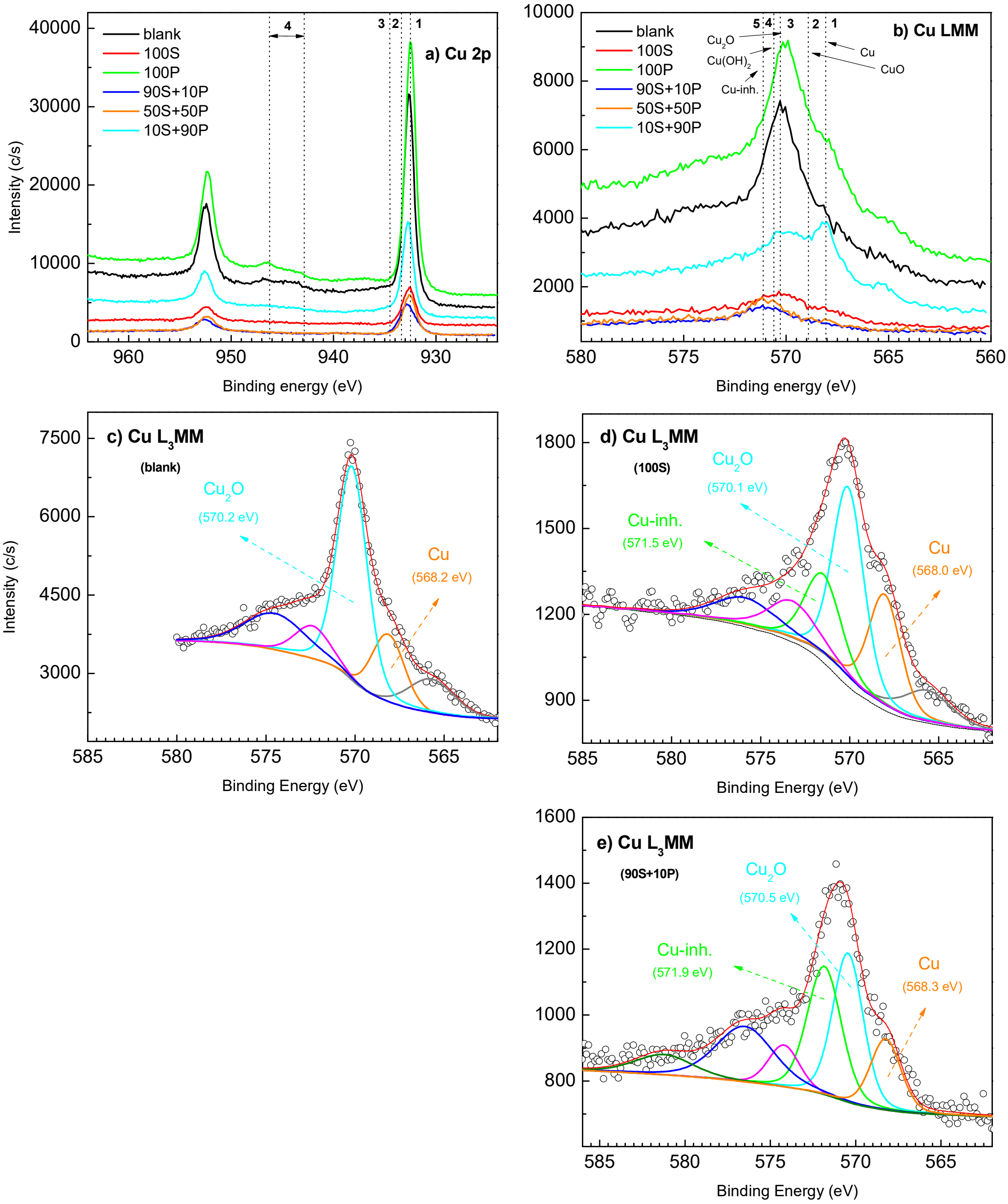

Figure 3.3: High-resolution XPS spectra of (a) Cu 2p and (b) Cu LMM recorded for non-inhibited and inhibited copper samples. Vertical lines denote the position of reference compounds: (a) 1: Cu/Cu_2O, 2: CuO, 3: $Cu(OH)_2$, 4: Cu(II) satellite peaks, (b) 1: Cu, 2: CuO, 3: Cu_2O, 4: $Cu(OH)_2$, 5: Cu-inhibitor. Deconvoluted high-resolution spectra of Cu LMM for (c) blank, (d) 100S and (e) 90S+10P. All samples before analysis were immersed for 24 h in 3 wt.% NaCl solution with or without the addition of 1 mM inhibitor(s). Experimental data are presented by symbols, fitted curve as a solid red line and component peaks are presented as solid lines of different colours. Please note that component peaks that are not assigned by arrow belong to Coster-Kronig transition peaks.

In addition, other contaminants adsorbed from the air, such as characteristic oxidized carbon species, are observed too. Binding energies that are above the main peak, i.e., at 1.2–1.5 eV, 2.8–3.0 eV and 3.6–4.3 eV, are assigned to alcohol or ether type (C–OH, C–O–C), carbonyl type (C=O), and acid or ester type (O–C=O) bonds, respectively [136]–[138]. The narrow peak representing the blank becomes wider and more intense in solutions containing inhibitor, reflecting that in addition to the presence of carbon–hydrogen and carbon–oxygen bonds, other carbon bonds, such as carbon–nitrogen at 286.1 eV and/or carbon–sulphur at 287.5 eV, also exist [41]. The contribution of these interactions will later be considered in detail in the deconvoluted spectra of nitrogen and sulphur.

The presence of oxide layers and contaminants on the surface can be further verified by considering the high-resolution spectra of O 1s (Fig. 3.4b). Oxygen was not detected on the surface of the 50S+50P (not shown) and was present in an almost negligible content on the 90S+10P. This indicates that the inhibitor layers covering the metal surface are quite thick (> 10 nm). Another observation is that the peak maximum of 100S is strongly shifted to higher binding energies; this peak is deconvoluted and compared to the blank. The O 1s spectrum of the Cu sample, exposed to chloride solution containing 100S for 24 h, represents a broad peak (Fig. 3.4c) deconvoluted into four components at 530.3, 531.5, 532.7 and 533.8 eV. Two oxide peaks are distinguished: lattice Cu_2O at 530.3 eV and defective Cu_2O at 531.5 eV, according to the literature [132], [136], [138]. The most intense peak at 532.7 eV was attributed to the alcohol/ether (C–O) functional groups due to airborne contamination, while the component found at a higher binding energy of 533.8 eV belongs to the ester type [137]. Less intense oxide peaks indicate the presence of a thin inhibitor layer above the oxide that protects the surface from corrosive attack. For comparison, the O 1s spectrum of the blank solution (Fig. 3.4d) shows a very dominant high-intensity Cu_2O peak at 530.7 eV. Finally, the centre of the high-intensity peak of the sample immersed in a 100P-containing solution is shifted toward the binding energy of copper(I) oxide, which is consistent with the lack of formation of a bond between the phosphono group and the copper substrate (Fig. 3.4b).

Nitrogen was present only on the surface of the samples containing sulphur atoms (Table 3.4, Fig. 3.5a). The high-resolution N 1s spectra show that the peak centres do not lie at the same binding energies (Fig. 3.5a). In addition, the intensity of the N 1s spectrum is higher for 50S+50P and 90S+10P than for 100S, which is compatible with the synergistic effect collected from the electrochemical investigation (Fig. 3.1). Moreover, two peaks can be easily observed for 100S, while the single peak is dominant for other samples (50S+50P and 90S+10P). The two peaks can be assigned to the nitrogen atoms of pyridine (C=N–C, peak 1) and pyrrole (C–NH–C, peak 2) (Fig. 3.6).

Interestingly, only a single pyridine peak exists in the binary inhibitor sample 10S+90P (i.e. one without synergistic effect), but pyrrole predominates for the other binary inhibitor samples, 50S+50P and 90S+10P. The presence of different chemical states of nitrogen certainly indicates a variation in the mechanisms by which the inhibitor molecule binds to the copper substrate [41], [73]. In addition, it proves that both thiolate and thione tautomers exist, since thione does not contain pyridine in its structure (Fig. 3.6). To better understand this issue, the N 1s spectra were deconvoluted (Fig. 3.5b and Fig. 3.5c). Sample 100S contained a pyridine (C=N–C) peak at 398.9 eV and a pyrrole (C–NH–C) peak at 400.3 eV (Fig. 3.5b). The intensity ratio of $I_{pyridine}/I_{pyrrole}$ is almost 1:1, with the pyridine peak slightly higher, which is also consistent with the ratio between the areas $A_{pyridine}/A_{pyrrole}$, suggesting that mercapto molecules are adsorbed on the copper surface as deprotonated thiolates due to the presence of equal contribution of the two chemical states which is manifested by the appearance of two equal peaks. Xue et al. found that the FTIR spectra of MBI and its reaction products with copper oxides show vibrations of the C=S bond, while these vibrations do not exist in the spectrum of the product formed between copper metal and MBI [139]. Moreover, DFT calculations [73] ruled out the presence of the thiol form because the thione form is significantly more stable than thiol in solutions (Fig. 3.6).

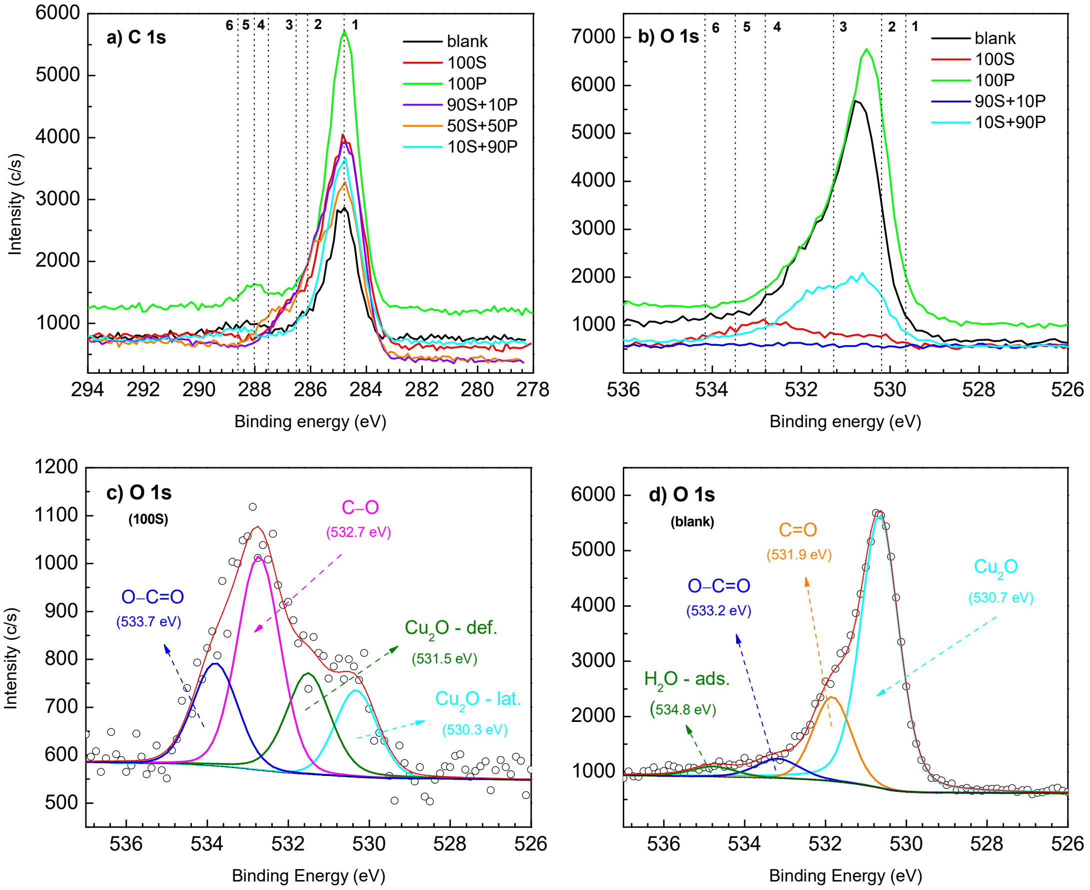

Figure 3.4: High-resolution XPS spectra of (a) C 1s and (b) O 1s recorded for all copper samples. Vertical lines denote the position of reference compounds: (a) 1: C—C/C—H, 2: C—N, 3: C—O—H/C—O—C, 4: C—S, 5: C=O, 6: O—C=O, (b) 1: CuO, 2: lattice Cu_2O, 3: C=O/defective Cu_2O, 4: C—O—H/C—O—C, 5: O—C=O, 6: H_2O. Deconvoluted high-resolution XPS spectra of O 1s recorded for (c) 100S and (d) blank. All samples before analysis were immersed for 24 h in 3 wt.% NaCl solution with or without the addition of 1 mM inhibitor(s). Experimental data are presented by symbols, fitted curve as a solid red line and component peaks are presented as solid lines of different colours.

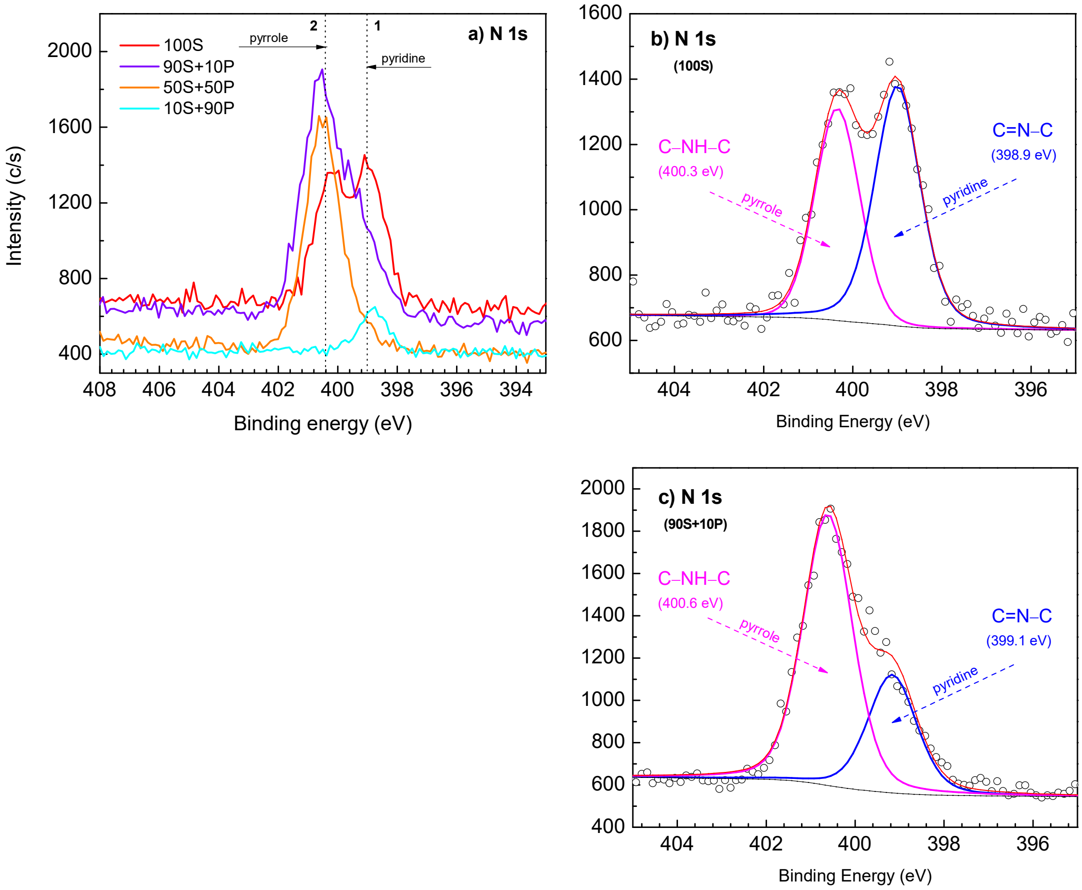

Figure 3.5: High-resolution XPS spectra of (a) N 1s recorded for all copper samples. Vertical lines denote the position of reference compounds: 1: C=N–C, 2: C–NH–C. Deconvoluted high-resolution XPS spectra of N 1s recorded for (b) 100S and (c) 90S+10P. All samples before analysis were immersed for 24 h in 3 wt.% NaCl solution with or without the addition of 1 mM inhibitor(s). Experimental data are presented by symbols, fitted curve as a solid red line and component peaks are presented as solid lines of different colours.

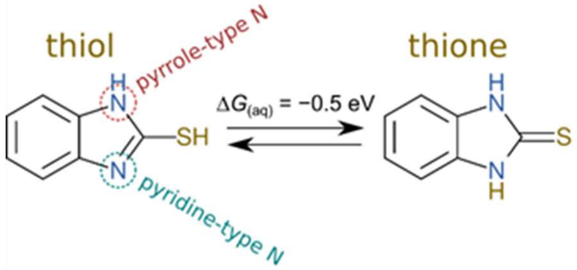

Figure 3.6: Skeleton structures of thiol (left) and thione (right) tautomers of MBI; note that thione is by about 0.5 eV more stable than thiol [73].

These calculations further showed that the S—H bond of the adsorbed thiol would dissociate rapidly, resulting in the adsorbed thiolate form of MBI. For the 90S+10P sample (Fig. 3.5a), the pyrrole peak at 400.6 eV is the dominant one. The $A_{pyridine}/A_{pyrrole}$ ratio of 1:2 (Fig. 3.5c), which stoichiometrically corresponds to two thiolate molecules and one thione molecule,[2] indicates that the inhibitor—metal bonding mechanism changes when two inhibitors are present in the NaCl solution. These observations are compatible with the DFT results presented in Sec. 3.3, suggesting that MBI can bond to copper surfaces either as a thione or thiolate, with the preference between the two depending on surface detail. In some cases, thiolate is better described as deprotonated thione (Fig. 3.6). Apparently, the presence of OPA modifies the surface so that a significant fraction of MBI binds to the surface in the form of thione. In addition, during the adsorption of MBI [72], the molecule—surface bond induces a change in the electron environment of one N atom compared to another N atom, leading to peak broadening. The FWHM values of pyridine and pyrrole peaks of 90S+10P are broader (FWHM ≈ 1.3) than those for 100S (FWHM ≈ 1.2). Although it is not yet clear how the presence of phosphorus compound in the synergized formulation improves corrosion protection properties, since it is not detected on the copper surface by XPS analysis (Table 3.4), it is clear that it alters the inhibitor—metal bonding mechanism, possibly by changing the structure and chemical composition of copper surface (cf. Figs. 3.3d,e).

The sulphur 2p core-level spectrum has closely spaced spin-orbit components (Fig. 3.7a), S $2p_{3/2}$ and S $2p_{1/2}$, with an intensity ratio of $2p_{1/2}/2p_{3/2}$ of about 0.5 and a peak separation of 1.2 eV. The centres of the maxima were shifted toward higher binding energies following the same chemical shift trend as for the N 1s spectra. It is of great importance to emphasize the absence of signals for undesired oxidized sulphur species such as sulfonate at about 167 eV, which would result in the degradation of surface films [41], [72]. The high-resolution XPS spectrum of sulphur (Fig. 3.7b), for the samples exposed to 100S inhibitor solution, was deconvoluted into one pair of doublet identified as S $2p_{3/2}$ at 162.6 eV and $2p_{1/2}$ at 163.8 eV, corresponding to a single chemical state relating to metal—mercapto compounds, mainly thiolates (i.e. Cu—S—C bond) [41], [72], [110]. Also, the high-resolution spectrum of the 90S+10P sample was deconvoluted into a single doublet (Fig. 3.7c). The $2p_{3/2}$ peak of higher intensity at 162.9 eV and a $2p_{1/2}$ peak at 164.1 eV are attributed to the same metal—mercapto species. Finally, when we compare the S 2p deconvoluted spectra of 100S and 90S+10P, the latter seems to be wider, especially at higher binding energies. As the pyridine content in the N 1s spectrum of 90S+10P becomes lower (Fig. 3.5c), the $2p_{1/2}$ component peak of S 2p increases. This could reflect a change in the chemical environment of the sulphur belonging to the adsorbed inhibitor compound, which, in addition to C—S (thiolate), may include C=S (thione) species, as already argued above based on the N 1s spectra. It should be emphasized that there is a lot of confusion in the literature regarding the interpretation of the S 2p spectra. Some papers attribute the new chemical state to the $2p_{1/2}$ spin-orbit component of the S 2p doublet, which is incorrect. The S 2p doublet, including $2p_{3/2}$ and $2p_{1/2}$, represents the same chemical state. In this study, this is the bound thiolate.

The presence of chloride on the metal surface is often associated with surface contaminants, especially when the corrosion medium is NaCl. The high-resolution Cl 2p spectra consist of a single chemical state with two spin-orbit split peaks separated by 1.6 eV (Fig. 3.7d). The corresponding peaks, Cl $2p_{3/2}$ at 198.2 eV and Cl $2p_{1/2}$ at 199.8 eV, were attributed to metal—chloride bonds (CuCl or $CuCl_2$ overlaps) [41]. Interestingly, the chloride signal exists only in the spectra of the samples with the greatest anticorrosive

---

[2] Thiolate contains one pyrrole-type and one pyridine-type N atom, whereas thione contains two pyrrole-type N atoms (Fig. 4), hence 2×thiolate + 1×thione correspond to $2\times(N_{pyrrole} + N_{pyridine}) + 2N_{pyrrole} = 2N_{pyridine} + 4N_{pyrrole}$ and therefore $N_{pyridine}:N_{pyrrole} = 1:2$.

properties and synergistic effect, 50S+50P and 90S+10P, which at the same time contain the highest amounts of sulphur (Table 3.4). It seems that chlorides could be involved in the formation of a protective inhibitor complex on the surface of the copper substrate, as will be discussed in the next chapter.

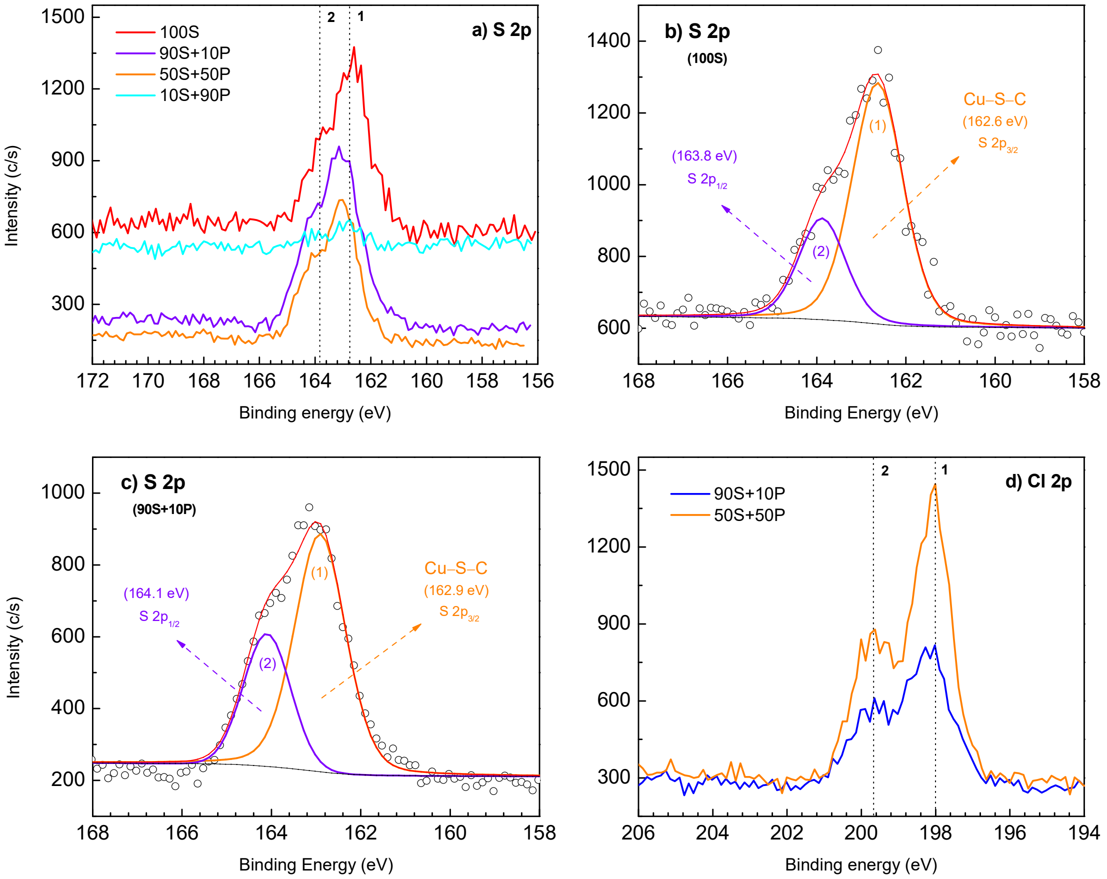

Figure 3.7: High-resolution XPS spectra of (a–c) S 2p and (d) Cl 2p recorded for copper samples. Vertical lines denote the position of reference compounds: (a) 1: S $2p_{3/2}$, 2: S $2p_{1/2}$, (d) 1: Cl $2p_{3/2}$, 2: Cl $2p_{1/2}$. Deconvoluted high-resolution XPS spectra of S 2p recorded for (b) 100S and (c) 90S+10P. All samples before analysis were immersed for 24 h in 3 wt.% NaCl solution with or without the addition of 1mM inhibitor(s). Experimental data are presented by symbols, fitted curve as a solid red line and component peaks are presented as solid lines of different colours.

3.3.1.4 Fourier transform infrared spectroscopy

Complementary IR measurements were carried out to prove the adsorption of the inhibitor molecules on metal substrates. FTIR analysis was performed on the Cu samples immersed for 24 h in 3 wt.% NaCl solutions with and without adding 1 mM MBI, OPA, 90S+10P, 50S+50P, 10S+10P. These data can therefore be compared with electrochemical ones (Figs. 3.1a,b) and XPS data (Figs. 3.3-3.7).

IR spectra were recorded for the copper surface exposed only to NaCl (designated as a blank), as well as to solutions 100S, 90S+10P, 50S+50P and 10S+90P (Fig. 3.8). As a reference, the FTIR spectrum for MBI in solid (powder) form is also presented. All stretching absorptions corresponding to unsaturated hydrocarbon (–C=C–H) occur between 3100–3000 cm^{-1} [140]. All samples treated with MBI inhibitor showed a weak to moderate band at about 3060 cm^{-1}, which unambiguously indicates the presence of unsaturated compounds and/or aromatic rings. The absorptions resulting from C=S stretching vibrations depend on the type of compound, particularly to what atoms the carbon atom of the C=S group is bonded. Thus, Rao and Venkataraghavan differentiated the two classes [141]. Namely, when the C=S group is attached to elements other than nitrogen, the unambiguous assignment of its stretching frequency could be performed only when there are no significant coupling effects. In the case of nitrogen-containing thiocarbonyl derivatives, three bands should appear due to mixed vibrations.

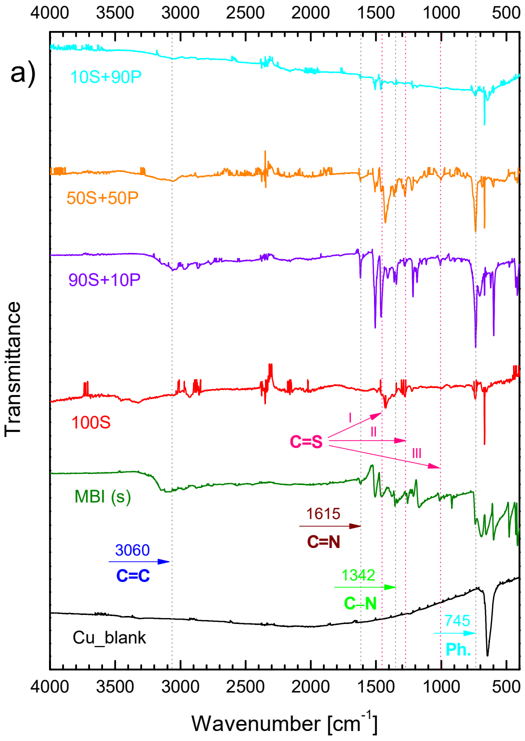

Figure 3.8: FTIR spectra of reference MBI solid (powdered) and Cu samples (Cu blank, 100S, 90S+10P, 50S+50P and 10S+90P), and (b) reference OPA (powdered) and Al samples (Al blank, 100P, 90S+10P, 50S+50P and 10S+90P). Before analysis, all samples were immersed for 24 h in 3 wt.% NaCl solution with or without the addition of 1 mM inhibitor(s). Vertical lines denote the position of C=C, C–N, C=N, C=S and Ph (phenyl) bands according to reference and literature data, as described in the text.

Thus, in Fig. 3.8 the frequency regions of 1530–1420 cm^{-1}, 1350–1240 cm^{-1} and 1140–940 cm^{-1} (marked by lines I, II and III, respectively) represent the –N–C=S group in qualitative terms. One important factor to bear in mind is not only the presence of certain bands in the spectrum but also the absence of other important bands. The C–S and S–H bonds produce strong spectral activity in the Raman spectrum, due to their high polarizability, compared to very weak absorptions in the infrared spectrum [140], [142]. Therefore, the absence of their bands is reasonable. In addition, no evidence of the presence of thiol tautomers is consistent with the fact that in the solid and aqueous states, MBI molecules exist in the form of thione tautomer [143]. Furthermore, the absence of C=S bands on the surface of the 100S sample suggests that the MBI molecule binds to the Cu substrate as a thiolate. On the other hand, the C=S bands are present in the spectra of the samples of binary inhibitor 90S+10P, 50S+50P and 10S+90P, probably due to the existence of multiple layers of inhibitor in the form of thione, especially in the sample 90S+10P.

In addition, C=S bands of the 90S+10P sample resemble those in the powder MBI spectrum. These results follow the XPS results (Figs. 3.3–3.5 and 3.7). Double-bonded nitrogen groups, such as imino groups (C=N), exhibit an absorption around 1615 cm^{-1} [140], [142], [144], whereas the stretching frequency at 1342 cm^{-1} is designated to aromatic amines (C–N) [140], [145]. Finally, the frequency of 745 cm^{-1}, designated to the phenyl ring out-of-plane bending vibration [146], was found for all samples except the blank. Overall, these spectra clearly show that MBI is adsorbed on Cu samples. In addition, on the surface of samples treated with solutions containing binary inhibitors, there is no evidence of detected phosphono group vibrations, which would otherwise appear at around 1100 cm^{-1} [142], which is consistent with the results of XPS surface analysis (Table 3.4).

3.3.1.5 Water contact angle measurements

The wettability of the samples modified with different inhibitor solutions was tested by measuring water contact angles (WCA, θ) on the surface of Cu samples immersed for 24 h in 3 wt.% NaCl solutions with and without the addition of 1 mM MBI, OPA, 90S+10P, 50S+50P, 10S+90P (Table 3.5).

The hydrophilic nature of the blank copper sample with a value of $\theta = 58°$ was not significantly changed by modifying its surface with MBI ($\theta = 70°$); hence the surface remained hydrophilic.[3] On the other hand, the contact angle of the sample 100P decreased ($\theta = 26°$), i.e., it became more hydrophilic. This implies that the phosphonate molecules were not adsorbed on the copper surface because the octyl chains of the adsorbed OPA would be directed outwards, making the surface more hydrophobic. Electrochemical data show that copper is subject to corrosion in a solution containing 100P (Fig. 3.1c), which is confirmed by XPS data showing a higher peak of metallic Cu, which prevails even for blank (i.e., NaCl) (Fig. 3.3b). In contrast, no metallic Cu peak was observed after immersion in blank NaCl and 100S solutions (Fig. 3.3b). These facts indicate that copper actively corrodes in 100P solution at pH 3 (Table 3.1) since the native oxide film is unstable due to spontaneous dissolution [147]. Contradictory, the corresponding XPS O 1s peak is high, implying the presence of an oxide layer after immersion in 100P (Fig. 3.4b); however, the absence of an oxide layer cannot be directly demonstrated by ex-situ XPS analysis because native oxide may be formed during sample transfer from the cell to the XPS spectrometer. Considering these facts, we assume that the reduced θ for the 100P sample is related to the corroded Cu surface.

Table 3.5: Contact angles of water drop and wettability modes for Cu after 24 h of immersion in 3 wt.% NaCl with and without the addition of single and binary inhibitors.

Sample	**Contact angle (θ)**	**Wettability**
Cu_bl	58 ± 5	hydrophilic
Cu_100S	70 ± 4	hydrophilic
Cu_100P	26 ± 1	hydrophilic
Cu_90S+10P	115 ± 2	hydrophobic
Cu_50S+50P	70 ± 2	hydrophilic
Cu_10S+90P	36 ± 2	hydrophilic

---

[3] We use the following standard criteria: superhydrophilic ($\theta < 10°$), hydrophilic ($10° \leq \theta \leq 90°$), hydrophobic ($90° < \theta \leq 150°$) and superhydrophobic ($\theta > 150°$).

The 10S+90P sample has a θ value similar to that for 100P, 36°, which is consistent with low pH processes as described above. As the concentration of OPA in binary inhibitor solutions decreases, the surface becomes less hydrophilic with $\theta = 70°$ for the 50S+50P sample, which is equivalent to that for the 100S sample, indicating incomplete surface coverage. The 90S+10P sample, however, shows the largest θ of 115° and is thus hydrophobic. This confirms the change in the chemical composition of the surface (Figs. 3.3–3.7, 3.8) but may also be associated with a significant change in the surface morphology (as will be presented in *Chapter 4*). The reduced wettability contributes to the best anti-corrosion protection of this sample.

3.3.1.6 Tentative mechanism of synergistic inhibition of Cu by 90S+10P

The most straightforward explanation for the synergistic inhibition of Cu by 90S+10P would be the mixed adsorption of MBI and OPA with a favourable effect of the two compounds on their mutual adsorption. However, this scenario can be ruled out, as OPA was not detected by XPS and FTIR on Cu samples, while both methods detected MBI. Furthermore, 100P does not show inhibition of Cu corrosion, which further confirms the lack of adsorption. This aspect is particularly puzzling, as DFT calculations reveal that MBI and phosphonic acid display a similar tendency to adsorb on copper surfaces. Furthermore, the adsorption of phosphonic acids on oxidized copper surfaces was proved experimentally by Hoque et al. [80] by liquid deposition in ethanol solution. However, current experimental conditions differ considerably because an aqueous solution containing chloride ions is used instead, and therein, the presence of OPA considerably lowers pH (Table 3.1). This implies that low pH and the presence of chloride ions somehow prevent the adsorption of OPA. It seems that resolving these apparently conflicting aspects is the key to explaining the synergism.

To this end, the first relevant observation is that the thicknesses of the 100S and 90S+10P layers differ considerably, with the former being several nanometres thick and the latter much thicker, as evidenced by preliminary ToF-SIMS and cross-section/EDX analysis [102]. This difference most likely stems from different pH solutions, i.e., 100S and 90S+10P. Namely, Cu oxides are stable in the aqueous medium in the pH range of 8–12, whereas at lower pH, the onset of Cu dissolution is expected. For the 100S sample at pH 5.5, the formation of a thin Cu(I)MBI film is reasonable because, at this pH, the Cu_2O is sufficiently stable not to produce enough Cu^+ ions to go beyond the monolayer or a few layers of thick films (Fig. 3.9c) [135], [148]. In contrast, for the 90S+10P sample at lower pH of 4, the amount of Cu^+ ions produced was boosted, and a much thicker Cu(I)MBI film formed (Fig. 3.9b) by the dissolution-precipitation mechanism.[4] Similar observations were reported by Ogle and Poling, who demonstrated that the corrosion of Cu in Cl^- solutions containing benzotriazole (BTA) depends on the thickness of the native surface oxide [148]. Their results revealed the formation of a thin Cu(I)BTA complex film in near-neutral environments above the limiting pH (pH_L) and a thick Cu(I)BTA complex film in acidic environments below pH_L, where $4 > pH_L > 3.5$.

In the present study, pH_L falls into the same pH range (Fig. 3.9). The growth of inhibitor layers is, therefore, more intense in acidic than in near-neutral solutions due to the continuous availability of Cu ions formed by dissolution in an acidic environment. However, lowering the pH should not be overdone because even at lower pH values of 50S+50P (pH = 3.3) and 10S+90P (pH = 3), a thick compact Cu(I)MBI film does not form but a

---

[4] Taking into account the evidence including the absence of Cu(II) in XPS spectra (Fig. 3.3) and the presence of Cu(I) and Cu–inhibitor peaks in the Cu LMM spectrum (Fig. 3.3e) it can be proposed that copper, in the tentative polymeric structure of the thick Cu(I)MBI complex film shown in Fig. 3.9b, is in the Cu(I) state having a coordination number of 2.

voluminous gelatinous product arises (Fig. 3.9a) that does not offer corrosion protection for 10S+90P. Indeed, the morphology and consistency of the surface products formed for 90S+10P, 50S+50P and 10S+90P after 24 h of immersion differ significantly (Videos 1–4 in Appendices). For 90S+10P (pH = 4), precipitation of a bluish-grey insoluble film was observed during 24 h of immersion (Video 1), while the formation of the abundant gelatinous envelope is seen for 50S+50P at pH 3.3 (Video 2) and for 10S+90P at pH 3 (Video 3). This gelatinous product is easily detached from the Cu substrate only by shaking (Video 4).

However, the superior inhibition efficiency of 90S+10P cannot be attributed solely to a lower pH of 4. Electrochemical measurements of samples immersed in 100S solution with pH adjusted to 4 by HCl reveal inferior corrosion inhibition than 90S+10P (Fig. A.15). Therefore, OPA itself appears to play an important role, although it has not been detected in copper samples. Indeed, no inhibition of Cu corrosion was observed for 100P (pH = 3).

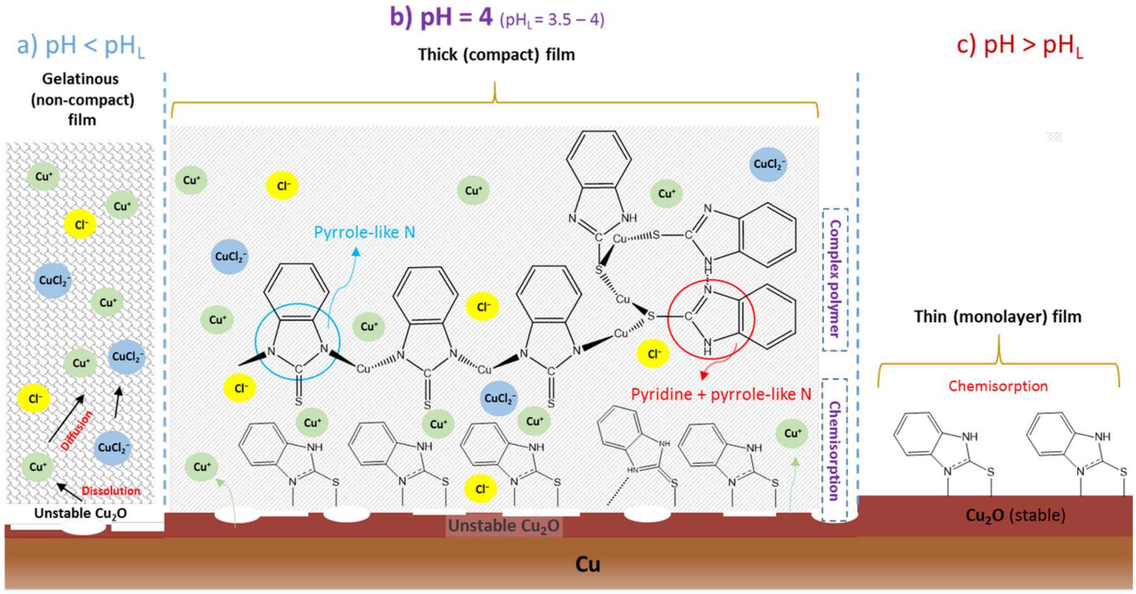

Figure 3.9: Proposed tentative polymeric structures of Cu–MBI: (a) the non-compact voluminous gelatinous film forms at pH < pH$_L$ (for 10S+90P and 50S+50P at pH 3 and 3.3, respectively), (b) the thick protective film forms at pH 4 for 90S+10P, and (c) for 100S the thin film forms at pH 5.5 (pH > pH$_L$).

At this pH, copper corrodes to form Cu^{2+} ions as a stable species; hence the formation of Cu(II)OPA complexes is probably favoured because phosphonic acid is a good complexing agent [149].[5] A similar situation occurs in mixed systems 10S+90P and 50S+50P, where voluminous products that do not contain OPA are formed. Given that the bonding of phosphonates to copper surfaces should be strong, as shown by DFT results, chelating seems to be strongly favoured in this case. It is also possible that transient adsorption of phosphonates occurs at some point but is rapidly accompanied by the formation of more stable Cu(II)OPA complexes released to the bulk solution. This results in a change of surface activity which for the 90S+10P becomes more prone to adsorption of MBI compared to 100S. Indeed, OPA should affect the bonding mechanism of MBI, as

---

[5] Phosphonates are well-known chelating agents and potent scale inhibitors of mineral precipitation and growth [149]. They display very high affinity towards alkali and 3d metal ions; for the latter the stability constants follow the trend [154]: $Mn^{2+} < Fe^{2+} < Co^{2+} < Ni^{2+} < Cu^{2+} > Zn^{2+}$, i.e. the most stable complexes are formed with Cu^{2+}.

the pyrrole component in the XPS spectrum of N 1s is dominant only for 90S+10P (Fig. 3.8c), indicating the presence of thione in addition to thiolate.

Furthermore, the exceptionally high water contact angle obtained for 90S+10P (Table 3.5) can be attributed, in part, to the modified surface topography relative to 100S [102]. Therefore, the formation of a protective inhibitor layer in the presence of both MBI and OPA appears to be due to an interplay between the condensation of adsorbed inhibitor species on the surface and the chelating of dissolved metal ions. The balance between these two processes determines the outcome. Regarding the role of the critical micelle concentration (CMC) of OPA, it should be noted that at 22 °C, the CMC of OPA is 8.5×10^{-3} M [150], which is almost one order of magnitude higher than the highest concentration of OPA used in our study. Therefore, the CMC effect is excluded.

Lastly, the role of chloride ions should also be considered. According to the Cl 2p peak in the XPS spectrum of 90S+10P (Fig. 3.7d), the effect of CuCl should be taken into account as a possible intermediate step. CuCl reacts with Cl^- to form $CuCl_2^-$ (Eq. 1.9), which can partake not only in the formation of Cu_2O (Eq. 1.12) but also in the formation of insoluble Cu-inhibitor complexes, as demonstrated by Modestov et al. in the case of the benzotriazole/copper system [10]. Furthermore, chloride ions may also be present in the structure of Cu(I)MBI complexes because the detected XPS Cl 2p peak (Fig. 3.7d) may indicate the existence of chlorido-metallorganic complexes. This possibility is supported by our ToF-SIMS analysis [102] to be presented in the next chapter.

3.3.2 Aluminium

3.3.2.1 Potentiodynamic polarization curves

The potentiodynamic polarization curve recorded for aluminium in 3 wt.% NaCl after 24 h rest at OCP is shown in Fig. 3.10a. Bare Al was subject to immediate pitting when polarized anodically. The shape of the cathodic curve expresses a mixed mass control with an increased contribution of diffusion control.

The 100S curve notifies a moderate reduction in cathodic current densities but with an immediate increase in anodic current density following E_{corr} due to dissolution of Al, similar to that of the uninhibited sample (Fig. 3.10a). Meanwhile, the behaviour of Al in 100P reflects a large inhibition effect with a broad ΔE_{pass} of 330 mV. Together with a reduced j_{corr} down to $2.03\ 10^{-8}$ A cm^{-2} compared to 2.18×10^{-7} A cm^{-2} in NaCl, we can thus classify 100P as a mixed inhibitor for Al with a predominantly anodic impact. 100P does not show a sharp transition to passivation, i.e. it lacks a well-defined E_{pp} so that the current density is not entirely independent of increasing potential, but the increase is slowed to such an extent that can be interpreted as pseudo-passivation [114].

The results, summarized in Table 3.6, are consistent with the different tendencies of 100S and 100P inhibitors to chemisorb on the aluminium substrate and reduce the rate of anodic dissolution or cathodic oxygen reduction [84], [115]. The possible synergistic effect was first studied for the 10S+90P mixture (Fig. 3.10a). The curve is similar to that for the 100P sample, with a slightly smaller j_{corr}, but a smaller shift of E_{corr} and, consequently, narrower E_{pass}. However, compared to 100S, the addition of OPA compound significantly improves the inhibition action. As the S/P ratio increases (Fig. 3.10b, Table 3.6), so do j_{corr} and E_{pit} decrease, which is contrary to the results for copper. So, there is no synergism, but 10S+90P shows pronounced stability for aluminium. The term stability refers to the fact that the presence of the S inhibitor in the S+P mixture does not interfere with the inhibitory ability of P.

In contrast, the term synergistic refers to the improvement of the inhibitory ability of S+P compared to either S or P. Among the binary combinations, the sample denoted as

10S+90P shows the highest ΔE_{pass} of 270 mV, and although it possesses no synergistic activity, it can be considered the most suitable for further analysis and comparison with the action of individual inhibitors.

Table 3.6: Electrochemical parameters – corrosion potential (E_{corr}), corrosion current density (j_{corr}), pitting potential (E_{pit}), passive range (ΔE_{pass}), anodic Tafel slope (b_{a}) and cathodic Tafel slope (b_{c}) – deduced for Al from the potentiodynamic polarization curves (Fig. 3) after 1 day of immersion in 3 wt.% NaCl.

Sample	E_{corr} (mV)	j_{corr} (A cm^{-2})	E_{pit} (mV)	$\Delta E_{\text{pass}} = \lvert E_{\text{pit}} - E_{\text{corr}}\rvert$ (mV)	b_{a} (mV/dec)	$-b_{\text{c}}$ (mV/dec)
1d_Al_bl	−630	2.18×10^{-7}	–	–	–[a]	243
1d_Al_100S	−670	4.56×10^{-8}	–	–	–[a]	186
1d_Al_100P	−540	2.03×10^{-8}	−210	330	134	188
1d_Al_90S+10P	−610	2.84×10^{-8}	−460	150	168	202
1d_Al_50S+50P	−630	1.65×10^{-8}	−400	230	155	167
1d_Al_10S+90P	−600	1.16×10^{-8}	−340	270	140	133

[a] The polarization curves with not well defined anodic Tafel region were extrapolated by inspecting only a linear fit of the cathodic Tafel curve, which intersects the E_{corr}.

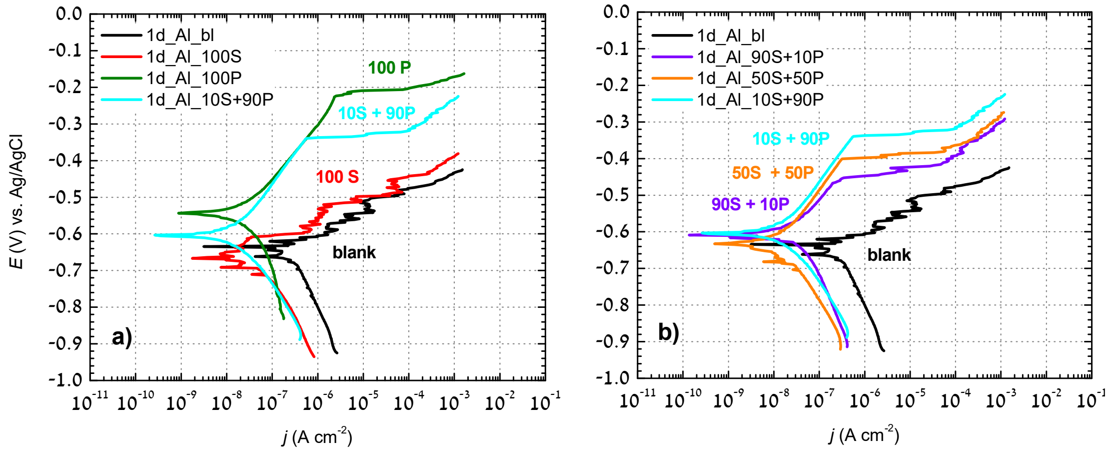

Figure 3.10: Potentiodynamic curves recorded for aluminium in 3 wt.% NaCl solution with and without the addition of 1 mM of (a) 100S, 100P and binary 10S+90P after 1 day of immersion, (b) binary inhibitors 90S+10P, 50S+50P and 10S+90P after 1 day of immersion. The scan rate was 1 mV/s.

3.3.2.2 X-ray photoelectron spectroscopy

3.3.2.2.1 Surface composition

Table 3.7, deduced from the survey spectra, outlines the surface composition of aluminium substrates before and after exposure to chloride-containing medium with and without added inhibitors. The blank sample contained 16.2 at.% Al and 43.7 at.% O due to the presence of aluminium oxide on the surface. The addition of MBI inhibitor (100S) does not cause adsorption on the metal surface because the high content of metallic aluminium, oxygen, and carbon remains almost the same as in the case of the blank sample. On the other hand, the adsorption of octylphosphonic acid (100P) is confirmed by a significant decrease in the content of Al and O together with increased content of C. The most important indicator of OPA adsorption is the presence of phosphorus in the amount of 5 at.%. Important information is obtained by analysing Al samples immersed in solutions containing binary inhibitors in different molar ratios. It is easy to see that the adsorption affinity of OPA molecules is maintained for binary combinations as well. Among the three binary mixture ratios, the 90S+10P sample showed the weakest adsorption tendency. Furthermore, the other two samples, 50S+50P and 10S+90P, have a similar phosphorus content with 100P, indicating high molecular coverage. It should be emphasized that the formulations of the binary inhibitor do not show any significant synergistic effect but retain the tendency to adsorption with guaranteed inhibition stability (Fig. 3.10b). Namely, the non-inhibiting MBI compound neither reduces nor stimulates the inhibitory action of the OPA inhibitor.

3.3.2.2.2 Evaluation of chemical states

The high-resolution Al 2p spectra for six different samples are shown in Fig. 3.11a. The peak maxima for the samples with high phosphorus content (50S+50P, 10S+90P and 100P) were shifted towards higher binding energies, and the shift was the largest for 100P. For further analysis of the Al 2p spectra, peaks fitting was performed and compared with the blank sample. Deconvoluted Al 2p spectrum for a sample immersed in NaCl without added inhibitor (Fig. 3.11b) was described by a metallic Al peak at 72.6 eV [110], substrate suboxide (AlO_x) related peak at 73.1 eV [115], Al_2O_3 at 74.3 eV and $Al(OH)_3$ at 74.9 eV, indicating the presence of oxyhydroxides in the near-surface region [116]. All fitting parameters are tabulated in Fig. A.16. Adsorption of octylphosphonic acid changes the shape and FWHM of the Al 2p spectrum (Fig. 3.11c and 3.11d). Four peaks are attributed to oxides and hydroxides at 74.0 eV and 75.2 eV, respectively, and two peaks located at higher binding energies of 76.2 eV and 77.1 eV can be attributed to the bonding between aluminium and phosphono functional groups (Al—O—P) [116], [151]. The Al 2p spectrum for 10S+90P (Fig. 3.11d) consists of the same four peaks at almost the same binding energy values as for 100P (Fig. 3.11c). In addition, the contribution of peaks corresponding to Al—O—P bonding was reduced, which is in line with Table 3.7 and the expected higher degree of adsorption of OPA on the aluminium substrate.

Oxygen peak is very important to check for the presence of different phosphorus species. An interesting difference between the blank and the inhibitor-treated substrates appears in the high-resolution spectra of O 1s (Fig. 3.12a). The intensity of oxygen peaks for aluminium samples treated with phosphorus-containing inhibitors is much lower than the intensity of blank and 100S. Deconvoluted curves for the blank Al surface (Fig. 3.12b) represent a large contribution of Al—O interactions [84], [115] from Al oxides/hydroxides at the energy positions of 530.5 eV and 531.8 eV. Also, high content of adsorbed contamination containing oxygen [137] is detected at 532.9 eV, consistent with the C 1s spectrum for the blank (*vide infra,* Fig. 3.13a). For inhibitor-treated samples, deconvoluted O 1s spectra show the contribution of different adsorbed components belonging to the phosphonate functional group (Figs. 3.12c and 3.12d). The phosphonic anchor group chemisorbs on hydroxylated oxidized Al surfaces via a condensation mechanism [79], [115] (Eq. 3.4), which involves dissociative adsorption (via cleavage of the molecular O-H bond) by replacing a surface OH group and forming a water molecule as a side product:

$$\text{P-O-H} + \text{OH-Al}^* \longrightarrow \text{P-O-Al}^* + \text{H}_2\text{O} \tag{3.4}$$

where Al* stands for surface Al ion. This reaction results in a monodentate bonded phosphonate.

Adsorption via condensation mechanism was confirmed by the absence of hydroxide peaks (Al—OH) in both samples, 100P and 10S+90P. The deconvoluted spectrum of the 100P sample (Fig. 3.12c), compared to the blank, seems to expand towards more positive values of binding energy followed by the shoulder on the lower energy side of the envelope, indicating the presence of new components assigned to P=O and Al—O—P located at 531.2 eV and 532.4 eV [81], respectively.

Table 3.7: Chemical composition of the aluminium surface after 24 h of immersion in 3 wt.% with and without the addition of 1 mM 2-mercaptobenzimidazole (100S), octylphosphonic acid (100P) and the binary inhibitors with the molar ratio 90:10 (90S+10P), 50:50 (50S+50P) and 10:90 (10S+90P).

Element	**Surface composition (at.%)**					
	blank (NaCl)	**100S**	**100P**	**90S+10P**	**50S+50P**	**10S+90**
Al	16.2	13.7	6.4	8.5	5.7	5.7
O	43.7	43.5	28.2	34.6	25.8	24.9
C	39.4	41.9	59.8	54.4	63.3	64.6
N	0.7	0.5	–	–	–	–
S	–	–	–	–	–	–
Cl	–	0.4	–	–	–	–
Na	–	–	0.6	–	–	–
P	–	–	5	2.5	5.2	4.8

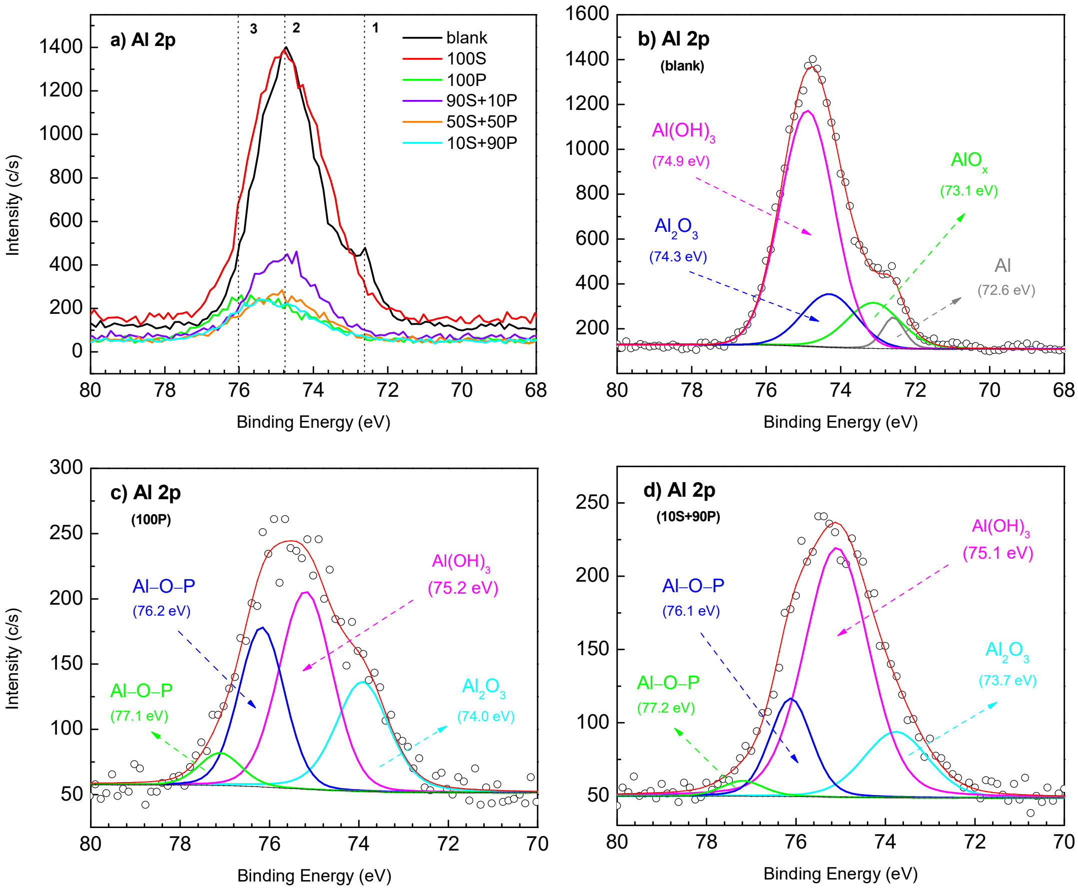

Figure 3.11: High-resolution XPS spectra of (a) Al 2p recorded for all aluminium samples. Vertical lines denote the position of reference compounds: (a) 1: Al, 2: Al(III) oxyhydroxides, 3: Al—O—P. Deconvoluted high-resolution XPS spectra of Al 2p recorded for (b) blank, (c) 100P and (d) 10S+90P. All samples before analysis were immersed for 24 h in 3 wt.% NaCl solution with or without the addition of 1mM inhibitor(s). Experimental data are presented by symbols, fitted curve as a red solid line and component peaks are presented as solid lines of different colours.

In addition, after adsorption of OPA, oxygen contamination disappeared on account of evolving components attributed to H—O—P at 533.7 eV [81], [116], [119]. Furthermore, as the hydroxide peak vanished (Fig. 3.12c), the presence of oxide at 530.2 eV remained, confirming that phosphono groups are adsorbed only on the hydroxylated parts of the surface, which is consistent with the reduced $Al(OH)_3$ peak (Fig. 3.11c). On the other hand, the O 1s spectrum of 10S+90P (Fig. 3.12d) is not as broad as the spectrum of 100P, which means that the extent of contribution of phosphono group components is different. Indeed, the intensities of specific phosphono groups (P=O, Al—O—P and H—O—P) are reduced, suggesting that the adsorption mechanism may be slightly altered due to lower concentration of OPA or steric effects between MBI and OPA.

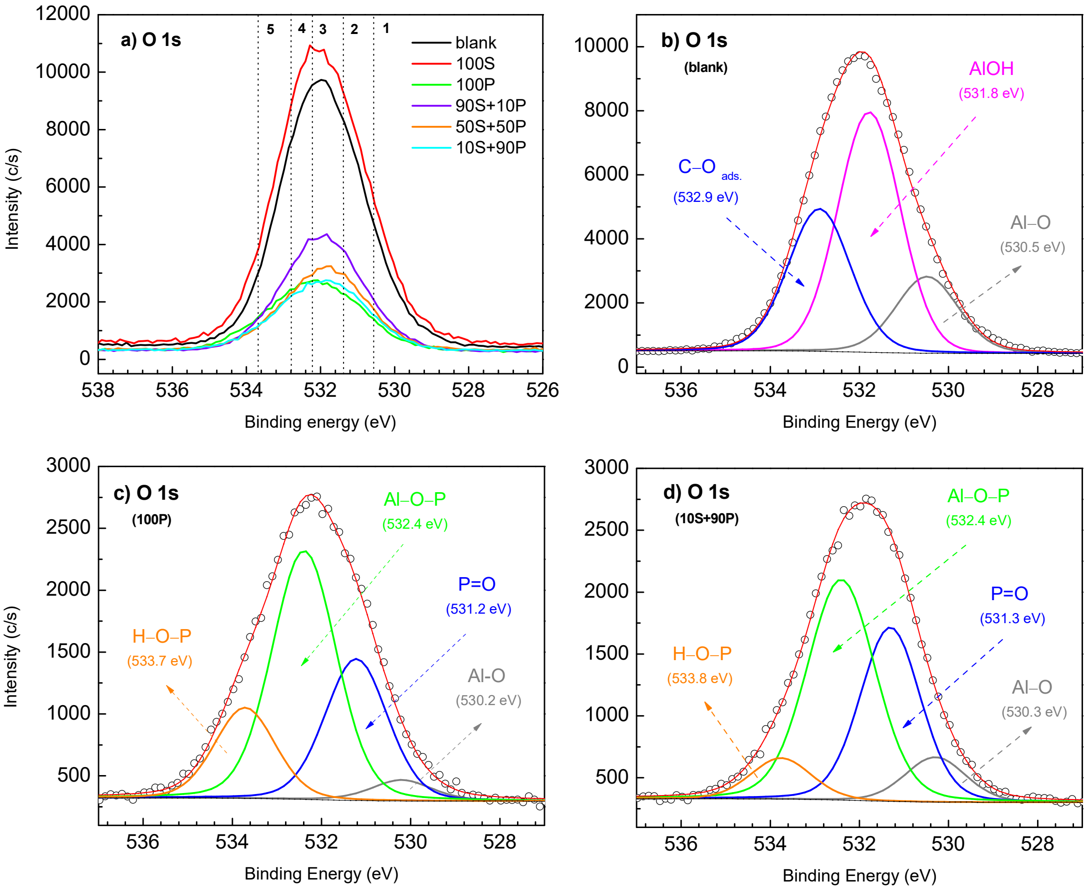

Figure 3.12: High-resolution XPS spectra of (a) O 1s recorded for all aluminium samples. Vertical lines denote the position of reference compounds: (a) 1: Al(III) oxides, 2: Al(III) hydroxides, 3: C=O, 4: C–O–H/C–O–C, 5: O–C=O. Deconvoluted high-resolution XPS spectra of O 1s recorded for (b) blank, (c) 100P and (d) 10S+90P. All samples before analysis were immersed for 24 h in 3 wt.% NaCl solution with or without the addition of 1mM inhibitor(s). Experimental data are presented by symbols, fitted curve as a red solid line and component peaks are presented as solid lines of different colours.

The C 1s peak was resolved into four assignments (Fig. 3.13a). The main peak (peak 1), centred at E_b = 284.8 eV, is unambiguously associated with adventitious compounds [84], [115], [120]. Various oxygen-containing functional groups are likely to be present as well, consisting of alcohol/ether (peak 2), carbonyl (peak 3) and carboxyl/ester (peak 4) [84], [115], [136]. The intensity of the main peak decreases and becomes narrower with increasing phosphorus content. Also, peaks 3 and 4, which correspond to oxygen contaminants, disappear upon adsorption of inhibitors containing larger amounts of phosphorus.

The bonding of phosphorus to the surface of the aluminium substrate is supported by a high-resolution P 2p spectra. Phosphorus peak was detected for all samples exposed to phosphorus-containing inhibitors (Fig. 3.13b). The peak intensities are quite similar, without a shift in binding energy. For the 10S+90P binary inhibitor sample, the doublet was used for fitting (Fig. 3.13d) attributed to spin-orbit splitting at 133.3 eV and 134.2 eV ($2p_{3/2}$ and $2p_{1/2}$, respectively) of the P 2p core level with an expected peak separation of

0.84 eV [80], [116], [119]. These two component peaks are ascribed to metal—phosphonate bonding (P—O—Al). Finally, the sample exposed to only 100P (Fig. 3.13c) showed a broader peak in which a second P 2p doublet was required to fit the data [119]. Thus, there are four component peaks: at 133.1 eV (P $2p_{3/2}$) and 133.9 eV (P $2p_{1/2}$) related to P—O—Al bonds, and at 134.3 eV (P $2p_{3/2}$) and 135.2 eV (P $2p_{1/2}$) related to P=O bonds; one set of spin-orbit components for each chemical state. There is a possible explanation for the appearance of this second doublet observed only for the 100P. Namely, at a higher concentration of 100P, a second layer may begin to form on top of the first layer, as would be expected from the tendency of phosphonates to form dimers and trimers in solutions [152]. In addition to metal—phosphono bonding, the presence of two additional characteristics (P=O, P—OH) in the O 1s spectrum upon adsorption suggests that the bonding of phosphonate does not occur via tridentate mode, or at least does not dominate (Figs. 3.12c and 3.12d).

Moreover, the ratio between the areas of the P $2p_{3/2}$ peaks ($A_{\text{low BE}}/A_{\text{high BE}}$) is 1.6, which indicates a certain degree of mixed monodentate and bidentate modes (Fig. 3.13d). Bauer et al. performed a computational study showing that the thermodynamically preferred binding mode between phosphonates and aluminium substrate varies depending on the surface structure and the amount of residual water, as mono-, bi-, and tridentate [77]. In a recent study, Milošev et al. [79] showed that phosphonic acids are bound to either two or three Al atoms at the surface. According to their DFT calculations, formations of bidentates and tridentates are viable but only near OH vacancies. In the present study, the presence of the monodentate mode was also confirmed by the increased intensity of the P—OH component in the O 1s spectrum of 100P sample, compared to the 10S+90P sample (Figs. 3.12c and 3.12d).

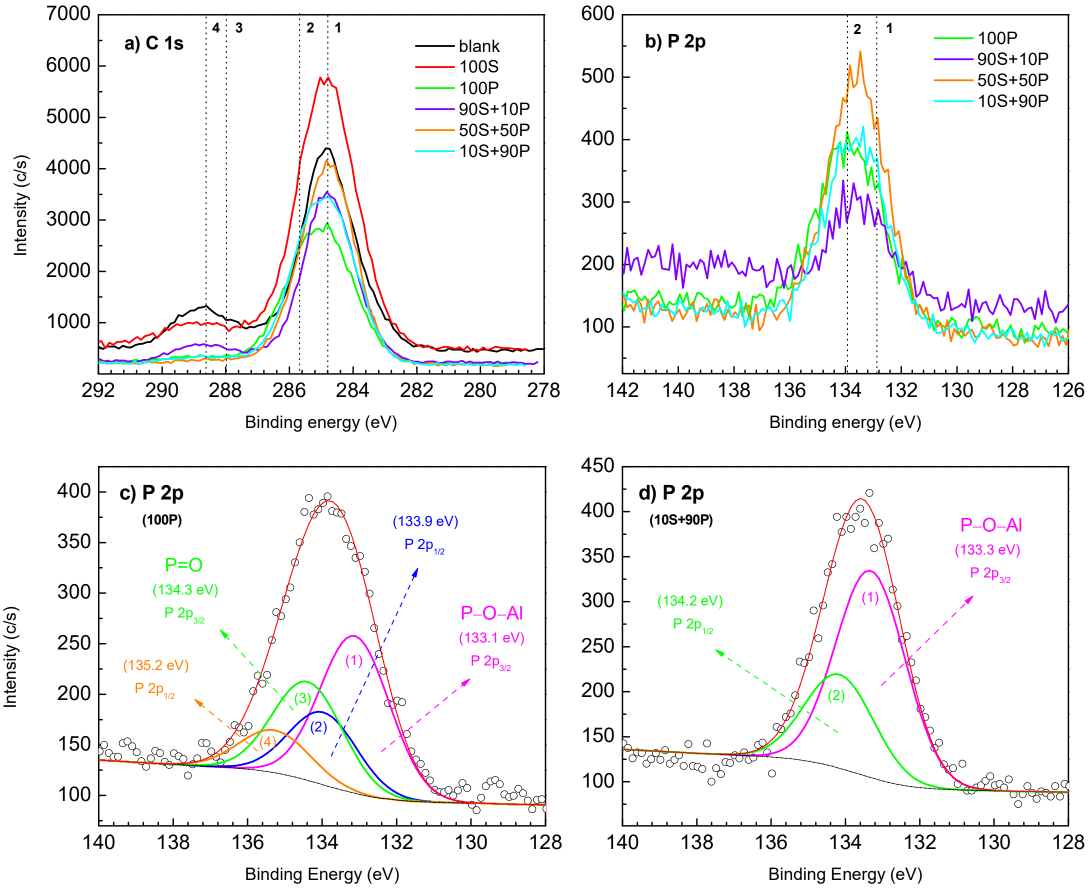

Figure 3.13: High-resolution XPS spectra of (a) C 1s and (b) P 2p recorded for all aluminium samples. Vertical lines denote the position of reference compounds: (a) 1: C—C/C—H, 2: C—O—H/C—O—C, 3: C=O, 4: O—C=O, (b) 1: P $2p_{3/2}$, 2: P $2p_{1/2}$. Deconvoluted high-resolution XPS spectra of P 2p recorded for (c) 100P and (d) 10S+90P. All samples before analysis were immersed for 24 h in 3 wt.% NaCl solution with or without the addition of 1mM inhibitor(s). Experimental data are presented by symbols, fitted curve as a solid red line and component peaks are presented as solid lines of different colours.

3.3.2.3 Fourier transform infrared spectroscopy

The peak observed at 935 cm^{-1} originates from the Al—O and Al—OH bending vibrations [153] due to an oxidised and hydroxylated layer on the surface of the blank sample (Fig. 3.14). Compounds that do not have a C=C bond show C—H stretches only below 3000 cm^{-1} [140]. Thus, absorptions in the range between 2800—3000 cm^{-1} can be unambiguously attributed to symmetric and asymmetric C—H stretching vibrations of methylene group (—CH_2—) together with the C—H bending at 1465 cm^{-1}, which ultimately indicates the presence of OPA molecules at the oxyhydroxide/solution interface for all samples containing OPA inhibitor. The centre of the high-intensity vibration at 1090 cm^{-1} may be characteristic of a P=O functional group that is consistent with either a mono or bidentate bonding of a phosphono group; further, this band may also indicate the presence of PO_3^{2-} stretching modes that may be associated with bidentate and/or tridentate [81], [117], [142].

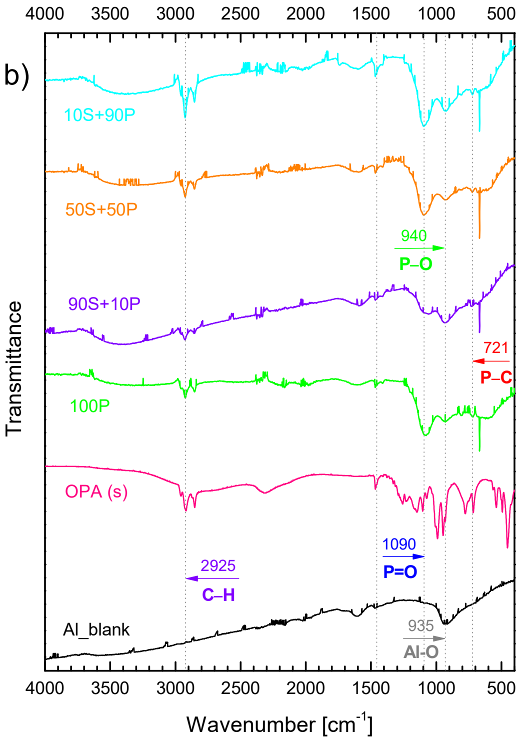

Figure 3.14: FTIR spectra of reference OPA (powdered) and Al samples (Al blank, 100P, 90S+10P, 50S+50P and 10S+90P). Before analysis, all samples were immersed for 24 h in 3 wt.% NaCl solution with or without the addition of 1mM inhibitor(s). Vertical lines denote the position of C=C, C–N, C=N, C=S and Ph (phenyl) bands according to reference and literature data, as described in the text.

Another characteristic band of phosphonic acid is due to the associated P—C stretching vibration at 721 cm^{-1} [83] found for all samples exposed to a solution containing OPA. The low-intensity peaks occurring in the range of about 940—1015 cm^{-1} and corresponding to P—O symmetric stretching vibrations indicate that the phosphonate structure is bound to aluminium oxide via anchor groups that form alkylphosphonic salts [83], [142]. The band from this absorption range is considered to be masked by the presence of aluminium oxyhydroxide vibrations because they have overlapping absorptions. In addition, detection difficulties during FTIR measurements due to very thin (a few nm thick) inhibitor layers on the top of the metal substrate should be considered. The obtained results for organophosphorus layers follow the XPS results (Figs. 3.11-3.13).

3.3.2.4 Water contact angle measurements

$\theta = 24°$ shows the hydrophilic nature of the blank aluminium sample (Table 3.8). WCA measurements confirmed that MBI does not significantly affect the surface wettability (θ is reduced to 17°); MBI does not bond to the Al surface as proven by XPS (Fig. 3.11a) and polarization curve (Fig. 3.10a), which confirms corrosion of Al in 100S solution. In contrast, the OPA-treated sample showed a considerable change in wettability with $\theta = 127°$; this value is in line with better corrosion protection properties, as shown in Fig. 3.10. Hydrophobicity is closely related to the degree of packing of monolayers with hydrophobic methyl groups oriented outward and van der Waals interactions between alkyl chains [81],

[86]. It has already been reported [84], [115] that surface aluminium-hydroxyl species are responsible for the tendency of phosphonate to undergo a condensation reaction to form aluminium-phosphonate and H_2O as a byproduct, reactions (Eq. 3.4).

Table 3.8: Contact angles of water drop and wettability modes for Al after 24 h of immersion in 3 wt.% NaCl with and without the addition of single and binary inhibitors.

Sample	**Contact angle ($\boldsymbol{\theta}$)**	**Wettability**
Al_bl	24 ± 6	hydrophilic
Al_100S	17 ± 2	hydrophilic
Al_100P	127 ± 9	hydrophobic
Al_90S+10P	86 ± 11	hydrophilic
Al_50S+50P	114 ± 3	hydrophobic
Al_10S+90P	120 ± 7	hydrophobic

Binary inhibitors did not show any synergism according to electrochemical measurements and surface characterization; hence as the fraction of OPA in a mixed inhibitor solution decreased, $\boldsymbol{\theta}$ gradually decreased, resulting in a change from hydrophobic to hydrophilic, with corresponding values of 120°, 114° and 86° for samples 10S+90P, 50S+50P and 90S+10P. However, even the latter value is higher than the 100S sample (17°). This behaviour differs from that observed for binary inhibitors on Cu: while Al samples became hydrophobic or nearly hydrophobic when exposed to 100P and all three binary mixtures ($\boldsymbol{\theta}$ between 86° and 127°), Cu samples showed a hydrophobic surface only when exposed to 90S+10P ($\boldsymbol{\theta} = 115°$). This also indicates a different adsorption mechanism and synergistic effect of these compounds on the two metals.

It is important to note that phosphonic acids also form strong complexes not only with Cu^{2+} but also with Al^{3+} [154]. Unlike experiments performed for Cu at pH ≤ 4, however, the availability of Al^{3+} ions at pH 7 is very low due to the presence of a protective spontaneously formed Al(III)-oxide layer that acts as a barrier and does not allow the formation of free Al^{3+} that chelates. Therefore, under these conditions, the formation of a condensed phosphonate layer on aluminium surfaces predominates over chelation.

3.4 Conclusions

MBI (or S) and OPA (or P) and their binary mixtures (xS+yP, where x and y are molar ratios in %) were tested as corrosion inhibitors for Cu and Al in 3 wt.% NaCl solution using the electrochemical polarization experiments. The adsorption of inhibitors was characterized by surface analyses, density functional theory (DFT) calculations and wettability measurements.[45]

For the 100S sample at pH 5.5, the formation of a thin Cu(I)MBI film is reasonable because, at this pH, the Cu_2O is sufficiently stable not to produce enough Cu^+ ions to go beyond the monolayer or a few layers thick films. In contrast, for the 90S+10P sample at lower pH of 4, where the onset of a Cu dissolution is expected, the amount of produced Cu^+ ions is boosted, and a much thicker Cu(I)MBI film forms by dissolution-precipitation mechanism. At pH smaller than limiting pH 3.5–4, the thick compact Cu(I)MBI film does not form due to intensive dissolution of the Cu_2O underlayer resulting in the formation of a voluminous product. The 90S+10P synergistic mixture of pH 4 assured the formation of a thick insulating film on a copper substrate, with high inhibitory effectiveness [45]. Nitrogen and sulphur were detected in the outermost surface of this film, indicating the formation of a pure Cu-MBI metal-organic structure. Phosphorus was not detected, but its contribution within the inner layers could not be ruled out. In addition to the large thickness visible to the naked eye, another interesting feature was that this film contained chlorine [45]. The presence of Cl in the surface film is usually associated with degradation of the latter; however, this film acted as an effective barrier to the corrosion of Cu. These observations were in line with the statement by Chadwick and Hashemi [135] that the thickness of the inhibitor layer is closely related to the pH of the treatment solution which reflects the stability of the Cu_2O layer. In contrast to the thick layer formed in an MBI+OPA mixture, a layer of only a few nanometres thick inhibitor layer was formed in NaCl that contained only MBI at pH 5.6.[45]

In contrast to Cu, binary inhibitor S+P combinations do not act synergistically on Al. Nevertheless, the S+P/Al system is stable in the sense that the presence of the S inhibitor in the S+P mixture does not obstruct the inhibitory ability of P. In addition to 100P, the combination 10S+90S also performs well. Both 100P and 10S+90P form layers with strong hydrophobic characters.

Chapter 4

Roles of Chloride Ions in the Formation of Corrosion Protective Films on Copper

4.1 Literature Review

Since the first published study by Cotton almost sixty years ago [69], numerous studies have been carried out on benzotriazole (BTA) as an inhibitor of Cu corrosion [71], [89], [129], [148], [155]–[157]. Further, in the past few decades, MBI has been established as an effective inhibitor, both singly [41], [70], [72], [73], [139], [158] and in binary combination, aiming to reach a synergistic effect [45], [74]. In 1979, Chadwick and Hashemi reported the formation of inhibitory surface films as a function of the preparation method [135]. In a slightly acidic, chloride-containing solution at pH > 4, a thin Cu-MBI film was formed on a Cu_2O layer which, by dissolution, supplies Cu^+ ions for film formation resulting in a precipitated inhibitor layer. In contrast, at pH 3, where the stability of the Cu_2O layer is decreased and that of cupric Cu^{2+} ions increased, the thickness of the Cu-MBI film was greater [135]. When formed on an oxide-free Cu surface, the Cu-MBI complex could be identified, but it was extremely thin. High efficiency of the inhibition of corrosion of MBI for copper in near-neutral 3 wt.% NaCl aqueous solution and its bonding mechanism was reported by Finšgar [70], [72] and Milošev et al. [41], [73]. The latter group also compared the inhibition performance of MBI and BTAH over time at a concentration of 1 mM [159]. During the first few hours of immersion, BTAH and MBI performed almost identically, but during longer immersion for up to 100 h, BTAH was only slightly superior to MBI [159]. MBI is, therefore, like BTA, an important corrosion inhibitor for Cu and deserves further attention.

Nowadays, many efforts are being devoted to improving the effectiveness of inhibition by investigating various reliable synergistic systems [74], [123], [124], [127], [160]–[162]. Based on literature data and the present study, two major points deserve further attention and have been considered in this work: (1) unambiguous identification of polymeric Cu-MBI and, possibly, Cu-Cl-MBI chains, and (2) clarification of the role of chlorine in these chains. Since the literature on BTAH is more abundant than MBI, parallels have been drawn between MBI and BTAH, including revisiting the pioneering studies on these two inhibitors. The formation of a thin inhibitor MBI layer on the surface of Cu in the NaCl medium was confirmed by XPS [16,18,19,21,24], but this cannot explicitly prove the existence of a polymerized structure. Nevertheless, the polymerized structure has been proposed for MBI [70], [139], [163] and BTAH [71] but has not yet been proved. This can be considered by a limited number of techniques, such as ToF-SIMS, which would enable fragments of the inhibitor molecule and chains of the related molecules to be studied, bonded or not to one or more metal atoms. The ToF-SIMS studies on these inhibitors are rare. The early study by Brusic et al., however, offered clear evidence, by ToF-SIMS, that polymerized Cu-BTA structure was formed [147] and that the distribution of light and heavy mass ion fragments is dependent on the preparation method used. The build-up of a polymerized network was strongly favoured on an oxidized surface (neutral pH, where Cu_2O is stable), where only a few nano-thick films were formed with self-limiting growth [147], [164]. These films contained heavy ion fragments at mass-to-charge ratio (m/z) of 388 and m/z 480, ascribed to $BTA_2Cu_2CN^-$ and $BTA_3Cu_2^-$, respectively, these being the most protective ones [147]. In contrast, films formed at a low pH of 2 were much thicker but non-protective. They contained mainly light mass fragments (up to m/z 300), indicating that they were less polymerized. This study led us to investigate the Cu(I)MBI films by ToF-SIMS to establish its polymerized structure, although, in our case, the thicker film, formed by the combined action of MBI and OPA, was more protective than the thin film formed in a solution containing MBI alone [45]. This observation is opposite to that for less protective Cu-BTA films prepared by Brusic et al. at lower pH [147]. Ogle and Poling reported results consistent with our findings, where thick, acicular crystallites, several hundred nm thick, were formed in an acidic solution of BTA on Cu [148].

Regarding the role of chlorine in the inhibitor film, several authors have reported that the relation to Cl^- may be an important factor. In fact, at an early stage of their studies, Hashemi and Hoghart [11] postulated, based on XPS results, the existence of a „chlorine-bridge“ for the copper/benzotriazole system formed through the CuCl intermediate. The authors suggested that the disproportionation of the Cu^+ ions takes place to form a Cu_2Cl-BTA complex [11]. However, up to the present time, strong evidence for the presence of chlorine-containing polymerized inhibitor chains, such as $[\text{Inh-Cl-Cu}]_n$, has not been reported. Further, Chadwick and Hashemi mentioned that thick surface Cu-MBI films could be formed only in chloride solution through $CuCl_2^-$ intermediate [135], whereas Modestov and co-workers [10] suggested that Cl^- ions, which were trapped in the film, act as a catalyst for film formation. Further evidence was provided by Izquierdo et al. [9], who reported that the presence of chloride ions promoted the formation of thicker and more protective MBI layers, unlike those formed in its absence. Based on literature data, it can be stated that the role of Cl^- ions remains a subject of profound debate – with doubt as to whether they act as an intermediate, a catalyst or a promoter.

4.2 Experimental

4.2.1 Materials, substrate preparation and chemicals

This part has already been described in *Chapter 2*, the *Experimental section.*

4.2.2 Preparation of adsorbed organic layers

Organic layers were prepared by simple liquid-phase deposition, i.e. by immersion of individual Cu samples in a 150 mL beaker containing an aqueous aggressive chloride medium with the addition of organic inhibitors. Samples were placed in the beaker at an angle of 45°, as described in Fig. 2.2 [45]. Before immersion, the prepared Cu specimens were kept in a desiccator for 24 h. The blank solution was 3 wt.% NaCl (denoted as NaCl). Organic compounds were added to NaCl at a concentration of 1 mM as (i) individual inhibitors MBI (denoted as 100S+NaCl) and OPA (denoted as 100P+NaCl), and (ii) a mixture of MBI and OPA at a total concentration of 1 mM in a molar ratio of 9:1 (denoted as 90S+10P+NaCl). Note that the choice of the molar ratio was based on the investigation conducted in Chapter 2 [45]. All solutions were used as-prepared with pH values of 5.5 for samples immersed in NaCl, 5.6 for 100S+NaCl, 3.0 for 100P+NaCl and 4.0 for 90S+10P+NaCl. Where not stated otherwise, the immersion time was 1 day. For selected measurements, the immersion time was 7 days (denoted as 90S+10P+NaCl_7d). After removing the solutions, the samples were gently double rinsed with deionized water, blown dry with nitrogen gas, and subjected to electrochemical and surface characterization.

4.2.3 Electrochemical measurements

Experiments involving cyclic voltammetry (CV) were carried out with a PGSTAT M204 Autolab (Metrohm Autolab, Utrecht, Netherlands) multichannel potentiostat/galvanostat, controlled by NOVA software (version 2.1.4). This employed an open-to-air conventional three-electrode cell assembly under stagnant conditions at 25 °C. The working electrode (WE) was a copper disc pressed against a Teflon o-ring with a 1 cm^2 exposed surface area. A Pt mesh and an $Ag/AgCl/KCl_{sat.}$ (0.197 V vs. standard hydrogen electrode) were employed as the counter electrode and the reference electrode, respectively. The latter was used with a Luggin capillary to minimize the IR drop at the WE surface. In the text, potentials are given with respect to $Ag/AgCl/KCl_{sat}$ electrode.

Pre-immersed copper samples used as the WE were prepared as described above: NaCl, 100S+NaCl, 100P+NaCl and 90S+10P+NaCl. Note that the same notation is used for solutions and the samples. Electrochemical measurements of these pre-immersed samples were always conducted in the same type of solution but freshly prepared, as was the solution for pre-immersion. One set of experiments was conducted by pre-immersion in inhibitor-containing NaCl, and then electrochemical measurements were carried out in NaCl (denoted as without an MBI reservoir).

After immersion in the electrochemical cell, the specimens were allowed to rest for approximately 1 h until a near steady-state of open circuit potential (OCP), denoted as E_{OCP}, was established. The cyclic voltammograms were then recorded through a linear potential sweep in the potential range from −1 V to 1 V with a scan rate of 1 mV s^{-1}. For some measurements, five consecutive CV cycles were recorded. The results are based on at least three experiments to ensure reproducibility.

4.2.4 Surface characterization

Time-of-flight secondary ion mass spectrometry (ToF-SIMS) is a powerful technique that provides detailed elemental and molecular information on the structure and polymerization of organic films [165]. In general, ToF-SIMS provides more chemical information about organic surfaces than XPS, yielding characteristic positive and negative secondary ions [166]. The major benefit of ToF-SIMS is that it offers a greater surface sensitivity than XPS (1-2 nm for SIMS vs. 3-10 nm for XPS, depending on the detection angle), with a relatively low detection limit (ppm to ppb), and high lateral and in-depth resolution. In addition, whole organic molecules with corresponding characteristic fragments on the metal surface can be detected, including direct evidence related to inhibitor adsorption [167], [168]. It is often used, in combination with XPS, because the strengths of SIMS are the weaknesses of XPS and vice versa. ToF-SIMS analyses were performed using a ToF-SIMS 5 spectrometer (ION TOF GmbH – Münster, Germany) equipped with a bismuth liquid metal ion gun operating at a kinetic energy of 30 keV (Bi^+ and Bi_3^+ ions). Beam currents were, in the cases of our measurements, in the range of 0.25 – 0.35 pA. Analyses were conducted in an ultra-high vacuum chamber at 10^{-8} to 10^{-9} mbar. Information from the outermost surface, i.e. within 2 nm, was obtained by rastering a 100 × 100 μm^2 area with a Bi_3^+ cluster ion beam. ToF-SIMS spectra were obtained in positive and negative polarity in the mass-to-charge ratio (*m/z*) range of 0-875, but only the distinct spectra regions are presented. Since the ToF-SIMS ion spectra (in static mode) provide molecular information from the topmost surface only (one to three monolayers) [169], thicker films were analysed by depth profiling as well (dynamic SIMS). Positive ion depth profiles were acquired using an O_2^+ sputter ion beam with an energy of 1 keV and a beam current of 110 nA. Negative ion profiles were acquired using a Cs^+ sputter ion beam, again with an energy of 1 keV. The current was, in this case, between 45 and 55 nA. The sputtering rate was assessed by comparison of ToF-SIMS depth profile and SEM cross-section image and estimated to be between 0.3 and 0.8 nm/s.

The performances of X-ray photoelectron spectroscopy (XPS) analysis were already explained in *Chapter 3*, the Experimental section. Note that the sample 100S+NaCl_PD, used to detect the dimer by both ToF-SIMS and XPS, was collected from the bottom of the measuring cell after electrochemical polarization up to 1 V, followed by subsequent filtration and drying in an oven. For analysis of the subsurface region, ion sputtering with Ar-ions of energy 1 keV was applied in combination with XPS analyses. The sputtering rate was about 1 nm/min measured on the reference sample of Ni/Cr multilayer with layers of known thickness.

Scanning electron microscopy combined with energy-dispersive X-ray spectroscopy (SEM-EDS) was already explained in *Chapter 2*, *Experimental section*.

Focused ion beam microscopy (FIB) coupled with EDS revealed the composition and thickness of layers at the cross-section of Cu-MBI film on the Cu substrate. First, an FEI Helios Nanolab 650 microscope, equipped with EDS (Oxford Instruments Aztec system with X-max SDD detector), was employed to deposit two Pt protection layers – electron-beam-assisted and ion beam (Ga^+)-assisted ones with thicknesses of 0.2 and 1 μm, respectively. A trench was then opened by milling under rough conditions with Ga^+ ions of 2.5 nA at 30 kV, followed by rough polishing (0.77 nA, 30 kV) and fine polishing (0.4 nA, 30 kV). Within the trench, the cross-section across the inhibitor film and the substrate was analysed by SEM-EDS.

4.3 Results and Discussion

4.3.1 ToF-SIMS analysis: the chemical composition and structure of the surface films

ToF-SIMS analyses were applied to evaluate the surface structure and composition of Cu samples immersed for one day in 3 wt. % NaCl solution (NaCl) and in NaCl with added 1 mM MBI (100S+NaCl), OPA (100P+NaCl), and MBI+OPA (90S+10P+NaCl). Note that the skeletal chemical structures of OPA and 2-MBI are given in inserts in Figs. 4.1 and 4.2, respectively. The secondary positive ions, such as Cu_2^+ and Cu_3^+ represent the metallic copper[6] (Fig. 4.1). Other ions that belong mainly to copper oxide (Cu_3O^+, $Cu_2{}^{65}CuO^+$) and copper hydroxide fragments (Cu_2OH^+, $Cu^{65}CuOH^+$) indicate that the surfaces for both NaCl (Fig. 4.1a) and 100P+NaCl (Fig. 4.1b) are covered with a native oxyhydroxide layer,

---

[6] Cu^+ is not appropriate for the representation of metallic Cu as it is heavily influenced by the matrix effect.

in line with our previous XPS data [45]. No OPA fragments[7] were detected on the 100P+NaCl copper substrate (Fig. 4.1b), as reported in our previous study [45].

The positive ion mass spectra for 100S+NaCl and 90S+10P+NaCl reveal the presence of MBI ($C_7H_6N_2S$) inhibitor within 1 nm of the topmost surface by detecting the characteristic intense inhibitor fragment peaks, such as $C_7H_7N_2S^+$, $C_7H_6N_2Cu^+$, and $C_7H_5N_2SCu_2^+$ (Fig. 4.2). It can be seen that the relative intensities of the lighter and heavier fragment ions for 100S+NaCl (Fig. 4.2a) and 90S+10P+NaCl (Fig. 4.2b) are functions of the conditions of the film preparation, i.e., solution composition and, consequently, film thickness (vide infra). Namely, high mass ions are abundant in the 90S+10P+NaCl spectrum, whereas low mass ions prevail in the 100S+NaCl spectrum. A list of some crucial positive ion fragments, with their corresponding masses, is presented in Fig. A.17.

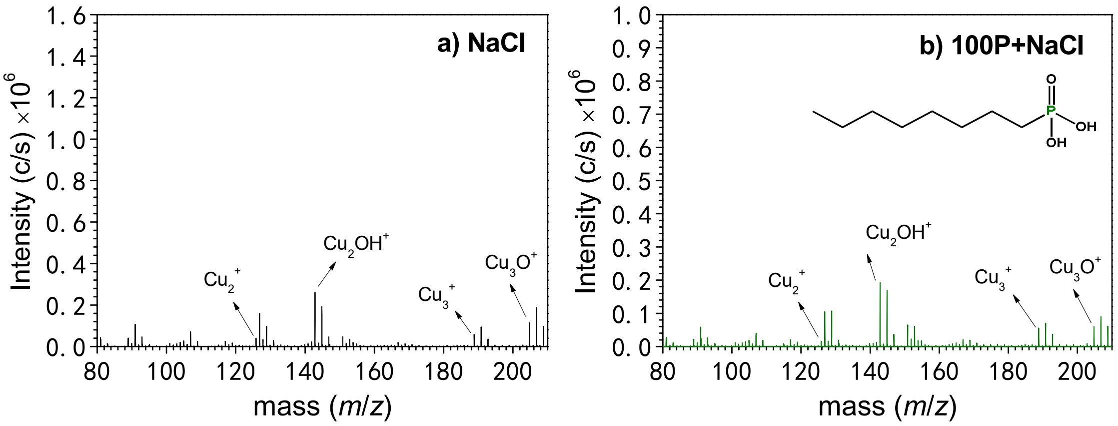

Figure 4.1: ToF-SIMS positive ion spectra obtained for Cu immersed for 1 day in (a) 3 wt.% NaCl (NaCl), and (b) 3 wt.% NaCl containing 1 mM octylphosphonic acid, OPA, (100P+NaCl). The structural formula of OPA is given in (b).

To distinguish the presence and the relative intensities of the fragment ions for NaCl, 100S+NaCl, and 90S+10P+NaCl, the parts of the spectra of interest are superimposed (Figs. 4.3 and 4.4). As expected, the NaCl does not contain either $C_7H_6N_2S^+$ at $m/z = 150$ (Fig. 4.3a) or $C_7H_7N_2S^+$ ion at $m/z = 151$ (Fig. 4.3b). On the other hand, the intensities of the fragment ions $C_7H_6N_2S^+$ (corresponding to the complete MBI formula) and $C_7H_7N_2S^+$ (corresponding to the MBI formula plus one hydrogen) for 90S+10P+NaCl are about one and two orders of magnitude, respectively, greater than that for 100S+NaCl, indicating the greater amount of inhibitor on the surface of 90S+10P+NaCl. This observation can be closely related to the presence of a thicker film or the greater extent of surface coverage on 90S+10P+NaCl. OPA mass fragments were not detected in any samples, indicating that this inhibitor is not present at the film surface, either when used singly or in the mixture with MBI. Its role in the synergism with MBI remains to be explained as a transient trigger of a change in surface activity [45].

The interaction of inhibitor with Cu is evident in Fig. 4.4 as a direct confirmation of the chemical adsorption of inhibitor on a copper substrate surface. The most intense peaks, i.e., the parent ion, for 90S+10P+NaCl correspond to a complete MBI inhibitor bonded to one Cu atom via N or S, i.e. $C_7H_6N_2SCu^+$ ($m/z = 213$), followed by its isotope counterpart fragment ion $C_7H_6N_2S^{65}Cu^+$ ($m/z = 215$) (Fig. 4.4a).

---

[7] In the negative polarity we aimed for the P^-, PO_2^- and PO_3^- ions as well as for the whole molecular ion and the fragments with partialy broken octyl chain.

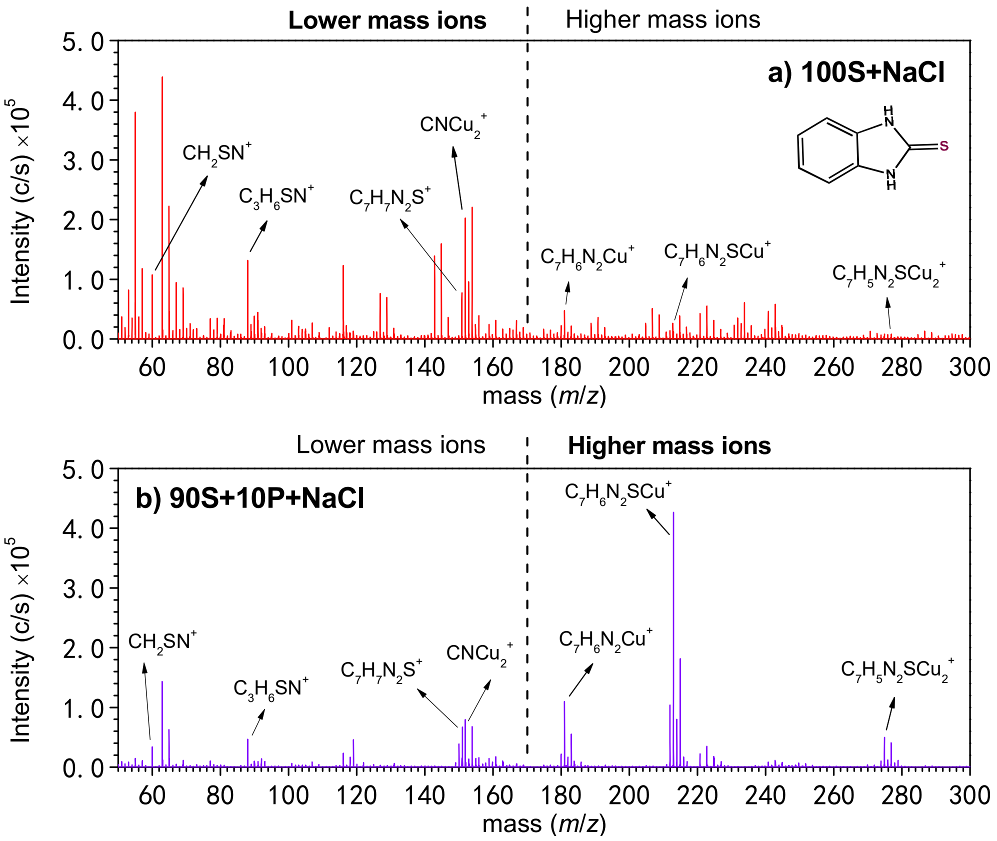

Figure 4.2: ToF-SIMS positive ion spectra obtained for Cu immersed for 1 day in (a) 3 wt.% NaCl containing 1 mM 2-mercaptobenzimidazole, MBI, (100S+NaCl), and (b) 3 wt.% NaCl containing 1 mM MBI and octylphosphonic acid, OPA, in the ratio 9:1 (90S+10P+NaCl). The structural formula of MBI is given in (a). Note that the m/z range was used arbitrarily for lower and higher mass ions (bold text denotes region with more abundant mass fragments).

For 100S+NaCl, these signals are very weak, i.e. almost insignificant (roughly three orders of magnitude less intense than those for 90S+10P+NaCl). In addition, the positive-ions for 90S+10P+NaCl, namely $C_7H_6N_2Cu^+$ ($m/z = 181$), together with their counterpart isotope ion $C_7H_6N_2{}^{65}Cu^+$ ($m/z = 183$) (Fig. 4.4b), correspond to the MBI inhibitor minus sulphur bonded to one Cu atom via N, and they are comparable (three times more intense) to those for 100S+NaCl. Furthermore, the evidence for inhibitor bonded to the surface by two Cu atoms (minus 1H) is provided in Fig. 4.4c. For 90S+10P+NaCl, the detection of positive-ion fragments such as $C_7H_5N_2SCu_2^+$ (m/z = 275), as well as similar fragment ions that include Cu isotope $C_7H_5N_2SCu^{65}Cu^+$ (m/z = 277) and $C_7H_5N_2S^{65}Cu_2^+$ (m/z = 279) suggests that the inhibitor is either chelated to the Cu substrate by bidentate mode or may form the Cu–MBI–Cu bridge bonds via N and/or S.

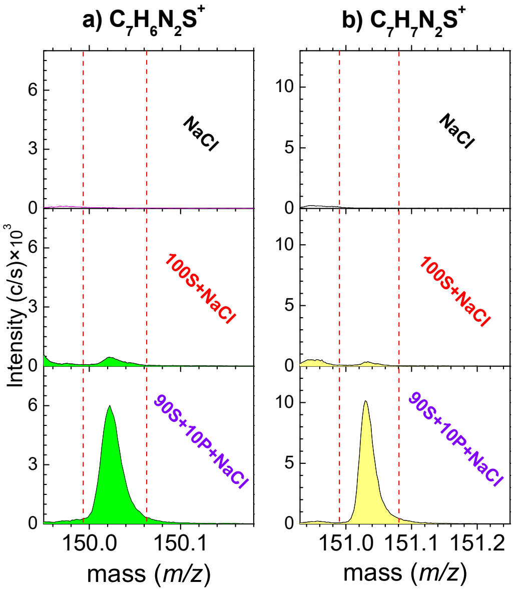

Figure 4.3: ToF-SIMS positive ion spectra as evidence for the presence of (a) $C_7H_6N_2S^+$, and (b) $C_7H_7N_2S^+$. Spectra were obtained on Cu immersed for 1 day in 3 wt.% NaCl, in 3 wt.% NaCl containing 1 mM 2-mercaptobenzimidazole, MBI, (100S+NaCl) and in 3 wt.% NaCl containing 1 mM MBI and octylphosphonic acid, OPA, in the ratio 9:1 (90S+10P+NaCl).

The latter prediction is reasonable since the analysis was performed at the uppermost layer of the very thick film (Fig. 4.4c), and it has yet to be confirmed by the presence of more complex (polymerized) fragments, as will be elaborated below. As for now, these ions could also form in the recombination processes accompanying ion sputtering. The fragment signals for 90S+10P+NaCl are about five times more intensive than those for 100S+NaCl. It is noteworthy that the spectra recorded for 90S+10P+NaCl exhibit approximately three times lower peak intensities at m/z 152 ($CNCu_2^+$), 154 ($CNCu^{65}Cu^+$), and 156 ($CN^{65}Cu_2^+$) than those recorded for 100S+NaCl (Fig. 4.4d), which correlates with the aforementioned fact that the lower mass ions are more pronounced in the spectrum of 100S+NaCl. In addition, lower mass positive ions CH_2SN^+ ($m/z = 60$) and $C_3H_6SN^+$ ($m/z = 88$), obtained from the spectrum of 90S+10P+NaCl, are also approximately three times less intense than those for 100S+NaCl (Fig. 4.2).

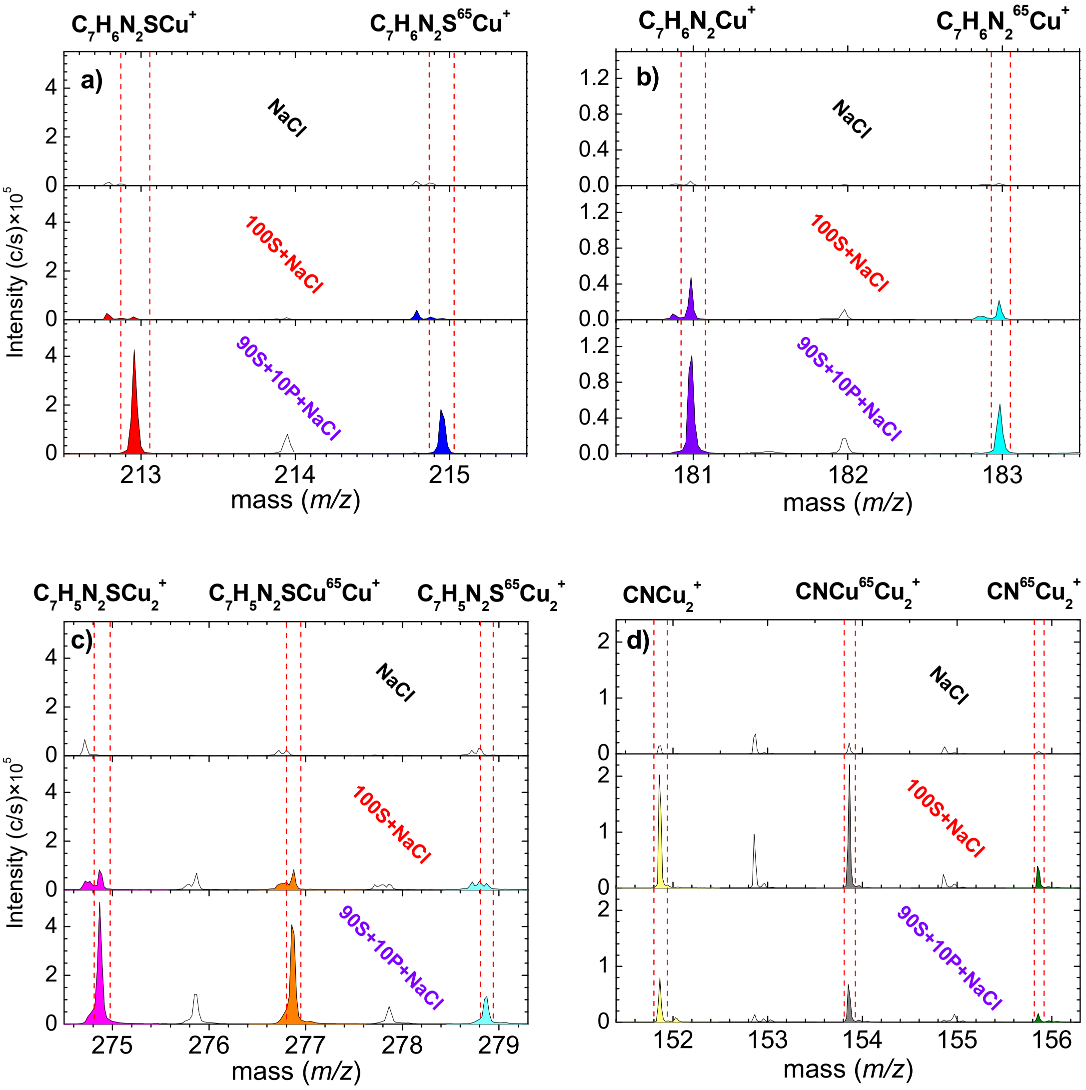

Figure 4.4: ToF-SIMS positive ion spectra providing evidence for MBI bonded to (a) one Cu atom via N or S, (b) one Cu via N, (c) two Cu via N and/or S, and (d) two Cu atoms bonded to the CN fragment. Spectra were obtained on Cu immersed for 1 day in 3 wt.% NaCl, in 3 wt.% NaCl containing 1 mM 2-mercaptobenzimidazole, on MBI (100S+NaCl), and on 3 wt.% NaCl containing 1 mM MBI and octylphosphonic acid, OPA, in the ratio 9:1 (90S+10S+NaCl).

Surface mapping (Fig. 4.5) was recorded to determine whether the MBI was distributed uniformly over the Cu substrate surface. For 100S+NaCl, preferential adsorption of MBI at some unspecific sites can be seen (represented by bright spots) (Fig. 4.5a). In contrast, for 90S+10P+NaCl, the inhibitor was spread uniformly all over the analysed area, correlated with the existence of a uniform and thick polymerized film (Fig. 4.5b). Note that the ToF-SIMS maps consist of sums of positive fragment ions (molecular signature of MBI) $C_7H_5SN_2Cu_2^+$, $C_7H_5SN_2Cu^{65}Cu^+$, $C_7H_6N_2Cu^+$, and $C_7H_6N_2{}^{65}Cu^+$.

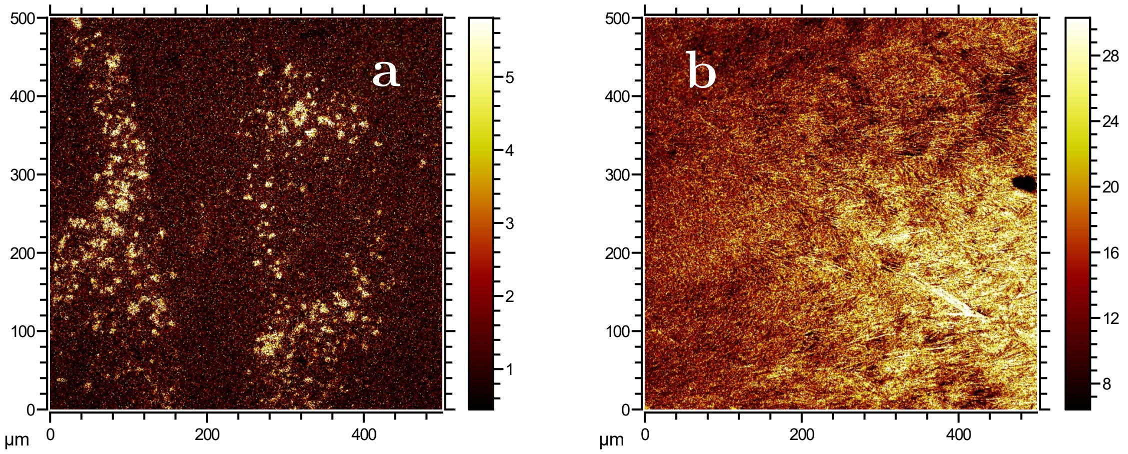

Figure 4.5: ToF-SIMS surface mapping for Cu immersed for 1 day in (a) 3 wt.% NaCl containing 1 mM 2-mercaptobenzimidazole, MBI, (100S+NaCl) and in (b) 3 wt.% NaCl containing 1 mM MBI and octylphosphonic acid, OPA, in the ratio 9:1 (90S+10P+NaCl), representing the intensity distributions (colour bar) of the positive fragments $C_7H_5SN_2Cu_2{}^+$, $C_7H_5SN_2Cu^{65}Cu^+$, $C_7H_6N_2Cu^+$ and $C_7H_6N_2{}^{65}Cu^+$ ions (the molecular signature of MBI).

Additionally, the analysis was performed for 90S+10P+NaCl Cu samples after seven days of immersion in a sodium chloride solution containing the mixture of MBI and OPA inhibitors (denoted as 90S+10P+NaCl_7d) to check whether the composition and thickness of the formed film as well as a degree of polymerization change with immersion time. The mass spectrum of 90S+10P+NaCl_7d is shown in Fig. A.18 to compare with Fig. 2b. No significant difference in the type and relative intensity of the present fragments was observed compared to 90S+10P+NaCl (one day of immersion). It indicates that the prolonged immersion induces no ageing effect associated with the oxidation processes of the film in the uppermost surface layer. De facto, the film retained its corrosion protection efficiency, as will be presented in the *Cyclic Voltammetry* section.

The negative-ion spectra for 100S+NaCl and 90S+10P+NaCl are presented in Fig. A.19. The importance of these two spectra is reflected in the detection of some chlorine-containing inhibitor fragments. The spectrum for 100S+NaCl Fig. A.19a shows only one small peak, attributed to $CuCNSCl^-$ at $m/z = 156$. In contrast, the spectrum for 90S+10P+NaCl 19b included three strong peaks corresponding to $CuCNSCl^-$ at $m/z = 156$, $Cu_2C_2N_2Cl^-$ at $m/z = 213$, and $Cu_2CNCl_2{}^-$ at $m/z = 222$.

To summarize, the presence of light and heavy mass fragments of the MBI inhibitor, revealed by the ToF-SIMS analysis, suggests the chemical bonding of MBI to copper substrate exposed to NaCl solution containing both MBI and OPA inhibitors in a ratio of 9:1. It was previously shown by XPS and DFT that the MBI bonds to Cu_2O [45]. Moreover, evidence is provided for bonding between MBI inhibitor and Cu atoms. The film formed also contains chlorine. These features – chemical bonding of inhibitors to more than one Cu atom and detection of Cl-containing fragments – triggered the idea of the possible existence of chlorine-containing polymeric Cu-MBI chains.

4.3.2 The promotive role of chloride ions

Firstly, the role of chloride would be elucidated by examining whether the Cu-MBI layer is formed in the absence of NaCl and, secondly, whether the promotive nature of chloride ions affects the formation of a thick Cu-MBI film. To examine this, the Cu specimen was immersed for one day in an aqueous solution of inhibitors 90S+10P with no chloride ions present. The pH of the solution was not affected by the absence of Cl^- and remained at 4, allowing any direct influence of chloride ions to be investigated. Contrary to 90S+10P+NaCl forming a thick, macroscopic protection film in one day of immersion [45], the Cu surface remained virtually unchanged, i.e., the thick Cu-MBI film was not formed. The ToF-SIMS spectrum (Fig. 4.6) shows the presence of ions such as Cu^+, Cu_2OH^+, and $CNCu_2^+$ with trace amounts of fragments for an inhibitor molecule, unlike that in the presence of NaCl (Fig. 4.2b), indicating the critical role of chloride ions as that of a promoter for the formation of the thick polymerized film between adsorbed MBI and Cu ions. Note the use of the term "promoter" since chloride ions also act as a reactant in the formation of the polymerized film (vide infra). Contrary to a promoter which, in a more general sense, might be consumed, a catalyst does not enter into reaction, thus not being applicable herein for the role of chloride, as shown in the next section.

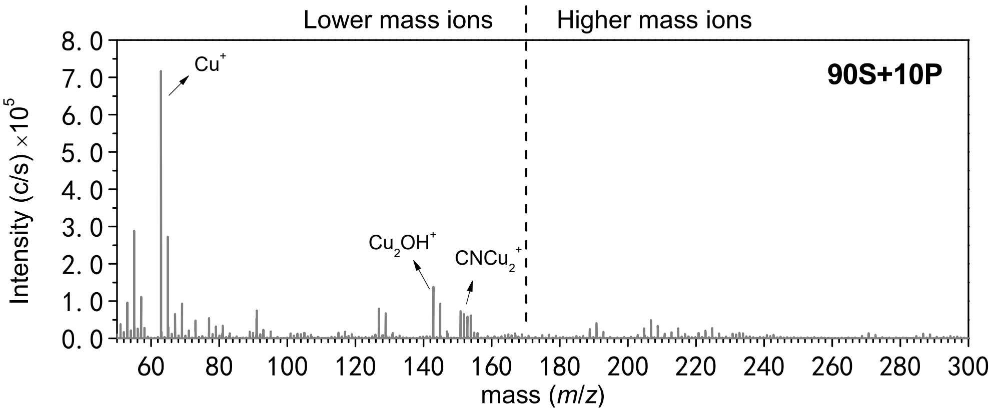

Figure 4.6: ToF-SIMS positive ion spectrum for a Cu specimen immersed for 1 day in 90S+10P (3 wt.% NaCl containing 1 mM 2-mercaptobenzimidazole, MBI, and octylphosphonic acid, OPA, in the ratio 9:1) solution with no chloride ions present. Note that the m/z range was arbitrarily used for lower and higher mass ions.

The promotive role of chloride ions in the formation of Cu-MBI/$[Cu\text{–}MBI]_n$ consists of two simultaneous processes: corrosion activation (Eq. 4.1), and chloride-assisted film formation, (Eq. 4.2). First, the Cu is attacked by corrosive chloride ions to produce cuprous chloride complex ions [10], [11], [44], [135]:

$$Cu + 2Cl^- \longrightarrow CuCl_2^- + e^- \tag{4.1}$$

which further react with MBI in the diffusion layer to form a Cu-MBI complex:

$$CuCl_2^- + MBI^- \rightleftarrows Cu\text{-}MBI + 2Cl^- \tag{4.2}$$

According to this mechanism, chloride ions act as a promoter of film formation but eventually are not incorporated in the Cu-MBI metal-organic film. This mechanism step can be regarded as chloride-assisted film formation without Cl^- incorporation. An example of such a mechanism is the formation of non-polymerized Cu-MBI film on 100S+NaCl.

4.3.3 The existence of polymeric $[Cu\text{–}MBI]_n$ and $[Cu\text{–}Cl\text{–}MBI]_n$ chains

As presented previously in the *literature review section*, the presence of polymer chains, especially those containing chlorine, has not yet been identified. Moreover, considerable controversy still exists as to whether chlorine itself is an integral part of those structures [11], [135]. This will be further examined here.

The fact that 90S+10P+NaCl possesses a greater abundance of heavier inhibitor fragments (in the m/z range 50-300) than 100S+NaCl (Fig. 4.2) led us to examine the spectrum at much heavier masses (in the m/z range 300-800) to confirm the presence of polymer chains. The ToF-SIMS analysis (Fig. 4.7) revealed the existence of ions $[Cu_n(MBI)_{n-1}]^+$ for n=3, and $[Cu_n(MBI)_{n-2}]^+$ for n=5. Clearly visible in Fig. 4.7a is the species with two inhibitor molecules $[C_{14}H_{10}N_4S_2Cu_3]^+$ at $m/z = 487$, including its corresponding isotope combinations $[C_{14}H_{10}N_4S_2Cu_2{}^{65}Cu]^+$ at $m/z = 489$, $[C_{14}H_{10}N_4S_2Cu{}^{65}Cu_2]^+$ at $m/z = 491$, and $[C_{14}H_{10}N_4S_2{}^{65}Cu_3]^+$ at $m/z = 493$, for 90S+10P. Note that the presence of isotope signals of appropriate ratio strengthens and confirms the ions/species identification. Also, the species with three MBI molecules in the chain are detected (Fig. 4.7b): $[C_{21}H_{15}N_6S_3Cu_4]^+$ at $m/z = 699$, $[C_{21}H_{15}N_6S_3Cu_3{}^{65}Cu]^+$ at $m/z = 701$, $[C_{21}H_{15}N_6S_3Cu_2{}^{65}Cu_2]^+$ at $m/z = 703$ and $[C_{21}H_{15}N_6S_3Cu{}^{65}Cu_3]^+$ at $m/z = 705$. The isotope combination $[C_{21}H_{15}N_6S_3{}^{65}Cu_4]^+$ is not shown due to its very low intensity. All these chain form ions unambiguously imply the polymerized nature of the thick Cu-MBI film for 90S+10P+NaCl, i.e. $[\text{Cu-MBI}]_n$ formed according to (Eq. 4.2). The formation of Cu-MBI coordination polymer $[\text{Cu-MBI}]_n$ film on 90S+10P+NaCl then proceeds via (Eq. 4.3):

$$n[\text{Cu-MBI}] \longrightarrow [\text{Cu-MBI}]_n \tag{4.3}$$

On the other hand, the chain form fragments are not found in the spectra of 100S+NaCl, indicating the absence of polymeric structure (Fig. 4.7). It seems that MBI is only chemisorbed on the surface of 100S+NaCl, forming either a monolayer or a few layers thick film (Eq. 4.2).

Secondly, since the fragment $CuCNSCl^-$ at m/z = 156 was detected in the negative-ion spectrum of 90S+10P+NaCl Fig. A.19, the presence of chain form fragments with high values of m/z, including chlorine atom(s), was also examined. Fig. 4.8 shows the evidence of the „chlorine bridge“ chain form fragment $[C_{14}H_{10}N_4S_2Cu_4Cl]^+$ at $m/z = 585$ for 90S+10P+NaCl, indicating the presence of Cu-chloro-MBI complex film.

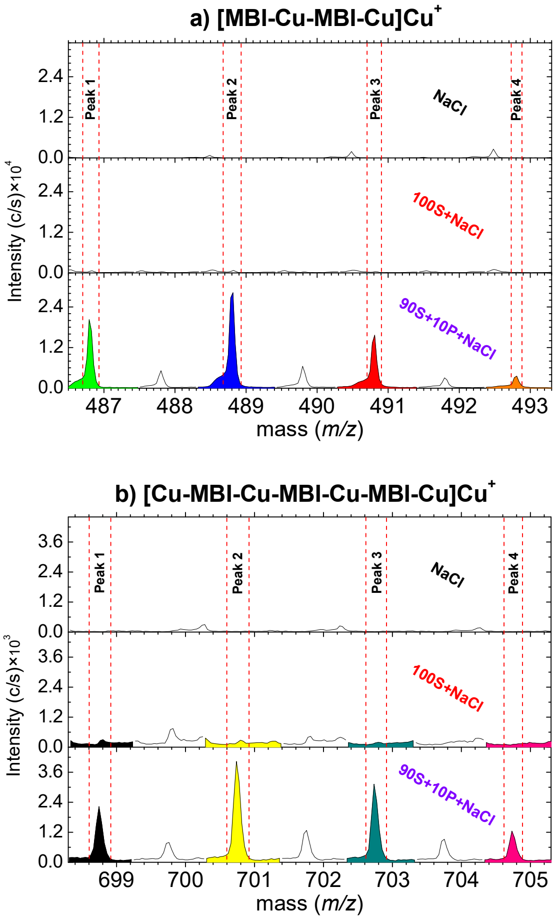

Figure 4.7: Evidence for the polymerization of 90S+10P+NaCl. Presented are the species (a) with two MBI molecules in the chain $[C_{14}H_{10}N_4S_2Cu_3]^+$ and (b) with three MBI molecules in the chain $[C_{21}H_{15}N_6S_3Cu_4]^+$. Spectra were obtained on Cu immersed for 1 day in 3 wt.% NaCl, in 3 wt.% NaCl containing 1 mM 2-mercaptobenzimidazole, MBI, (100S+NaCl) and in 3 wt.% NaCl containing 1 mM MBI and octylphosphonic acid, OPA, in the ratio 9:1 (90S+10P+NaCl).

To confirm the chlorine-bridge bonding mechanism, the ions with ^{63}Cu, ^{65}Cu and ^{35}Cl isotope combinations are shown in Fig. 4.8. In contrast, the chlorine-bridge ions were not detected in the positive-ion spectrum of 100S+NaCl despite $CuCNSCl^-$ being present in the negative-ion spectrum (this signal is much smaller than in the case of 90S+10P+NaCl), which is consistent with the absence of MBI polymerization. It is noteworthy that an XPS survey spectrum, recorded after 10 min sputtering at a film depth of about 10 nm, confirmed the presence of chlorine in the film but also revealed the absence of oxygen, ruling out the existence of a possible chlorohydroxo complex (Fig. A.20 and Table S20).

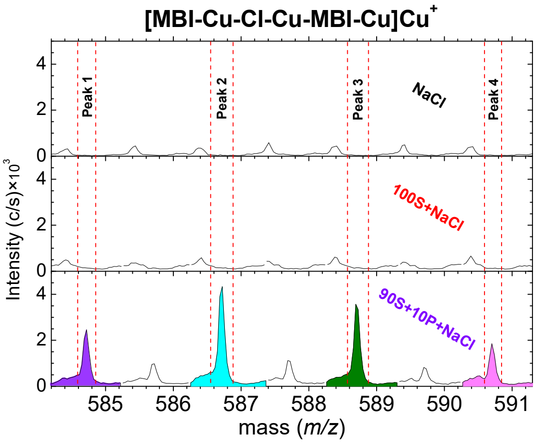

Figure 4.8: The evidence for the chlorine-bridge in the fragment of the polymer chain consisting of two inhibitor molecules in the surface layer. These are formed on Cu immersed for 1 day in 3 wt.% NaCl containing 1 mM 2-mercaptobenzimidazole, MBI, and octylphosphonic acid, OPA, in the ratio 9:1 (90S+10P+NaCl). Peak 1 corresponds to $[C_{14}H_{10}N_4S_2Cu_4Cl]^+$. Other fragments with ^{65}Cu isotope, such as $[C_{14}H_{10}N_4S_2Cu_3{}^{65}CuCl]^+$, $[C_{14}H_{10}N_4S_2Cu_2{}^{65}Cu_2Cl]^+$ and $[C_{14}H_{10}N_4S_2Cu^{65}Cu_3Cl]^+$, assigned to peak 2, 3 and 4, respectively, are also present.

These observations shed new light on the mechanism of Cu-MBI film formation in chloride-containing solutions. The first step of the mechanism is the same as that above for Cu-MBI, i.e. formation of a cuprous chloride complex, (Eq. 4.1). The second step – chloride-assisted film formation – differs from that operative in the formation of Cu-MBI, (Eq. 4.2), and results in incorporating Cl^- in the film, (Eq. 4.4). Therefore, here, chloride ions act as a promoter and a reactant:

$$CuCl_2^- + MBI^- \rightleftarrows Cu\text{-}Cl\text{-}MBI + Cl^- \tag{4.4}$$

Formation of a coordination polymer $[Cu\text{-}Cl\text{-}MBI]_n$ film on 90S+10P proceeds via (Eq. 4.5).

$$n[Cu\text{-}Cl\text{-}MBI] \longrightarrow [Cu\text{-}Cl\text{-}MBI]_n \tag{4.5}$$

4.3.4 Depth profiles of the polymerized films

In Fig. 4.9, ToF-SIMS positive ion depth profiles of 90S+10P+NaCl, 90S+10P+NaCl_7d and 100S+NaCl, and the negative ion depth profile of 90S+10P+NaCl are presented. These spectra consist of two main regions, the first corresponding to a passive film (thin, in the case of 100S+NaCl, and thick for 90S+10P+NaCl) and the second corresponding to the Cu substrate. The passive region of 90S+10P+NaCl (Fig. 4.9a), lying in the first ~2000 s of sputtering, is characterized by constant and high intensity signals for $C_7H_7SN_2^+$, $C_7H_7N_2^+$, $CuNH_3^+$, $C_7H_6SNCu_2^+$, $C_7H_6N_2Cu_2^+$ and $CNCu_2^+$ that are assigned to the presence of the inhibitor layer. Note that the intensity is presented by a logarithmic scale, emphasizing the low-intensity signals. The thickness of the film was assessed by comparison of ToF-SIMS depth profiles with SEM images of the cross-section (see below Fig. 4.16). Since ca. 2000 s was required to reach the interface, the estimated sputter rate is between 0.3 and 0.8 nm/s taking into account that the film thickness ranges between 600 nm and 1.6 µm (due to non-uniform film thickness, it is not possible to determine the sputter rate more accurately). After about 2000 s of sputtering, the $^{65}Cu^+$ signal started to decrease with gradual reduction of the number of inhibitor fragment ions. At the same time, polyatomic copper signals $Cu^{65}Cu_2^+$ and Cu_2^+ were increased, reaching their peak values and establishing the plateau. This observation can be explained by a matrix effect, which is very prominent and problematic in the cases of SIMS measurements. A depth profile of 90S+10P+NaCl_7d (i.e. after 7 days of immersion) (Fig. 4.9b) shows that the thickness of the precipitated film resembles that after one day of immersion and indicates that prolonged immersion does not influence film growth, i.e., the formation of a thicker film, as also shown in Fig. A.18. Furthermore, it should be emphasized that no OPA fragments were detected over the whole depth of the inhibitor film, ruling out the possibility of OPA molecules existing within the structure of MBI layers. Its absence from the layer surface was already shown in Figs. 4.1 and 4.2.

Additionally, the negative-ion depth profile for 90S+10P+NaCl (Fig. 4.9c) reveals the existence of chlorine-containing fragments such as ^{37}Cl, $CuCl_2^-$ and $Cu_2C_2N_2Cl^-$ over the whole depth of the MBI film. The gradual decrease of these ions follows that of inhibitor fragment ions found in the positive-ion depth profile (Fig. 4.9a), leading to the conclusion that the Cl, together with MBI, is part of the same building block of the polymerized chain.

Last but not least, in the thin-film region of the positive ion depth profile for 100S+NaCl (Fig. 4.9d) corresponding to the first 45 s of sputtering, the intensity signal of inhibitor fragments dropped sharply, together with the increase of the prevailing metallic Cu_3O^+, Cu_2O^+, $^{65}Cu_2^+$, and Na^+ ions. Afterwards, a plateau of prevailing ions was established in the Cu substrate region, with inhibitor fragments being neglected. The estimated thickness of a monolayer or a few-layer thick MBI inhibitor was about 1 to 5 nm. It is, therefore, reasonable to classify the inhibitor layer of 90S+10P+NaCl as the thick film since it is at least 100 times thicker, being approx. 600 nm. Note that this thickness is only partially consistent with the results obtained by FIB analysis (Section *SEM-EDS characterization at the cross-section of polymerized Cu-MBI film*) which revealed the non-uniform thickness of the inhibitor film.

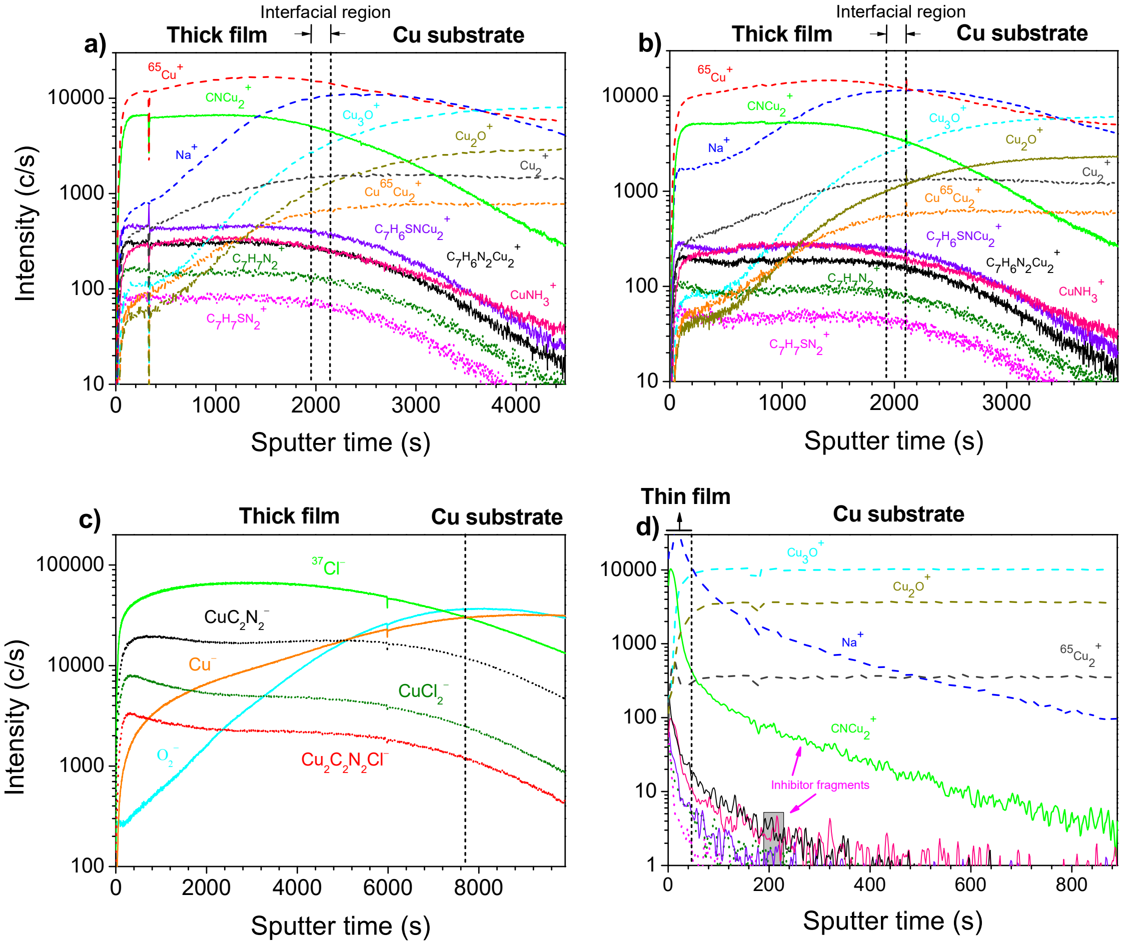

Figure 4.9: Tof-SIMS positive depth profiles obtained on Cu immersed for (a) 1 day and (b) 7 days in 3 wt.% NaCl containing 1 mM 2-mercaptobenzimidazole, MBI, and octylphosphonic acid, OPA, in the ratio 9:1 (90S+10P+NaCl). (c) Negative ion depth profile for 90S+10P+NaCl after 1 day of immersion. (d) Positive ion depth profile for Cu immersed for 1 day in 3 wt.% NaCl containing 1 mM MBI (100S+NaCl).

4.3.5 Cyclic voltammetry

Cyclic voltammetry has been employed to evaluate the degree and mechanism of inhibition of copper samples immersed for 1 day and 7 days in 3 wt. % NaCl solutions with and without added 1 mM MBI (100S+NaCl) and 90S+10P+NaCl (MBI+OPA). It must be noted that the CV measurement was not performed in a solution containing 100P+NaCl (OPA) since our previous work [45] showed its lack of corrosion inhibition on a copper surface.

4.3.5.1 Dissolution of Cu in chloride-containing medium

The cyclic voltammogram in Fig. 4.10a shows the first scan cycles of NaCl, 100S+NaCl, and 90S+10P+NaCl after one day of immersion. After immersion in NaCl, two anodic peaks appeared with maxima at 0.16 V (peak A_1) and 0.26 V (peak A_2), corresponding to the oxidation of Cu to Cu(I) and Cu(I) to soluble Cu(II) species. In the cathodic cycle, a single peak at −0.12 V (peak C_1) is attributed to the reduction of Cu(I) to Cu [10], [42],

[44], [170], [171]. The well-defined oxidation peak, A_1, is attributed to the formation of an insoluble CuCl salt layer, as depicted in (Eq. 1.8). Note that the formation of CuCl starts at about −0.05 V [172].

The next step might be the chemical reaction in excess chloride solution, leading to the formation of the soluble complex, $CuCl_2^-$ (Eq. 1.9). The active dissolution continues by further electro-oxidation, forming Cu^{2+}, ascribed to the shoulder peak A_2 (Eq. 1.10).

The overall mechanism of copper oxidation in chloride solutions can be described as electrochemical-chemical-electrochemical (ECE). At more positive potentials than that for the A_2 peak, a current plateau region was established that was ascribed to equilibrium between the formation of the CuCl surface layer and dissolution of the $CuCl_2^-$ complex [170]. The intensity of the plateau current indicates the porous nature of the film and hence its poor corrosion protection characteristics.

After the potential sweep reversal from 1 V to the negative direction, the current density gradually increased, growing to a counter-clockwise hysteresis loop (denoted as A_H) which can be attributed to pitting propagation, i.e., the autocatalytic character of the pitting phenomenon [99], [173]. The existence of a hysteresis loop indicates a delay in the repassivation of an existing pit. The larger the hysteresis loop, the greater the susceptibility to pitting, exhibiting poor repassivation performance [173]. Finally, at a potential where the hysteresis loop crosses the forward scan, denoted as the repassivation potential (E_{rp}), the pit growth is arrested [99], [173]. Also, on the reverse scan, a small reactivation anodic peak (denoted as A_R) can be observed at −0.02 V, indicating further oxidation of the porous and poorly protective film previously formed in the forward scan. At −0.12 V, there is an asymmetric cathodic peak C_1, which corresponds to the reduction of $CuCl_2^-$ or the CuCl layer [170]. Thus, the Cu^{2+} species formed in the anodic cycle leave the electrode surface and are considered unavailable for reduction processes. Finally, the lower potential limit of the scan, i.e. the sharp cathodic peak C_{HER} close to −1 V, corresponds to the onset of a hydrogen evolution reaction (HER).

4.3.5.2 The corrosion resistance and degradation of thin Cu-MBI film

In the forward scan of 100S+NaCl (Fig. 4.10a), the peak A_1, corresponding to copper dissolution, i.e. oxidation of Cu(0) to Cu (I), is entirely missing, which is indicative of strong inhibition of Cu(I) formation. Hence, the Cu-MBI film formed on the copper surface inhibits the transport of dissolution product $CuCl_2^-$. An interesting phenomenon occurs with the asymmetric peak A* (its contribution extends from 0.18 V upwards with the maximum at 0.62 V). The current density increases remarkably, despite the expectation that the current diminishes compared to NaCl since the 100S+NaCl possesses significant inhibitory features. The enlarged current densities could be assigned to the film degradation caused by oxidation of Cu(I)MBI (Eq. 2.1) that yields Cu(II) species and $(MBI)_2$. Woods and co-workers earlier reported similar results for 2-mercaptobenzothiazole (MBT) on Cu, suggesting that the oxidative dimerization takes place at potentials above 0.4 V vs. SHE in borate buffer of pH 9.2 [174] according to (Eq. 2.1).

We performed further investigations to confirm the degradation mechanism and reveal the composition of the products obtained following polarization of 100S+NaCl to 1 V. First, a high-resolution S 2p XPS analysis for 100S+NaCl (denoted as 100S+NaCl_PD) was carried out (Fig. 4.11b). The position of the peak centre at 163.1 eV can be attributed to the Cu–S–C bond [45]. There is no peak shift to about 167 eV [135], which is assigned to the thiosulfonate (S–S=O) as the final product of oxidation of sulphur, which suggests the absence of MBI dimers.

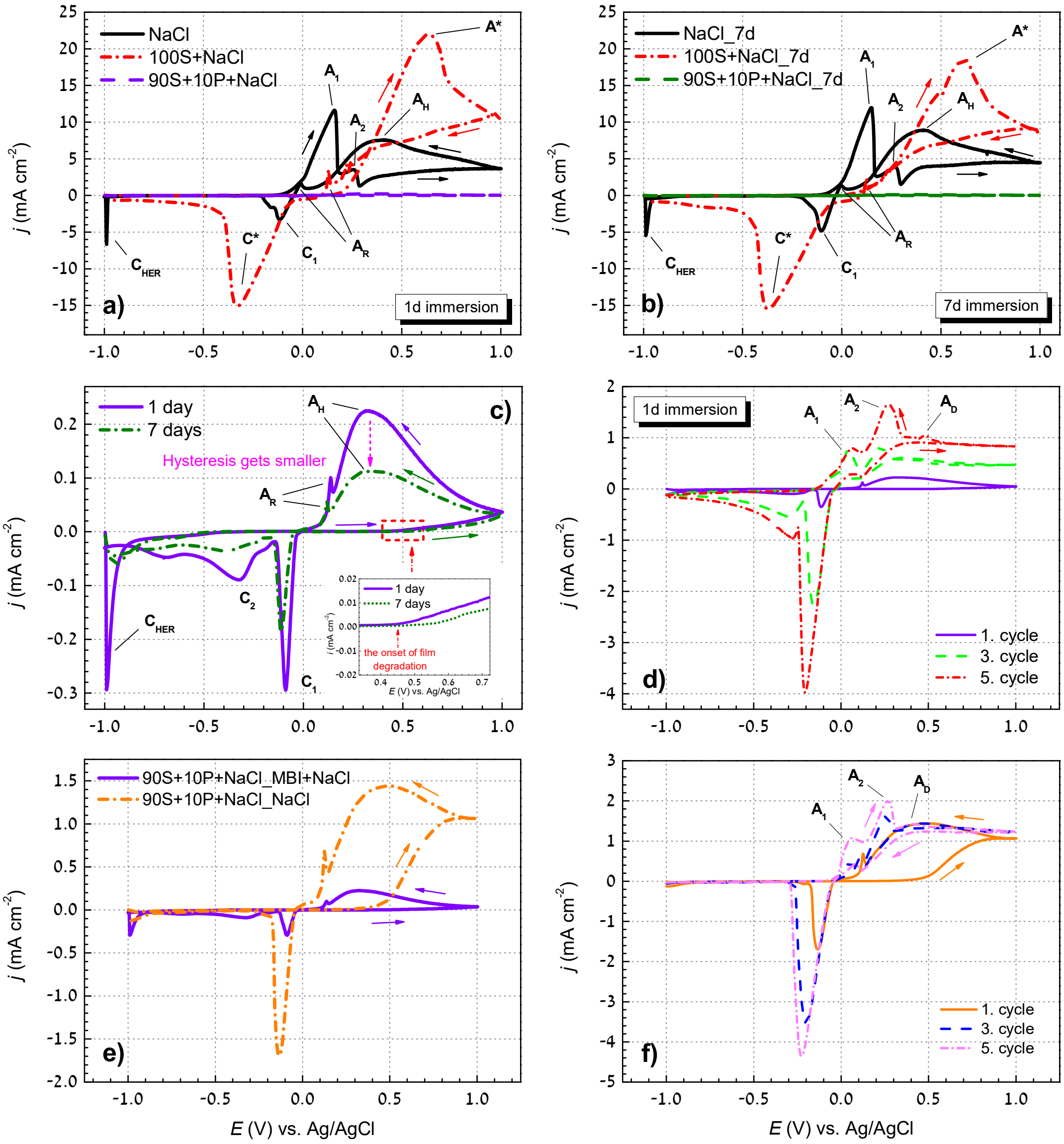

Figure 4.10: (a, b) Cyclic voltammograms recorded for copper in 3 wt.% NaCl solution and in 3 wt.% NaCl containing 1 mM of 2-mercaptobenzimidazole, MBI (100S) and in 3 wt.% NaCl containing 1 mM MBI and octylphosphonic acid, OPA, in the ratio 9:1 (90S+10P+NaCl) after (a) 1 day of immersion and (b) 7 days of immersion. (c) Cyclic voltammograms obtained for 90S+10S+NaCl after 1 day and after 7 days of immersion. (d) Consecutive scans of 90S+10P+NaCl after 1 day of immersion, (e) comparison between 90S+10P+NaCl_MBI+NaCl and 90S+10P+NaCl_NaCl after 1 day of immersion, and (f) consecutive scans of 90S+10P+NaCl_NaCl after 1 day of immersion.

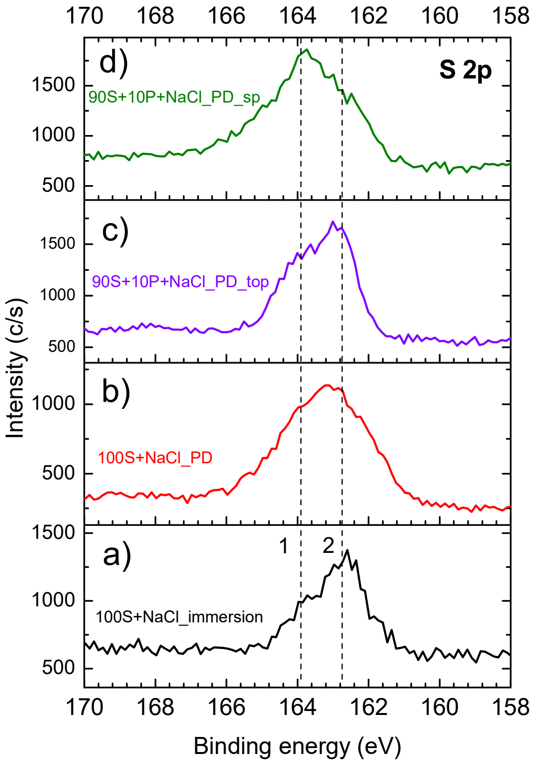

Figure 4.11: High-resolution XPS spectra of S 2p for (a) 100S+NaCl_immersion, (b) 100+NaCl_PD (100S+NaCl was polarized to 1 V), (c) 90S+10P+NaCl_PD_top (90S+10P+NaCl was polarized to 1 V and subsequently the XPS spectrum was recorded on the sample surface), and (d) 90S+10P+NaCl_PD_sp (90S+10P+NaCl was polarized to 1 V and subsequently the XPS spectrum was recorded at the depth of 10 nm). 100S+NaCl denotes 3 wt.% NaCl containing 1 mM 2-mercaptobenzimidazole, MBI, and 90S+10P+NaCl denotes 3 wt.% NaCl containing 1 mM MBI and octylphosphonic acid, OPA, in the ratio 9:1.

The S 2p signal for 100S+NaCl after one day of immersion without subsequent polarization (denoted as 100S+NaCl_immersion) is shown for comparison (Fig. 4.11a). The broadening of the peak at both low- and high-energy envelopes is observed after polarization, but oxidation can be excluded. No significant changes were observed in spectra for N 1s or Cu 2p, the latter excluding the formation of insoluble cupric species at the surface (results not shown). However, XPS cannot rule out the presence of MBI dimers since it is not sufficiently powerful to determine whether the S–S bridge exists at all. Note that XPS can predict the existence of an S–S bridge only in the case when the dimer undergoes further oxidation to sulfonate or thiosulfonate products. ToF-SIMS analysis, complementary to XPS, was therefore employed for the final determination of the potential S–S bridge species. In Fig. 4.12a, two pronounced fragments for MBI dimer are present – $C_{14}H_{11}N_4S_2^+$ at $m/z = 299$, and $C_{14}H_{10}N_4S_2Cu^+$ at $m/z = 361$. Its counterpart, Cu isotope $C_{14}H_{10}N_4S_2{}^{65}Cu^+$ at $m/z = 363$, which provides evidence for the existence of the dimer molecule bis(2-benzimidazolyl) disulfide, i.e. $(MBI)_2$, is included.

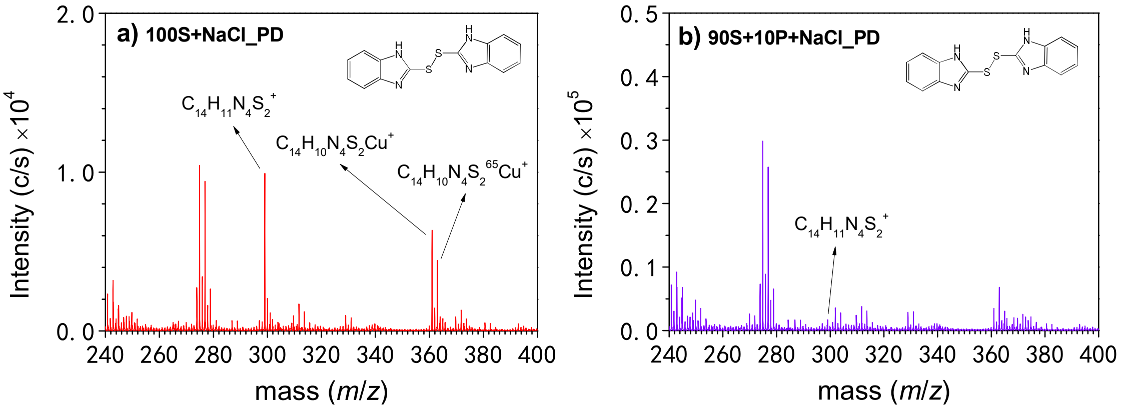

Figure 4.12: ToF-SIMS positive-ion spectra obtained on Cu after positive cyclic voltammogram scans up to 1 V in (a) 3 wt.% NaCl containing 1 mM 2-mercaptobenzimidazole, MBI, (100+NaCl_PD), and (b) 3 wt.% NaCl containing 1 mM MBI and octylphosphonic acid, OPA, in the ratio 9:1 (90S+10P+NaCl_PD).

We, therefore, report that the enlarged current densities for 100S+NaCl in Fig. 4.10a are due to the half-cell reactions where oxidation is occurring (Eqs. 2.2 and 2.3), which led to the degradation of Cu-MBI film.

During the reverse scan, a small anodic peak, A_R, is observed at 0.12 V (Fig. 4.10a), indicating that, in agreement with surface mapping (Fig. 5a), copper is not entirely covered by a protective layer of inhibitor. A large, single cathodic peak (C*) is present at −0.34 V that corresponds to the reduction of species formed in A* and A_R. Interestingly, the cathodic currents of peak C_{HER} are significantly reduced, indicating the inhibition of HER as well.

4.3.5.3 The corrosion resistance and degradation of thick polymerized Cu-MBI/Cu-Cl-MBI film

The faradaic currents for 90S+10P+NaCl are almost zero for forward and reverse scans (Fig. 4.10a). It is surprising that the polymerized Cu-MBI/Cu-Cl-MBI film exhibits a strong corrosion inhibiting effect, despite being subjected to aggressive chloride conditions.

The cyclic voltammograms in Fig. 4.10b show the first cycles of NaCl, 100S+NaCl, and 90S+10P+NaCl after seven days of immersion. For NaCl, there is no significant difference from that subjected to one day of immersion, except that the faradaic currents are slightly increased, which is consistent with the greater susceptibility of copper to corrosion processes at longer immersion. Supportive of this is a more intense current plateau, together with a larger hysteresis loop. For 100S+NaCl (Fig. 4.10b), however, a decrease of A_2 and A_R peaks indicates that longer immersion enhances the corrosion protection of Cu. Additionally, the shape of the asymmetric peak A_2 changed from that of the 100S+NaCl after 1 day of immersion. It appears that this composite peak consists of two or three coupled faradaic processes, i.e. closely spaced sub-peaks, which is much more complicated than the aforementioned single one.

Fig. 4.10c shows the comparison between 90S+10P+NaCl after 1 day and 7 days of immersion at a significantly enlarged current density scale compared to that in Figs. 4.10a,b. Only at this scale, the faradaic currents are easily compared for 90S+10P+NaCl samples. In the forward sweep, the pure capacitive currents, i.e. the passive region, persist until the anodic potential at 0.45 V is reached, where the increase in current density is noted, indicating the contribution of faradaic currents (inset in Fig. 4.10c). This gradual current increase, despite being regarded as almost negligible, eventually suggests the onset of film degradation (Eq. 2.1). Since there are practically no signs of the existence of peaks A_1 and/or A_2 (Fig. 4.10c), i.e. of oxidation of Cu and Cu(I), respectively, we may conclude that the polymerized Cu-MBI/Cu-Cl-MBI film prevents the onset of dissolution of Cu [163], [175], thus acting as an ohmic barrier between the substrate and the electroactive medium. In the reverse sweep, the counter-clockwise hysteresis loop (peak A_H), together with the reactivation peak, A_R, appears to be somewhat smaller for 90S+10P+NaCl after 7 days of immersion. This indicates an improvement in inhibition performance with time (Fig. 4.10c). At more negative potentials, the sharp peak C_1, and the smaller, broader cathodic peak, C_2, are attributed to the reduction of species oxidized during the forward and reverse scans. Peaks C_1 and C_2 of 90S+10P+NaCl are coupled to give a single, larger composite peak, C*, in the voltammogram of 100S+NaCl.

CVs in Fig. 4.10d show five consecutive cathodic and anodic cycles offering better insight into the inhibition and stability of the polymerized Cu-MBI/Cu-Cl-MBI film formed in 90S+10P+NaCl. The features of the first scan have already been discussed (vide supra Fig. 4.10a). From the second scan onwards, a stepwise increase in the currents of the peaks A_1 and A_2 is observed, with A_1 potential becoming fixed from the third scan onwards, accompanied by the shift of A_2 to more positive E values. It becomes difficult to clearly distinguish peaks A_1 and A_2 with cycling. New peak A_D appears at 0.45 V, which gradually merges with A_1 and A_2 into the three-headed composite peak (Fig. 4.10d) as already seen for 100S+NaCl after 7 days of immersion (Fig. 4.10b). The evolving shapes of these redox peaks suggest the occurrence of complex, multistep processes for which elucidation of the detailed mechanism is beyond the scope of this work. However, the understanding of the key processes has been highlighted. To conclude, despite an increasing trend of faradaic currents with successive scans, their magnitude is still much smaller than those of NaCl and 100S+NaCl, indicating the good retention of corrosion inhibition with gradual film degradation.

High-resolution S 2p XPS spectra, recorded after polarization of 90S+10P+NaCl, rule out the existence of thiosulfonates (S–S=O), either on top of the surface (denoted as 90S+10P+NaCl_PD_top) (Fig. 4.11c) or, after 10 min sputtering with Ar^+ ions, at a depth of about 10 nm (denoted as 90S+10P+NaCl_PD_sp) (Fig. 4.11d). The related S–S=O peak would appear at about 167 eV [135]. Only a weak signal for the dimer molecule fragment, $C_{14}H_{11}N_4S_2^+$ at $m/z = 299$, is detected for 90S+10P+NaCl_PD (Fig. 4.12b) as compared to 100S+NaCl_PD (Fig. 4.12a). This is consistent with the results of electrochemical measurements and indicates the remarkable stability of thick polymerized film compared with that of thin unpolymerized 100S+NaCl, which is subject to dimerization (Fig. 4.10a).

4.3.5.4 Effectiveness of inhibition and stability in the environment without an MBI reservoir

In the presence of an inhibitor, the defect sites on the specimen surface are blocked due to the availability of an inhibitor in the solution for additional formation of Cu-MBI during immersion. Ogle and Poling [148] referred to this as “protective film maintenance”. Fig. 4.10e shows the first cycle of CV for the 90S+10P in the presence and the absence of MBI in a chloride-containing medium. In the absence of an inhibitor (90S+10P+NaCl_NaCl), the capacitive currents prevail in the region of the forward scan where oxidation of Cu and Cu(I) was expected. However, the current increases sharply above around 0.4 V until reaching the plateau. Despite being unable to form the complete peak, the shape of the formed half-peak with a sudden and large jump in current resembles that of 100S+NaCl

(Fig. 4.10a), associated with the degradation of the polymerized Cu-MBI/Cu-Cl-MBI film, i.e. passive layer breakdown. The higher plateau currents, together with the larger hysteresis and reactivation peak, indicate that the polymerized Cu-MBI/Cu-Cl-MBI inhibitor film formed without MBI (90S+10P+NaCl_NaCl) is more susceptible to localized corrosion and degradation than when formed in its presence (90S+10P+NaCl_MBI+NaCl). Interestingly, five successive cycles in the absence of MBI (Fig. 4.10f) resemble those in the presence of MBI (Fig. 4.10d). These results confirm that the polymerized film retains its protectiveness, even after being exposed to an environment that contains no inhibitor, and thus represents an effective and impermeable physical barrier to the inward diffusion of chloride ions.

4.3.6 SEM-EDS characterization of the surface of Cu-MBI films

The surfaces of NaCl, 100S+NaCl, 90S+10P+NaCl, and 90S+10P+NaCl_7d were examined by FE-SEM at lower and higher magnifications to determine the morphology of the surface layers (Fig. 4.13). At first glance, the presence of large aggregates attributed to the corrosion products is observed on the surface of NaCl (Fig. 4.13a) at lower magnification. At higher magnification (inset in Fig. 4.13a), the morphology of the surface looks very rough due to the aggressive nature of the electrolyte solution, which causes the corrosion processes to occur. The existence of corrosion products is minimized significantly after exposure of the Cu surface to the solution containing 100S+NaCl (Fig. 4.13b). The surface became much smoother, even exposing scratches from the grinding process, indicating substantial corrosion inhibition with the formation of a thin Cu-MBI layer. The inset in Fig. 4.13b represents the morphology of agglomerates at higher magnification; it does not look like the corrosion products formed on the NaCl surface and, most probably, originate from the inhibitor. Figs. 4.13c and 4.13d reveal the porous straw-like structure of polymerized Cu-MBI/Cu-Cl-MBI film formed in 90S+10P+NaCl after 1 day and 7 days of immersion, with a morphology resembling “hay straws”. The thickness of straws ranges from nm to µm. Trapped air within the gaps between straws across the surface (inset in Figs. 4.13c and 4.13d) leads to the establishment of air pockets, which might be responsible for additional contributions to the hydrophobicity of films, as reported in our previous study (contact water angle of 115 ± 2 °) [45]. Higher magnifications revealed that the hay straws have a cuboid shape with smooth sides (Fig. 4.14a). Their surface is granular, with a grain size of about 15 nm (Fig. 4.14b).

SEM-BSE images, together with EDS analysis for NaCl, 100S+NaCl, 90S+10P+NaCl after one day of immersion, and 90S+10P+NaCl_7d after seven days of immersion, are given in Figs. 4.15 and A.21. The NaCl surface consists mainly of copper oxide (Fig. 4.15a, locations 2 and 3, Table 4.1) and corrosion products containing Cl (Fig. 4.15a, location 1, Table 4.1). The surface of 100S+NaCl contains inclusions of SiC particulates (Fig. 4.15b, spots 1, 2, and 5, Table 4.2) originating from the mechanical pre-treatment. Interestingly, at locations of these inclusions, the absence of chloride was observed, suggesting the effectiveness of inhibition of corrosion. On spots 3 and 4 (Fig. 4.15b, Table 4.2), only Cu was observed since the MBI layer is only a few nm thick and thus cannot be detected by EDS. In contrast, for 90S+10P+NaCl, the SiC particulates were not found on the surface (Fig. 4.15c, Table 4.3) due to the large thickness of the polymerized film (vide infra).

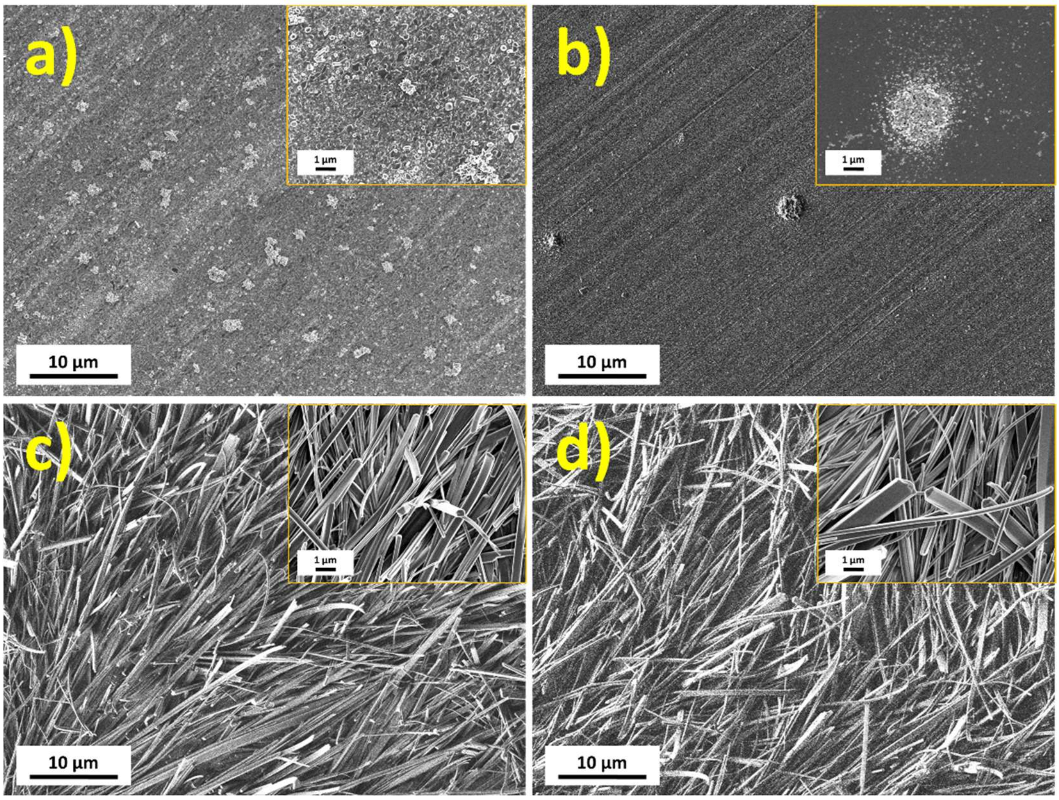

Figure 4.13: SEM secondary electron images for copper immersed for (a) 1 day in 3 wt.% NaCl, (b) 1 day in 3 wt.% NaCl containing 2-mercaptobenzimidazole, MBI, (100S+NaCl), (c) 1 day in 3 wt.% NaCl containing 1 mM MBI and octylphosphonic acid, OPA, in the ratio 9:1 (90S+10P+NaCl,) and (d) for 7 days in 90S+10P+NaCl (90S+10P+NaCl_7d). Insets represent the morphology at higher magnification.

The EDS analysis at different locations on the surface showed more or less consistent atomic ratios between N, S, and Cl atoms (Table 4.3). The atomic ratio of N/S is in the range of 2.1 to 3.4 (Table 4.4), which is greater than the stoichiometric ratio of N/S, being 2 for an MBI molecule. It should be kept in mind that the interpretation of N values needs to be taken with caution due to difficulties in detecting low energy elements such as nitrogen by EDS. Thus, it should not be surprising that, at location 6 (Fig. 4.15c, Table 4.3), the nitrogen was not detected but only sulphur, originating from the MBI molecule.

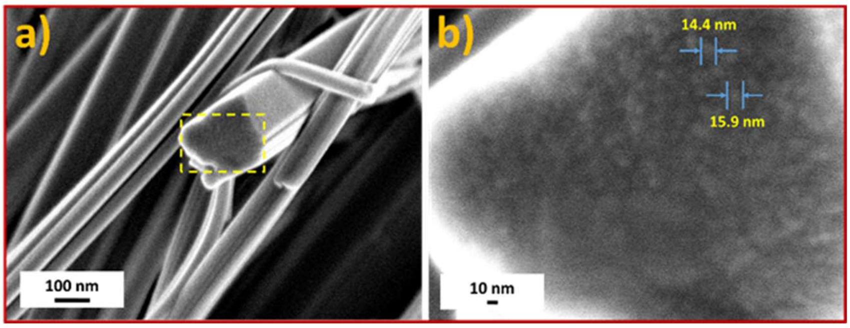

Figure 4.14: SEM secondary electron (SE) images for Cu immersed for 1 day in 3 wt.% NaCl containing 2-mercaptobenzimidazole, MBI, and octylphosphonic acid, OPA, in the ratio 9:1 (90S+10P+NaCl), recorded at (a) lower and (b) higher magnifications, reveal the granular surface of the hay straw with a grain size of about 15 nm.

However, the presence of nitrogen in the polymerized Cu-MBI/Cu-Cl-MBI film should not be questioned based on XPS analysis (Fig. A.20 and Table S20). The chlorine was observed at all locations (Table 4.3), and the atomic ratio of S/Cl (Table 4.4) is relatively constant at around 1. These results correlate well with ToF-SIMS results (Fig. 4.8), which demonstrated the existence of Cl throughout the polymerized film and its participation in the polymer chain structure. 90S+10P+NaCl_7d obeys the same atomic ratio S/Cl trend as 90S+10P+NaCl, being around 1 (Fig. 4.15d, Table 4.5, Table 4.6). At some micrograph locations, the nitrogen was not detected despite the presence of sulphur (spots 1, 2, and 4, Table 4.5), as for 90S+10P+NaCl (Fig. 4.15c, spot 6, Table 4.3).

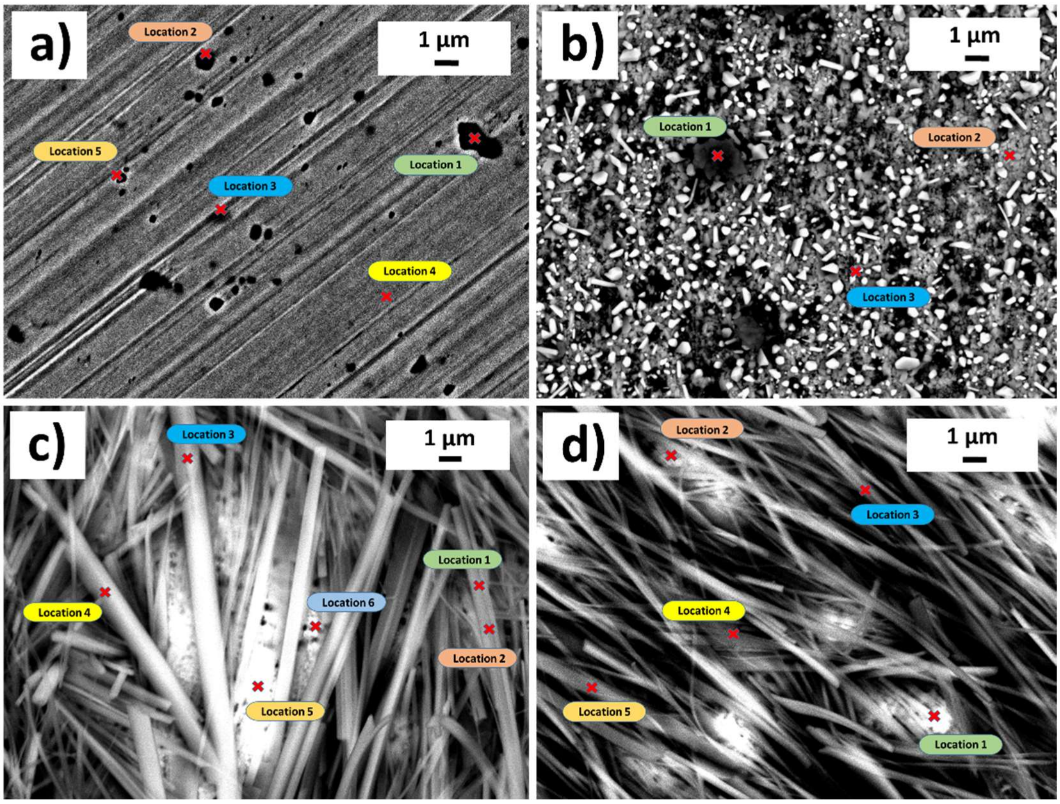

Figure 4.15: SEM images recorded in backscattered electron (BSE) mode for Cu immersed (a) for 1 day in 3 wt.% NaCl, (b) for 1 day in 3 wt.% NaCl containing 1 mM 2-mercaptobenzimidazole, MBI, (100S+NaCl), (c) for 1 day and (d) 7 days, both in 3 wt.% NaCl containing MBI and octylphosphonic acid, OPA, in the ratio 9:1 (90S+10P+NaCl and 90S+10P+NaCl_7d). Locations denoted by a cross mark indicate the spots where EDS analysis was conducted (Tables 4.1 – 4.3 and 4.5).

Table 4.1: EDS analysis of Cu immersed for 1 day in NaCl. Analyses were performed at locations 1 to 3, as denoted in Fig. 4.15a.

Location	at.% Cu	at.% O	at.% Ca	at.% Cl
1	34.5	48.2	16.9	0.4
2	84.3	15.7	—	—
3	88.0	12.0	—	—

Table 4.2**:** EDS analysis of Cu immersed for 1 day in 100S+NaCl. Analyses were performed at locations 1 to 5, as denoted in Fig. 4.15b.

Location	at.% Cu	at.% O	at.% Si
1	35.3	9.0	55.7
2	64.9	6.1	29.0
3	100.0	—	—
4	100.0	—	—
5	78.5	—	21.5

Table 4.3: EDS analysis of Cu immersed for 1 day in 90S+10P+NaCl. Analyses were performed at locations 1 to 6, as denoted in Fig. 4.15c.

Location	at.% Cu	at.% N	at.% S	at.% Cl
1	38.6	34.4	14.2	12.8
2	45.2	31.6	11.8	11.4
3	37.1	32.6	15.7	14.6
4	31.1	43.6	12.8	12.5
5	61.9	23.7	7.8	6.6
6	83.2	—	8.6	8.2

Table 4.4: Atom ratio of chemical elements identified on Cu immersed for 1 day in 90S+10P+NaCl (Table 4.3). Analyses were performed at locations 1 to 6, as denoted in Fig. 4.15c.

Location	N/S	S/Cl
1	2.4	1.1
2	2.7	1.0
3	2.1	1.1
4	3.4	1.0
5	3.0	1.2
6	—	1.0

Table 4.5: EDS analysis of Cu immersed for 7 days in 90S+10P+NaCl_7d. Analyses were performed at locations 1 to 5, as denoted in Fig. 4.15d.

Location	at.% Cu	at.% N	at.% S	at.% Cl
1	81.4	—	9.7	8.9
2	76.9	—	11.8	11.3
3	42.3	33.7	12.6	11.4
4	69.4	—	17.1	13.5
5	34.7	43.1	10.8	11.4

4.3.7 SEM-EDS characterization of the cross-section of polymerized Cu-MBI/Cu-Cl-MBI film

SEM micrographs of the cross-section, with corresponding EDS analysis of marked locations (denoted by white squares from 1 to 6) and EDS mapping of the selected region for 90S+10P+NaCl, were obtained at the polymerized Cu-Cl-MBI film/substrate interface (Fig. 4.16). The most interesting result is that the thickness of the inhibitor film is non-uniform and ranges between approx. 200 nm and 1.6 µm (Figs. 4.16b, 4.16d). Further, it should be emphasized that the polymerized Cu-MBI/Cu-Cl-MBI film is compact with no cracks at the substrate/inhibitor interface (Figs. 4.16b, 4.16d), which correlates with its superior corrosion protection (see Fig. 4.10). However, some relatively small defects are present within the inhibitor layer, marked with green circles (Figs. 4.16b, 4.16d).

The initial structure of the thick polymeric film with the hay straw morphology and inner cross-section obtained by focused ion-milling is presented in Fig. 4.13c and Fig. 4.16a, respectively. Note that the hay straws cannot be easily observed in Fig. 4.16a since the Pt is deposited on top of the polymeric film by means of filling the space between the hay straws. It is noteworthy that due to the hay straw morphology of the polymeric film, the uniform deposition of the protective Pt layer during the FIB pre-treatment of the sample was a rather difficult task. Protruded stick, being approximately 400 nm thick, is marked in Fig. 4.16b. It is evident that it originates from the polymeric film with hay straw morphology and is occluded by deposited Pt. These features are believed to contribute to the total hydrophobicity [45] of the 90S+10P+NaCl surface, as stated in the previous section. EDS analysis of the enlarged SEM micrograph is shown in Fig. 4.16b. Six different locations on the cross-section of the sample were considered, each with a gradual shift from the substrate to the inhibitor film to monitor the contribution of different elements. Phase I is characterized only by the presence of Cu (Fig. 4.16c, location 1, Table 4.7). At the border of two phases, I and II, O is present (Fig. 4.16c, location 2, Table 4.7). Phase II contains the largest content of O, assigned to the oxide layer, approximately 150 nm thick (Fig. 4.16c, location 3, Table 4.7). Interestingly, the presence of S and Cl accompanies the O in the bottommost part of the oxide layer (Fig. 16c, location 2, Table 4.7). After the oxygen peak point in the inner part of the oxide layer was reached, its contribution became smaller in the upper parts, followed by an increased content of S and Cl (Fig. 4.16c, locations 4 and 5, Table 4.7). This increase culminates in phase III, where N was also detected, confirming the existence of the Cu-MBI/Cu-Cl-MBI layer (Fig. 4.16c, location 6, Table 4.7). It should be pointed out that the S/Cl ratio is still around 1 (Table 4.7), which is consistent with the EDS analysis of the surface of 90S+10P+NaCl (Table 4.3). In contrast, we found an N to S atom ratio of 0.4, compared to the theoretical value for the stoichiometry of the MBI molecule (2:1) (Fig. 4.16c, location 6, Table 4.7). We assume that it could be associated with the partial decomposition of the molecule during the etching process, with Ga^+ ions experiencing relatively high local temperatures [176]. This phenomenon is in agreement with the recent findings of Wu et al. [177] in which adsorption of 2-mercaptobenzthiazole (2-MBT) vapour on a Cu(111) surface under ultra-low pressure by STM, XPS, AES, and LEED was investigated. They noted that the Moiré pattern of 2-MBT was rich in S due to molecule decomposition after the sample temperature was increased above 150 °C, probably due to the high affinity of sulphur to copper [177].

Besides, the Moiré structure appears poor in N, suggesting the desorption of molecular fragments after decomposition [177]. The uppermost part of the cross-section (Fig. 4.16c) consists of the two protecting layers, phase IV and V, assigned to electron-beam-assisted and ion beam (Ga^+)-assisted Pt deposition, respectively.

Finally, the EDS analysis, with the distribution of elements at the 90S+10P+NaCl cross-section, is presented in Fig. 4.16c and Table 4.8. The mapping images show different phases. In the uppermost part, S and Cl in the inhibitor layer were detected. Note that the expected signal for N was not detected (Table 4.8). Such anomalous trends, including missing nitrogen signals together with enrichment in sulphur, are due to the above-mentioned phenomena. In the bottommost layer, copper oxide is present on top of Cu metal. This result confirms the existence of a Cu_2O underlayer below the MBI inhibitor film, agreeing with the electrochemical study of Modestov et al. [10] in which they reported that the formation of the Cu-inhibitor layer was accompanied by the formation of a Cu_2O underlayer. It is believed that the role of the Cu-inhibitor overlayer is to stabilize the Cu_2O underlayer, maintaining its high electrical resistance by establishing the highly impermeable physical barrier to the inward diffusion of Cl^- ions [10], or, as Cotton and Scholes wrote, the inhibitor layer “serves as a reinforcement to the protection afforded by the oxide layer” [178]. However, the deposition of a Cu_2O underlayer in solution with pH 4, as in the case of 90S+10P+NaCl, constitutes an enigma since the existence of Cu_2O under such low pH conditions is thermodynamically unstable [44], [49].

A possible scenario would be that the polymerized Cu-MBI/Cu-Cl-MBI overlayer, as a low permeable membrane, enables physical separation of the Cu_2O underlayer from such a harsh environment, as suggested by Modestov and co-workers [10]. Cohen et al. and Brusic et al. reported that Cu_2O does not appear to be a prerequisite for the uptake of BTA [147], [164]. The presence of Cu^+ facilitates the growth of Cu(I)BTA film but is not necessary for the formation of a chemisorbed layer of BTAH on both Cu and CuO surfaces. Its thickness is, however, limited to that of a monolayer [147], [164]. A similar conclusion was reported by Chadwick and Hashemi for both BTAH [11] and MBI [135], emphasising the importance of a Cu_2O underlayer as a source of Cu^+ ions that contribute to the precipitation of inhibitor film.

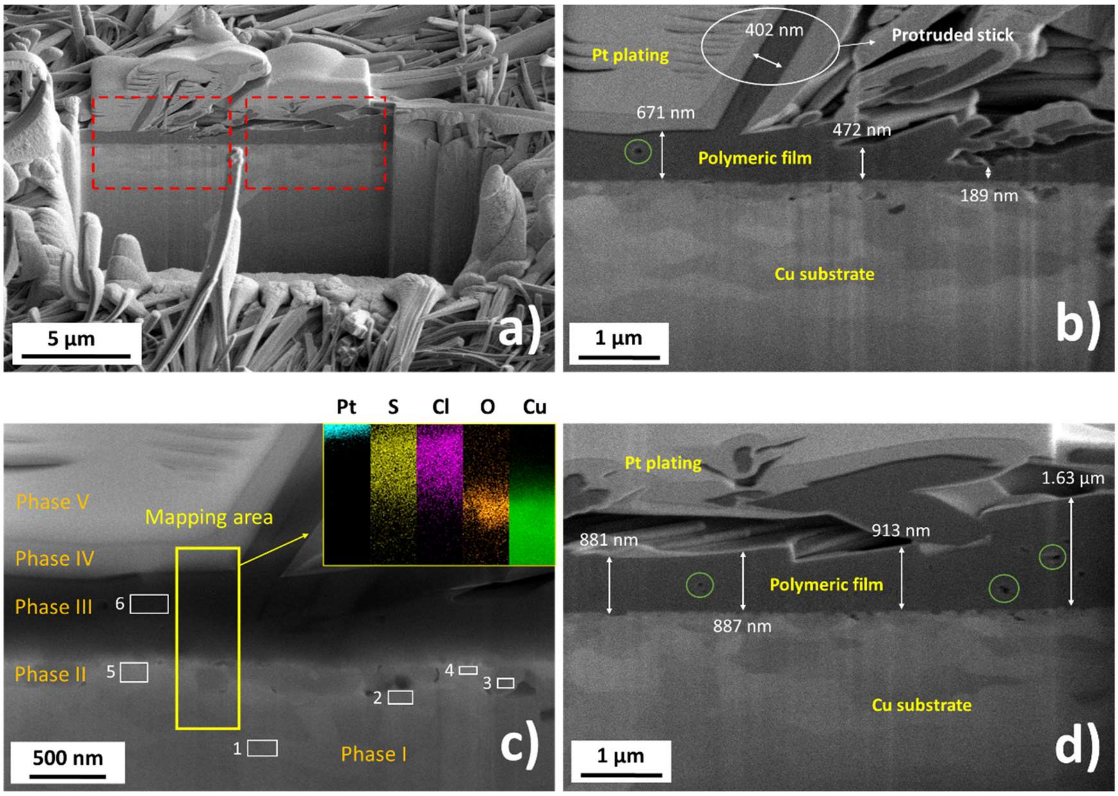

Figure 4.16: SEM images, with EDS analysis at the cross-section within the trench made by FIB, recorded for Cu immersed for 1 day in 3 wt.% NaCl containing 2-mercaptobenzimidazole, MBI, and octylphosphonic acid, OPA, in the ratio 9:1 (90S+10P+NaCl). (a) Sideward view (left and right rectangles represent the enlarged images b and d, respectively), (b) the cross-section of the polymeric inhibitor film on copper substrate, indicating the thickness of the protruding stick and the non-uniform thickness of the inhibitor film. (c) EDS mapping of the cross-section of image (b) indicates six different phases. The recorded mapping area is denoted by a yellow vertical rectangle (Table 4.8). White horizontal rectangles denote the spots where EDS analysis was performed (Table 4.7). (d) The cross-section of polymeric inhibitor film on copper substrate, indicating a very thick and non-uniform inhibitor layer. Green circles indicate locations where relatively small defects are noted within the inhibitor layer.

Table 4.6: Atom ratio of chemical elements identified on Cu immersed for 7 days in 90S+10P+NaCl_7d (Table V). Analyses were performed at locations 1 to 5, as denoted in Fig. 4.15d.

Location	N/S	S/Cl
1	—	1.1
2	—	1.0
3	2.7	1.1
4	—	1.3
5	4.0	0.9

Table 4.7: EDS analysis of Cu immersed for 1 day in 90S+10P+NaCl. Analyses were performed at locations 1 to 6 (white rectangles), as denoted in Fig. 4.16c.

Location	at.% Cu	at.% N	at.% S	at.% Cl	at.% O
1	100	—	—	—	—
2	96.1	—	0.9	0.9	2.1
3	93.0	—	1.0	0.8	5.2
4	93.4	—	2.2	2.0	2.4
5	93.9	—	1.8	1.8	2.5
6	63.0	6.0	14.1	13.6	3.3

Table 4.8: EDS analysis of Cu immersed for 1 day in 90S+10P+NaCl. Analyses were performed at the mapping area denoted by a yellow rectangle (Fig. 16c). The composition given represents the average composition of colour mapping in the inset of Fig. 4.16c.

Element	Content
at.% Cu	83.8
at.% N	—
at.% S	4.8
at.% Cl	4.5
at.% O	4.1
at.% Pt	2.8

4.4 Conclusions

The formation of a thick inhibitor film on copper takes place by the combined action of 2-mercaptobenzimidazole and octylphosphonic acid in 3 wt.% NaCl solution at pH 4 (i.e. 90S+10P+NaCl). Since the film possesses strong inhibitory properties against corrosion, several findings are succinctly presented regarding the mechanism of its formation and degradation, composition, structure, and stability.

1. The high-intensity fragments at m/z 487 and 699, obtained by ToF-SIMS, indicate a great degree of Cu-MBI polymerization. Further, high-intensity fragments at m/z 585, referring to polymerized Cu-MBI chains containing Cl, were also identified. Therefore, the anti-corrosion film formed on Cu in NaCl containing MBI and OPA consists of polymerized $[\text{Cu-MBI}]_n$ /$[\text{Cu-Cl-MBI}]_n$ film.

2. A mechanism is postulated for the formation of film. The first step is the activation of corrosion by dissolution of Cu and the resulting formation of $CuCl_2^-$. Once formed, $CuCl_2^-$ ions are involved in the second step, i.e. the formation of Cu-inhibitor complex addressed as chloride-assisted film formation. Two reaction paths are operative: (i) without Cl^- being incorporated in the film, i.e. $[\text{Cu-MBI}]_n$, and (ii) with Cl^- being incorporated in the film, i.e. $[\text{Cu-Cl-MBI}]_n$. In (i) chloride ions act as promotors of film formation and in (ii) chloride ions act simultaneously as promoters and reactants, thus revealing their dual role in the formation of polymerized Cu-Cl-MBI chains. We believe that such a scenario can also be expected for other metal-organic inhibitor systems. Hence, the pure catalytic role of chloride ions is excluded since they are consumed in the reaction.

3. The inhibitor film is characterized by the non-uniform thickness that reaches over one micrometre in size. Its porous, straw-like morphology, recorded by SEM, leads to establishing the air pockets, possibly being responsible for the higher hydrophobicity, thus contributing to overall protection.

4. FIB/SEM/EDS confirmed that the precipitation of the Cu-MBI was accompanied by the formation of the Cu_2O underlayer, even at pH 4, where the cuprous oxide is thermodynamically unstable. This anomalous stability can be attributed to the physical separation of the oxide layer from an aggressive electrolyte by the thick polymerized Cu-MBI/Cu-Cl-MBI film that prevents the Cu_2O from being doped by the Cl^-. It is believed that the non-doped/slightly doped Cu_2O is responsible for the observed resistance to corrosion processes.

5. Cyclic voltammetry revealed that the polymerized Cu-MBI/Cu-Cl-MBI film, in the presence of an inhibitor reservoir, i.e. 90S+10P+NaCl, exhibited an impressive reduction of the Cu corrosion, the anodic currents being smaller by factors of $\simeq$ 12 000 times and of $\simeq$ 40 times, compared to those of NaCl and 100S+NaCl, respectively. However, even more important is the fact that 90S+10P+NaCl manifests excellent protection against corrosion, even in the chloride solution that does not contain an MBI or MBI/OPA reservoir. Moreover, the faradaic currents after 5 cycles in the absence of an inhibitor reservoir are almost equal to those in a constant supply of inhibitors in solution. This indicates significant retention of inhibition efficiency. The absence of an inhibitor container is suitable for applications that are not limited just to closed systems.

6. The combination of ToF-SIMS and XPS techniques, together with cyclic voltammetry, enabled the mechanism of degradation of the Cu-MBI films to be postulated. On polarization, the Cu-MBI complex was subject to degradation, leading to an increase in the faradaic currents and the formation of the MBI dimer, bis(2-benzimidazolyl) disulfide, i.e., $(MBI)_2$. This resulted in the Cu-MBI film peeling off. The degradation taking place above 0.45 V was prominent for 100S+NaCl, whereas, for 90S+10P+NaCl, the stability and resistance toward degradation were impressive. This is corroborated by the anodic currents being about 1000 times smaller for 90S+10P+NaCl than 100S+NaCl.

Chapter 5

Investigation of Localised Corrosion Processes and Corrosion Inhibition of Al/Cu Galvanic Couple by 2-Mercaptobenzimidazole and Octylphosphonic Acid

5.1 Literature Review

To find an effective and reliable corrosion inhibitor for AA2024, it is crucial to understand the mechanism governing the corrosion inhibition processes. This aluminium alloy consists mainly of copper-rich intermetallic particles, such as Al_2Cu and Al_2CuMg [61], [62], having an average size of 7.6 ± 5.2 µm [60], so monitoring the localized corrosion (i.e., accurately measuring the potentials and currents) at these sites can be quite challenging. Because the degradation of the A2024 is mainly due to the local galvanic coupling between the IMPs and the surrounding matrix, a reasonable approach would be to mimic the intermetallic phases of the 2024 system by testing an appropriate galvanic couple model such as Al/Cu to provide key information to better understand the behaviour of alloy systems.

Conventional electrochemical techniques used in previous chapters provide global information (i.e., obtained for the entire surface of the exposed metal substrate) that lack sufficient spatial resolution, which is very important for elucidating the mechanism involved. To this end, microelectrochemical techniques such as SVET and SECM provide *in situ* topographic and electrochemical information on the reactivity of corrosion processes, which are resolved simultaneously in space and time.

Snihirova et al. [24] observed the synergistic inhibition effect for various organic mixtures on a model Al-Cu-Mg sample. The results obtained by scanning vibrating electrode technique revealed the highest synergy for the mixture of 2,5-dimercapto-1,3,4-thiadiazolate (DMDT) + 8-HQ. Shi et al. [179] used SVET and scanning-ion-selective electrode technique (SIET) to measure the distribution of current densities and pH on coupled Al_2Cu-Al and Al_3Fe-Al models by cerium cinnamate. While the adsorbed cerium cinnamate mainly influenced the corrosion inhibition on Al_3Fe-Al, the precipitation of cerium oxide/hydroxide inhibited the activity on the Al_2Cu-Al surface. Coelho et al. [180] elaborated on the inhibitive effect of the synergistic combination of BTA and $CeCl_3$ on the Al/Cu model. The SVET analysis revealed permanent corrosion protection for 46 h of immersion in aerated NaCl solutions, while the ToF-SIMS suggested that the protective phase $Ce(OH)_3$ appeared to precipitate over previously formed Cu-BTA film. Ramirez-Cano et al. employed the EQCM and SVET to locally investigate the interaction between the organic compounds 3-amino-1,2,4-triazole (ATA) [30] and 2-mercaptobenzothiazole (2-MBT) [29] and Au-Cu galvanic couple. Measurements showed that the ATA was physisorbed on both metals and caused an increase in the ionic current density range, i.e., accelerated the corrosion instead of inhibiting it. On the other hand, 2-MBT could significantly reduce the ionic current density range related to the electrochemical reactivity of Au-Cu samples in 1 mM NaCl solution. Izquierdo et al. [181] combined a novel microelectrochemical strategy to study corrosion inhibitors employing the SVET and dual potentiometric/amperometric operation in SECM. To this end, the authors investigated the cathodic inhibition by BTA of the galvanic corrosion of copper coupled to iron. The results revealed that the inhibitor layer formed on the Cu surface shifted the cathodic sites to the less noble iron surface, originally the anodic site, making Cu electrochemically inactive. The literature also reports research on localized corrosion processes on other galvanic couple systems such as zinc coupled with iron [182], [183].

5.2 Experimental

5.2.1 Materials, substrate preparation and chemicals

A simple model consisting of an aluminium/copper (Al/Cu) couple was used to study the interaction between the inhibitors and the matrix and Cu-rich intermetallic particles. Fig. 5.1 illustrates the working electrode prepared from pure metals Al (99.0%) and Cu (99.9%) purchased from Goodfellow. The diameter of the Al disc was 14 mm. In its centre, a hole with a diameter of 5 mm was drilled, in which the copper disc was mechanically inserted. The assembly of the two metals gave a perfectly joined interface, avoiding crevice corrosion and surface defects.

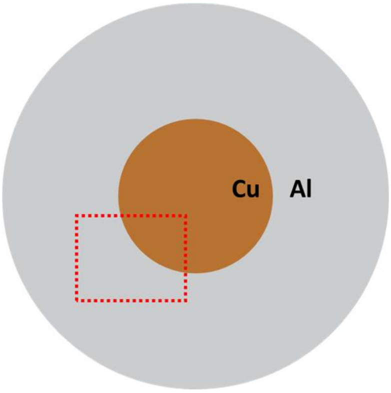

Figure 5.1: Scheme of Al/Cu galvanic couple model. The red rectangle approximates the scanning area.

Once prepared, Al/Cu sample (physically connected) (Fig. 5.2a) was mounted into an insulating Epofix (Struers, Ballerup, Denmark) resin sleeve. In addition, another type of Al-Cu sample was mounted in epoxy resin consisting of the Al and Cu discs physically separated (Fig. 5.2b). For the galvanic couple experiments, the two electrodes embedded in the resin could be connected electrically at the back of the mount. Before SVET and SECM measurements, these samples were ground in water with SiC paper up to 4000 grit. The resulting surfaces were subject to ultrasonic cleaning in absolute ethanol for 3 min, thoroughly rinsed with Millipore deionized water and dried with nitrogen gas.

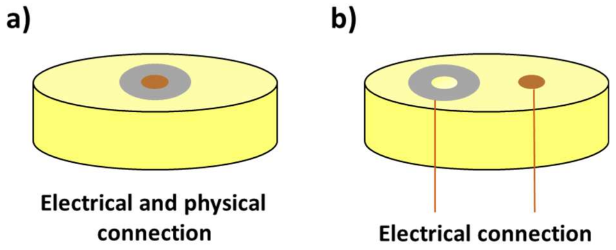

Figure 5.2. Scheme of mounted Al/Cu sample including (a) electrical and physical connection and (b) physical separation with the possibility to be electrically connected.

The electrochemical cell was built by glueing the cylindrical plastic body on top of the epoxy resin creating a small flat cell with an internal volume of approx. 4 mL. The sample was located at the bottom of the measuring cell, thus exposing the upper surface upwards to the test solution, as depicted in Fig. 5.3. In this case, the samples were allowed to be investigated using scanning electrochemical techniques in the same cell after electrolyte exchange. Chemicals have already been explained in *Chapter 2*, the *Experimental section*.

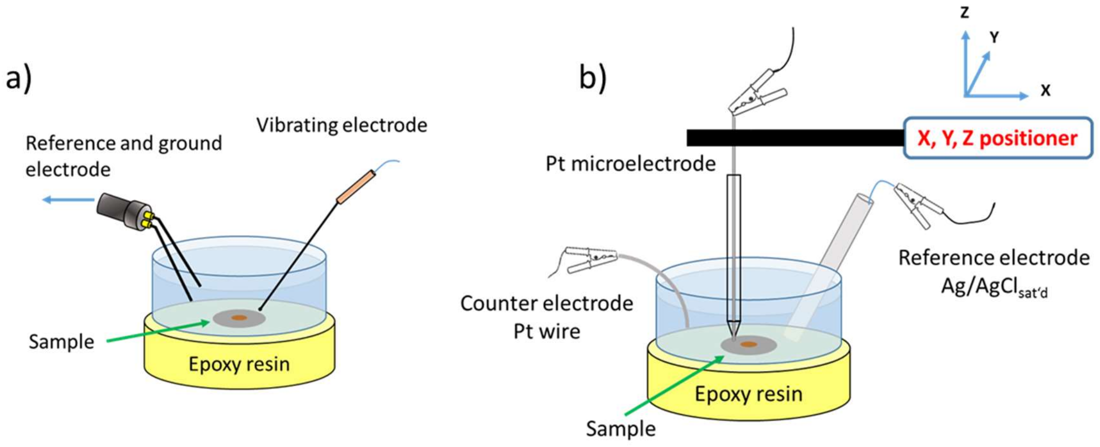

Figure 5.3: The scheme of electrochemical cell for (a) SVET and (b) SECM measurements.

5.2.2 SVET instrumentation and experimental procedure

The Scanning Vibrating Electrode Technique (SVET) was employed to detect local anodic and cathodic activities above the Al/Cu galvanic couple spontaneously corroding at the free corrosion potential. Electrochemical information is sensed by the SVET as small potential variations in solution, which are associated with the ionic fluxes due to the oxidation and reduction reactions occurring on the active surface [21], [182].

SVET experiments were carried out using a system manufactured by Applicable Electronics Inc. (Forestdale, MA, USA). The vibrating probe consisted of Pt/Ir (80%/20%) wires, insulated with the paralene C® except at the tip which was platinized to produce a spherical platinum black deposit at the tip with a diameter of 20 µm, which served as a sensor. Two Pt wires were employed as signal and reference electrodes. Mapping of electrochemical activity was performed in a constant height regime with a mean distance between the microelectrode and the sample surface of 100 µm, determined by a video-microscope. In addition to determining the tip-sample distance, video-camera was also employed to monitor the movement of the vibrating electrode over the sample during operation and record images of the substrate surface in real-time. The measurements were made with the electrode tip vibrating both normal and parallel to the sample embedded horizontally in the epoxy resin and facing upwards.

Microelectrochemical measurements were performed at room temperature under naturally aerated conditions in either 10 mM NaCl-containing 1mM MBI or OPA inhibitors or just 10 mM NaCl solution. Al/Cu pair samples (with Al and Cu metals physically connected) were used for all SVET measurements. *In-situ* measurements of the corrosion inhibition consisted of two stages: first, the measuring cell was filled with 1mM MBI or OPA + 10 mM NaCl solution (i.e., with an inhibitor reservoir) for 24 h, and then the solution was replaced by 10 mM NaCl (i.e., without inhibitor reservoir) for 12 h. The electrochemical activity was monitored throughout the immersion period. In addition, corrosion of a control sample (blank) was monitored in 10 mM NaCl for 12 h.

5.2.3 SECM instrumentation and experimental procedure

The SECM measurements were carried out with the CH900 scanning electrochemical microscope (CH Instruments, Austin, TX, USA). The system was placed inside a Faraday cage to prevent electrical and acoustic noise and mechanical vibrations. The electrochemical interface was a bipotentiostat; however, the system was operated in a three-electrode configuration where the Al/Cu couple sample was left unbiased (i.e., the samples were at their corresponding OCP) during measurements. A platinum microelectrode of a 10 µm-radius was used as the working electrode. The size of the SECM-tip defined the spatial resolution of the measurements. An Ag/AgCl, KCl (sat'd) and platinum wire were employed as reference and counter electrode, respectively, completing the electrochemical cell.

The distance between the tip and the substrate was determined by slowly approaching the surface and simultaneously recording the approach curve (i.e., recording the measured current at the microelectrode vs. Z displacement) in positive or negative feedback mode. For that purpose, ferrocene-methanol (Fc-MeOH, 0.5 mM) dissolved in the $NaClO_4$ (0.1 M) test electrolyte acted as an electrochemical mediator at the tip. To enable the oxidation of the ferrocene-methanol, the tip was kept at a constant potential of +0.50 V (Ag/AgCl), corresponding to the oxidation of Fe(II) to Fe(III). Fitting the measured negative feedback plot to the theoretical model, for which it was assumed that the reduction of the mediator at the surface was under kinetic control, helped determine the exact tip-sample distance. When recording the approach curve, the microelectrode stopped when the measured current was equal to 75% of the diffusion-limited current in the bulk of the electrolyte. Therefore, according to the fitting procedure, the microelectrode was placed 5 µm above the substrate. This value was considered the operating distance for SECM mapping without any additional retraction of the tip from the surface. Sufficiently high surface resolution is achieved by selecting significantly smaller areas for imaging and rastering the tip over the sample at heights equivalent to the one tip diameter or even less.

The tip potential was set at different values to investigate the local concentrations of the various species involved in the corrosion process. The effect of the negative feedback character is used to monitor the formation of insulating films on metal surfaces, thus revealing the effectiveness of corrosion inhibition. Experiments performed in the negative-feedback mode were carried out at +0.50 V using Fc-MeOH in solution as a mediator. In the case of an insulator, the proximity of the sample surface hindered the diffusion of the mediator to the measuring tip, resulting in a smaller current at the tip than in the bulk of the electrolyte.

Sample generation/tip collection (SG/TC) mode was used without a mediator where corroding aluminium releases H_2 molecules from the anodic sites (i.e., pits), which can be imaged directly on the Pt tip by selecting the appropriate potential value. Therefore, the microelectrode was polarized at 0.0 V (vs. Ag/AgCl) to image the currents corresponding to the oxidation of H_2 to H^+ ions.

On the other hand, SECM was also able to monitor the reduction of dissolved oxygen in the so-called redox-competition mode after the tip was kept at a constant potential of −0.70 V (vs. Ag/AgCl). In this mode, the sites which consume oxygen will compete for ORR with the polarized microelectrode, resulting in smaller currents being sensed at the tip. It should be emphasized that the current measured at the tip, which originates from the oxygen electroreduction, can also be directly correlated to the surface topography in the negative feedback mode.

All measurements were done by moving the tip in an XY plane parallel to the sample at a fixed distance, even though the tip also passed over a defective area, in which case the substrate surface was effectively at a greater distance from the tip. *In situ* images were acquired by moving the microelectrode in a raster-type motion. Line scans were acquired in the zig-zag scan direction (i.e., meander pattern) using a step/acquire scheme where the increment of X-line and Y-line was 5 µm and 25 µm, respectively. The scan rate was 30 µm s^{-1}. To ensure reproducibility of results, at least three parallels were imaged for each sample.

Two types of Al/Cu samples were used, with Al and Cu metals in physical contact or not. In the latter case, the separation between both metals was sufficient to avoid any eventual product formed on one metal to modify the local chemistry of the other. For these samples, the electrical coupling of the two metals was established at the back of the epoxy resin by connecting their corresponding wire contacts.

Inhibitory films were prepared *ex-situ* on the Al/Cu surface by pouring the chloride-containing inhibitor solution into the measuring cell, with the upper sample surface facing the electrolyte. During the immersion period, the tip was not in contact with the solution to avoid the potential interaction of inhibitor molecules with the Pt probe. The testing electrolyte was 0.5 mM FcMeOH + 0.1 M $NaClO_4$ for the negative feedback measurements and 50 mM NaCl for the measurements carried out in SG/TC and redox-competition mode.

5.3 Results and Discussion

5.3.1 Characterization of the galvanic coupling of aluminium and copper by SVET

5.3.1.1 Corrosion of Al/Cu in chloride solution

Fig. 5.4 shows the ionic current distributions for physically and electrically connected Al/Cu immersed in aerated 10 mM NaCl solution for different exposure times, i.e., 1 min, 6 h and 12 h, in the absence of an inhibitor. The observed positive currents are due to the flux of Al^{3+} ions released from the aluminium surface, according to (Eq. 1.1).

The anodic activity at the aluminium sample is not homogeneously distributed but is localised near the copper surface with extremely high currents, with a maximum current density of 320 µA cm^{-2}, which refers to the formation of pitting (Fig. 5.4a). This is not surprising because aluminium is known to be susceptible to localized corrosion attacks in the presence of Cl^-, which leads to the breakdown of the passive film [184]–[186].

Galvanic coupling of aluminium to copper leads to the removal of the cathodic reaction from aluminium to copper, where it is homogeneously distributed over the entire surface of the metal. Negative currents up to −52 µA cm^{-2}, measured over the copper surface, result from the flux of hydroxide ions generated by the reduction of dissolved oxygen and are responsible for alkalizing the electrolyte near the reactive site (Eq. 1.7).

It is interesting that the anodic behaviour was observed in the part of the cathodic region of Al/Cu (Figs. 5.4b and c), i.e., on the copper surface, which can be attributed to the fluxes of Al^{3+} cations departing from the aluminium surface as a result of dissolution reaction within the pits and their subsequent diffusion through the electrolyte.

Furthermore, the cathodic activity can be blocked or significantly reduced by the consumption of OH^- species in the coupled chemical reaction, such as metal ions precipitation, as depicted in the optical micrograph in Fig. 5.4b and c. The evolution of the electrochemical activity with the time of exposure in chloride solution can be monitored by reviewing successive ionic current maps, as shown in Fig. 5.4. It can be observed that local anodic sites tend to change location or disappear with immersion time. This can be explained by two assumptions: (i) repassivation of existing pits and initiation of new pits may occur (Figs. 5.4a and b, Fig. A.22a and b), and (ii) the surface may become progressively blocked by precipitation of corrosion products due to the close proximity of the cathodic region. The latter would result in the detection of smaller Al^{3+} ionic currents (Figs. 5.4b and c, Fig. A.22b). More corrosion products were deposited at the interface between Al and Cu metals after 12 h of immersion in chloride solution than in earlier stages of the corrosion process, i.e., after 1 min and 6 h of immersion (Fig. 5.4), which indicates corrosion progression over time.

Generally, pitting corrosion occurs in a series of consecutive steps [186]. After the nucleation stage, the pit can be repassivated immediately, or it can propagate further. The propagation of a corrosion pit requires the accumulation of an aggressive environment inside the pit, i.e., local saturation of aluminium chloride; otherwise, repassivation occurs. If the current is high enough and/or the site is sufficiently occluded (less open pit sites), the pit can grow for a more prolonged period, so-called metastable pit growth. Metastable pit propagates under a diffusion-controlled process. The electrode reaction in the mass transport limited region is assumed to be $Al(c) + 3Cl^- (aq) \longrightarrow AlCl_3(c) + 3e^-$, in which a layer of anhydrous $AlCl_3$ salt covers the metal [187]. Aluminium chloride dissolves at the salt/electrolyte interface, and aluminium ions are transported away.

The SVET is not effective in distinguishing pitting stages, but it provides valuable information on activation-passivation phenomena that occur on longer time scales, which can be seen from successive maps. The scanning electrochemical microscopy is more suitable for detecting nucleation and metastable stages due to the small distance between the tip and the hot spot on the substrate surface. To be correctly detected by SVET, a pit must remain active for a period greater than the time taken for an individual SVET scan (here ∼30 minutes). This implies that all the anodic pits visible in Fig. 5.4 are stable as metastable pitting events for AA2024-T3 are generally much less than 60 s [36]. Pit 1 seems to repassivate relatively quickly as it was not detected on the following scan obtained after 30 min of immersion (Fig. A.22a). Furthermore, we suggest that pits 2 and 3 in Fig. 5.4a propagate over time, which can be inferred from pits 2 and 3 in Fig. A.22a, b and in Fig. 5.4b, where the pit current densities and sizes are much higher than in Fig. 5.4a. In addition, a decay in the rate of stable pitting (the pits 2 and 3) with exposure time (after 12 h of immersion) was observed in Fig. 5.4c.

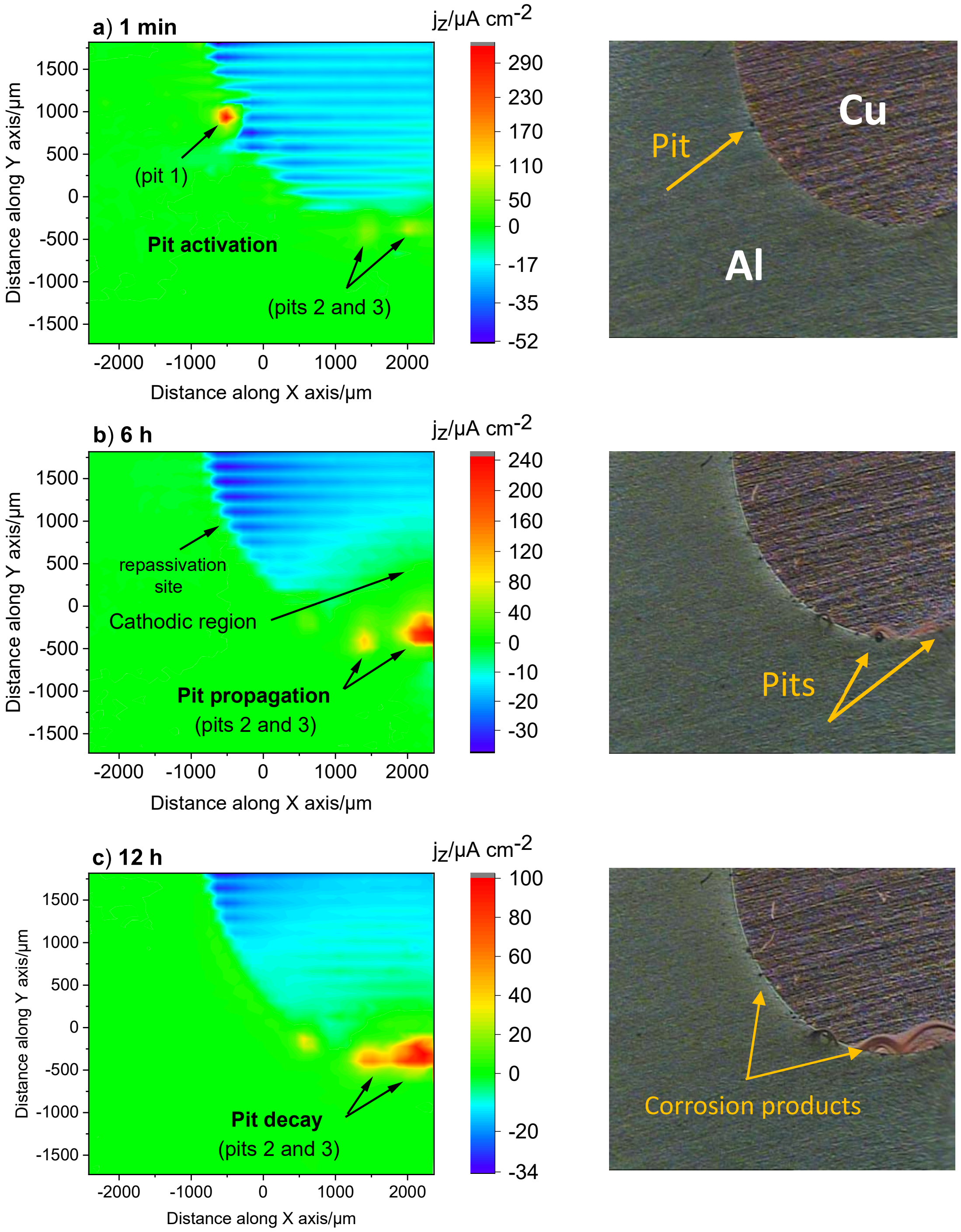

Figure 5.4: SVET maps (left) obtained for an aluminium-copper galvanic couple immersed in 10 mM NaCl with corresponding optical micrographs (right) taken just before the SVET measurements. The recording of the maps was initiated after: (a) 1 min , (b) 6 h and (c) 12 h immersion of the sample in the electrolyte solution.

Another characteristic of pitting corrosion is that the gas bubbles (Video 5) evolved from active corrosion sites (the pitting sites) at the Al-Cu interface, which can almost certainly be attributed to hydrogen evolution. As a consequence, pit current densities and sizes may be in error due to the underestimation of the true anodic pit current due to H_2 evolution inside the pits; $j_{\mathrm{net}} = j_{\mathrm{a}} - |j_{\mathrm{H_2}}|$. In the literature, it was reported that the true anodic pit current could be 16% larger than the measured anodic pit current [187], [188]. Interestingly, the cathodic reaction, such as the hydrogen evolution reaction (HER), takes place in the anodic region of the Al/Cu electrode where Al preferentially corrodes, i.e., within the pits. The H^+ reduction current is masked by the greater oxidation current of Al. That is the limitation of SVET.

For aluminium metal, having low oxidation potential, the cathodic reaction of hydrogen evolution is thermodynamically possible during free corrosion, but the rate might be controlled by the presence of protective or partially protective oxide/hydroxide film on the metal surface [189]. Surprisingly, many authors have reported hydrogen flows from hydrogen active corrosion sites, which increase during anodic polarization [188], [190], [191]. This observation is named „negative difference effect“ and can also be observed in the galvanic coupling with copper, which induces (mimics) the anodic polarization of bare aluminium. The phenomenon is elaborated on in more detail in the *SECM* section.

5.3.1.2 Corrosion of Al/Cu in chloride solution containing MBI inhibitor

The electrochemical activity of Al/Cu was significantly reduced when the copper surface was treated with an MBI inhibitor, as shown in the current density range in Figs. 5.5a and b. In the early stage of corrosion inhibition, i.e., after 1 min immersion in 1mM MBI + 10 mM NaCl solution (with inhibitor reservoir), both the anodic and cathodic reactions were suppressed, suggesting that the MBI inhibitor was instantly effective (Fig. 5.5a, Fig. A.23a). In addition, no pitting was observed, with the anodic currents being homogeneously distributed with values almost within the background noise. After 24 h immersion in a chloride solution containing MBI (Fig. 5.5b, Fig. A.23b), an additional decrease in the ionic current density range was observed, with an anodic maximum at 1.6 µA cm^{-2} and a cathodic maximum at -6 µA cm^{-2}, which is associated with the isolation of one metal from another metal due to the inhibitory effect of MBI on one or both metals. For copper, the MBI molecule has been shown to exhibit a high corrosion inhibition efficiency in near-neutral chloride solutions [9], [41], [45], [72], [73], [102], [135], [139], acting as a mixed type (anodic and cathodic) inhibitor with a stronger anodic effect, while the thiol group does not adsorb on Al surfaces [79]. Based on this, we believe that the copper surface was so effectively blocked by the thicker Cu-MBI that the cathodic reaction had to take place quantitatively on the aluminium surface along with the anodic sites (Fig. 5.5b).

Organic inhibitors provide limited protection *in-situ* and even less after the metal substrate is removed from the solution containing the inhibitor. Therefore, after 24 h of *in-situ* measurements in the MBI reservoir, the cell was rapidly washed with distilled water to remove traces of inhibitor and then filled with 10 mM NaCl solution to define effectiveness against corrosion in a chloride environment containing no MBI reservoir.

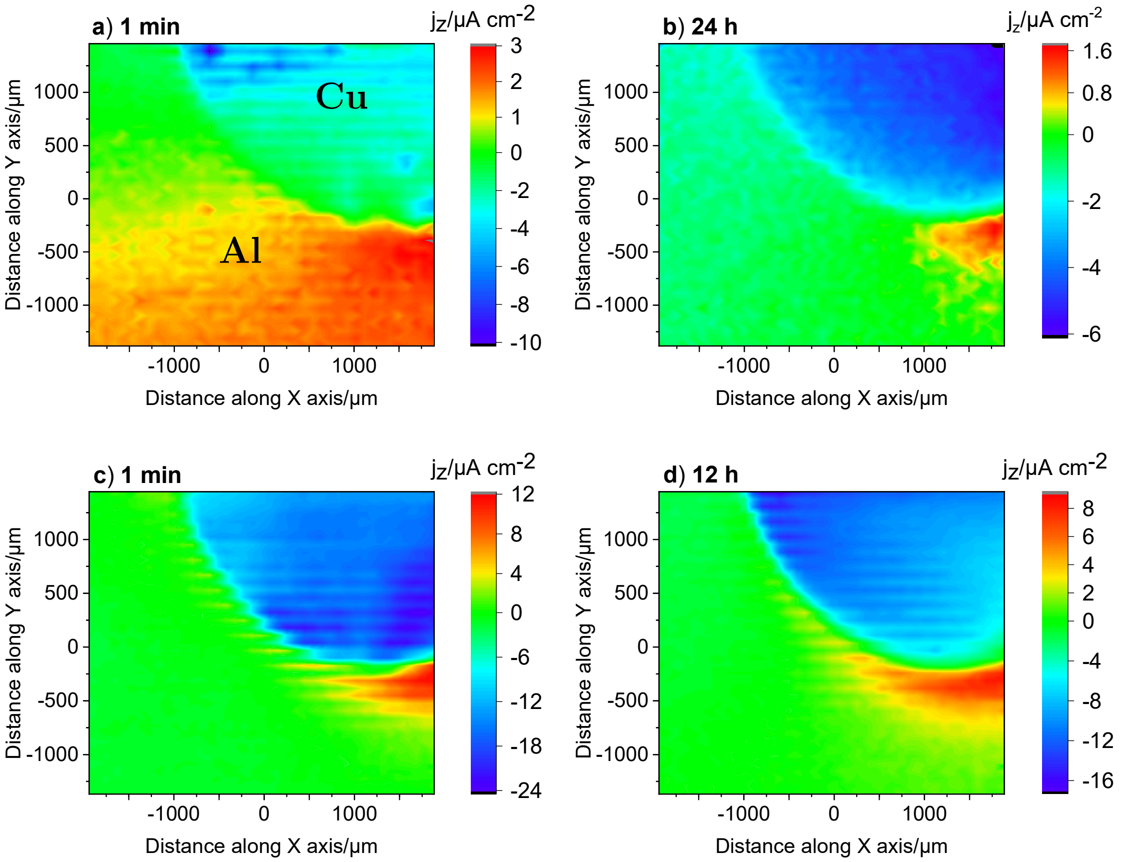

Figure 5.5: Ionic current mapping recorded above an aluminium-copper galvanic couple during immersion in 1mM MBI + 10 mM NaCl at selected exposure times: (a) 1 min and (b) 24 h. The inhibitor solution was then replaced with 10 mM NaCl, and the maps were taken after (c) 1 min and (d) 12 h immersion.

In the early stage of immersion in a chloride-containing solution, i.e., after 1 min of immersion (Fig. 5.5c, Fig. A.23c), the ionic current density range increased compared to the MBI-containing solution (Fig. 5.5b). However, the ionic currents were significantly lower than in the case of the blank sample (Fig. 5.5). With time exposure to the chloride solution, i.e., after 12 h of immersion (Fig. 5.5d, Fig. A.23d), the currents remained low, indicating moderate retention of inhibitory properties. It should be highlighted that no pit formation was observed even after 12 h immersion in 10 mM NaCl.

5.3.1.3 Corrosion of Al/Cu in chloride solution containing OPA inhibitor

When the Al/Cu pair was treated with OPA (Figs. 5.6a and b), the ionic current densities decreased, compared to the untreated sample (blank) (Fig. 5.4), but not as significantly as in the case of MBI treatment. First, after 1 min of immersion in 1mM OPA + 10 mM NaCl solution, the maximum current density range was between −34.6 µA cm^{-2} and 17.4 µA cm^{-2} (Figs. 5.6a, Fig. A.24a), then the anodic currents after 24 h immersion increased to 21.6 µA cm^{-2}, but without traces of pitting, while the cathodic currents slightly increased to −25 µA cm^{-2} (Figs. 5.6b, Fig. A.24b). Such fairly large cathodic current densities, compared to MBI treatment, can be explained because OPA does not possess inhibitory properties against Cu corrosion [45] but is instead recognized as a satisfactory inhibitor for

Al [79], [81], [84], [91]. This is reflected in the fact that no pitting of Al was observed, although significant anodic currents were recorded at the Al side of the Al-Cu interface.

Figs. 5.6c and d show the distribution of ionic current density recorded on the Al/Cu sample after replacing the OPA solution (inhibitor reservoir) with 10 mM NaCl (without inhibitor reservoir), as in the case of MBI experiments. After 1 min of immersion (Fig. 5.6c, Fig. A.24c), the range of ionic current densities increased significantly compared to the OPA-containing solution (Fig. 5.6b), while the cathodic currents were comparable to the untreated sample (blank) (Fig. 5.4).

It is interesting to note that the ionic current density range decreased significantly after 12 h of immersion in 10 mM NaCl (Fig. 5.6d, Fig. A.24d), with currents even smaller than those observed after 24 h of immersion in OPA reservoir solution (Fig. 5.6b). Currently, the deposition of corrosion products as a possible reason cannot explain such a result. The obtained results suggest that the MBI is a much more effective inhibitor in reducing Al/Cu corrosion than OPA. Theoretically, the galvanic corrosion should be limited by the cathodic reaction (ORR) that takes place on the copper surface [182]. The MBI met these expectations, promising for potential application on a more complex system such as aluminium alloy 2024.

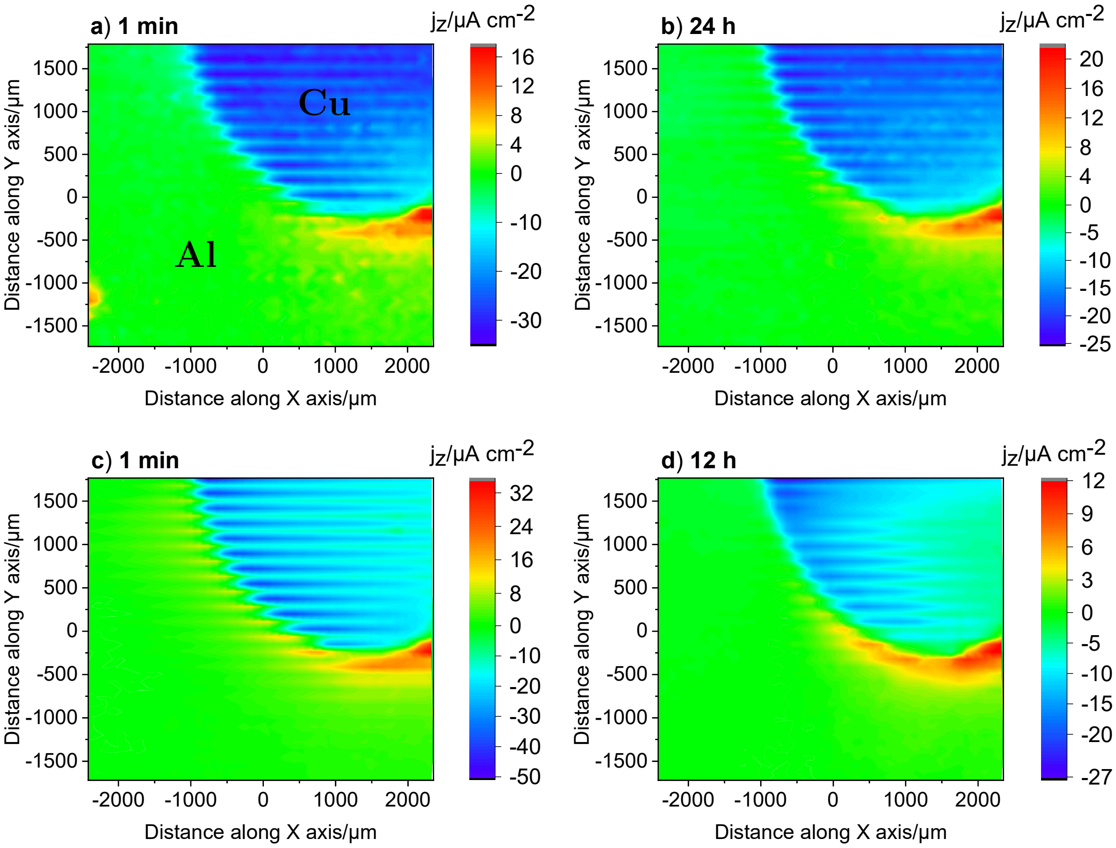

Figure 5.6: Ionic current mapping recorded above an aluminium-copper galvanic couple during immersion in 1mM OPA + 10 mM NaCl at selected exposure times: (a) 1 min and (b) 24 h. The inhibitor solution was then replaced with 10 mM NaCl, and the maps were taken after (c) 1 min and (d) 12 h immersion.

5.3.2 Characterization of the galvanic coupling of aluminium and copper by SECM

SECM is a microelectrode technique that is very attractive because it combines high spatial and electrochemical resolution [18]–[20], [192], [193] and therefore offers insights that are not possible with other methods, such as SVET.

5.3.2.1 Characterization of the ultramicroelectrode (UME) and estimation of the tip-substrate distance

The diffusion steady-state current density is governed by the mass transfer of R (i.e., reduced species) in solution to the probe (as given by the Cotrell equation, Eq. 5.1), i.e., it is related to the bulk concentration of the electroactive species, but also the thickness of the diffusion layer [192].

$$i_{\mathrm{T},\infty} = 4nFDca \tag{5.1}$$

where n is the number of electrons passed per reactant, F is Faraday's constant, D is the diffusion coefficient, c is the concentration of the reactant in solution, and a is the radius of the microelectrode.

The cyclic voltammogram of Pt microelectrode with a diameter of 10 µm (Fig. 5.7a) at a scan rate of 10 mV s^{-1} depicts the electrochemical reactions associated with the 0.5 mM ferrocene-methanol (FcMeOH or shortly Fc) mediator + 0.1 M $NaClO_4$ electrolyte. A single voltammetric wave was observed at potentials more positive than 0.20 V, which corresponds to the oxidation of ferrocene (Fc) to ferrocinium (Fc^+), i.e., Fe(II)/Fe(III) electrode reaction. From the inspection of the S-shaped curve, it was decided to set the microelectrode at a potential equal to +0.50 V, at which the oxidation of the mediator is the diffusion-limited process.

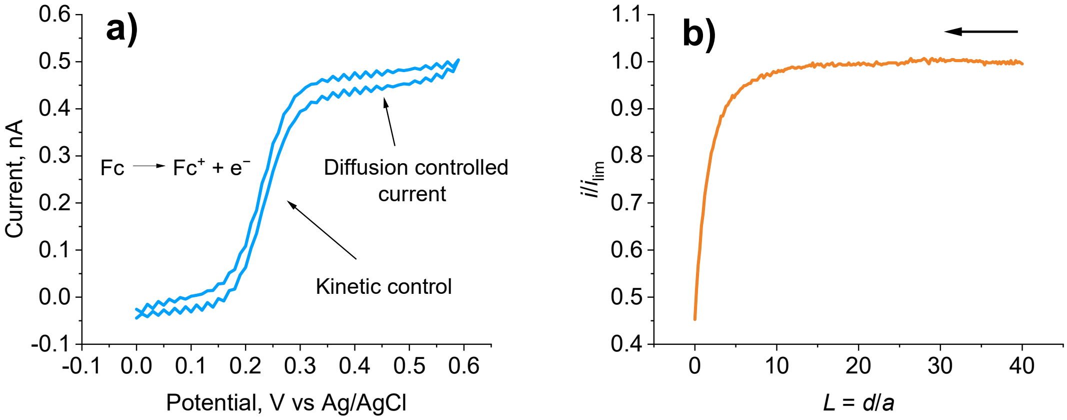

Figure 5.7: a) Cyclic voltammogram of a Pt microelectrode in 0.5 mM ferrocene-methanol (with 0.1 M $NaClO_4$) solution. Ferrocene-methanol (FcMeOH) undergoes oxidation above 0.2 V to form the ferrocenium ion (Fc^+). b) Approach curve measured at the SECM-tip at +0.50 V in 0.5 mM FcMeOH + 0.1 M $NaClO_4$ and performed on the resin surface to get the characteristic negative feedback effect. This curve is given in dimensionless form by plotting $I_T = i_T/i_{T,\infty}$ (the tip current normalized by the current far from the substrate) vs. $L = d/a$ (the tip–substrate separation normalized by the tip radius). The arrow indicates the direction of movement of the microelectrode.

In the same manner, the oxidation of Fc at the microelectrode can be used to deduce the position of the sample (along the Z axis) from the Pt tip. To this end, the polarized Pt tip is simultaneously approached (moved along Z direction) towards the surface (Fig. 5.7b).

After the Pt tip reaches very close to the sample surface, the diffusion of the Fc is hindered, and the currents recorded by the tip will vary significantly from the steady diffusion limited-current, depending on whether the sample is an insulator or a conductor. When the substrate is conductive, the oxidized form O (Fc^+), formed at the tip, can be reduced (i.e., regenerated) at the substrate, producing R (Fc), which diffuses back to the tip. Consequently, i_T becomes higher than when the tip is far ($d \longrightarrow \infty$) from the substrate, i.e, $i_T > i_{T,\infty}$. The smaller d, the larger the "feedback" component of the current. This increase in current is called positive feedback (Fig. 5.8) [18], [19], [192]. On the other hand, in the case of an insulator, the diffusion of O (Fc^+) to the tip will be partially blocked, and therefore the smaller feedback currents will be measured as the tip approaches the substrate (i.e., negative feedback) (Fig. 5.8). Thus, the ratio $i_T/i_{T,\infty}$ is a measure of the distance, d, between tip and substrate and an indicator of the nature (insulating or conductive) of the sample. To prevent the tip from touching the surface, the approach curve was controlled by stopping the microelectrode when the measured current was reduced to 50% of the limiting current in the bulk electrolyte. In this way, the electrode is located in the immediate vicinity of the sample. After the distance between the tip and the substrate is set to about 5 µm, all remaining experiments were performed by maintaining the constant Z-position, including rastering the Al/Cu sample along the X and Y axes to obtain maps of the surface.

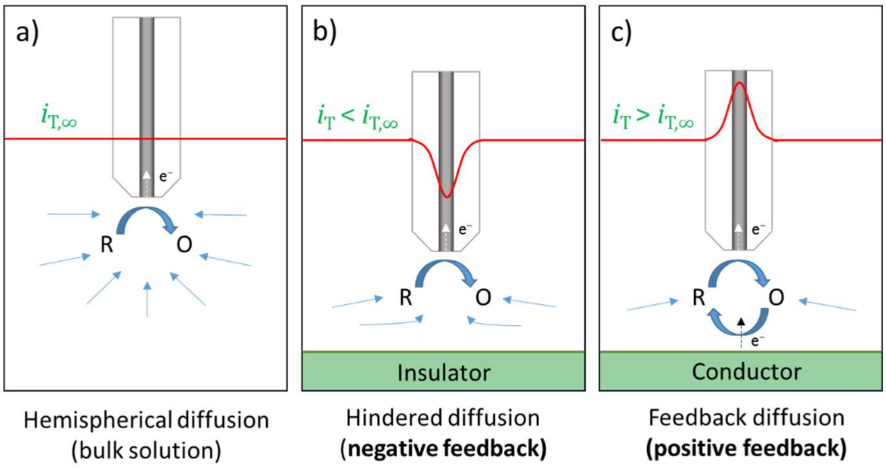

Figure 5.8: Basic principles of scanning electrochemical microscopy (SECM): (a) far from the substrate, diffusion leads to a steady-state current, $i_{T,\infty}$; (b) near an insulating substrate, hindered diffusion leads to $i_T < i_{T,\infty}$; (c) near a conductive substrate, feedback diffusion leads to $i_T > i_{T,\infty}$.

5.3.2.2 Corrosion phenomena on Al/Cu substrate

In-situ electrochemical reactivity of the Al/Cu surface in 50 mM NaCl solution at free corrosion potential was investigated by SECM under amperometric operation.

First, SECM was employed in substrate generation-tip collection (SG/TC) mode to image cathodic sites on the Al surface galvanically and physically coupled with copper, wherein the platinum (Pt) tip oxidizes H_2 evolving from the specimen surface after the tip was biased at 0.0 V (Fig. 5.9a). The corresponding SECM map (Fig. 5.10a) shows the local concentrations of hydrogen gas over Al metal characterized by high-current transients (with a current maximum of 0.43 nA) associated with electrochemical activity at the Pt tip, i.e., the oxidation of hydrogen gas. This is direct evidence of pitting corrosion of Al, which is believed to be caused by the presence of depassivating medium (chloride) that induces local rupture of the oxide film [184]–[186]. It is interesting to note the existence of „extended current signals“ belonging to the detection of hydrogen, which is due to the movement of electrolyte during rastering by the tip. To avoid such an effect, line scans should be performed at slower scan rates at the expense of longer scan times, but this choice depends on which information is of the utmost importance to us.

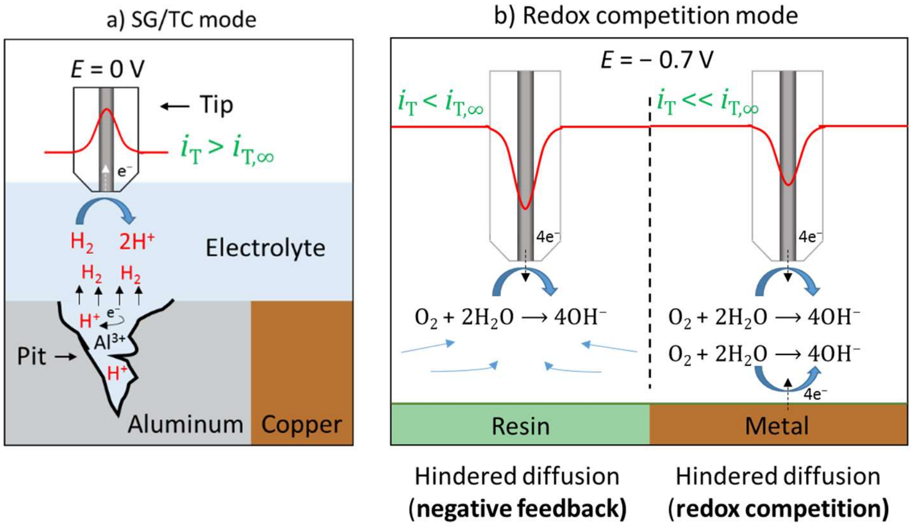

Figure 5.9: The different modes of SECM operation employed in this work: (a) amperometric substrate generation-tip collection (SG/TC) for the detection of hydrogen evolution using Pt probe and (b) redox-competition, which is based on the competition between the metal and the Pt tip for the electroreduction of dissolved oxygen in solution.

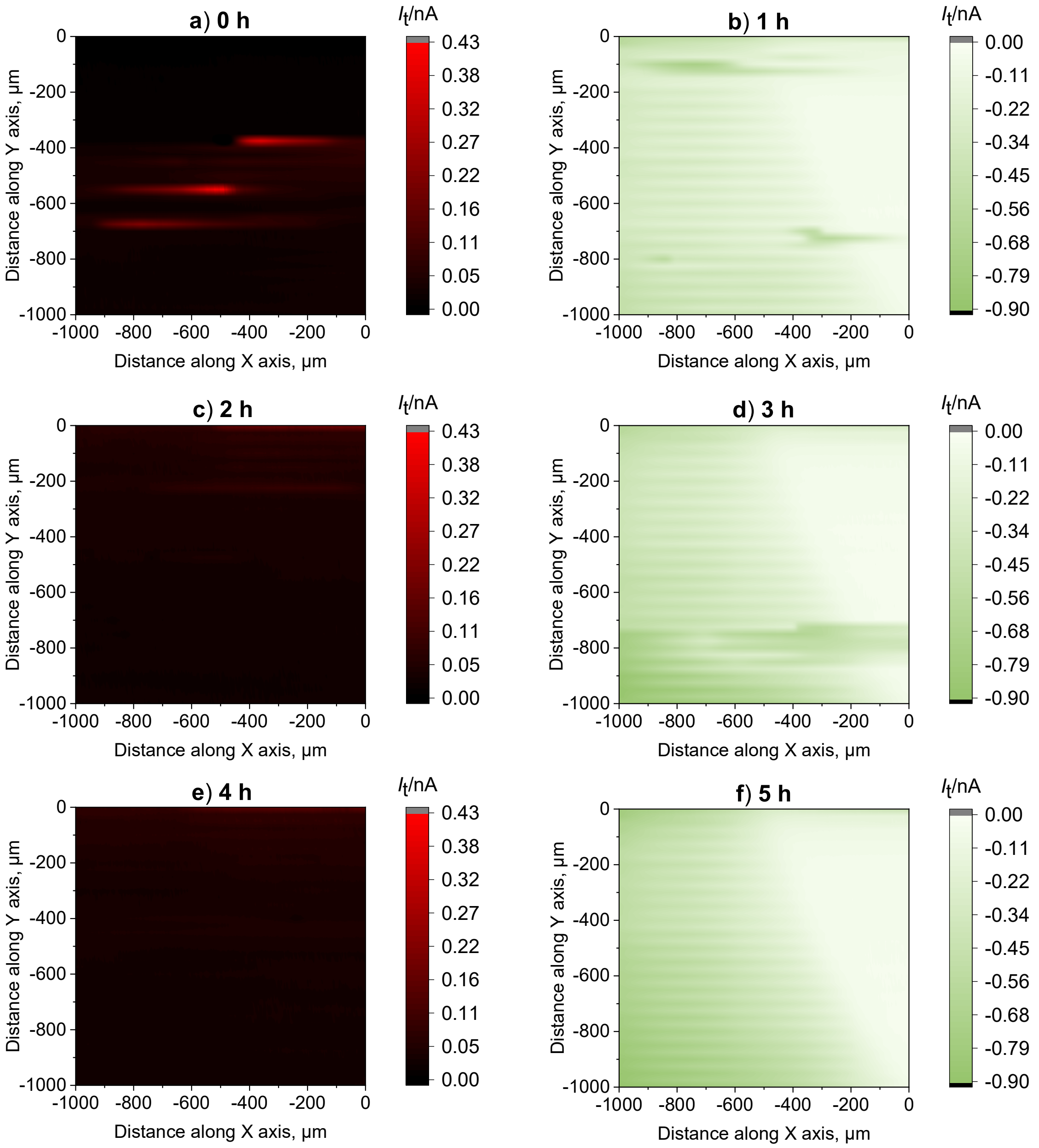

Figure 5.10: Consecutive maps of physically and electrically coupled Al/Cu sample obtained alternately by two different SECM modes in 50 mM NaCl solution during 5 h of immersion at open-circuit potential (OCP). The images were recorded in substrate generation-tip collection (SG/TC) mode at tip potential of 0.0 V vs. Ag/AgCl, KCl (sat'd) after a) 0 h, c) 2 h, and e) 4 h of immersion, and in redox-competition mode at tip polarized to −0.7 V vs. Ag/AgCl, KCl (sat'd) after b) 1 h, 3 h and 5 h of immersion. Tip diameter: 10 µm. Tip substrate distance: 5 µm. Scanned area: 1000 µm × 1000 µm. Scan rate: 30 µm s^{-1}. The scales are adjusted to make the measurements directly comparable based on their colour intensity.

After hydrogen detection, another cathodic reaction, reduction of dissolved oxygen in solution, was also monitored over the Al/Cu sample in the same solution used in the previous measurement. To this end, the redox-competition (RC) measurements, in which the Pt tip and the sample compete for reactions with the same analyte (O_2 in this case), were performed at a tip-potential of −0.70 V, corresponding to the oxygen consumed in the reaction (Eq. 1.7) (Fig. 5.9b). The SECM map, obtained after 1 h of immersion in 50 mM NaCl solution (Fig. 5.10b), shows two distinct regions. Very low current values (closer to zero) were homogeneously distributed over copper metal as expected in the Al/Cu galvanic system, where copper represents the cathodic site. Oxygen consumption occurs at the Cu surface, and therefore less oxygen is available for electroreduction at the tip. Although the two regions need to differ, there is no distinctly clear boundary and the difference between them. This can be attributed to the Al/Cu sample in which the two metals are physically connected, allowing electrochemical reactions to intertwine within the electrolyte resulting in interference at the tip. In addition, the movement of the electrolyte, which is the result of the rastering by the tip, contributes to the extended current signals and thus to additional interference.

Scanning was continued consecutively, so SG/TC mode was applied after 2 h (Fig. 5.10c) and 4 h (Fig. 5.10e) immersion, and redox-competition mode after 3 h (Fig. 5.10d) and 5 h (Fig. 5.10f) immersion. Successive current maps for hydrogen detection showed a very small stationary tip current as they scanned the entire Al/Cu surface without evidence of pitting corrosion. This means that the pits have been repassivated over time, as demonstrated by SVET. On the other hand, successive current maps for oxygen reduction revealed that the currents measured above copper after 5 h of immersion approached zero, attributed to prolonged corrosion, i.e., the cathodic oxygen consumption by copper. Also, it is important to note that the boundary between the two metals became more evident with the immersion time.

5.3.2.3 Possibilities and limitations

In one set of experiments, during the measurements performed in redox-competition mode (Fig. 5.11a), some interesting characteristics were observed. Namely, after 1 min of immersion, homogeneously distributed low currents (values close to zero) were detected on most of the Al/Cu surface, which is quite correlated with the observation reported in Fig. 5.10b. But also, some 'hot spots' were discovered that were tempting to relate to certain electrochemical activity on the surface. They may have their origin in the reduction of local cathodic activity, or they may indicate the topographic information concerning the evolution of a corroding Al surface.

For aluminium, it is known in the literature [188], [189], [194]–[196] that the rate of hydrogen evolution increases during anodic polarization (by external circuit), although it is contrary to what electrochemical theory would predict. This phenomenon is called „negative difference effect“ or „superfluous“ hydrogen evolution. The same scenario was observed during free corrosion by galvanic coupling with copper (cathodically active region), mimicking the effect of intermetallics. Therefore, it is assumed that there is a possibility that the observed current signals can be attributed to artefacts due to the superfluous hydrogen evolution, although this has not been observed in previous experiments, as shown in Fig. 5.10.

For this purpose, after mapping in RC mode (Fig. 5.11a), a consecutive mapping was performed, but this time in SG/TC mode, where H_2 oxidation currents are detected by the Pt tip. It was not trivial to find the superfluous hydrogen hot spots on a relatively small scanning area of Al using SECM. However, the corresponding SECM profile (Fig. 5.11b) shows the hydrogen streams from the active corrosion sites, with faradaic currents up to 2 nA. Furthermore, it was also observed that some signals originating from electroreduction of O_2 and oxidation of H_2 almost overlap, as shown in Figs. 5.11c and d (extracted insert from Figs. 5.11a and b, respectively).

However, it should be emphasized that this is not the actual appearance of the signals as they are constructed here in an image with a ratio of 50 µm × 1000 µm. The actual image size is shown in Fig. A.25 and Fig. A.26 where the signals are quite elongated. To determine whether the 'hot spot' represents a decrease in local cathodic activity, the existence of an attacked site, or an artefact, the first three line scans that originally interpolated to form an SECM image (Figs. 5.11c) were extracted as shown in Fig. 5.11e. All these line scans show noise-like fluctuations; however, the line scan recorded at $y = 25$ µm (Fig. 5.11e) shows a current transient extending over 200 µm, i.e., from 600 to 800 µm at a distance along X-axis, which is correlated with initial and maximum current corresponding to H_2 oxidation (Fig. 5.11f, line scan at $y = 25$ µm). This may indicate that the SECM in redox competition mode can topographically record pit(s) or attacked site(s) above the Al surface. To confirm this, other advanced modes and techniques, such as shear-force SECM and AFM-SECM [197], could separate the effect of surface topography from surface reactivity.

At this stage, it could be discussed why all the signals from the RC mode (Fig. 5.11a) do not overlap with the signals obtained in SG/TC mode (Fig. 5.11b).

This could be partially rationalized based on several facts: the nature of pitting is metastable (the time difference between the consecutive scans is 1 h) and convection is not completely neglected due to insufficiently slow rastering but also due to the formation of H_2 bubbles on the surface which pushes the electrolyte away in a radial direction. Therefore, the microelectrode may be blocked (partially isolated) by growing or rapidly evolving H_2 bubbles from the active sites, resulting in reduced metal activity (false signal). However, the presented finding remains an open question. It is important to note that H^+ released into the electrolyte during H_2 oxidation at the Pt tip can significantly contribute to local acidification in the vicinity of the Al surface and thus increase its dissolution.

To draw some conclusions so far, it is not a good strategy to use an Al/Cu sample in which Al and Cu are in physical contact; therefore, in the rest of the experiments, the two metals are separated.

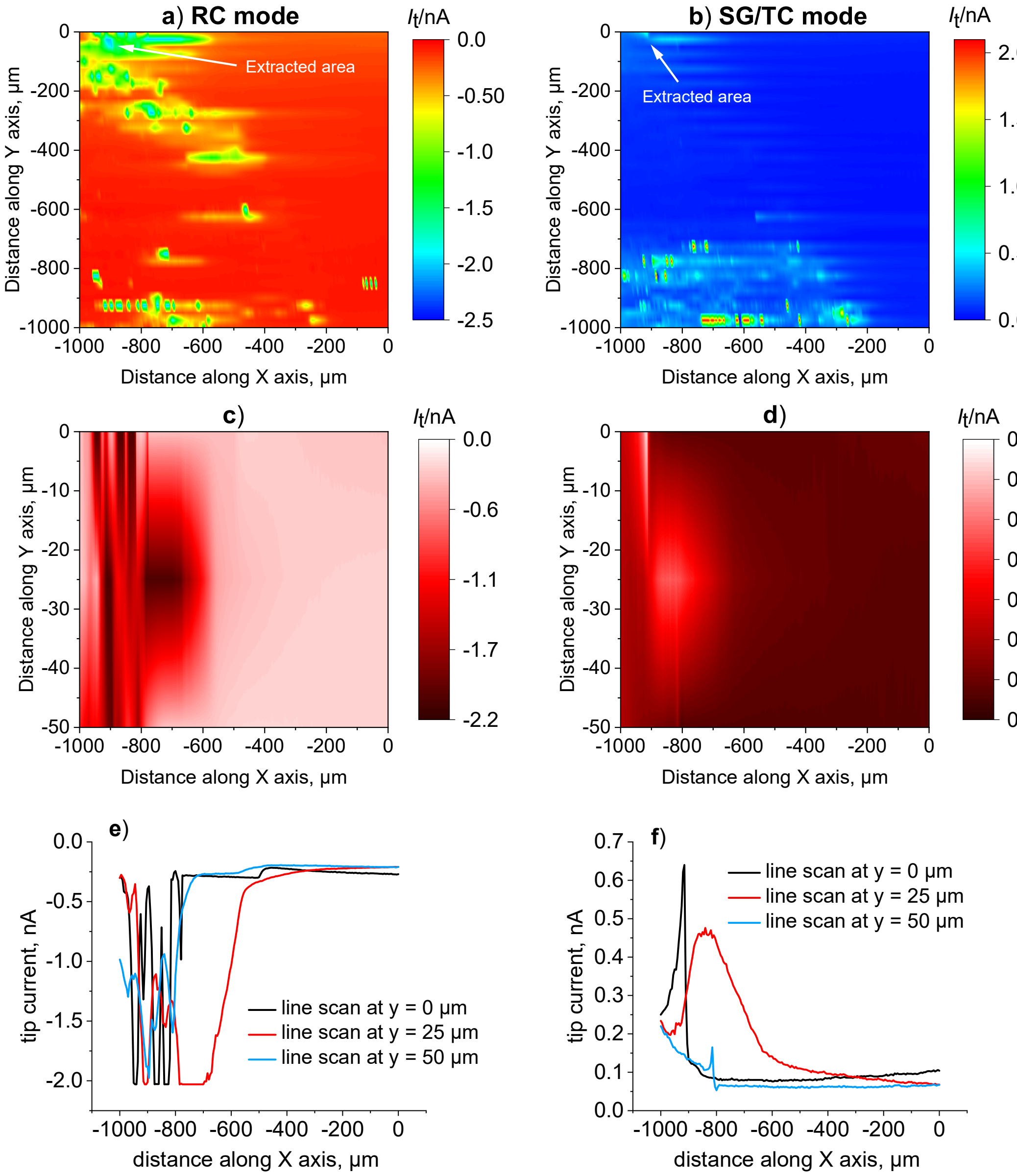

Figure 5.11: Images of physically and electrically coupled Al/Cu sample generated by SECM in a) redox competition mode after 1 min of immersion and b) SG/TC mode after 33 min of immersion in 50 mM NaCl solution at OCP. Images c) and d) represent the extracted insets from maps a) and b), respectively. Tip diameter: 10 µm. Tip substrate distance: 5 µm. Scan rate: 30 µm/s. Increment of X-line: 5 µm. Increment of Y-line: 25 µm. Graphs e) and f) represent the three line scans extracted from the interpolated images c) and d), respectively.

5.3.2.4 The Pt tip blockage effect

It was observed during measurements in feedback modes above the copper surface, using ferrocene-methanol as a redox mediator biased at +0.5 V, that the Pt tip gets blocked when the Cu is coupled with Al. This effect is shown in Fig. 5.12, which presents four consecutive images. The first image consists of rastering by Pt tip above Cu/resin surface that is not electrically connected to Al (Fig. 5.12a). The black and red areas of the image correspond to resin and Cu, respectively. Large currents above the Cu surface are attributed to the regeneration of the mediator above the conductor. When Cu was electrically coupled with Al (Image 2, Fig. 5.12b), faradaic currents after scanning were instantaneously lower than in the first image. Furthermore, after a few line scans, the currents in the image were almost zero, indicating that the tip was possibly blocked. To confirm the effect, another set of consecutive maps was made in which the metals were either isolated (image 3, Fig. 5.12c) or electrically connected (image 4, Fig. 5.12d). Similar to the first image, the detected currents in the third image were homogeneously distributed over the Cu surface, but the magnitude of the currents was very small, indicating that the Pt tip was already blind. When Cu and Al were reconnected, the same effect was observed as in the case of the second image, i.e., the tip was additionally blocked.

The explanation for the blockage of the Pt tip can lie in the Pourbaix diagram for platinum [40], from which it can be concluded that the platinum tip biased at 0.5 V oxidizes into $Pt(OH)_2$ at pH values above 7.5. When copper is coupled with aluminium, the cathodic reaction takes place exclusively on copper, with the rapid release of OH^- ions, which in turn leads to a significant increase in pH.

To avoid the evident Pt tip blockage effect, measurements should be performed above the Cu surface that is not electrically connected to Al. In this way, we will still be able to obtain information on the conductive/insulating properties of the copper surface. Another option is to use a redox mediator with an operating potential well below 0.5 V.

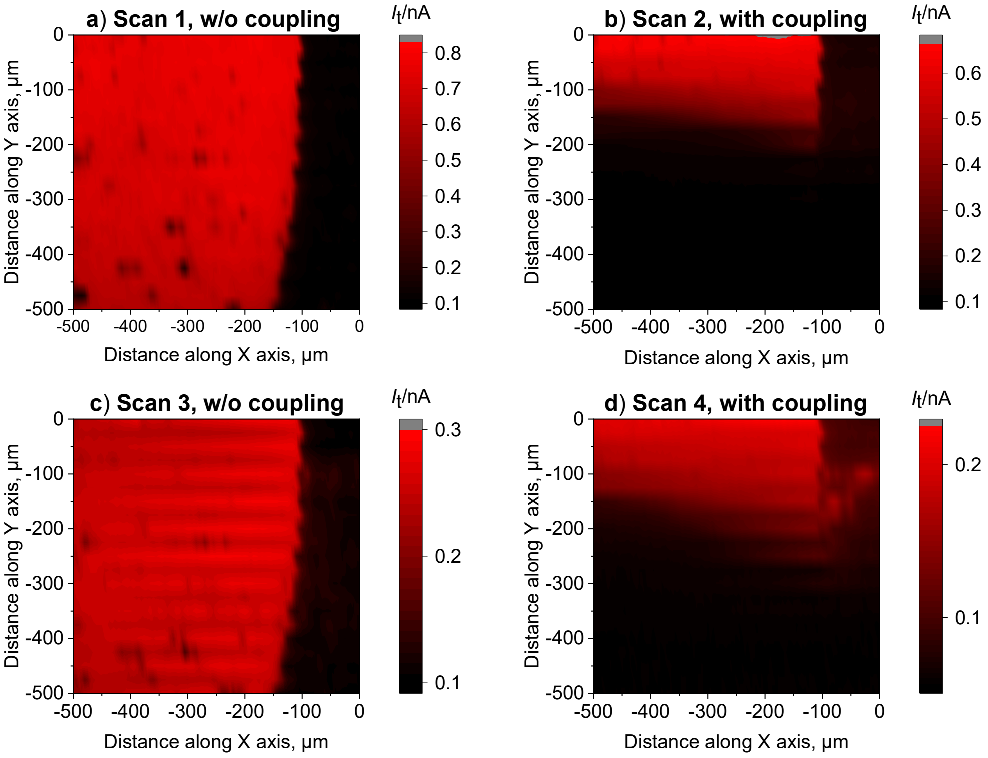

Figure 5.12: Consecutive SECM images, recorded in 0.5 mM FcMeOH + 0.1 M $NaClO_4$ solution under feedback operational mode, represent the Pt tip blockage effect. Tip potential: +0.50 V vs. Ag/AgCl, KCl (sat'd). Scanned surface: copper/resin. The copper was not in electrical contact with aluminium in a) scan 1 and c) scan 3, but the electrical contact between the two metals existed in b) scan 2 and d) scan 4.

5.3.2.5 The protection of Al/Cu surface by 2-mercaptobenzimidzole

In this set of experiments, physically separated aluminium and copper were mounted in epoxy resin with an electrical connection between the two metals. If necessary, the coupling between the metals could be removed. Before collecting spatial electrochemical micrographs by SECM, the approach curve measurement was performed, followed by determining the desired location on the metal/resin.

Fig. 5.13 shows three series of maps, each of which includes three different scans above Cu/resin with an area of 500 µm × 500 µm, recorded in feedback and redox-competition mode. Scans were performed for Cu samples previously treated with or without an MBI inhibitor. It was of primary interest to monitor the current profile only on the Cu surface because of its known interaction with MBI, which is not the case with Al.

In the first series of maps, i.e., for the Cu sample without prior MBI treatment, scan 1 (Fig. 5.13a) showed measurement in the imaging mode in the electrolyte solution consisting of FcMeOH + $NaClO_4$ (without the addition of corrosive chloride) to visualize the surface for feedback operation. During the scan, the Pt tip was held at +0.50 V to allow a redox reaction to occur at the tip operating under diffusion-limited conditions. In this measurement, Cu was not electrically coupled to Al due to the possibility of a Pt tip blockage effect, which is explained in the previous section. The observed high faradaic currents (i.e., the characteristic positive feedback effect) are associated with the regeneration of ferrocene-methanol species on a conductive copper substrate. Thereafter, the test solution inside the microcell was replaced with 50 mM NaCl, and the probe potential was set to −0.70 V, corresponding to the reduction of dissolved oxygen in the solution.

Low current values were detected above the bare copper surface (Fig. 5.13b), which can be correlated with a pronounced cathodic activity where oxygen consumption occurs; therefore, less oxygen is available for electroreduction at the tip. On the other hand, when Cu and Al were brought into electrical contact (Fig. 5.13c), the map obtained in the redox-competition mode showed higher electrochemical activity manifested by additional reduction of faradaic currents, compared to scan 2, where the two metals were isolated (Fig. 5.13b). Increased activity may be associated with galvanic coupling with Al, which has shifted the cathodic reaction to take place exclusively on the copper surface, where it is homogeneously distributed over the entire metal surface.

When scan 3 was completed, the electrical connection between the two metals was still maintained, and the Pt probe was removed from the solution along the Z direction. In this way, the possibility of interaction between the surface of Pt and the MBI molecules is removed, which could otherwise result in partial blockage of the sensing tip [28]. The previous solution was then replaced with 1 mM MBI + 50 mM NaCl so that Cu was immersed in the inhibitor solution for 2 hours.

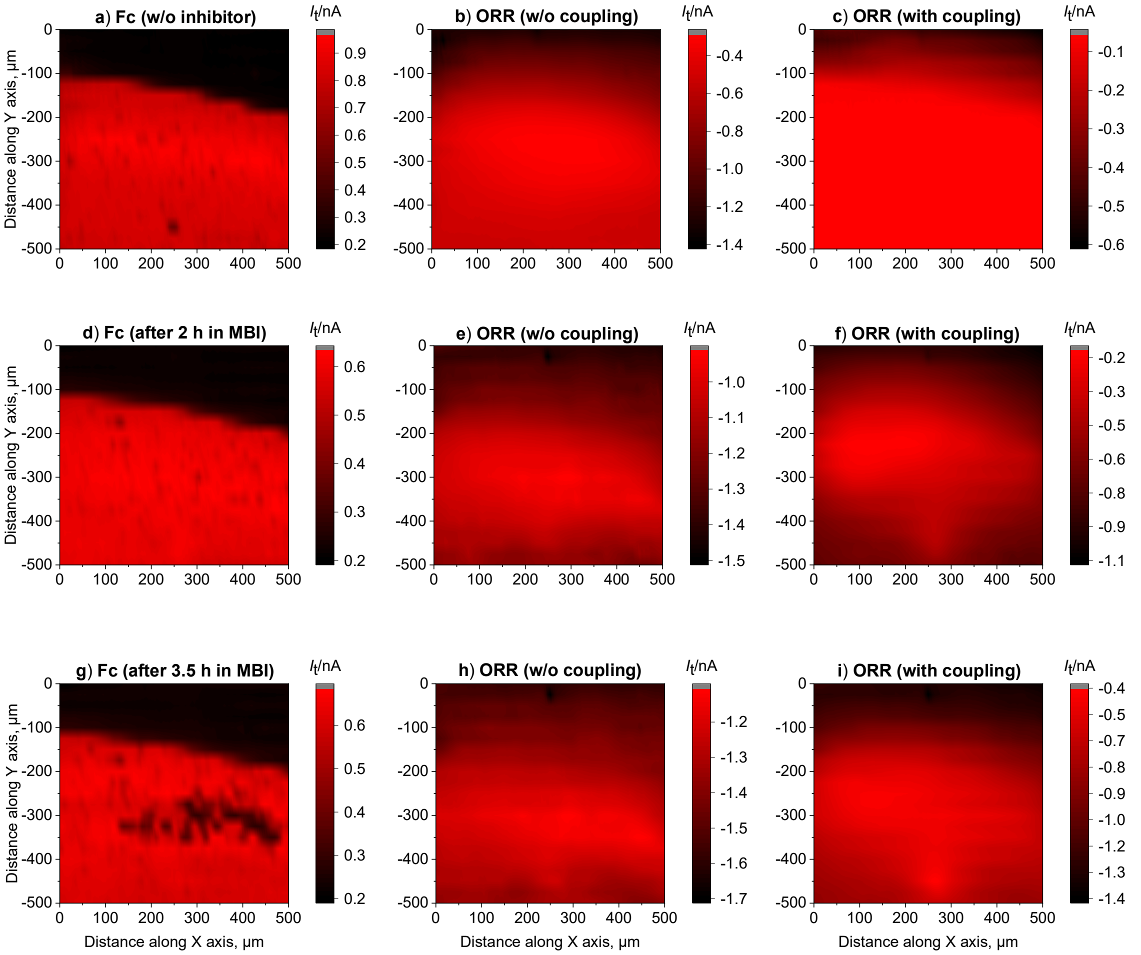

Figure 5.13: SECM images represent the three series of maps, each of which includes three different scans above Cu/resin (with and without electrical contact with Al), recorded in feedback and redox-competition mode. First, the Cu surface without pre-treatment with 2-mercaptobenzimidazole (MBI) was scanned a) in feedback mode, followed by scanning in redox-competition mode either with b) and without c) coupling to Al. Cu was then treated with a solution containing MBI for different immersion times, i.e., for d-f) 2 h and g-i) an additional 1.5 h so that the total immersion time was 3.5 h. After each treatment with MBI, measurements were performed in feedback and redox-competition mode as in the case of the blank, i.e., without prior treatment with an inhibitor. Scanned area of 500 µm × 500 µm. Tip potential and electrolyte solution: in the feedback mode +0.50 V 0.5 mM FcMeOH + 0.1 M $NaClO_4$ solution, and in the redox competition mode −0.7 V Ag/AgCl, KCl (sat'd) for 50 mM NaCl. The feedback mode was used to confirm the degree of adsorption of MBI on the Cu surface with immersion time, while the redox-competition mode revealed the stability of the inhibitory film in corrosive media, such as NaCl.

After the *ex-situ* immersion stage, the inhibitor solution was replaced with an electrolyte containing a mediator (namely, 0.5 mM FcMeOH + 0.1 M $NaClO_4$) and the Pt tip was moved along the *Z*-axis toward the surface until it reached the same position as in the previous measurements, i.e., all experiments were performed by maintaining a constant *Z* position. The microelectrode was biased at +0.50 V to allow scanning in feedback mode, and the electrical connection between Cu and Al was removed. Fig. 5.13d depicts the SECM image recorded for the Cu sample after 2 h immersion in a solution containing MBI. The detected faradaic currents over the Cu surface are less than in scan 1 (Fig. 5.13a), which is an indication that the Cu surface is covered by the MBI inhibitor. The extent of the positive feedback effect is reduced because the formed Cu-MBI film on the surface of the Cu sample hinders the regeneration of FcMeOH on the substrate due to the less-conductive substrate. After scan 4, the electrolyte solution was again replaced with 50 mM NaCl, and the probe potential was polarized at −0.70 V to monitor the cathodic activity measured at the tip through the redox-competition process. Fig. 5.13e shows the increase in faradaic currents, compared to scan 2 (Fig. 5.13b), measured when the tip passed over the Cu surface as a result of reduced competition between the tip and the Cu surface due to the existence of a protective Cu-MBI layer that effectively blocks the cathodic sites. However, when the electrical contact is established between Cu and Al, as depicted in scan 6 (Fig. 5.13f), the galvanic coupling makes copper exclusively a cathodic site where the redox competition effect is even more pronounced. This is reflected in the increased current range revealing that an inhibitory film effectively protects a large part of the metal surface.

After scan 6, the third series of maps was recorded that included additional treatment with the MBI inhibitor. To this end, while the electrical connection between the two metals was still present, the Pt probe was removed from the solution along the *Z* direction, and the electrolyte solution in the microcell from the previous experiment was replaced with 1 mM MBI + 50 mM NaCl. Cu was thus additionally immersed in the inhibitor solution for 1.5 hours, i.e., the total immersion time from the beginning of the experiment was 3.5 h. When *ex-situ* immersion was complete, the inhibitor solution was replaced with the 0.5 mM FcMeOH + 0.1 M $NaClO_4$ electrolyte solution, and the Pt tip was positioned back to constant height as in previous measurements. The microelectrode was then held at +0.50 V to allow scanning in feedback mode while the electrical connection between Cu and Al was removed. Fig. 5.13g displays the SECM map obtained for the Cu sample after 3.5 h of immersion in a solution containing MBI. There are some areas on the Cu surface where the regeneration of the redox mediator has been almost completely stopped, which can be attributed to improved insulating characteristics, i.e., improved inhibitory film thickness due to prolonged *ex-situ* exposure to MBI-containing solution. Despite a significant reduction in positive feedback (i.e., lower faradaic currents) for longer immersions (after 3.5 h), we believe that no negative feedback effect was observed. Finally, the electrolyte solution was replaced with 50 mM NaCl and the probe potential was polarized at −0.70 V to monitor the consumption of dissolved oxygen by copper protected by an inhibitory layer. Fig. 5.13h shows that higher currents, measured above the Cu surface, are associated with reduced affinity for cathodic oxygen consumption, i.e., redox competition between the tip and the copper surface is significantly impeded. When Cu was coupled to Al, the oxygen affinity on the copper surface increased, and consequently, the corresponding currents detected at the tip were lower. However, the reported currents were higher than in the case of scan 6, which implies that the Cu-MBI film was more resistant to corrosion after 3.5 h of *ex-situ* immersion. Measurements performed in redox competition mode are consistent with measurements in feedback mode.

5.3.2.6 The protection of Al/Cu surface by octylphosphonic acid

The set of experiments shown in Fig. 5.14 consists of a series of maps obtained for an aluminium substrate that includes galvanic coupling with copper or electrical insulation. The current profiles were monitored only on the Al surface because we showed in *Chapter 2* [45] that OPA is a good inhibitor for Al but not Cu. Measurements were performed on an aluminium/resin surface of 500 µm × 500 µm in three different operational arrangements, i.e., in feedback, substrate generation-tip collection (SG/TC) and redox-competition mode, with and without pre-treatment with an OPA inhibitor.

First, the surface of bare aluminium (which is not electrically connected to Cu) was evaluated by polarizing the Pt tip at +0.50 V in the feedback mode to monitor the redox reaction at the tip operating under diffusion-limited conditions (Fig. 5.14a). Variations in the measured faradaic currents are observed, i.e., higher currents are detected above the metallic surface, in contrast to the resin, due to the regeneration of the Fc mediator on the conductive surface. The ferrocene solution was then replaced with 50 mM NaCl electrolyte solution, and the tip was held at 0.0 V to measure the local concentration of hydrogen gas above the Al surface galvanically coupled to Cu, which is associated with hydrogen oxidation at the tip (Fig. 5.14b). The significant electrochemical activity was not observed in scan 2 because the measured currents did not exceed the current value of 0.15 nA, equating with the noise level. It is difficult to predict the location of pitting corrosion, especially on such a small surface as scanned here, because pitting is a stochastic phenomenon.

The tip was then polarized in the same electrolyte solution to −0.70 V to monitor the cathodic activity measured on the Pt probe through the redox-competition process (Fig. 5.14c). Since the cathodic reaction occurs exclusively on the copper surface when Al and Cu are in electrical contact, a decrease in tip currents due to redox competition was not observed when the microelectrode rastered above the aluminium surface.

After scan 3, the Pt probe was removed from the solution along the Z direction, and the electrolyte solution in the microcell from the previous experiment was replaced with 1 mM OPA + 50 mM NaCl. The Al surface electrically coupled to the copper was exposed to the inhibitor solution for 2 hours. After the *ex-situ* immersion was completed, the electrical connection between the metals was removed to reduce the potential risk of platinum tip contamination. The inhibitor solution was then replaced with 0.5 mM FcMeOH + 0.1 M $NaClO_4$, and the Pt tip was positioned back to constant height as in the previous measurements. After applying the potential of the tip at +0.5 V, the Al surface was scanned in feedback mode (Fig. 5.14d). Compared to scan 1 (Fig. 5.14a), the resulting reduced feedback currents indicate that OPA is adsorbed on the substrate surface. However, the currents are not homogeneously distributed over the entire surface of aluminium, which may be related to the lower efficiency of the octylphosphonic chain to form a dense inhibitory layer. It is well known that what determines the effective corrosion inhibition of organic molecules is their ability to form a dense organic film on the metal surface [75], [79].

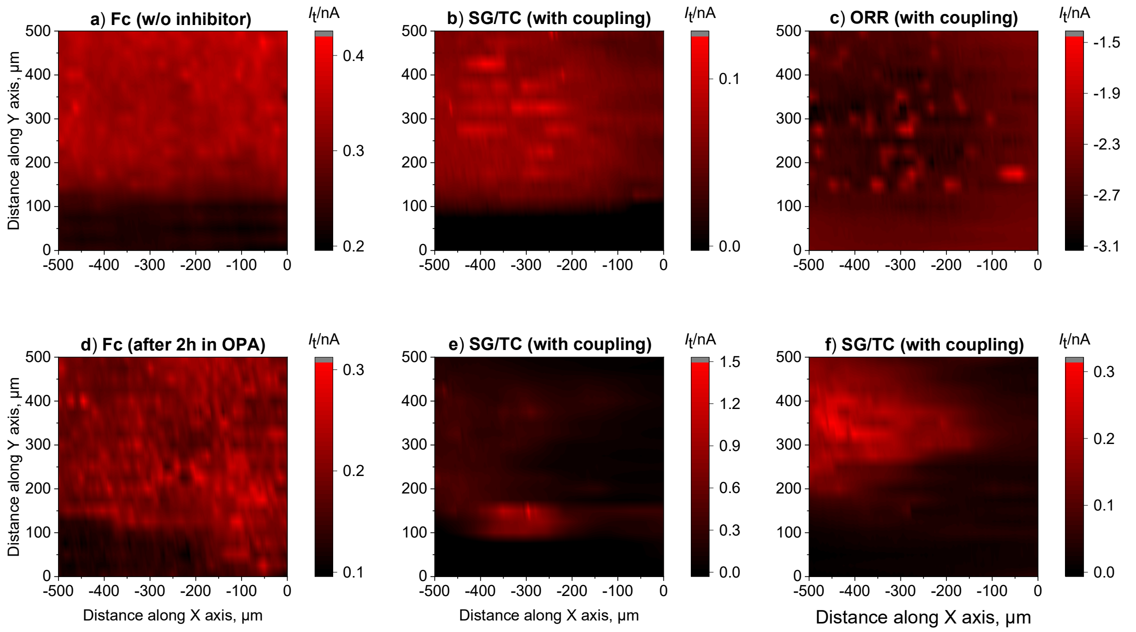

Figure 5.14: SECM images represent the two series of maps, each of which includes three different scans above Al/resin (with and without electrical contact with Cu), recorded in feedback, substrate generation-tip collection (SG/TC) and redox-competition mode. First, the Cu surface without pre-treatment with octylphosphonic acid (OPA) was scanned in a) feedback mode, followed by scanning in b) SG/TC and c) redox-competition mode under electrical connection with Cu. Al was then treated with a solution containing OPA for 2 h. After treatment with OPA, measurements were performed in d) feedback mode and then two consecutive maps, e) and f) were recorded using SG/TC mode.

The ferrocene solution was then replaced with 50 mM NaCl, and the tip was biased at 0.0 V to ensure the oxidation of hydrogen above the Al surface galvanically coupled to Cu (Fig. 5.14e). High faradaic currents (about 1.5 nA) were detected at several locations on the Al surface, which is associated with pitting corrosion. Likely, the OPA film does not provide sufficient barrier properties against the ingress of aggressive ions, such as chloride. Finally, another consecutive map (Fig. 5.14f) recorded in SG/TC mode revealed the repassivation of a metastable pit that existed in the previous scan and localized activity at another location. It is assumed that the maximum time difference between the detected metastable pit in scan 5 and the observed repassivation of that pit in scan 6 is about 9 minutes since the same amount of time is required to record one 500 µm × 500 µm map. It can be concluded that OPA is not a very effective inhibitor against localized corrosion attack on galvanically coupled Al/Cu.

5.4 Conclusions

The SVET was employed to study the evolution of the electrochemical activity of Al/Cu galvanic couple with the time of exposure in chloride solution with and without added MBI and OPA at free corrosion potential. The surface of the control sample (i.e., without inhibitor) was characterized by pitting, which propagated over time. However, the electrochemical activity of Al/Cu was significantly reduced when the copper surface was treated with an MBI inhibitor. After 24 h immersion in 1mM MBI + 10 mM NaCl solution (with inhibitor reservoir), both the anodic and cathodic reactions were significantly suppressed, which is associated with the isolation of copper metal from aluminium due to the inhibitory effect of MBI on copper. We believe that the thicker Cu-MBI so effectively blocked the copper surface that the cathodic reaction had to take place quantitatively on the aluminium surface along with the anodic sites. The effectiveness against corrosion in a chloride environment containing no MBI reservoir was also defined. To this end, after 12 h of immersion, the ionic current density range increased compared to the MBI-containing solution but was significantly lower than in the case of the control sample, indicating moderate retention of inhibitory properties. It should be highlighted that no pit formation was observed even after 12 h immersion in 10 mM NaCl. On the other hand, when the Al/Cu pair was treated with OPA, the ionic current densities decreased, compared to the control sample, but not as significantly as in the case of MBI treatment. In addition, in a chloride environment containing no OPA reservoir, the range of ionic current densities increased significantly compared to the OPA-containing solution, while the cathodic currents were comparable to the control sample.

The localized corrosion and corrosion inhibition behaviour was also investigated with SECM. First, the cathodic sites on the Al surface galvanically and physically coupled with copper were consecutively imaged in substrate generation-tip collection (SG/TC) and redox-competition (RC) modes in 50 mM NaCl at free corrosion potential. The corresponding SECM map showed that the local concentrations of hydrogen gas over Al metal characterized by high-current transients were associated with the pitting corrosion of Al. Also, it was shown that very low current values (close to zero) in RC mode were homogeneously distributed over copper metal as expected in the Al/Cu galvanic system, where copper represents the cathodic site for oxygen reduction. Although the two regions need to differ, there was no distinctly clear boundary between them. This was attributed to the Al/Cu sample in which the two metals were physically connected, allowing electrochemical reactions to intertwine within the electrolyte resulting in interference at the tip. In addition, the movement of the electrolyte, which is the result of the rastering by the tip, contributed to the extended current signals and thus to additional interference. Therefore, it is not a good strategy to use an Al/Cu sample in which Al and Cu are in physical contact.

In one set of experiments, it was also observed that some signals originating from electroreduction of O_2 and oxidation of H_2 almost overlap after a consecutive mapping was performed in 50 mM NaCl solution. To confirm this, first three line scans that originally interpolated to form an SECM image were extracted. The line scan recorded in redox-competition mode at $y = 25$ µm showed a current transient correlated with initial and maximum current corresponding to H_2 oxidation. This may indicate that the SECM in redox competition mode can topographically record pit(s) or attacked site(s) above the Al surface.

It was observed during measurements in feedback modes above the copper surface, using ferrocene-methanol as a redox mediator biased at +0.5 V, that the Pt tip gets blocked when the Cu is coupled with Al. This occurs because the cathodic reaction takes place exclusively on copper, with the rapid release of OH^- ions, which in turn leads to a significant increase in pH. This finding is in accordance with the Pourbaix diagram for platinum, where the platinum tip biased at 0.5 V oxidizes into $Pt(OH)_2$ at pH values above 7.5. To avoid the evident Pt tip blockage effect, measurements should be performed above the Cu surface that is not electrically connected to Al.

The protection of Al/Cu surface by MBI was explored with consecutive imaging in feedback and RC modes. In the first series of maps, i.e., the Cu sample without prior MBI treatment was imaged in the electrolyte solution consisting of FcMeOH + $NaClO_4$ (without the addition of corrosive chloride), where the Pt tip was held at +0.50 V to visualize the surface for feedback operation (control sample). In the feedback measurement, Cu was not electrically coupled to Al due to the possibility of a Pt tip blockage effect. Then, the map obtained in the redox-competition mode, by setting the probe potential to −0.70 V, showed higher electrochemical activity in 50 mM NaCl when the two metals were brought into electrical contact than when they were isolated due to the shift of the cathodic reaction that takes place exclusively on the copper surface.

After the *ex-situ* immersion stage in 1 mM MBI + 50 mM NaCl, the same consecutive mapping procedure was applied as for the control sample. Less feedback currents detected over the Cu surface than in the control sample indicate that the Cu surface is covered by the MBI inhibitor. In addition, the cathodic activity measured at the tip through the redox-competition process showed an increase in faradaic currents, compared to the control sample, as a result of reduced competition for oxygen reduction between the tip and the Cu surface due to the existence of a protective Cu-MBI layer that effectively blocks the cathodic sites.

The protection of Al/Cu surface by OPA was explored with consecutive imaging in feedback and SG/TC modes. After the *ex-situ* immersion stage in 1 mM OPA + 50 mM NaCl, the resulting reduced feedback currents, compared to the control sample, indicate that OPA was adsorbed on the substrate surface. However, the currents were not homogeneously distributed over the entire surface of aluminium, which may be related to the lower efficiency of the octylphosphonic chain to form a dense inhibitory layer. In addition, high faradaic currents were detected at several locations on the Al surface in SG/TC mode, which is associated with pitting corrosion. Likely, the OPA film does not provide sufficient barrier properties against the ingress of aggressive ions, such as chloride.

Chapter 6

Inhibition of Localised Corrosion of AA2024 Using 2-Mercaptobenzimidazole and Octylphosphonic Acid

6.1 Literature Review

Since the localized pitting corrosion initiates at the most dominant intermetallic inclusions such as S-phase (Al_2MgCu), suppression of S-phase dealloying and copper redistribution would be a reasonable approach to inhibit corrosion at localized sites. To this end, organic molecules with a preference to form insoluble complex compounds with the content from S-phase are promising candidates for highly effective inhibition. Some interesting studies are listed below.

Lamaka et al. [198] showed that the quinaldic acid, salicylaldoxime and 8-hydroxyquinoline (8-HQ) mitigate corrosion of AA2024 by forming a thin organic layer of insoluble complexes on the alloy surface, which is due to the suppression of dissolution of Mg, Al and Cu from the intermetallic particles. Marcelin and Pébère [124] investigated the 8-HQ + BTA mixture on Al/Cu couple and AA2024 by localized electrochemical impedance spectroscopy. The study reported that the corrosion inhibition effect of BTA was mainly limited to the copper-rich intermetallic particles, whereas 8-HQ acted on the Al matrix due to its chelating properties. González-García et al. [199] presented the experimental approach for monitoring the early stages of corrosion activity and subsequent healing mechanism offered by the release of silyl-ester into a coating defect on AA2024 substrate. The response originating from the dissolved oxygen reduction showed a transition from redox-competition at the tip (corrosion activity) to a negative-feedback behaviour (protected system) during immersion in NaCl solution.

Coelho et al. [122] explored the inhibitive effects of BTA and $CeCl_3$ on AA2024, individually and combined, in 0.05 M NaCl electrolytes, utilizing electrochemical impedance spectroscopy (EIS). From the analysis of the fitted parameters, it was suggested that there is a synergistic effect between the two inhibitors up to 14 days of immersion.

An interesting approach by Williams et al. [27], who used SVET to quantify the effect of a number of copper complexing/precipitation reagents on the kinetics of pitting corrosion affecting AA2024 immersed in 5% aqueous NaCl solution, should be noted. The results showed that 2,5 dimercapto, 1,3,4 thiadiazolate (DMTD), benzotriazole (BTA) and N,N-diethyl, dithiocarbamate (DEDTC) effectively inhibit pitting corrosion by the formation of a metal-inhibitor film on Cu rich intermetallic particles (IMPs). On the other hand, ethylenediaminetetraacetic acid (EDTA) is shown to prevent Cu replating but without any decrease in localised corrosion currents. This finding suggests that sufficient cathodic oxygen reduction can be sustained on Cu-rich IMPs and dealloyed IMPs to drive the observed pitting corrosion without any copper replating.

6.2 Experimental

6.2.1 Materials, substrate preparation and chemicals

Flat sheets of AA2024 clad, 0.5 mm thick, distributed by Kaiser Aluminum, USA, were cut in the shape of discs, 15 mm in diameter. The alloy contains Cu (4.4 wt.%), Mg (1.3 wt.%), Mn (0.5 wt.%), Fe (0.3 wt.%), Si (0.1 wt.%), and the rest is Al. The sample's surface was water-ground first with P600-grit SiC emery paper to remove the alclad layer, and then further polished with P2400- and P4000-grit, rinsed with deionised water, and ultrasonically cleaned in absolute ethanol. Chemicals have already been listed in *Chapter 2*, the *Experimental section.*

6.2.2 Electrochemical measurements

The scanning vibrating electrode technique (SVET) has been explained in detail in *Chapter 5*, the *Experimental section.* The only difference is that instead of the Al/Cu sample, AA2024-T3 was investigated.

Potentiodynamic polarization curves have already been explained in *Chapter 2*, the *Experimental section.*

6.2.3 Surface characterization

Scanning electron microscopy combined with energy-dispersive X-ray spectroscopy (SEM-EDS) was already explained in *Chapter 2*, the *Experimental section.*

6.3 Results and Discussion

6.3.1 Scanning vibrating electrode technique

6.3.1.1 Corrosion of AA2024 in chloride solution

The ionic current density distributions were determined as a function of time above the surface of an unpolarised AA2024 sample, freely corroding in aerated 10 mM NaCl solution without inhibitor, by repetitive *in situ* SVET scanning. The IMPs are generally considered the initiation sites for localized corrosion in chloride media due to the galvanic coupling between the IMPs and the surrounding matrix. Among the IM phases, Al_2CuMg (S-phase) is the most active and contributes the most to localized corrosion. The S-phase IMPs are subject to anodic attack, followed by the copper redistribution on the alloy surface, leading to significant changes in electrochemical activity towards cathodic oxygen reduction [58]–[63]. Fig. 6.1 shows the representative current density maps carried out immediately on immersion (i.e., after 1 min), after 30 min, 6 h and 12 h. An SVET scan recorded upon immediate immersion revealed the local anodic activity ($j_z \leq 85$ µA cm^{-2}) at a certain number of places, indicating that localized corrosion is initiated within a minute of exposure to the chloride-containing solution (Fig. 6.1a). Successive scans show that individual pits propagate and remain active over 12 hours, while many others tend or become passive, accompanied by a reduced magnitude of current density in the latter case (Figs. 6.1a-d).

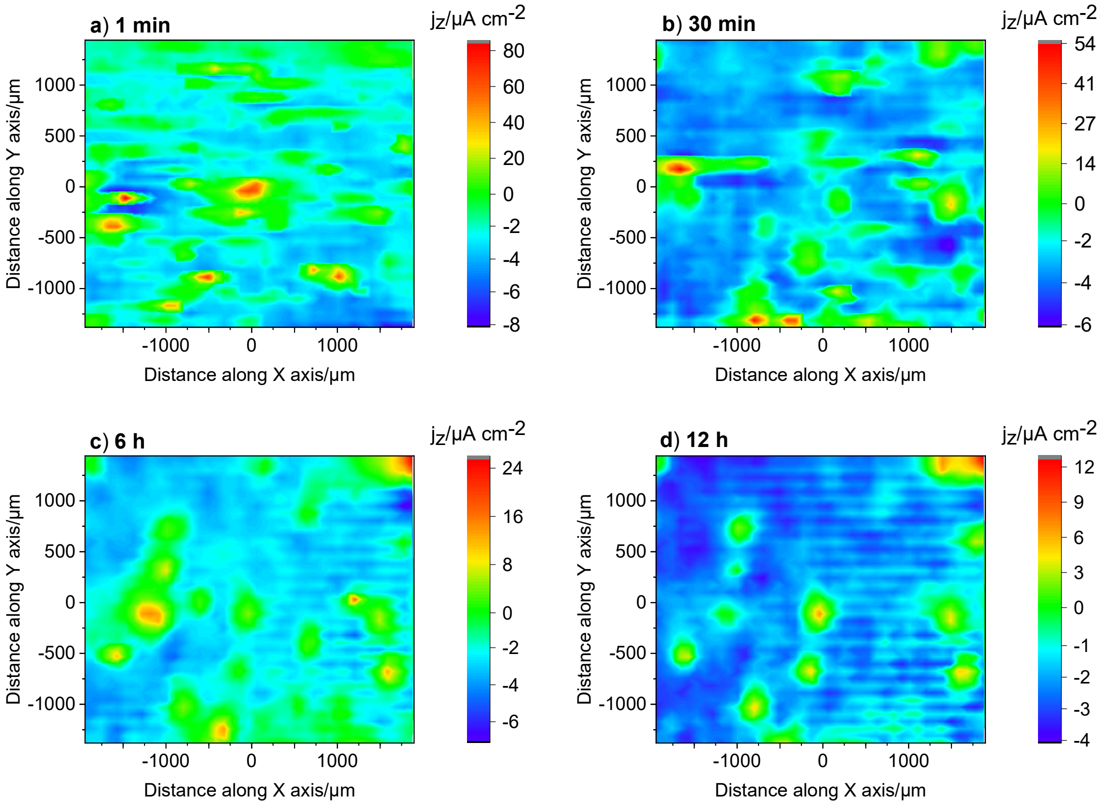

Figure 6.1: SVET maps recorded above an AA2024 during immersion in 10 mM NaCl at selected exposure times: (a) 1 min and (b) 24 h. The maps were obtained after: (a) 1 min, (b) 30 min, (c) 6 h and (d) 12 h immersion of the sample in the electrolyte solution.

The visual appearance of the sample surface after 1 min and at the end of the 12 h immersion period is shown in Fig. 6.2. The pit openings that coincide with the location of the local anodic current densities are particularly pronounced during prolonged immersion; however, the current densities decrease, which can be attributed to the deposition of corrosion products over time.

Whilst each pit can be considered a point anode, the cathodic reaction, which is assumed to be ORR, covers the surrounding regions. Due to the excessive copper redistribution around the pit openings, as well as on most of the Al matrix surface, new cathodic sites are formed that support even greater oxygen reduction over time, which is reflected in more pronounced negative values of current density (Figs. 6.1a, d).

It should be noted that the pits shown in Fig. 6.2b are much larger compared to the pits in Fig. 6.2a due to an increase in local alkalinity resulting from the generation of OH^- ions during oxygen reduction at the cathodic sites, causing further localized attack at the periphery of Cu-containing IMPs. One promising strategy to increase the corrosion resistance of AA2024 is to suppress the dissolution of S-phase particles. For this purpose, two corrosion inhibitors, MBI and OPA, were tested as potential candidates for mitigation pitting corrosion of AA2024.

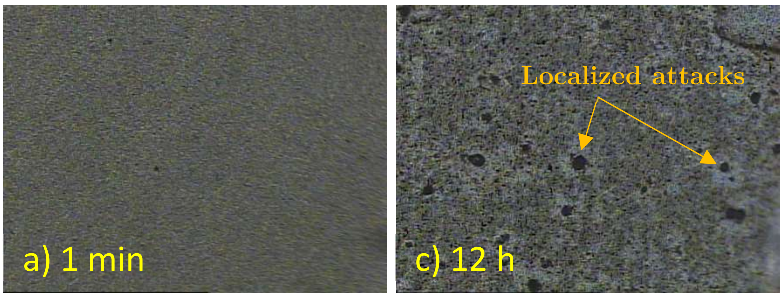

Figure 6.2: Optical micrographs corresponding to the SVET images from Fig. 6.1.

6.3.1.2 Corrosion of AA2024 in chloride solution containing MBI inhibitor

Fig. 6.3 shows the maps of the ionic current density distributed above the surface of the AA2024 sample spontaneously corroding at the free corrosion potential during *in situ* immersion in MBI-containing solution (i.e., 10 mM NaCl + 1 mM MBI). The current density map carried out upon immediate immersion (i.e., after 1 min) did not reveal local electrochemical activity indicating that the MBI inhibitor was instantly very effective against pitting corrosion (Fig. 6.3a). The ionic currents were homogeneously distributed over the sample surface with values almost within the background noise. After 24 h immersion, an additional decrease in the ionic current density was observed, with anodic activity $j_z \leq 0.5$ µA cm^{-2}, which may be due to preventing the dissolution of S-phase particles since the MBI is a well-known inhibitor for Cu (Fig. 6.3b). After that, the cell was rapidly washed with distilled water to remove traces of inhibitor and then filled with 10 mM NaCl solution to define its effectiveness against corrosion in a chloride environment containing no MBI reservoir.

In the early phase of immersion in NaCl solution (i.e., after 1 min), one localized anodic site with activity not exceeding 5 µA cm^{-2} was observed, which was deactivated after 12 h. However, the surface of the sample was slightly active due to the reported cathodic currents ($j_z \leq -4.5$ µA cm^{-2}) originating from the reduction of dissolved oxygen. This implies moderate retention of inhibitory properties in the environment without the presence of MBI.

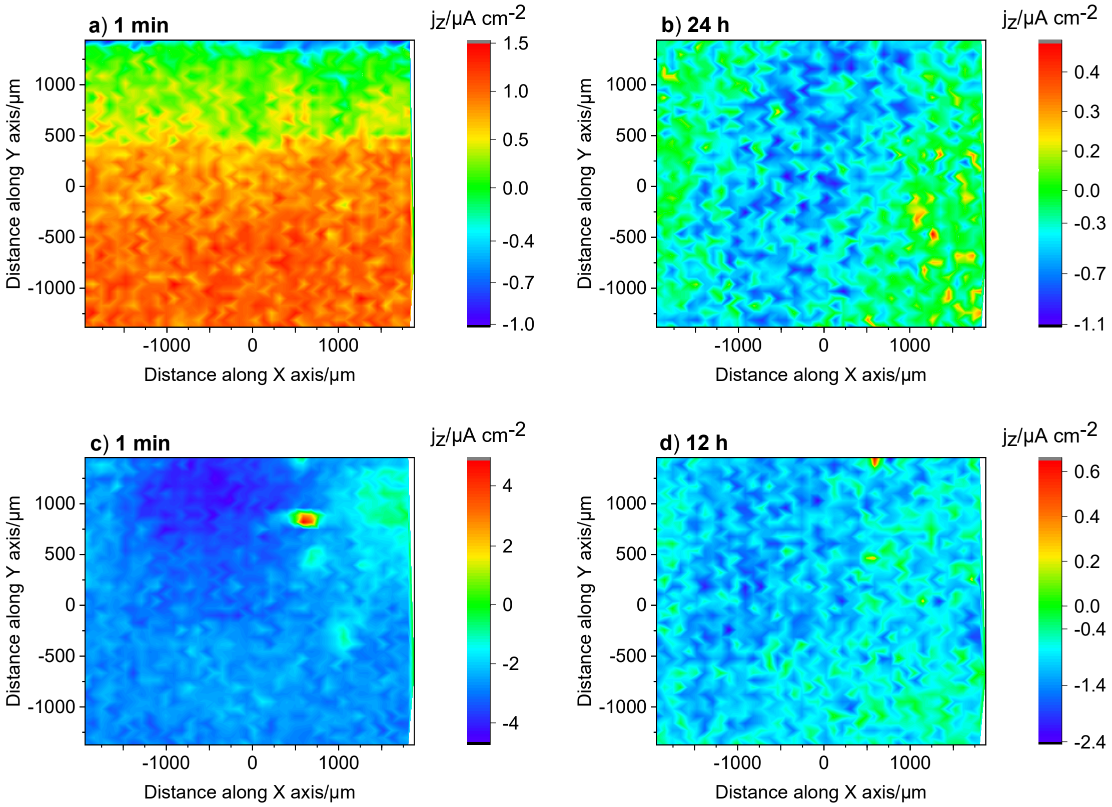

Figure 6.3: Ionic current mapping recorded above an AA2024 during immersion in 1 mM MBI + 10 mM NaCl at selected exposure times: (a) 1 min and (b) 24 h. The inhibitor solution was then replaced with 10 mM NaCl, and the maps were taken after (c) 1 min and (d) 12h immersion.

6.3.1.3 Corrosion of AA2024 in chloride solution containing OPA inhibitor

Unlike MBI inhibitor treatment, when the AA2024 was exposed to a solution containing an OPA inhibitor (i.e., 1mM OPA + 10 mM NaCl), localized corrosion was observed at several points at a very early stage of immersion with an anodic current density of 28 µA cm^{-2} (Fig. 6.4). Moreover, the anodic activity increased dramatically during prolonged immersion (i.e., after 24 h, $j_z \leq 180$ µA cm^{-2}). Interestingly, the cathodic currents were not observed over the entire surface but only near the pits, indicating that OPA is a good inhibitor for Al matrix but does not prevent pitting corrosion. Due to the pitting in the presence of OPA, the experiment was not further conducted to investigate behaviour without an inhibitor container, i.e., in NaCl solution.

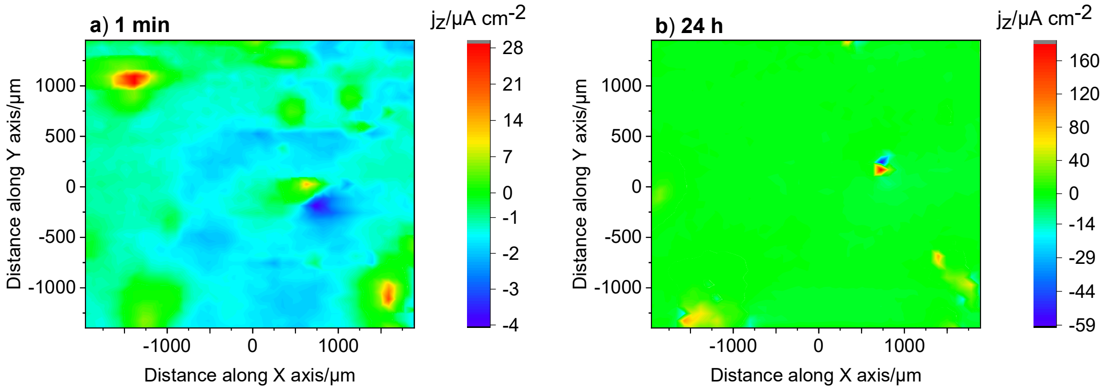

Figure 6.4: Ionic current mapping recorded above an AA2024 during immersion in 1 mM OPA + 10 mM NaCl at selected exposure times: (a) 1 min and (b) 24 h.

6.3.2 Polarization measurements

Fig. 6.5 illustrates the overall E-log j behaviour of AA2024 in 3 wt.% NaCl aerated solution with and without the presence of inhibitor molecules MBI and OPA. In aerated chloride conditions, corrosion should proceed at the pitting potential; upon anodic polarisation, the current rapidly increases due to the immediate onset of stable pitting, as previously shown in SVET maps. However, Fig. 6.5 presents the slightly pseudo-passive region, which is likely to occur due to the use of cladding AA2024. Although we ensured the clad layer was entirely removed from the surface to mimic bare material, there might be that some copper in the core diffused into the cladding material during the solution heat treatment process, and as a result, the copper depletion immediately adjacent to the cladding could impact corrosion characteristics. During open-circuit corrosion, the dominant cathodic reaction on IMPs is the ORR under the mixed kinetic regime [62]. Upon cathodic polarization, the oxygen reduction is mainly controlled by mass transport. In addition, activation-controlled HER takes place within a region of cathodic polarization initiation (−250 mV away from OCP).

The introduction of corrosion inhibitors may change the corrosion behaviour of AA2024. The OCP of all inhibitor systems was raised compared to the blank. Furthermore, while the 100P curve (i.e., 1 mM OPA + 3 wt.% NaCl) showed neither inhibition of ORR nor mitigation of pitting, the presence of 100S (i.e., 1 mM MBI + 3 wt.% NaCl) reduced the cathodic current density by about an order of magnitude. In addition, the change in the cathodic Tafel slope indicates a higher contribution of the activation-controlled ORR with respect to the control sample (blank). Synergistic inhibitor solution (i.e., 0.9 mM MBI + 0.1 mM OPA + 3 wt.% NaCl) was also investigated, and the results showed the inhibition of cathodic reaction, but the effect was lower than for 100S, which was attributed to a lower concentration of MBI. It is thus concluded that a synergistic effect was not observed on AA2024 as in the case of the Cu substrate (*Chapter 3*).

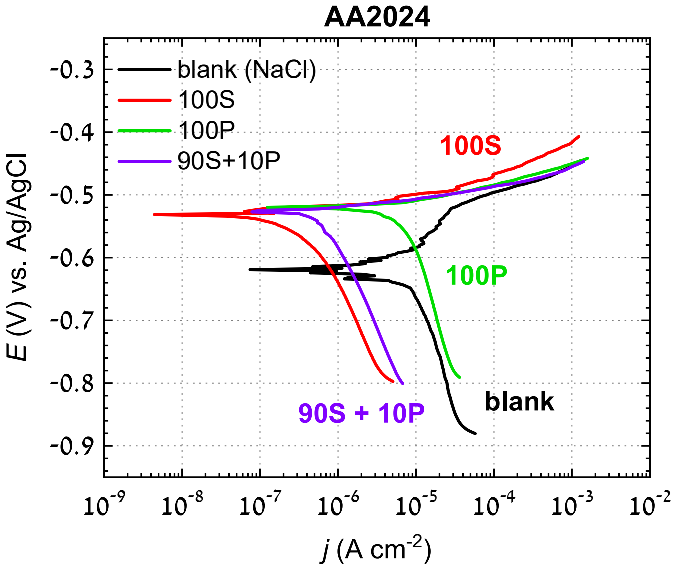

Figure 6.5: Potentiodynamic polarization curves recorded for AA2024 in 3 wt.% NaCl solution with and without the addition of 1mM of (a) 100S (MBI), (b) 100P (OPA) and (c) 90S+10P after 1 day of immersion. The scan rate was 1 mV/s.

6.3.3 Scanning electron microscopy combined with energy-dispersive X-ray spectroscopy characterization

Ex-situ observations of the AA2024 surface were performed by SEM-EDS after 24 h of immersion in 3 wt.% NaCl electrolyte with and without the addition of MBI and OPA corrosion inhibitors (Fig. 6.6). The surface of the control sample (i.e. NaCl only) shows drastic changes due to localized corrosion processes, including the Cu deposits over the entire surface (Fig. 6.6a). The sample pretreated with MBI inhibitor has an insignificant number of these Cu deposits, while for the OPA sample, a bunch of Cu particles surrounded the dealloyed S-phase (Fig. 6.6b). This may imply that the MBI inhibits the dealloying of S-phase particles and thus prevents copper redistribution, which enhances the kinetics of cathodic activity at the local sites.

The EDS maps in Fig. 6.7 provide information regarding the elemental distributions after corrosion attack in NaCl free-inhibitor solution. There was evidence of porous Cu residual, which is a result of Al and Mg preferential dealloying in the particle and galvanic corrosion of the Al matrix, subsequently causing the trenching around these particles. The high O counts around the particle may suggest a thicker oxide than the surrounding matrix.

For the MBI-treated sample, EDS elemental maps (Fig. 6.8) show the distribution of S and N constituting MBI. This suggests that the MBI molecules form precipitates on copper-rich intermetallic particles via stable Cu–S and Cu–N bonds, thus blocking ORR sites [45], [72].

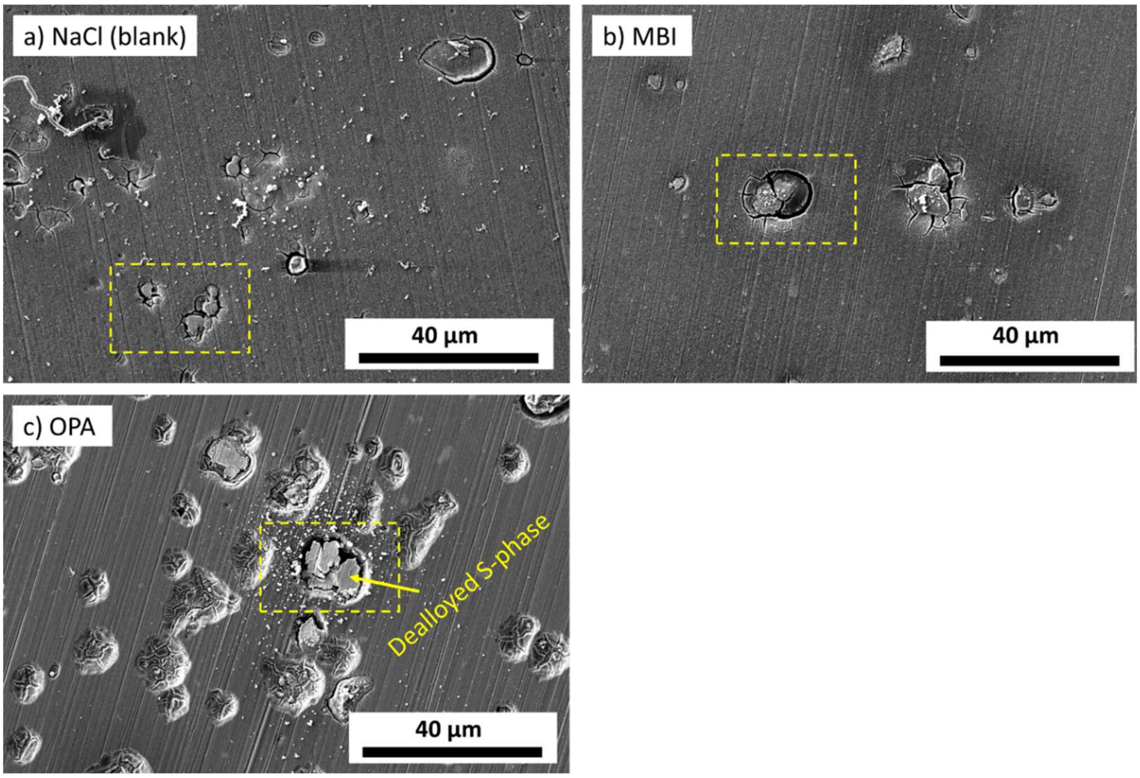

Figure 6.6: SEM secondary electron images for AA2024 immersed for 24 h in (a) 3 wt.% NaCl solution, (b) 3 wt.% NaCl containing 1 mM MBI and (c) 3 wt.% NaCl containing 1 mM OPA.

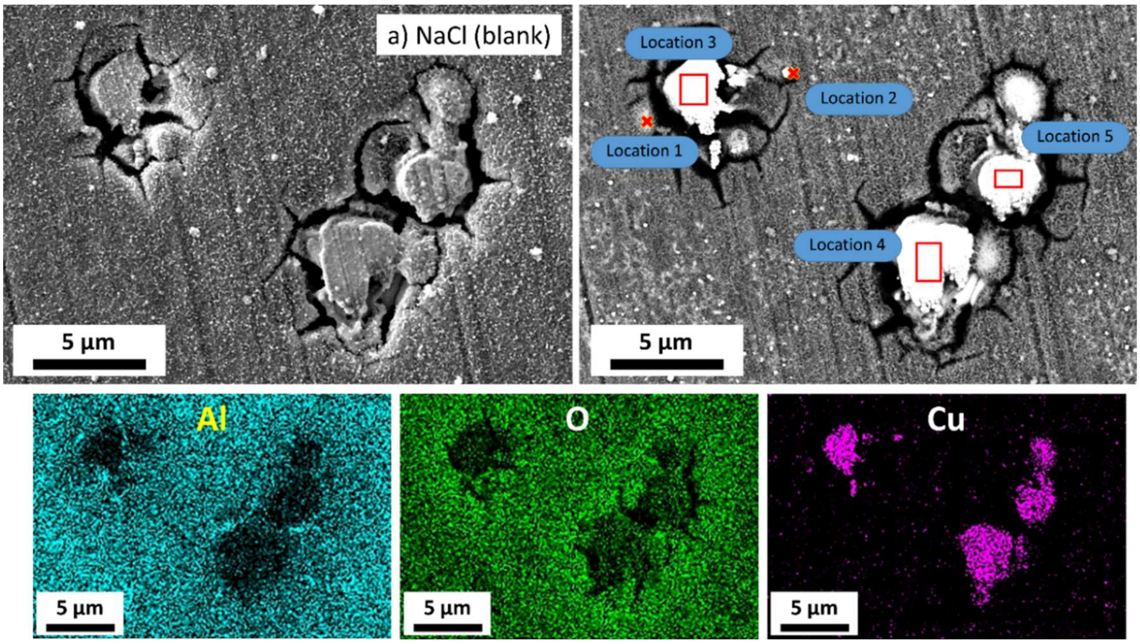

Figure 6.7: SEM-EDS analysis of local corrosion induced by S-phase (Al_2CuMg) particles (in Fig. 6.6a) recorded in secondary electron (SE) mode (left) and backscattered mode (right) after 24 h immersion in 3 wt.% NaCl solution. Locations denoted by a cross mark, square and rectangle indicate the areas/spots where EDS analysis was conducted (Table 6.1). The elements were labelled in EDS maps.

Table 6.1: EDS analysis of AA2024 immersed for 24 h in NaCl. Analyses were performed at locations 1 to 5, as denoted in Fig. 6.7.

Location	at.% Al	at.% O	at.% Cu	at.% Fe	at.% Mg
1	25.7	51.5	19.3	3.5	—
2	3.0	7.1	89.9	—	—
3	8.9	23.4	66.8	—	0.9
4	13.0	30.6	56.4	—	—
5	15.2	31.3	52.4	—	1.1

MBI also precipitated on the Al matrix, most likely on Cu-containing domains in the solid solution (Fig. 6.8, Table 6.1), because it had previously been shown that MBI was not adsorbed on the bare aluminium surface (*Chapter 2*). It should be emphasized that the copper/iron-rich IMP (most probably $Al_7Cu_2Fe(Mn)$) was significantly attacked but still not wholly corroded based on the remaining Al in the particle (Locations 3 and 4, Table 6.2) and the lack of bright ring around the particle corresponding to the O counts, i.e. oxide deposits.

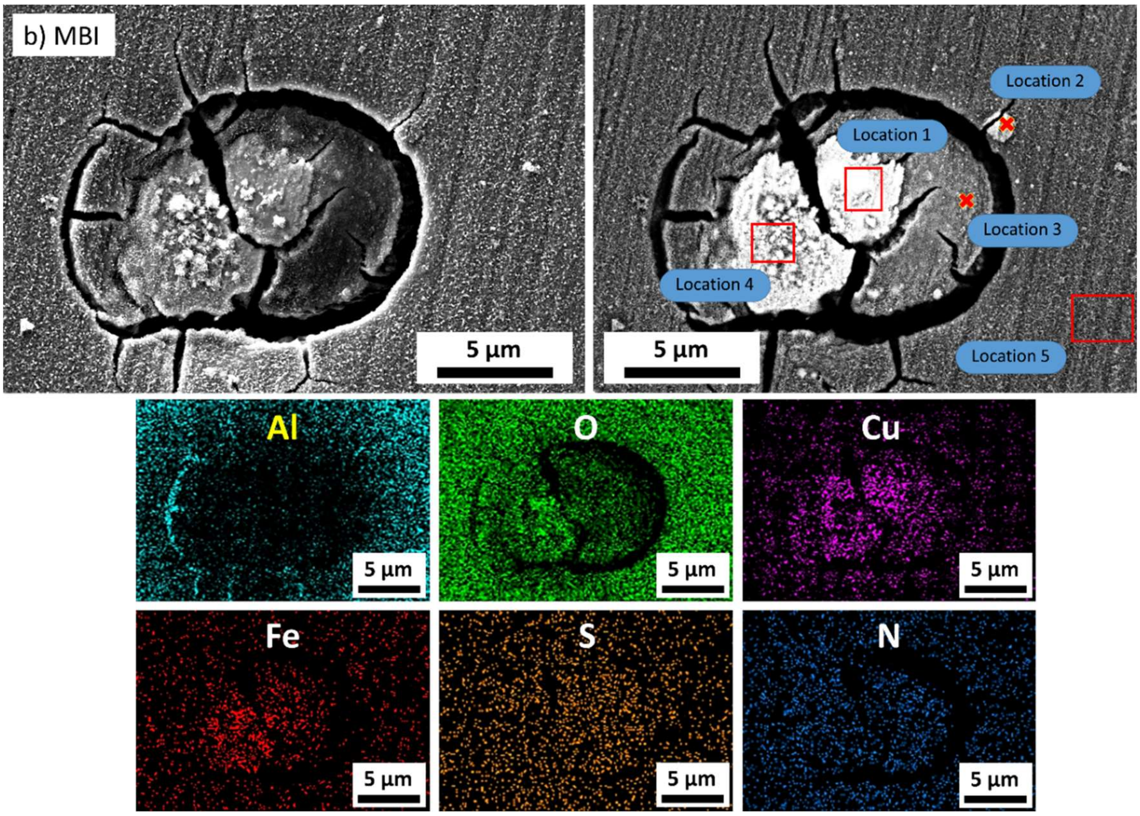

Figure 6.8: SEM-EDS analysis of local corrosion induced by Al_7Cu_2Fe particle (in Fig. 6.6b) recorded in secondary electron (SE) mode (left) and backscattered mode (right) after 24 h immersion in 3 wt.% NaCl solution containing 1 mM MBI. Locations denoted by a cross mark, square and rectangle indicate the spots where EDS analysis was conducted (Table 6.2). The elements were labelled in EDS maps.

Table 6.2: EDS analysis of AA2024 immersed for 24 h in MBI+NaCl. Analyses were performed at locations 1 to 5, as denoted in Fig. 6.8.

Location	at.% Al	at.% O	at.% Cu	at.% S	at.% N	at.% Fe	at.% Mg
1	8.2	31.2	28.2	13.8	11.1	7.6	—
2	19.9	48.2	11.9	7.0	6.1	6.9	—
3	13.8	32.6	16.0	18.2	19.4	—	—
4	11.9	39.4	16.3	8.9	8.1	15.4	—
5	54.7	40.0	2.5	2.3	—	—	0.6

Additionally, Fig. 6.9 shows a cross-section of an S phase particle (Fig. A.27) to determine the dealloying penetration depth. The preferentially attacked particle resulted in a spongy morphology of dealloyed S phase with a continuous solid S phase remnant network. EDS analysis of the S phase particle at the cross-section revealed that dissolution gradually evolved from the surface inwards. However, the presence of S, N and C (Fig. 6.9, locations 4 and 5, Table 6.3) indicates that MBI was adsorbed on the porous copper surface resulting from dealloyed S-phase particle. Also, the remaining Mg with a significant amount of S, N and C present (Fig. 6.9, locations 4 and 5, Table 6.3) indicates that the Al_2CuMg was not fully corroded. It is likely that MBI does not completely prevent the dissolution of the S phase but reduces the dissolution rate and the rate of oxygen reduction on the porous copper remnant, as shown by potentiodynamic polarisation measurements. Therefore, this behaviour is believed to be similar to the interaction of MBI with bare copper, as shown in *Chapter 1*. The observed Pt and Ga signals originate from the FIB pre-treatment of the sample.

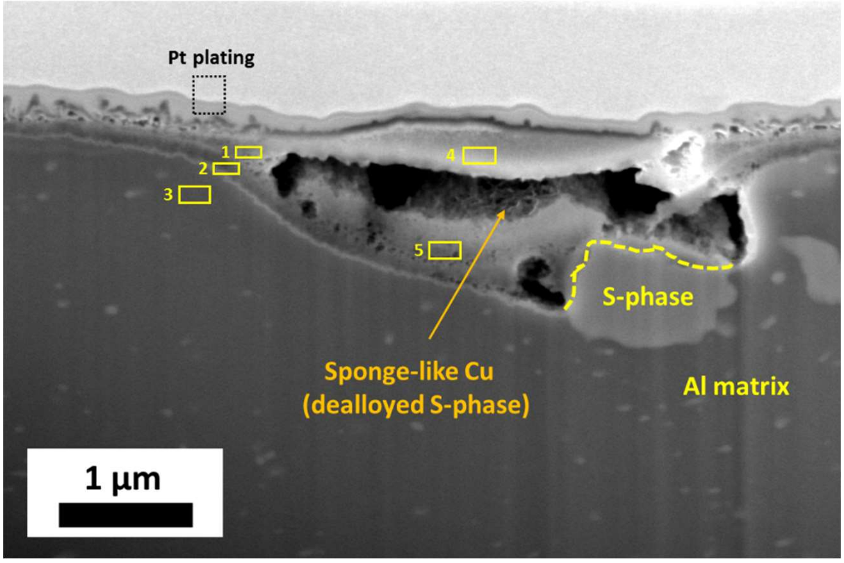

Figure 6.9: FIB/SEM (cross-section) analysis of local corrosion induced by Al_2CuMg phase after 24 h immersion of AA2024 in 3 wt.% NaCl containing 1 mM MBI. Yellow horizontal rectangles denote spots where EDS analysis was performed (Table 6.3).

Table 6.3: EDS analysis of AA2024 immersed for 24 h in MBI+NaCl. Analyses were performed at locations 1 to 5, as denoted in Fig. 6.9. The results are presented as atomic percentages (at.%).

Location	Al	O	Cu	Mg	S	N	Cl	Si
1	65.4	27.7	4.2	0.9	—	—	—	1.8
2	64.9	25.6	3.2	0.5	3.8	—	1.1	0.9
3	92.5	4.5	1.7	1.3	—	—	—	—
4	8.2	23.1	38.6	0.9	10.7	5.1	3.4	—
5	49.4	31.9	6.2	0.4	7.0	3.5	1.1	0.5

On the other hand, the S-phase of the OPA-pretreated sample was characterized by complete corrosion where Al and Mg were selectively dissolved in the first stage, leaving the Cu-rich remnant exposed to a corrosion environment (Fig. 6.10). The particle was almost entirely dealloyed and undercut from its adjacent matrix. Although a large number of copper redeposits surround the IMP, EDS point analysis showed that these deposits have a rather more complex composition consisting of Cu, Al, O and P. The role of these deposits is out of the scope of this chapter. In addition, the phosphorus map showed that the OPA was not adsorbed on the IMP or Cu remnant, but it was adsorbed on the Al matrix (Fig. 6.10, locations 3, 4 and 5, Table 6.4), which is in line with the results obtained in *Chapter 2*. However, the adsorption of OPA was not sufficient to prevent the AA2024 from corroding.

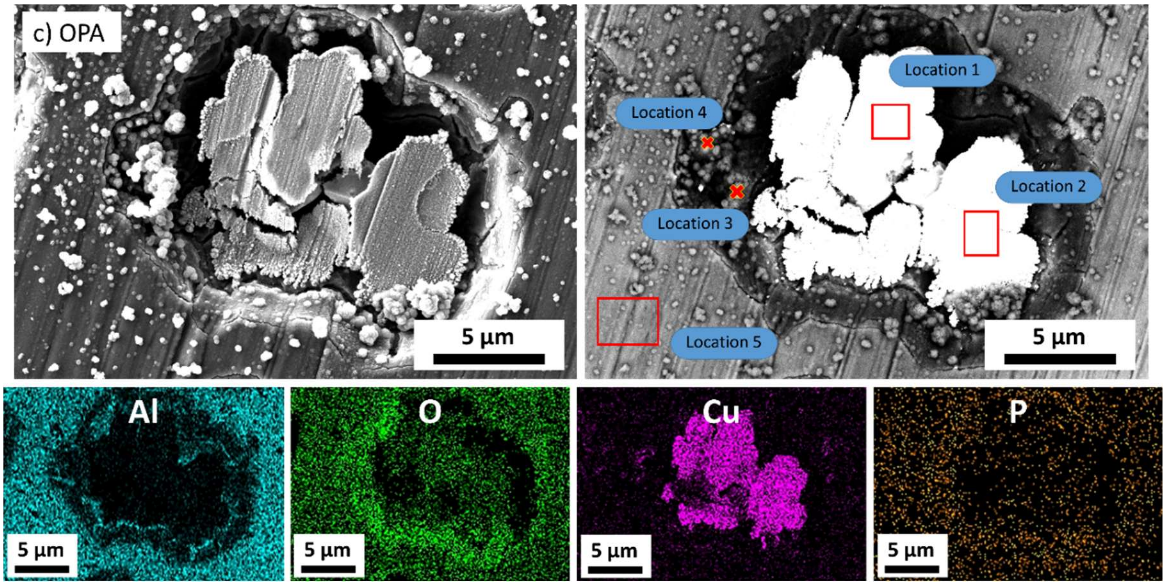

Figure 6.10: SEM-EDS analysis of local corrosion induced by S-phase (Al_2CuMg) particles (in Fig. 6c) recorded in secondary electron (SE) mode (left) and backscattered mode (right) after 24 h immersion in 3 wt.% NaCl containing 1 mM OPA. Locations denoted by a cross mark, square and rectangle indicate the spots where EDS analysis was conducted (Table 6.4). The elements were labelled in EDS maps. The Mg map was not shown because Mg is present only in the matrix.

Table 6.4: EDS analysis of AA2024 immersed for 24 h in OPA+NaCl. Analyses were performed at locations 1 to 5, as denoted in Fig. 6.10.

Location	at.% Al	at.% O	at.% Cu	at.% P	at.% Mg
1	6.8	18.5	74.8	—	—
2	5.1	15.9	79.1	—	—
3	17.2	59.8	4.3	18.7	—
4	11.2	31.8	54.2	2.8	—
5	78.1	15.9	1.4	3.4	1.2

6.4 Conclusions

The corrosion protection of AA2024 was monitored by scanning vibrating electrode technique (SVET), potentiodynamic polarization curves and focused ion beam scanning electron microscopy (FIB-SEM) coupled with energy-dispersive X-ray spectroscopy (EDS).

Successive SVET scans for the control sample in 10 mM NaCl show that some pits propagate and remain active over 12 hours, while many others tend or become passive, followed by a reduced magnitude of current density in the latter case, which can be attributed to the deposition of corrosion products over time. Whilst each pit can be considered a point anode, the cathodic reaction, which is assumed to be ORR, covers the surrounding regions. No local electrochemical activity was detected by *in situ* immersion in MBI-containing solution (i.e., 10 mM NaCl + 1 mM MBI) for 24 h, indicating that the MBI inhibitor was very effective against pitting corrosion which may be due to preventing the dissolution of S-phase particles. In addition, one localized anodic site was observed upon immediate immersion in the chloride solution that does not contain an MBI container, which was deactivated after 12 h. However, the surface remained slightly active, indicating moderate retention of inhibitory properties. In contrast, *in situ* immersion in OPA-containing solution (i.e., 10 mM NaCl + 1 mM OPA) during 24 h caused significant localized corrosion. Unlike MBI inhibition, when applying OPA cathodic activity was not homogeneously distributed over the entire surface but only near the pits, indicating that OPA is a good inhibitor for Al matrix but does not prevent pitting corrosion.

Furthermore, while the polarization curve for 100P (i.e., 1mM OPA + 3 wt.% NaCl) showed neither inhibition of ORR nor mitigation of pitting, the presence of 100S (i.e., 1mM MBI + 3 wt.% NaCl) reduced the cathodic current density by about an order of magnitude. SEM-EDS analyses showed that the sample pretreated with MBI inhibitor was less attacked by aggressive medium compared to the sample pretreated with OPA inhibitor. MBI molecules formed precipitates on copper-rich intermetallic particles thus blocking ORR sites, whereas OPA was exclusively adsorbed on the Al matrix surface resulting in complete corrosion where Al and Mg were selectively dissolved in the first stage, leaving the Cu-rich remnant exposed to a corrosion environment. In addition, EDS analysis performed at the cross-section of the sample pretreated with MBI revealed the MBI layer on the porous copper surface. Besides, the remaining Mg suggested that the Al_2CuMg was not fully corroded. From this, it follows that MBI reduces the dissolution rate of dealloying of S phase, but also the rate of ORR on the copper remnant sites.

Chapter 7

Conclusions

The synergistic action of organic inhibitors to mitigate corrosion of aluminium, copper, and aluminium alloy 2024-T3 in chloride solution was successfully studied and discussed. This chapter provides the answers to whether hypotheses have been confirmed or refuted.

1) The chemical surface pre-treatment improves the adsorption of organic inhibitors on Cu and Al.
The electrochemical and surface characterization showed that the chemical surface pre-treatment slightly enhances the adsorption of MBI on a copper substrate but significantly improves the adsorption of OPA on an aluminium substrate. It should also be noted that the choice of solvent for liquid-phase deposition was crucial. Metal-inhibitor films were formed only from aqueous solutions.
The hypothesis was confirmed in Chapter 2.

2) The binary mixture MBI+OPA acts synergistically in corrosion inhibition of AA2024, but shows no synergy on individual metals Al and Cu. The possible synergistic effect will be irreversible under optimal conditions.
Regarding the binary combination of MBI (S) and OPA (P), three different molar ratios were used; 90S+10P, 50S+50P and 10P+90S (numbers represent the molar ratio of S and P inhibitors). Contrary to our expectation, it was observed that the binary mixture 90S+10P synergistically boosts corrosion inhibition of copper substrate, whereas this effect was not reported for aluminium under any of the above concentration conditions for MBI+OPA. Furthermore, the results revealed that the binary combination 90S+10P did not synergistically inhibit the corrosion processes of AA2024, i.e., the inhibition of cathodic reaction was evident, but the effect was lower than for 100S, which was attributed to a lower concentration of MBI in a binary mixture.
The hypothesis was refuted in Chapter 3.

3) Formed Cu-MBI layer(s) in NaCl medium possess a polymerized structure. The chloride ions have multiple roles: as catalysts of layer formation and as integral components of the layer's structure.
A detailed ToF-SIMS study unambiguously reported that Cu-MBI films possess a polymerized structure. Moreover, chlorine has been found to be an integral part of the formed polymerized structure, revealing the dual role of chloride ions as promoters and reactants. The pure catalytic role of chloride ions is excluded.
The hypothesis was partially confirmed in Chapter 4.

4) The degradation of the Cu-MBI layer results in the formation of dimers.

The cyclic voltammetry with the help of XPS and ToF-SIMS showed that Cu-MBI films were subject to degradation at potentials above 0.45 V only for thin films (i.e., 100S), while the thick polymerized films of 90S+10P showed impressive stability and resistance toward degradation. The characterization of the products after the degradation stage revealed the dimeric structure, i.e., $(MBI)_2$.
The hypothesis was confirmed in Chapter 4.

5) SECM analyses can detect local reactive sites of the hydrogen evolution reaction (HER), as well as the oxygen evolution reaction (OER) on the surface of Al/Cu substrate.
SECM operating in substrate generation-tip collection (SG/TC) mode detected the local concentrations of hydrogen gas over Al metal in Al/Cu substrate characterized by high-current transients, which was associated with the pitting corrosion of Al. Furthermore, redox-competition (RC) measurements for Al/Cu substrate showed very low current values (close to zero) homogeneously distributed over copper metal, compared to the currents recorded over aluminium metal, indicating that copper represents the cathodic site for oxygen reduction.
The hypothesis was confirmed in Chapter 5.

6) The use of SVET can distinguish between cathodic and anodic sites on the Al/Cu galvanic couple and AA2024-T3, and define the effectiveness of MBI and OPA inhibitors.
Galvanic coupling of aluminium to copper leads to the removal of the cathodic reaction from aluminium to copper, where it is homogeneously distributed over the entire metal surface. In-*situ* SVET measured the negative currents (cathodic sites) over the copper surface, resulting from the flux of hydroxide ions generated by the reduction of dissolved oxygen. In addition, the observed positive currents (anodic sites) were due to the flux of Al^{3+} ions released from the aluminium surface. On the other hand, for AA2024, SVET detected the local anodic activity, attributed to the S-phase particle, which was generally considered the initiation sites for localized corrosion in chloride media due to the galvanic coupling between the IMPs and the surrounding matrix. The addition of MBI and OPA led to a significant reduction in ionic currents recorded over Al/Cu, making it possible to monitor changes in anodic and cathodic reactions and thus study the effectiveness of corrosion inhibition.
The hypothesis was confirmed in Chapter 6.

Chapter 8

Appendices

A.1: Linear relationship vs square root of sweep rate ($v^{1/2}$) for mc-aq (Fig. 2.6a).

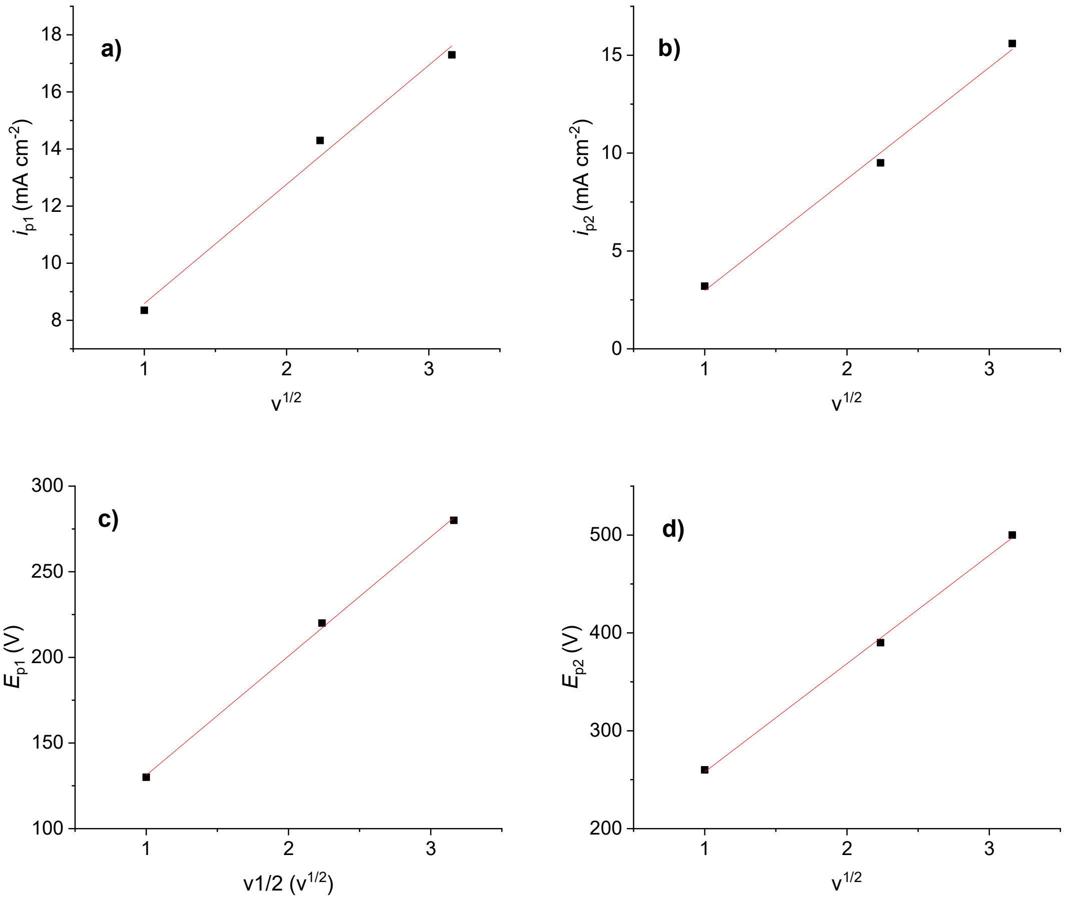

A.2: Linear relationship vs square root of sweep rate ($\nu^{1/2}$) for ch-aq (Fig. 2.6b).

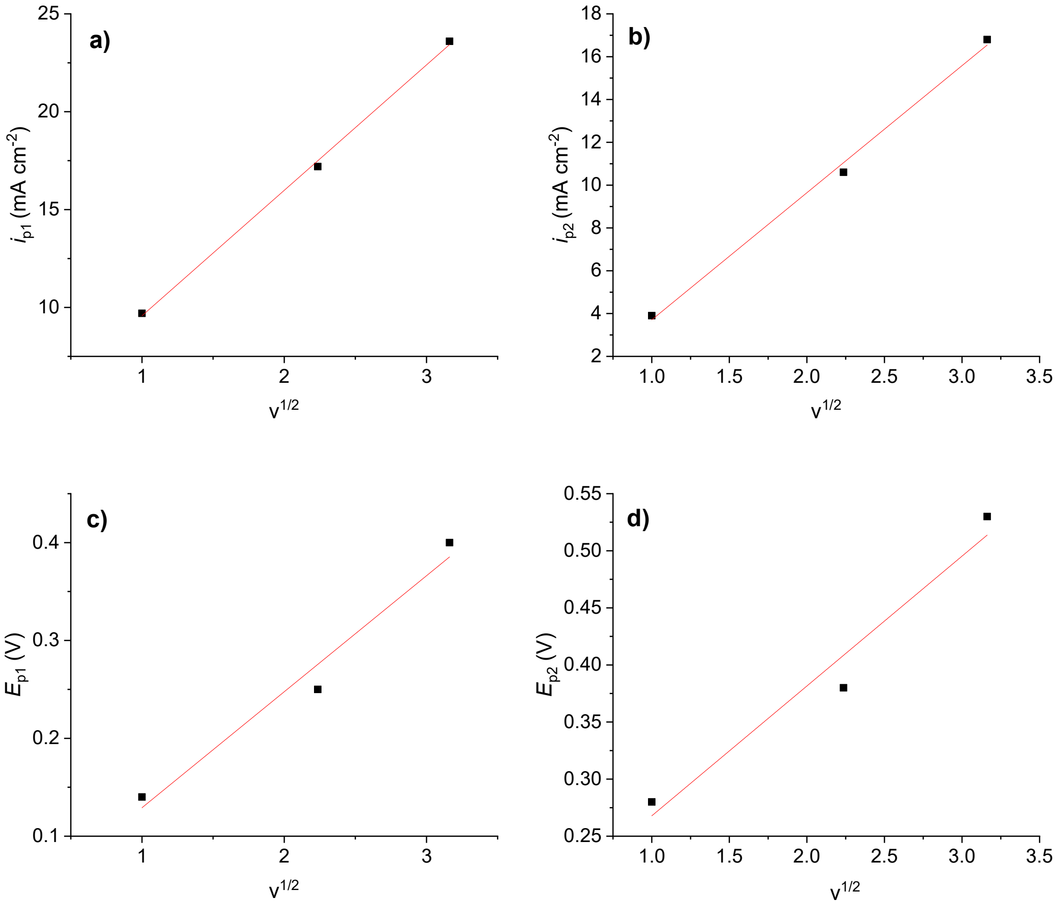

A.3: Linear relationship vs square root of sweep rate ($\nu^{1/2}$) for mc-S-aq(Fig. 2.6c).

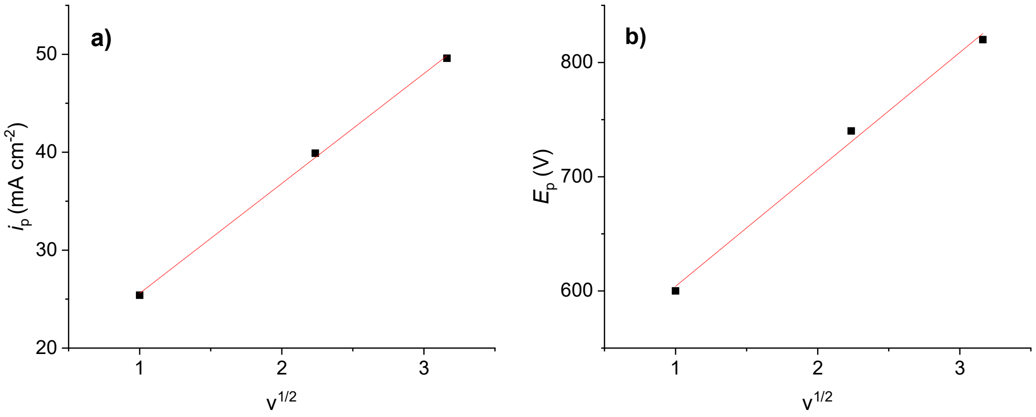

A.4: Linear relationship vs square root of sweep rate ($\nu^{1/2}$) for ch-S-aq (Fig. 2.6d).

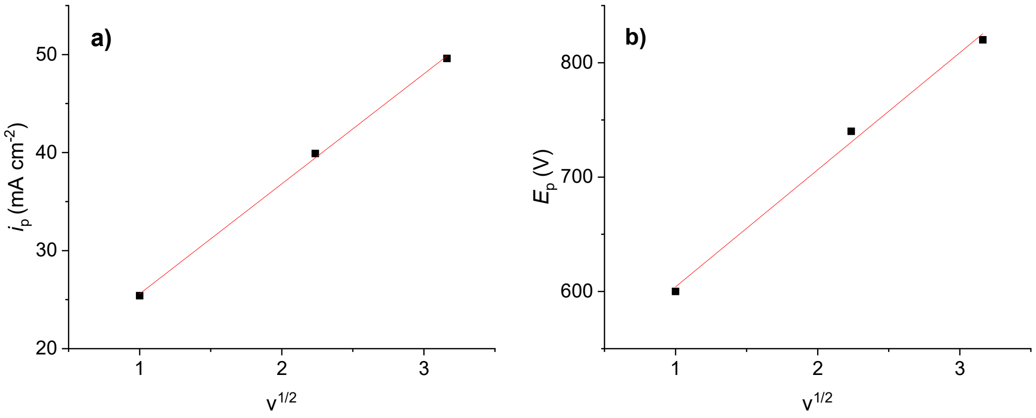

A.5: Linear relationship vs square root of sweep rate ($\nu^{1/2}$) for mc-P-aq (Fig. 2.6e).

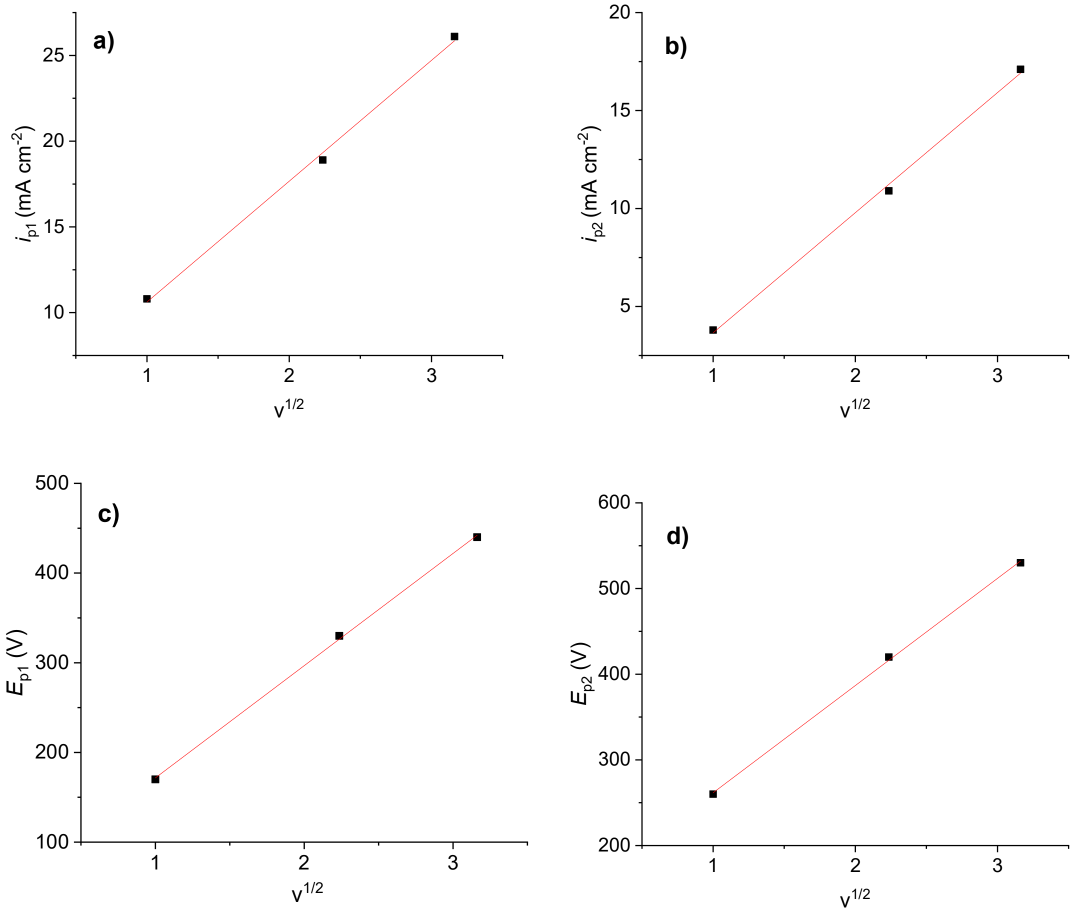

A.6: Linear relationship vs square root of sweep rate ($\nu^{1/2}$) for ch-P-aq (Fig. 2.6f).

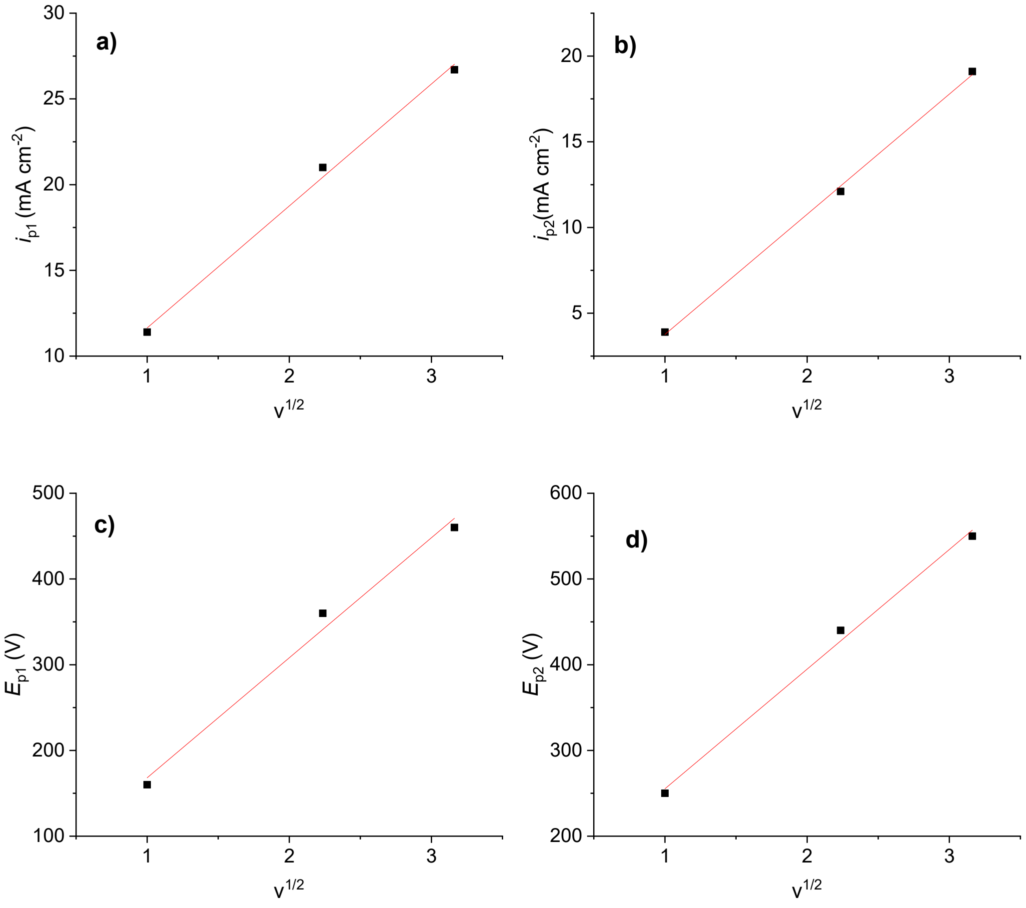

A.7: SEM secondary electron images recorded after 30 min immersion of copper in ethanol solution containing 1 mM MBI or OPA followed by 24 h immersion in 3 wt.% NaCl solution. The copper surface before recording the images implies: (a) mechanical pre-treatment + MBI deposition from ethanol solution, (b) mechanical pre-treatment + OPA deposition from ethanol solution, (c) chemical pre-treatment + MBI deposition from ethanol solution, (d) chemical pre-treatment + OPA deposition from ethanol solution.

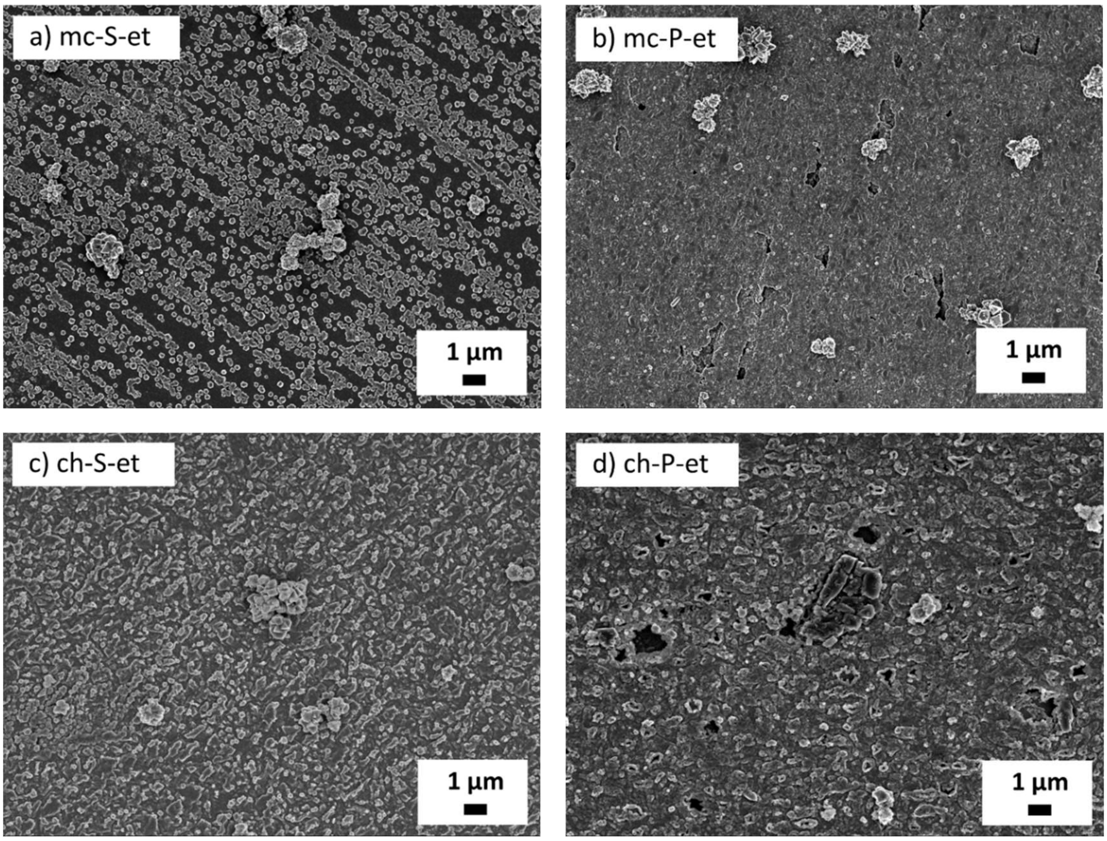

A.8: SEM images recorded in backscattered electron (BSE) mode after 30 min immersion of copper in ethanol solution containing 1 mM MBI or OPA followed by 24 h immersion in 3 wt.% NaCl solution. The copper surface before recording the images implies: (a) mechanical pre-treatment + MBI deposition from ethanol solution, (b) mechanical pre-treatment + OPA deposition from ethanol solution. Locations denoted by a cross mark indicate the spots where EDS analysis was conducted (charts to the right of the SEM images).

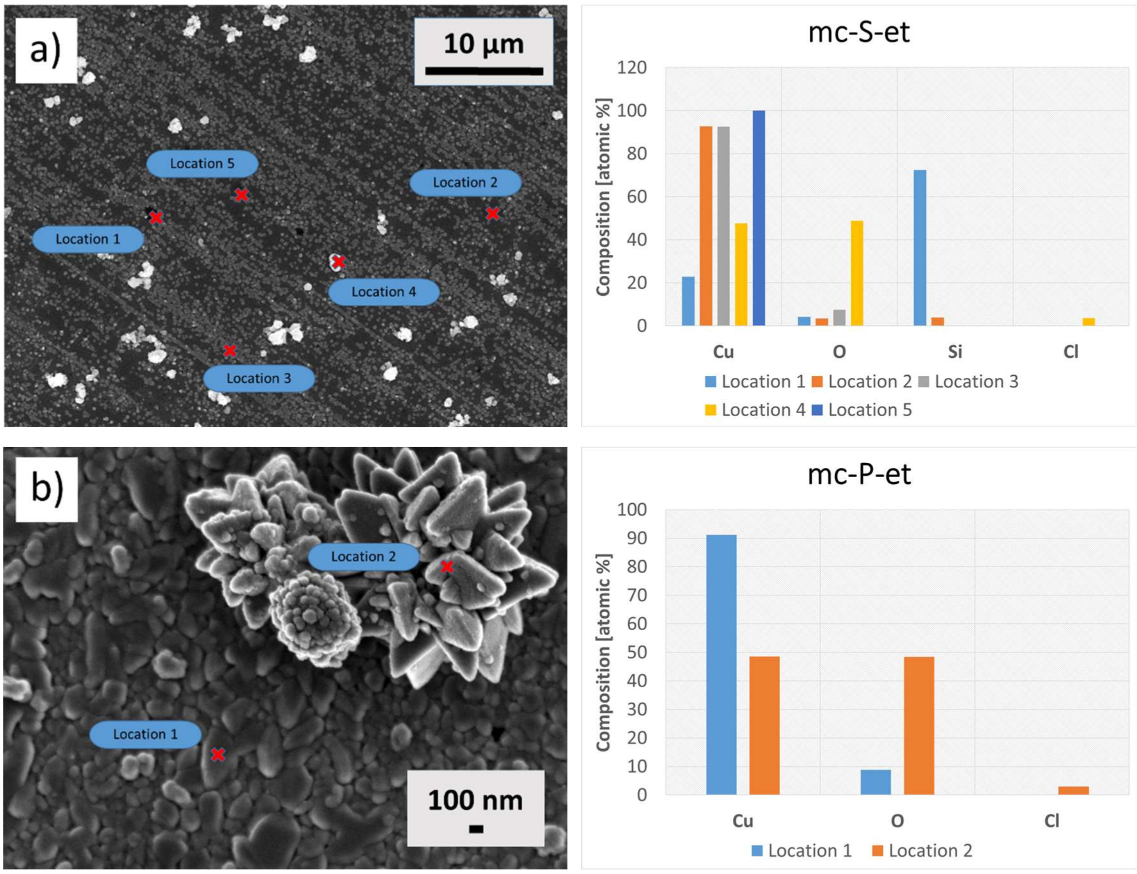

A.9: SEM images recorded in backscattered electron (BSE) mode after 30 min immersion of copper in ethanol solution containing 1 mM MBI or OPA followed by 24 h immersion in 3 wt.% NaCl solution. The copper surface before recording the images implies: (a) chemical pre-treatment + MBI deposition from ethanol solution, (b) chemical pre-treatment + OPA deposition from ethanol solution. Locations denoted by a cross mark indicate the spots where EDS analysis was conducted (charts to the right of the SEM images).

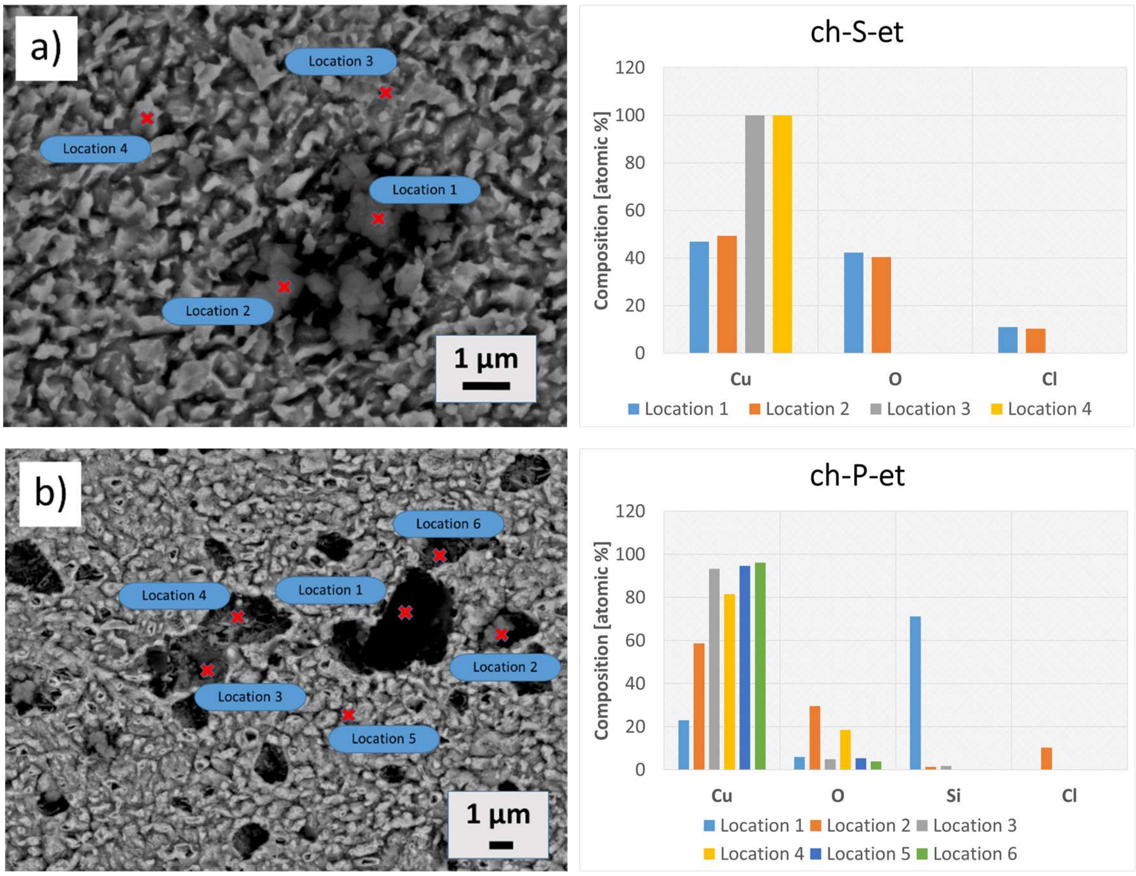

A.10: SEM secondary electron images recorded after 30 min immersion of aluminium in ethanol solution containing 1 mM MBI or OPA followed by 24 h immersion in 3 wt.% NaCl solution. The aluminium surface before recording the images implies: (a) mechanical pre-treatment + MBI deposition from ethanol solution, (b) mechanical pre-treatment + OPA deposition from ethanol solution, (c) chemical pre-treatment + MBI deposition from ethanol solution, (d) chemical pre-treatment + OPA deposition from ethanol solution.

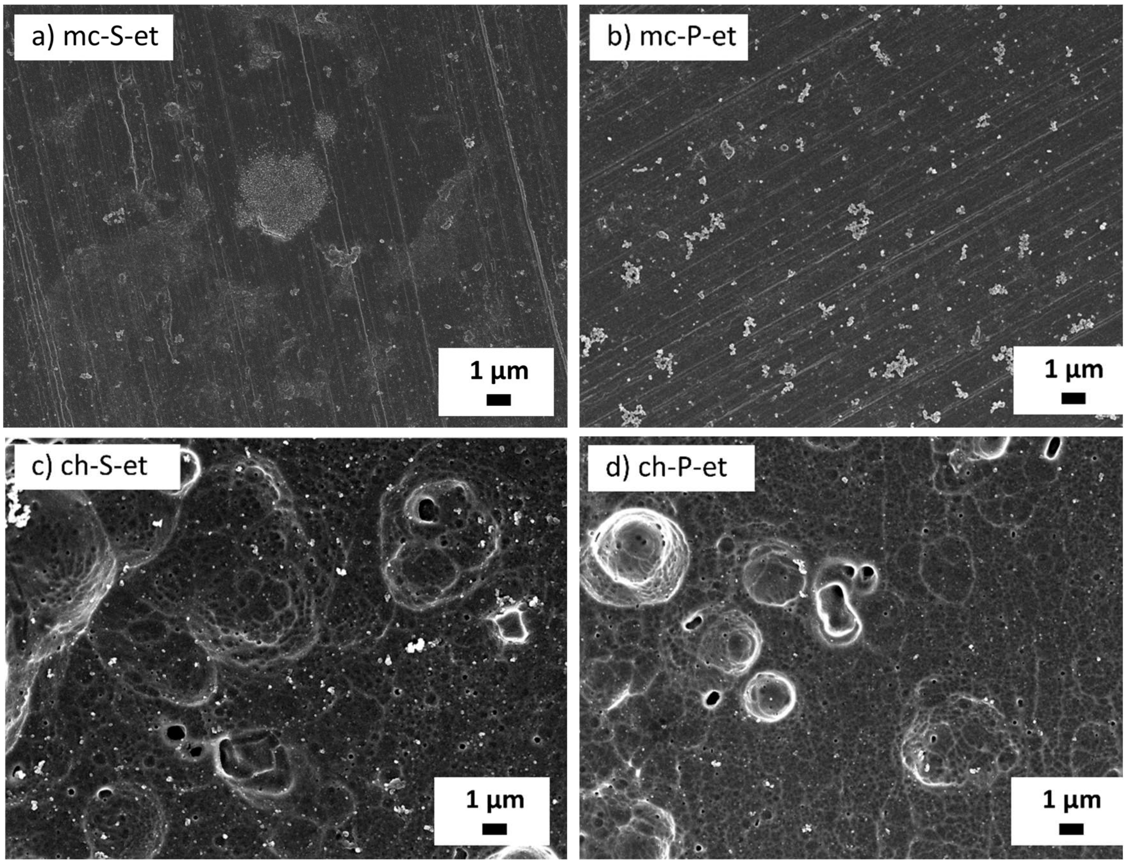

A.11: SEM images recorded in backscattered electron (BSE) mode after 30 min immersion of aluminium in ethanol solution containing 1 mM MBI or OPA followed by 24 h immersion in 3 wt.% NaCl solution. The aluminium surface before recording the images implies: (a) mechanical pre-treatment + MBI deposition from ethanol solution, (b) mechanical pre-treatment + OPA deposition from ethanol solution. Locations denoted by a cross mark indicate the spots where EDS analysis was conducted (charts to the right of the SEM images).

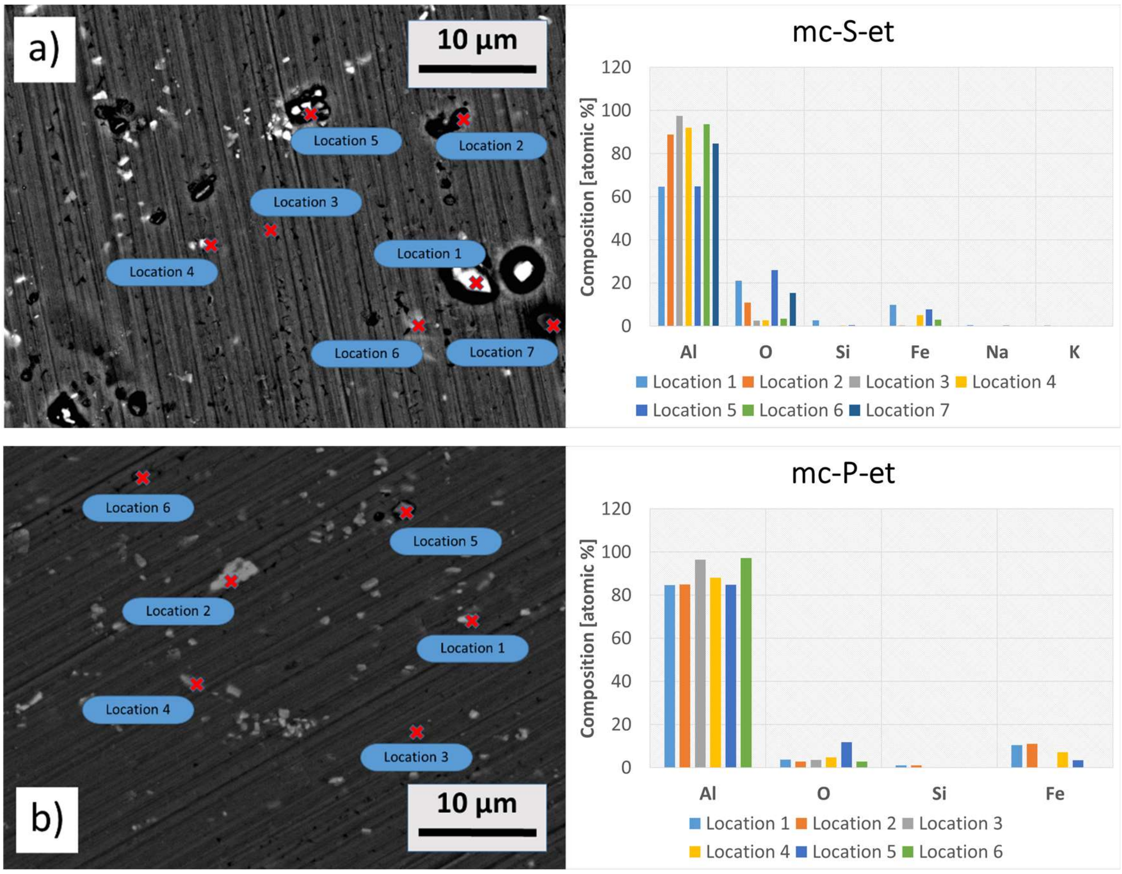

A.12: SEM images recorded in backscattered electron (BSE) mode after 30 min immersion of aluminium in ethanolic solution containing 1 mM MBI or OPA followed by 24 h immersion in 3 wt.% NaCl solution. The aluminium surface before recording the images implies: (a) chemical pre-treatment + MBI deposition from ethanol solution, (b) chemical pre-treatment + OPA deposition from ethanol solution. Locations denoted by a cross mark indicate the spots where EDS analysis was conducted (charts to the right of the SEM images).

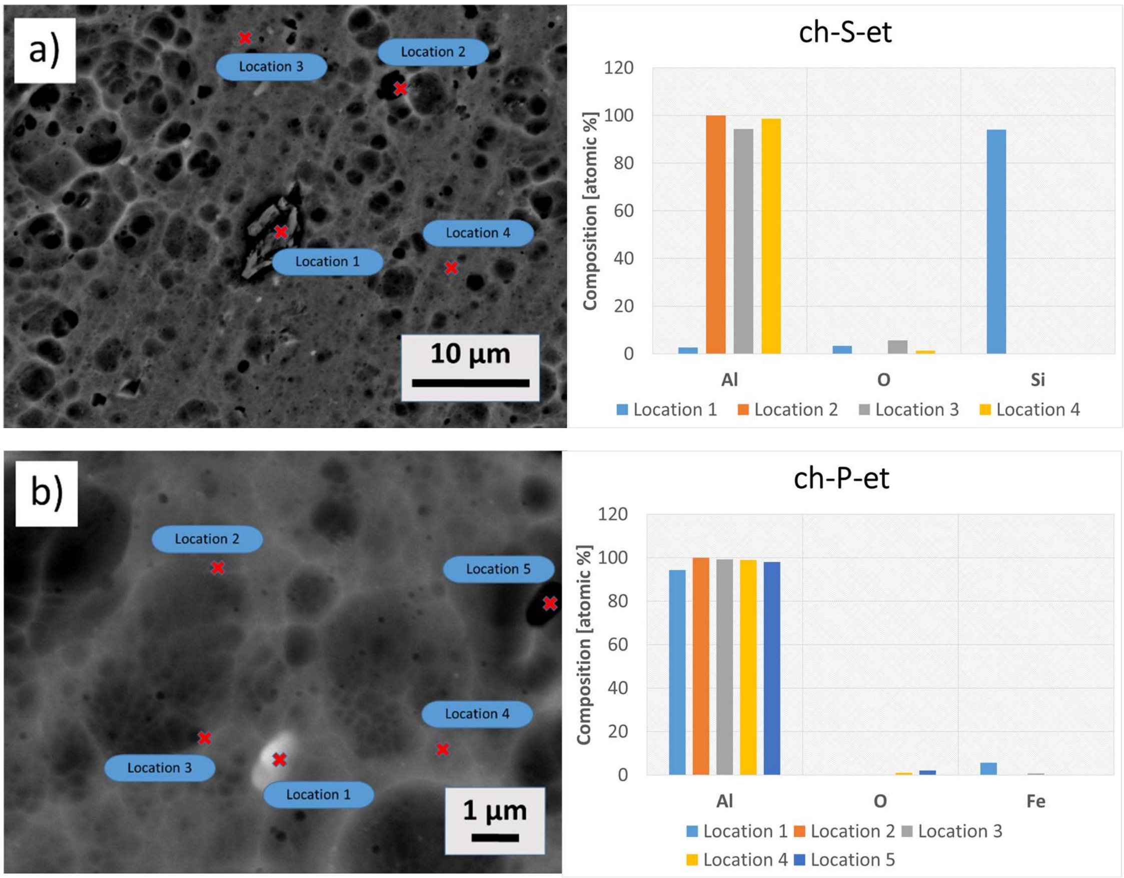

A.13: The S parameter, represented by dashed arrows, indicates the span of the degree of synergy, i.e. how much is the corrosion protection of 90S+10P, in terms of R_p as a function of immersion time, better than that of 100S (not better than itself). Note that due to the smaller R_p value for 100P compared to a blank (Table 3.3), and thus simplicity, the R_p values for 100S and 100P were not represented by a common line. Instead, the relative comparison between R_p for 90S+10P and 100S is shown.

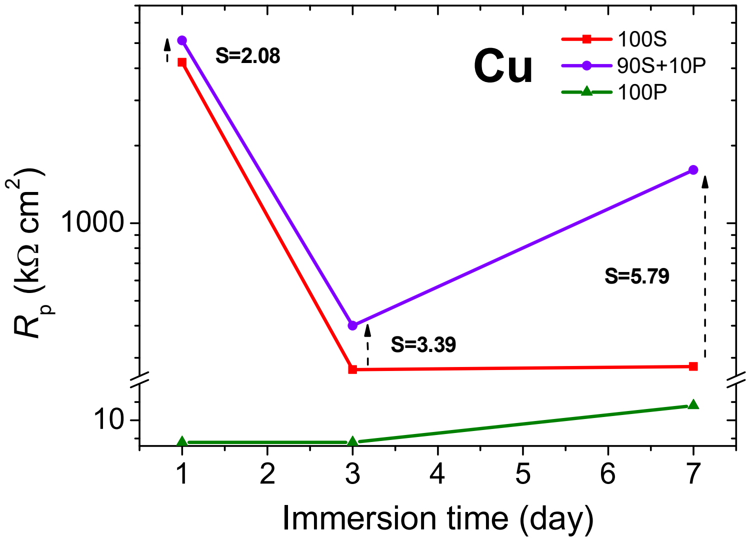

A.14: Fitting parameters used for deconvolution of experimental spectra of Cu samples (Figs. 3.1, Fig. 3.3-3.5 and Fig. 3.7).

Cu samples	**Species**	**Assignment**	***E*** E_b **(eV)**	**FWHM (eV)**	**%Area**
blank	Cu LMM		565.76	3.03	10.61
	Cu LMM	Cu	568.18	2.13	15.35
	Cu LMM	Cu_2O	570.21	1.98	48.61
	Cu LMM		572.43	2.35	8.76
	Cu LMM		574.54	4.00	16.67
	O 1s	Cu_2O	530.70	1.11	70.48
	O 1s	$C{=}O/Cu(OH)_2$	531.87	1.10	20.14
	O 1s	O−C=O	533.20	1.30	6.04
	O 1s	H_2O ads.	534.81	1.30	3.34
100S	Cu LMM		565.63	3.10	8.46
	Cu LMM	Cu	568.01	2.10	20.53
	Cu LMM	Cu_2O	570.07	2.06	34.56
	Cu LMM		571.49	2.35	16.52
	Cu LMM		573.20	3.10	10.55
	Cu LMM		575.85	4.00	9.38
	O 1s	Lat. Cu_2O	530.30	1.23	16.22
	O 1s	Def. Cu_2O	531.48	1.28	22.01
	O 1s	C−O	532.70	1.25	41.09
	O 1s	O−C=O	533.77	1.30	20.68
	N 1s	C=N−C	398.92	1.21	55.82
	N 1s	C−NH−C	400.27	1.18	44.18
	S $2p_{3/2}$	Cu−S−C	162.61	1.35	72.50
	S $2p_{1/2}$		163.85	1.24	27.50
90S+10P	Cu LMM	Cu	568.26	2.1	12.79
	Cu LMM	Cu_2O	570.47	2.1	26.73
	Cu LMM		571.86	2.35	25.74
	Cu LMM		574.23	2.13	7.65
	Cu LMM		576.51	4.00	19.82
	Cu LMM		581.25	4.00	7.27
	N 1s	C=N−C	399.14	1.3	32.75
	N 1s	C−NH−C	400.58	1.31	67.25
	S $2p_{3/2}$	Cu−S−C	162.90	1.35	68.02
	S $2p_{1/2}$		164.09	1.24	31.98

A.15: Potentiodynamic polarization curves recorded for copper in 3 wt.% NaCl solution containing as-prepared 100S (pH=5.6), 100S modified with HCl (pH=4), and as-prepared 90S+10P (pH=4). Electrochemical parameters are given just for the HCl modified sample (100S_pH4). Note that the values for other samples are provided in Tables 3.2 and 3.3.

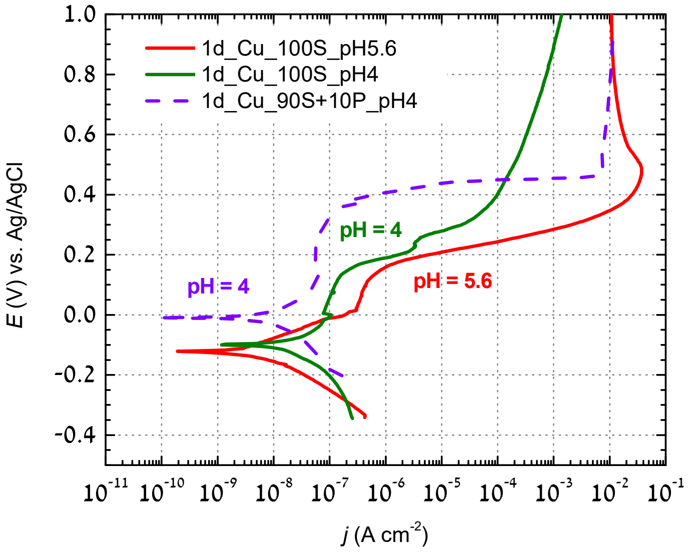

Sample	E_{corr} (mV$_{Ag/AgCl}$)	i_{corr} (A cm^{-2})	E_{pit} (mV)	ΔE$_{pass}$ (mV) = |E_{pit} − E_{corr}|	i_{pass} (A cm^{-2})	b_a (mV/dec)	$-b_c$ (mV/dec)
1d_Cu_100S_pH4	−100	3.75×10^{-8}	150	250	2.1×10^{-7}	251	244

Sample	1 day	
	R_p (kΩ cm^2)	IE (%)
Cu_100S_pH4	1191 ± 132	99.2 ± 0.3

A.16: Fitting parameters used for deconvolution of experimental spectra of Al samples (Figs. 3.11—3.13).

Al samples	**Species**	**Assignment**	E_b **(eV)**	**FWHM (eV)**	**%Area**
blank	Al2p	Al	72.57	0.70	4.01
	Al2p	AlO_x	73.11	1.70	13.87
	Al2p	Al_2O_3	74.29	1.70	15.14
	Al2p	$Al(OH)_3$	74.88	1.70	66.98
	O 1s	Al—O	530.47	1.65	17.17
	O 1s	Al—OH	531.76	1.65	51.37
	O 1s	$C{-}O_{ads.}$	532.88	1.65	31.46
100P	Al2p	Al_2O_3	73.97	1.41	25.00
	Al2p	$Al(OH)_3$	75.24	1.40	41.02
	Al2p	Al—O—P	76.22	1.20	28.40
	Al2p	Al—O—P	77.15	1.10	5.58
	O 1s	Al—O	530.17	1.60	4.39
	O 1s	P=O	531.19	1.65	27.89
	O 1s	Al—O—P	532.36	1.70	50.39
	O 1s	H—O—P	533.69	1.60	17.33
	P $2p_{3/2}$	Al—O—P	133.09	2.20	42.60
	P $2p_{1/2}$		133.93	2.15	19.17
	P $2p_{3/2}$	P=O	134.35	2.20	26.71
	P $2p_{1/2}$		135.25	2.20	11.52
10S+90P	Al2p	Al_2O_3	73.75	1.70	16.95
	Al2p	$Al(OH)_3$	75.07	1.70	64.04
	Al2p	Al—O—P	76.1	1.10	16.31
	Al2p	Al—O—P	77.18	1.10	2.70
	O 1s	Al—O	530.31	1.60	8.60
	O 1s	P=O	531.32	1.60	34.25
	O 1s	Al—O—P	532.42	1.81	49.22
	O 1s	H—O—P	533.77	1.60	7.93
	P $2p_{3/2}$	Al—O—P	133.33	2.20	68.97
	P $2p_{1/2}$		134.17	2.18	31.03

A.17: The list of some important positive-ion fragments of copper oxides and 2-mercaptobenzimidazole, MBI, ($C_7H_6N_2S$) with their corresponding masses.

S17. List of some important fragments

Sample	*m/z*	Positive-ion
NaCl	125.857	Cu_2^+
	188.788	Cu_3^+
	142.862	Cu_2OH^+
	204.784	Cu_3O^+
100P+NaCl	125.858	Cu_2^+
	188.789	Cu_3^+
	142.864	Cu_2OH^+
	204.787	Cu_3O^+
100S+NaCl	59.991	CH_2SN^+
	88.023	$C_3H_6SN^+$
	151.034	$C_7H_7SN_2^+$
	151.863	$CNCu_2^+$
	180.983	$C_7H_6N_2Cu^+$
	212.953	$C_7H_6N_2SCu^+$
	274.875	$C_7H_5N_2SCu_2^+$
90S+10P+NaCl	59.991	CH_2SN^+
	88.023	$C_3H_6SN^+$
	151.033	$C_7H_7SN_2^+$
	151.861	$CNCu_2^+$
	180.986	$C_7H_6N_2Cu^+$
	212.957	$C_7H_6N_2SCu^+$
	274.874	$C_7H_5N_2SCu_2^+$

A.18: ToF-SIMS positive ion spectra obtained for Cu immersed for 7 days in 3 wt.% NaCl containing 2-mercaptobenzimidazole, MBI, and octylphosphonic acid, OPA, in the ratio 9:1 (90S+10P+NaCl_7d). Note that the *m*/*z* range was arbitrarily used for lower mass ions and for higher mass ions.

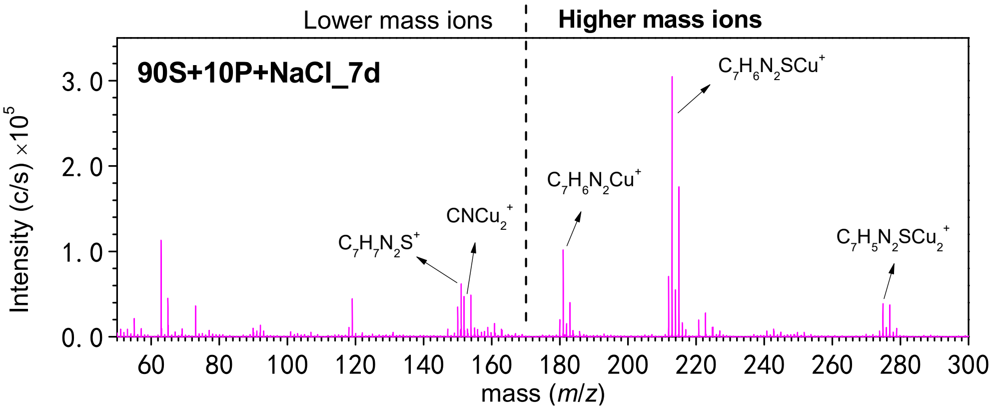

A.19: ToF-SIMS negative ion spectra obtained for Cu immersed in a) 3 wt.% NaCl containing 2-mercaptobenzimidazole, MBI, (100S+NaCl) and b) 3 wt.% NaCl containing MBI and octylphosphonic acid, OPA, in the ratio 9:1 (90S+10P+NaCl).

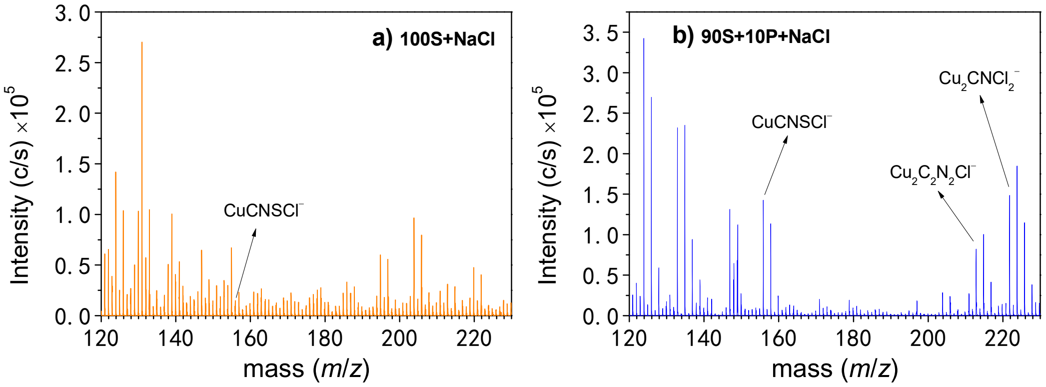

A.20: XPS survey spectrum of Cu immersed for 1 day in 3 wt.% NaCl containing 2-mercaptobenzimidazole, MBI, and octylphosphonic acid, OPA, in the ratio 9:1 (90S+10P+NaCl).

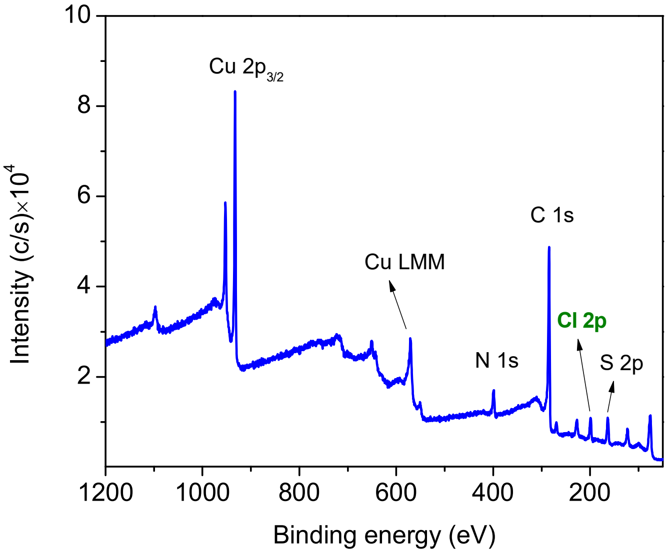

Table S20: Element composition of 90S+10P at a depth of 10 nm.

Element	Content (at.%)
Cu	16.1
C	68.6
N	6.5
S	5.1
Cl	**3.7**

A.21: SEM lower-magnification images recorded in backscattered electron (BSE) mode for Cu immersed for (a) 1 day in 3 wt.% NaCl, (b) 1 day in 3 wt.% NaCl containing 2-mercaptobenzimidazole, MBI (100S+NaCl), (c) 1 day and (d) 7 days in 3 wt.% NaCl containing MBI and octylphosphonic acid, OPA, in the ratio 9:1 (90S+10P+NaCl and 90S+10P+NaCl_7d, respectively). Red rectangles represent the area where higher-magnification images were taken and are shown in Fig. 4.15.

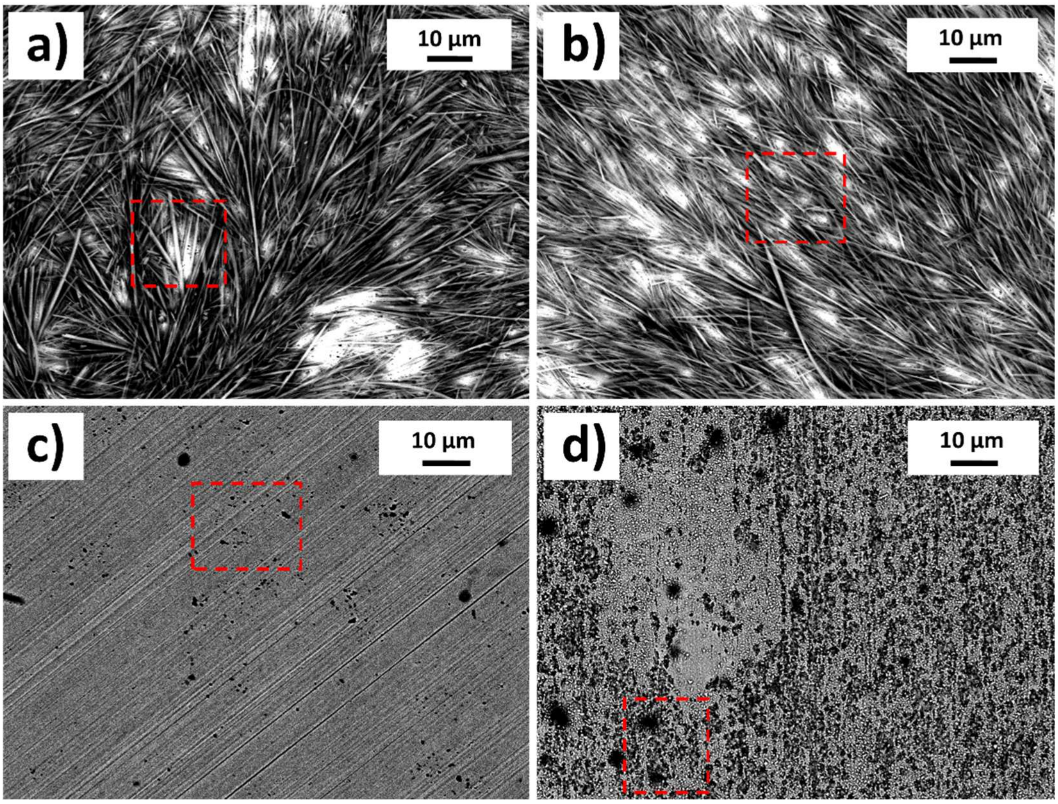

A.22: SVET images (left) obtained for an aluminium-copper galvanic couple immersed in 10 mM NaCl with corresponding optical micrographs (right) taken just before the SVET measurements. The recording of the maps was initiated after: (a) 30 min, and (b) 60 min immersion of the sample in the electrolyte solution.

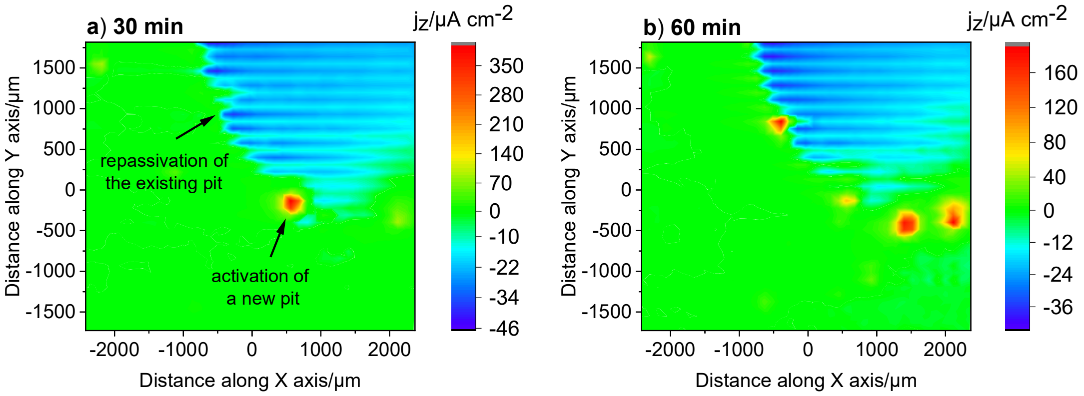

A.23: Optical micrographs corresponding to the SVET images from Fig. 5.5.

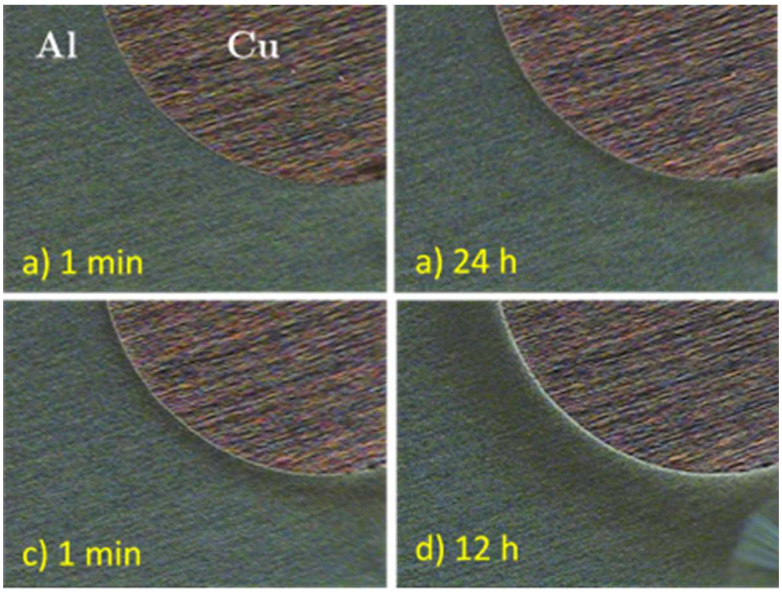

A.24: Optical micrographs corresponding to the SVET images from Fig. 5.6.

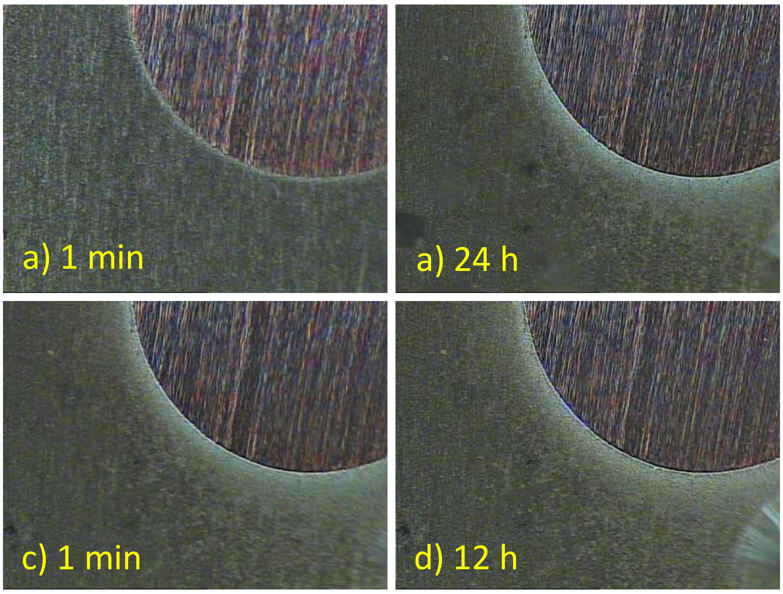

A.25: The actual size and look of the signal shown in Fig. 5.11c for electroreduction of oxygen at the Pt tip.

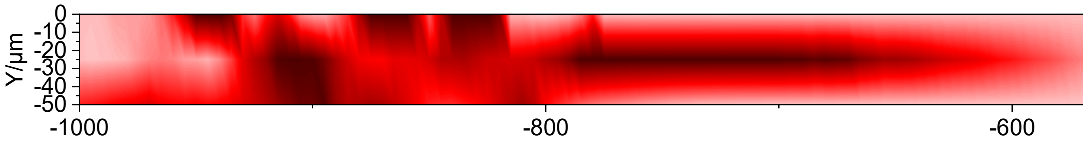

A.26: The actual size and look of the signal shown in Fig. 5.11d for oxidation of hydrogen at the Pt tip.

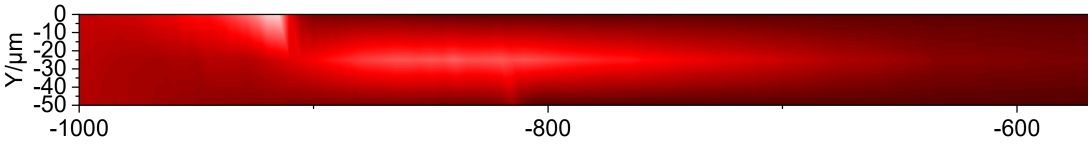

A.27: SEM-EDS analysis of local corrosion induced by S-phase (Al_2CuMg) particle (in Fig. 6.9) recorded in backscattered mode after 24 h immersion in 3 wt.% NaCl solution. The location marked with a yellow rectangle indicates where the EDS analysis was conducted (Table S27). The elements were labelled in EDS maps.

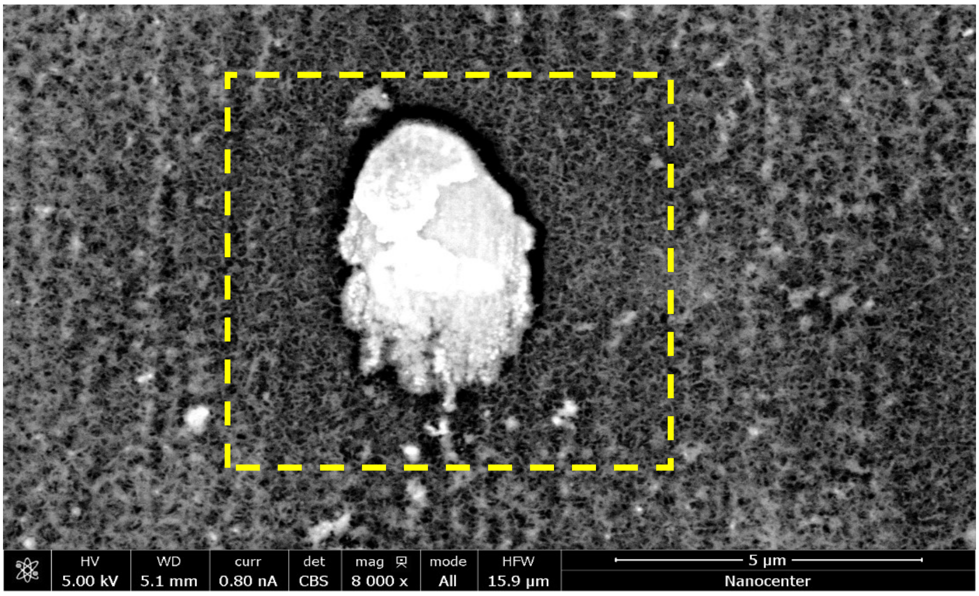

Table A27. EDS analysis of AA2024 immersed for 24 h in MBI+NaCl. Analyses were performed at the location marked with a yellow vertical rectangle, as denoted in Fig. S27.

Elements	at.% Al	at.% O	at.% Cu	at.% Mg	at.% S	at.% N	at.% Cl
	42.0	38.9	7.9	0.5	4.9	5.0	0.8

References

[1] "REACH," 2007. [Online]. Available: https://ec.europa.eu/environment/chemicals/reach/reach_en.htm.

[2] "Registration, Evaluation, Authorisation and Restriction of Chemicals," 2006. [Online]. Available: https://en.wikipedia.org/wiki/Registration,_Evaluation,_Authorisation_and_Restriction_of_Chemicals.

[3] M. W. Kendig and R. G. Buchheit, "Corrosion inhibition of aluminum and aluminum alloys by soluble chromates, chromate coatings, and chromate-free coatings," Corrosion, vol. 59(5), pp. 379–400, 2003.

[4] M. Costa and C. B. Klein, "Toxicity and carcinogenicity of chromium compounds in humans," Crit. Rev. Toxicol., vol. 36(2), pp. 155–163, 2006.

[5] A. Caglieri et al., "The effect of inhaled chromium on different exhaled breath condensate biomarkers among chrome-plating workers," Environ. Health Perspect., vol. 114, no. 4, 2006.

[6] O. Gharbi, S. Thomas, C. Smith, and N. Birbilis, "Chromate replacement: what does the future hold?," npj Mater. Degrad., vol. 2, no. 1, pp. 23–25, 2018.

[7] P. Visser, H. Terryn, and J. M. C. Mol, "On the importance of irreversibility of corrosion inhibitors for active coating protection of AA2024-T3," Corros. Sci., vol. 140, 2018.

[8] J. Sinko, "Challenges of chromate inhibitor pigments replacement in organic coatings," Prog. Org. Coat., vol. 42, no. 3–4, 2001.

[9] J. Izquierdo, J. J. Santana, S. González, and R. M. Souto, "Scanning microelectrochemical characterization of the anti-corrosion performance of inhibitor films formed by 2-mercaptobenzimidazole on copper," Prog. Org. Coat., vol. 74, no. 3, pp. 526–533, 2012.

[10] A. D. Modestov, G. D. Zhou, Y. P. Wu, T. Notoya, and D. P. Schweinsberg, "A study of the electrochemical formation of Cu(I)-BTA films on copper electrodes and the mechanism of copper corrosion inhibition in aqueous chloride/benzotriazole solutions," Corros. Sci., vol. 36, no. 11, pp. 1931–1946, 1994.

[11] T. Hashemi and C. A. Hogarth, "The mechanism of corrosion inhibition of copper in NaCl solution by benzotriazole studied by electron spectroscopy," Electrochim. Acta, vol. 33, no. 8, pp. 1123–1127, 1988.

[12] X. Yang, D. Wang, Z. Sun, and H. Tang, "Adsorption of phosphate at the aluminum (hydr)oxides-water interface: Role of the surface acid-base properties," Colloids Surfaces A Physicochem. Eng. Asp., vol. 297(1–3), pp. 84–90, 2007.

[13] Z. Feng, Y. Liu, T. Hashimoto, G. E. Thompson, X. Zhou, and P. Skeldon, “Influence of surface pretreatments on the corrosion protection of sol-gel coated AA2024-T3 aluminium alloy,” Surf. Interface Anal., 2013, vol. 45, no. 10.

[14] L. Li, A. L. Desouza, and G. M. Swain, “Effect of Deoxidation Pretreatment on the Corrosion Inhibition Provided by a Trivalent Chromium Process (TCP) Conversion Coating on AA2024-T3,” J. Electrochem. Soc., vol. 161, no. 5, 2014.

[15] B. A. Abd-El-Naby, O. A. Abdullatef, H. M. El-Kshlan, E. Khamis, and M. A. Abd-El-Fatah, “Effect of alkaline etching on the inhibition of the acidic corrosion of aluminum by lupine extract,” Port. Electrochim. Acta, vol. 33, no. 1, 2015.

[16] S. G. Prolongo and A. Ureña, “Effect of surface pre-treatment on the adhesive strength of epoxy-aluminium joints,” Int. J. Adhes. Adhes., vol. 29, no. 1, 2009.

[17] S. Maddela, M. J. O’Keefe, V. C. M. Wang, and H. H. Kuo, “Influence of surface pretreatment on coating morphology and corrosion performance of cerium based conversion coatings on AZ91D alloy,” Corrosion, vol. 66, no. 11, 2010.

[18] A. J. Bard, F. R. F. Fan, J. Kwak, and O. Lev, “Scanning Electrochemical Microscopy. Introduction and Principles,” Anal. Chem., vol. 61, no. 2, 1989.

[19] A. J. Bard, F. R. F. Fan, D. T. Pierce, P. R. Unwin, D. O. Wipf, and F. Zhou, “Chemical imaging of surfaces with the scanning electrochemical microscope,” Science, vol. 254, no. 5028. 1991.

[20] R. M. Souto, S. V. Lamaka, and S. González, “Uses of Scanning Electrochemical Microscopy in Corrosion Research,” Microsc. Res. Tech. App. Educ., vol. 3, 2010.

[21] A. C. Bastos, M. C. Quevedo, O. V. Karavai, and M. G. S. Ferreira, “Review-On the Application of the Scanning Vibrating Electrode Technique (SVET) to Corrosion Research,” J. Electrochem. Soc., vol. 164, no. 14, 2017.

[22] S. Rossi, M. Fedel, F. Deflorian, and M. del Carmen Vadillo, “Localized electrochemical techniques: Theory and practical examples in corrosion studies,” Comptes Rendus Chim., vol. 11, no. 9, 2008.

[23] J. Izquierdo, B. M. Fernández-Pérez, A. Eifert, R. M. Souto, and C. Kranz, “Simultaneous atomic force - scanning electrochemical microscopy (AFM-SECM) imaging of copper dissolution,” Electrochim. Acta, vol. 201, 2016.

[24] D. Snihirova, M. Taryba, S. V. Lamaka, and M. F. Montemor, “Corrosion inhibition synergies on a model Al-Cu-Mg sample studied by localized scanning electrochemical techniques,” Corros. Sci., vol. 112, 2016.

[25] A. Asserghine, M. Medvidović-Kosanović, A. Stanković, L. Nagy, R. M. Souto, and G. Nagy, “A scanning electrochemical microscopy characterization of the localized corrosion reactions occurring on nitinol in saline solution after anodic polarization,” Sensors Actuators, B Chem., vol. 321, 2020.

[26] J. Izquierdo et al., “Imaging of Concentration Distributions and Hydrogen Evolution on Corroding Magnesium Exposed to Aqueous Environments Using Scanning Electrochemical Microscopy,” Electroanalysis, vol. 28, no. 10, 2016.

[27] G. Williams, A. J. Coleman, and H. N. McMurray, “Inhibition of Aluminium Alloy AA2024-T3 pitting corrosion by copper complexing compounds,” Electrochim. Acta, vol. 55(20), pp. 5947–5958, 2010.

[28] J. Izquierdo, J. J. Santana, S. González, and R. M. Souto, “Uses of scanning electrochemical microscopy for the characterization of thin inhibitor films on reactive metals: The protection of copper surfaces by benzotriazole,” Electrochim. Acta, vol. 55(28), pp. 8791–8800, 2010.

[29] J. A. Ramírez-Cano, L. Veleva, R. M. Souto, and B. M. Fernández-Pérez, “Investigating metal-inhibitor interaction with EQCM and SVET: 3-amino-1,2,4-triazole on Au, Cu and Au–Cu galvanic coupling,” Mater. Corros., 2018.

[30] J. A. Ramírez-Cano, L. Veleva, B. M. Fernández-Pérez, and R. M. Souto, “SVET study of the interaction of 2-Mercaptobenzothiazole corrosion inhibitor with Au, Cu And Au-Cu galvanic pair,” Int. J. Corros. Scale Inhib., vol. 6, no. 3, 2017.

[31] Joseph R. Davis, Corrosion: Understanding the Basics. Ohio: ASM International, 2000.

[32] D. A. Jones, Principles and Prevention of Corrosion. Michigan: Prentice Hall, 1996.

[33] V. S. Sastri, Green Corrosion Inhibitors: Theory and Practice. John Wiley & Sons, 2011.

[34] K. Xhanari and M. Finšgar, “Organic corrosion inhibitors for aluminum and its alloys in chloride and alkaline solutions: A review,” Arabian Journal of Chemistry. 2019.

[35] R. W. Revie, Uhlig’s Corrosion Handbook: Third Edition. John Wiley & Sons, 2011.

[36] A. Boag et al., “Stable pit formation on AA2024-T3 in a NaCl environment,” Corros. Sci., vol. 52(1), pp. 90–103, 2010.

[37] R. T. Foley, “Localized corrosion of aluminum alloys - a review.,” Corrosion, vol. 42, pp. 277–288, 1986.

[38] V. Branzoi, F. Golgovici, and F. Branzoi, “Aluminium corrosion in hydrochloric acid solutions and the effect of some organic inhibitors,” Mater. Chem. Phys., vol. 78(1), pp. 122–131, 2003.

[39] G. E. Totten and D. S. Mackenzie, Handbook of Aluminum: Volume 2: Alloy Production and Materials Manufacturing. New York, Basel: Marcel Dekker, Inc., 2003.

[40] M. J. N. Pourbaix, Atlas of Electrochemical Equilibria in Aqueous Solutions. Oxford: Pergamon, 1966.

[41] I. Milošev, N. Kovačević, J. Kovač, and A. Kokalj, “The roles of mercapto, benzene and methyl groups in the corrosion inhibition of imidazoles on copper: I. Experimental characterization,” Corros. Sci., vol. 98, pp. 107–118, 2015.

[42] J. Li, C. W. Du, Z. Y. Liu, X. G. Li, and M. Liu, “Inhibition film formed by 2-mercaptobenzothiazole on copper surface and its degradation mechanism in sodium chloride solution,” Int. J. Electrochem. Sci., vol. 11, pp. 10690–10705, 2016.

[43] I. Milošev and M. Metikoš-Huković, “Passive Films on 90Cu-10Ni Alloy: The Mechanism of Breakdown in Chloride Containing Solutions,” J. Electrochem. Soc., vol. 138(1), p. 61, 1991.

[44] D. Tromans and R. H. Sun, “Anodic polarization behavior of copper in aqueous chloride/benzotriazole solutions,” J. Electrochem. Soc., vol. 138, no. 11, pp. 3225–3244, 1991.

[45] D. K. Kozlica, A. Kokalj, and I. Milošev, “Synergistic effect of 2-mercaptobenzimidazole and octylphosphonic acid as corrosion inhibitors for copper and aluminium – An electrochemical, XPS, FTIR and DFT study,” Corros. Sci., vol. 145, p. 109082, 2021.

[46] L. M. Abrantes, L. V. Araújo, and M. D. Levi, “Voltammetric studies on copper deposition/dissolution reactions in aqueous chloride solutions,” Miner. Eng., vol. 8, no. 12, 1995.

[47] E. D’Elia, O. E. Barcia, O. R. Mattos, N. Pébère, and B. Tribollet, “High-Rate Copper Dissolution in Hydrochloric Acid Solution,” J. Electrochem. Soc., vol. 143, no. 3, 1996.

[48] A. El Warraky, H. A. El Shayeb, and E. M. Sherif, “Pitting corrosion of copper in chloride solutions,” Anti-Corrosion Methods Mater., vol. 51, no. 1, pp. 52–61, 2004.

[49] G. Kear, B. D. Barker, and F. C. Walsh, “Electrochemical corrosion of unalloyed copper in chloride media—a critical review,” Corros. Sci., vol. 1, no. 46, pp. 109–135, 2004.

[50] G. Bianchi, G. Fiori, P. Longhi, and F. Mazza, “″Horse shoe″ corrosion of copper alloys in flowing sea water: mechanism, and possibility of cathodic protection of condenser tubes in power stations.,” Corrosion, vol. 34, no. 11, 1978.

[51] M. Liu and J. Li, “In-situ Raman characterization of initial corrosion behavior of copper in neutral 3.5% (wt.) NaCl solution,” Materials (Basel)., vol. 12, no. 13, 2019.

[52] D. S. Chauhan, M. A. Quraishi, C. Carrière, A. Seyeux, P. Marcus, and A. Singh, “Electrochemical, ToF-SIMS and computational studies of 4-amino-5-methyl-4H-1,2,4-triazole-3-thiol as a novel corrosion inhibitor for copper in 3.5% NaCl,” J. Mol. Liq., vol. 289, p. 111113, 2019.

[53] M. Metikoš-Huković and I. Milošev, “Electrochemical methods in the study of localized corrosion attack,” J. Appl. Electrochem., vol. 22, no. 5, 1992.

[54] I. Milošev and M. Metikoš-Huković, “Effect of chloride concentration range on the corrosion resistance of Cu-xNi alloys,” J. Appl. Electrochem., vol. 29, no. 3, 1999.

[55] M. L. Zheludkevich, K. A. Yasakau, S. K. Poznyak, and M. G. S. Ferreira, “Triazole and thiazole derivatives as corrosion inhibitors for AA2024 aluminium alloy,” Corros. Sci., vol. 47, no. 12, 2005.

[56] “https://continentalsteel.com/blog/aluminum-in-the-aerospace-industry/.” .

[57] F. M. Queiroz, M. Terada, A. F. S. Bugarin, H. G. de Melo, and I. Costa, “Comparison of corrosion resistance of the aa2524-t3 and the aa2024-t3,” Metals (Basel)., vol. 11, no. 6, 2021.

[58] A. Kosari, F. Tichelaar, P. Visser, H. Zandbergen, H. Terryn, and J. M. C. Mol, “Dealloying-driven local corrosion by intermetallic constituent particles and dispersoids in aerospace aluminium alloys,” Corros. Sci., vol. 177, 2020.

[59] M. Olgiati, P. J. Denissen, and S. J. Garcia, “When all intermetallics dealloy in AA2024-T3: Quantifying early stage intermetallic corrosion kinetics under immersion,” Corros. Sci., vol. 192, 2021.

[60] R. Catubig et al., “The influence of rare earth mercaptoacetate on the initiation of corrosion on AA2024-T3 Part I: Average statistics of each intermetallic composition,” Corros. Sci., vol. 95, 2015.

[61] R. G. Buchheit, M. A. Martinez, and L. P. Montes, “Evidence for Cu ion formation by dissolution and dealloying the Al2CuMg intermetallic compound in rotating ring-disk collection experiments,” J. Electrochem. Soc., vol. 141(1), p. 119, 2000.

[62] M. A. Jakab, D. A. Little, and J. R. Scully, “Experimental and modeling studies of the oxygen reduction reaction on AA2024-T3,” J. Electrochem. Soc., vol. 152(8), p. B311, 2005.

[63] X. Zhang, T. Hashimoto, J. Lindsay, and X. Zhou, “Investigation of the de-alloying behaviour of θ-phase (Al_2Cu) in AA2024-T351 aluminium alloy,” Corros. Sci., vol. 108, 2016.

[64] A. Kosari et al., “In-situ nanoscopic observations of dealloying-driven local corrosion from surface initiation to in-depth propagation,” Corros. Sci., vol. 177, 2020.

[65] I. Milošev, “Contemporary modes of corrosion protection and functionalization of materials,” Acta Chim. Slov., vol. 66(3), pp. 511–533, 2019.

[66] D. Camila G. and G. Alexandre F., “Corrosion Inhibitors – Principles, Mechanisms and Applications, Camila G. Dariva and Alexandre F. Galio,” in Developments in corrosion protection, InTech, 2014, pp. 365–378.

[67] G. W. Critchlow and D. M. Brewis, “Review of surface pretreatments for aluminium alloys,” Int. J. Adhes. Adhes., vol. 16, no. 4, 1996.

[68] U. Tiringer, J. Kovač, and I. Milošev, “Effects of mechanical and chemical pre-treatments on the morphology and composition of surfaces of aluminium alloys 7075-T6 and 2024-T3,” Corros. Sci., vol. 119, 2017.

[69] I. Dugdale and J. B. Cotton, “An electrochemical investigation on the prevention of staining of copper by benzotriazole,” Corros. Sci., vol. 3, no. 2, pp. 69–74, 1963.

[70] M. Finšgar, “2-Mercaptobenzimidazole as a copper corrosion inhibitor: Part I. Long-term immersion, 3D-profilometry, and electrochemistry,” Corros. Sci., vol. 72, pp. 82–89, 2013.

[71] M. Finšgar and I. Milošev, “Inhibition of copper corrosion by 1,2,3-benzotriazole: A review,” Corros. Sci., vol. 52, no. 9, pp. 2737–2749, 2010.

[72] M. Finšgar, “2-Mercaptobenzimidazole as a copper corrosion inhibitor: Part II. Surface analysis using X-ray photoelectron spectroscopy,” Corros. Sci., vol. 72, pp. 90–98, 2013.

[73] N. Kovačević, I. Milošev, and A. Kokalj, “The roles of mercapto, benzene, and methyl groups in the corrosion inhibition of imidazoles on copper: II. Inhibitor-copper bonding,” Corros. Sci., vol. 98, pp. 457–470, 2015.

[74] G. Žerjav and I. Milošev, “Protection of copper against corrosion in simulated urban rain by the combined action of benzotriazole, 2-mercaptobenzimidazole and stearic acid,” Corros. Sci., vol. 98, pp. 180–191, 2015.

[75] I. Milošev et al., “Electrochemical, Surface-Analytical, and Computational DFT Study of Alkaline Etched Aluminum Modified by Carboxylic Acids for

Corrosion Protection and Hydrophobicity," J. Electrochem. Soc., vol. 166, no. 11, p. C3131, 2019.

[76] D. Costa, T. Ribeiro, P. Cornette, and P. Marcus, "DFT modeling of corrosion inhibition by organic molecules: Carboxylates as inhibitors of aluminum corrosion," J. Phys. Chem. C, vol. 120(50), pp. 28607–28616, 2016.

[77] T. Bauer, T. Schmaltz, T. Lenz, M. Halik, B. Meyer, and T. Clark, "Phosphonate- and carboxylate-based self-assembled monolayers for organic devices: A theoretical study of surface binding on aluminum oxide with experimental support," ACS Appl. Mater. Interfaces, vol. 5(13), pp. 6073–6080, 2013.

[78] M. Poberžnik, F. Chiter, I. Milošev, P. Marcus, D. Costa, and A. Kokalj, "DFT study of n-alkyl carboxylic acids on oxidized aluminum surfaces: from standalone molecules to self-assembled-monolayers," Appl. Surf. Sci., p. 146156, 2020.

[79] I. Milošev et al., "The Effect of Anchor Group and Alkyl Backbone Chain on Performance of Organic Compounds as Corrosion Inhibitors for Aluminum Investigated Using an Integrative Experimental-Modeling Approach," J. Electrochem. Soc., vol. 167, no. 6, p. 061509, 2020.

[80] E. Hoque, J. A. DeRose, B. Bhushan, and K. W. Hipps, "Low adhesion, non-wetting phosphonate self-assembled monolayer films formed on copper oxide surfaces," Ultramicroscopy, vol. 109, no. 8, pp. 1015–1022, 2009.

[81] R. Zhao, P. Rupper, and S. Gaan, "Recent development in phosphonic acid-based organic coatings on aluminum," Coatings, vol. 7(9), p. 133, 2017.

[82] A. Mahapatro, T. D. Matos Negrón, and A. Nguyen, "Spectroscopic evaluations of interfacial oxidative stability of phosphonic nanocoatings on magnesium," J. Spectrosc., p. 2015, 2015.

[83] K. Wapner, M. Stratmann, and G. Grundmeier, "Structure and stability of adhesion promoting aminopropyl phosphonate layers at polymer/aluminium oxide interfaces," Int. J. Adhes. Adhes., vol. 28(1–2), pp. 59–70, 2008.

[84] E. Hoque, J. A. Derose, G. Kulik, P. Hoffmann, H. J. Mathieu, and B. Bhushan, "Alkylphosphonate modified aluminum oxide surfaces," J. Phys. Chem. B, vol. 110, no. 22, pp. 10855–10861, 2006.

[85] A. M. A. Mohamed, A. M. Abdullah, and N. A. Younan, "Corrosion behavior of superhydrophobic surfaces: A review," Arab. J. Chem., vol. 8(6), pp. 749–765, 2015.

[86] S. Hu, Z. Chen, and X. Guo, "Inhibition effect of three-dimensional (3D) nanostructures on the corrosion resistance of 1-dodecanethiol self-assembled monolayer on copper in NaCl solution," Materials (Basel)., vol. 11(7), p. 1225, 2018.

[87] Ö. Özkanat, B. Salgin, M. Rohwerder, J. M. C. Mol, H. De Wit, and H. Terryn, "Scanning Kelvin probe study of (Oxyhydr)oxide surface of aluminum alloy," J. Phys. Chem. C, vol. 116(2), pp. 1805–1811, 2012.

[88] P. Thissen, M. Valtiner, and G. Grundmeier, "Stability of phosphonic acid self-assembled monolayers on amorphous and Single-crystalline aluminum oxide surfaces in aqueous solution," Langmuir, vol. 26(1), pp. 156–164, 2010.

[89] A. Kokalj, S. Peljhan, M. Finšgar, and I. Milošev, “What determines the inhibition effectiveness of ATA, BTAH, and BTAOH corrosion inhibitors on copper?,” J. Am. Chem. Soc., vol. 132, no. 46, pp. 16657–16668, 2010.

[90] G. Žerjav and I. Milošev, “Carboxylic acids as corrosion inhibitors for Cu, Zn and brasses in simulated urban rain,” Int. J. Electrochem. Sci., vol. 9, no. 5, 2014.

[91] T. Hauffman, O. Blajiev, J. Snauwaert, C. Van Haesendonck, A. Hubin, and H. Terryn, “Study of the self-assembling of n-octylphosphonic acid layers on aluminum oxide,” Langmuir, 2008.

[92] R. G. Kelly, J. R. Scully, D. W. Shoesmith, and R. G. Buchheit, Electrochemical techniques in corrosion science and engineering. New York: Marcel Dekker, Inc., 2003.

[93] D. G. Enos and L. L. Scribner, “The Potentiodynamic Polarization Scan,” Hampshire, 1997.

[94] P. J. Cumpson, “Guide to smoothing in AES and XPS,” 1998.

[95] M. Braun and K. Nobe, “Electrodissolution Kinetics of Copper in Acidic Chloride Solutions,” J. Electrochem. Soc., vol. 126, no. 10, 1979.

[96] A. L. Bacarella and J. C. Griess, “The Anodic Dissolution of Copper in Flowing Sodium Chloride Solutions Between 25° and 175°C,” J. Electrochem. Soc., vol. 120, no. 4, 1973.

[97] F. Hunkeler, G. S. Frankel, and H. Bohni, “On the mechanism of localized corrosion.,” Corrosion, vol. 43, no. 3, 1987.

[98] N. Benzbiria, M. Zertoubi, and M. Azzi, “Influence of copper surface pretreatment on the kinetics of oxygen reduction reaction in 0.5 M NaCl solution: Surface characterization and electrochemical studies,” Appl. Surf. Sci. Adv., vol. 4, 2021.

[99] E. McCafferty, Introduction to corrosion science. New York: Springer Science & Business Media, 2010.

[100] M. B. Vukmirovic, N. Vasiljevic, N. Dimitrov, and K. Sieradzki, “Diffusion-Limited Current Density of Oxygen Reduction on Copper,” J. Electrochem. Soc., vol. 150, no. 1, 2003.

[101] F. C. Walsh, L. F. Arenas, and G. Kear, “The electrode kinetics of oxygen reduction: A case study. the corrosion of copper and its alloys in aqueous chloride solution at a smooth rotating disk electrode,” in Encyclopedia of Interfacial Chemistry: Surface Science and Electrochemistry, 2018.

[102] D. K. Kozlica, J. Ekar, J. Kovač, and I. Milošev, “Roles of Chloride Ions in the Formation of Corrosion Protective Films on Copper,” J. Electrochem. Soc., vol. 168, no. 3, 2021.

[103] N. Elgrishi, K. J. Rountree, B. D. McCarthy, E. S. Rountree, T. T. Eisenhart, and J. L. Dempsey, “A Practical Beginner’s Guide to Cyclic Voltammetry,” J. Chem. Educ., vol. 95, no. 2, 2018.

[104] M. Finšgar, K. Xhanari, and H. O. Ćurković, “Cyclic Voltammetry as an Electroanalytical Tool for Analysing the Reaction Mechanisms of Copper in Chloride Solution Containing Different Azole Compounds,” Curr. Anal. Chem., vol. 16, no. 4, 2018.

[105] M. Finšgar, “EQCM and XPS analysis of 1,2,4-triazole and 3-amino-1,2,4-triazole as copper corrosion inhibitors in chloride solution,” Corros. Sci., vol. 77, 2013.

[106] M. C. Biesinger, L. W. M. Lau, A. R. Gerson, and R. S. C. Smart, “Resolving surface chemical states in XPS analysis of first row transition metals, oxides and hydroxides: Sc, Ti, V, Cu and Zn,” Appl. Surf. Sci., vol. 257(3), pp. 887–898, 2010.

[107] P. Druska and H. -H Strehblow, “Quantitative determination of the passive layer on Cu–Ni alloys,” Surf. Interface Anal., vol. 23(7-8), pp. 440–450, 1995.

[108] I. Milošev and H. H. Strehblow, “Electrochemical behavior of Cu-xZn alloys in borate buffer solution at pH 9.2,” J. Electrochem. Soc., vol. 150, no. 11, p. B517, 2003.

[109] G. Deroubaix and P. Marcus, “X-ray photoelectron spectroscopy analysis of copper and zinc oxides and sulphides,” Surf. Interface Anal., vol. 18(1), pp. 39–46, 1992.

[110] A. V. Naumkin, A. Kraut-Vass, S. W. Gaarenstroom, and C. J. Powell, “NIST X-ray Photoelectron Spectroscopy Database,” v4.1, 2012.

[111] P. M. Natishan and W. E. O’Grady, “Chloride Ion Interactions with Oxide-Covered Aluminum Leading to Pitting Corrosion: A Review,” J. Electrochem. Soc., vol. 161, no. 9, 2014.

[112] S. T. Pride, J. R. Scully, and J. L. Hudson, “Metastable Pitting of Aluminum and Criteria for the Transition to Stable Pit Growth,” J. Electrochem. Soc., vol. 141, no. 11, 1994.

[113] T. Hauffman, A. Hubin, and H. Terryn, “Study of the self-assembling of n-octylphosphonic acid layers on aluminum oxide from ethanolic solutions,” in Surface and Interface Analysis, 2013, vol. 45, no. 10.

[114] G. Viramontes-Gamboa, B. F. Rivera-Vasquez, and D. G. Dixon, “The Active-Passive Behavior of Chalcopyrite,” J. Electrochem. Soc., vol. 154(6), p. C299, 2007.

[115] E. Hoque, J. A. DeRose, P. Hoffmann, H. J. Mathieu, B. Bhushan, and M. Cichomski, “Phosphonate self-assembled monolayers on aluminum surfaces,” J. Chem. Phys., vol. 124, no. 17, p. 174710, 2006.

[116] J. Torras, D. S. Azambuja, J. M. Wolf, C. Alemán, and E. Armelin, “How organophosphonic acid promotes silane deposition onto aluminum surface: A detailed investigation on adsorption mechanism,” J. Phys. Chem. C, vol. 118(31), pp. 17724–17736, 2014.

[117] C. D. Wagner, A. V Naumkin, A. Kraut-Vass, J. W. Allison, C. J. Powell, and J. R. J. Rumble, “NIST Standard Reference Database 20, Version 3.4 (web version),” 2003. [Online]. Available: http:/srdata.nist.gov/xps/.

[118] M. R. Alexander, G. E. Thompson, and G. Beamson, “Characterization of the oxide/hydroxide surface of aluminum using X-ray photoelectron spectroscopy: A procedure for curve fitting the O 1s core level,” Surf. Interface Anal., vol. 29, no. 7, 2000.

[119] M. Wagstaffe, A. G. Thomas, M. J. Jackman, M. Torres-Molina, K. L. Syres, and K. Handrup, “An experimental investigation of the adsorption of a

phosphonic acid on the anatase TiO_2(101) surface," J. Phys. Chem. C, vol. 120(3), pp. 1693–1700, 2016.

[120] J. Van den Brand, P. C. Snijders, W. G. Sloof, H. Terryn, and J. H. W. De Wit, "Acid-base characterization of aluminum oxide surfaces with XPS," J. Phys. Chem. B, vol. 108(19), pp. 6017–6024, 2004.

[121] A. Kokalj and D. Costa, " Model Study of Penetration of Cl − Ions from Solution into Organic Self-Assembled-Monolayer on Metal Substrate: Trends and Modeling Aspects ," J. Electrochem. Soc., vol. 168, no. 7, 2021.

[122] L. B. Coelho, D. Cossement, and M. G. Olivier, "Benzotriazole and cerium chloride as corrosion inhibitors for AA2024-T3: An EIS investigation supported by SVET and ToF-SIMS analysis," Corros. Sci., vol. 130, pp. 177–189, 2018.

[123] D. Snihirova, S. V. Lamaka, P. Taheri, J. M. C. Mol, and M. F. Montemor, "Comparison of the synergistic effects of inhibitor mixtures tailored for enhanced corrosion protection of bare and coated AA2024-T3," Surf. Coatings Technol., vol. 303, pp. 342‑351, 2016.

[124] S. Marcelin and N. Pébère, "Synergistic effect between 8-hydroxyquinoline and benzotriazole for the corrosion protection of 2024 aluminium alloy: A local electrochemical impedance approach," Corros. Sci., vol. 101, pp. 66–74, 2015.

[125] P. Rodič, I. Milošev, M. Lekka, F. Andreatta, and L. Fedrizzi, "Study of the synergistic effect of cerium acetate and sodium sulphate on the corrosion inhibition of AA2024-T3," Electrochim. Acta, vol. 308, pp. 337–349, 2019.

[126] G. Xue, X. Huang, and J. Ding, "Surface reaction of 2-mercaptobenzimidazole on metals and its application in adhesion promotion," J. Chem. Soc. Faraday Trans., vol. 87(8), pp. 1229–1232, 1991.

[127] K. Aramaki and N. Hackerman, "Inhibition Mechanism of Medium-Sized Polymethyleneimine," J. Electrochem. Soc., vol. 116, no. 5, p. 568, 1969.

[128] E. McCafferty, "Validation of corrosion rates measured by the Tafel extrapolation method," Corros. Sci., vol. 47(12), pp. 3202–3215, 2005.

[129] M. M. Antonijevic and M. B. Petrovic, "Copper corrosion inhibitors. A review," Int. J. Electrochem. Sci., vol. 3, no. 1, pp. 1–28, 2008.

[130] S. A. Umoren and M. M. Solomon, "Synergistic corrosion inhibition effect of metal cations and mixtures of organic compounds: A Review," J. Environ. Chem. Eng., vol. 5(1), pp. 246–273, 2016.

[131] T. Du, D. Tamboli, V. Desai, and S. Seal, "Mechanism of Copper Removal during CMP in Acidic H_2O_2 Slurry," J. Electrochem. Soc., vol. 151(4), p. G230, 2004.

[132] S. Saikova et al., "X-ray photoelectron, Cu L 3 MM Auger and X-ray absorption spectroscopic studies of Cu nanoparticles produced in aqueous solutions: The effect of sample preparation techniques," Appl. Surf. Sci., vol. 258(20), pp. 8214–8221, 2012.

[133] N. Pauly, S. Tougaard, and F. Yubero, "LMM Auger primary excitation spectra of copper," Surf. Sci., vol. 630, pp. 294–299, 2014.

[134] D. P. Oyarzún Jerez et al., "Nanostructuring of anodic copper oxides in fluoride-containing ethylene glycol media," J. Electroanal. Chem., vol. 807, pp. 181–186, 2017.

[135] D. Chadwick and T. Hashemi, “Electron spectroscopy of corrosion inhibitors: Surface films formed by 2-mercaptobenzothiazole and 2-mercaptobenzimidazole on copper,” Surf. Sci., vol. 89, no. 1–3, pp. 649–659, 1979.

[136] M. C. Biesinger, “Advanced analysis of copper X-ray photoelectron spectra,” Surf. Interface Anal., vol. 49(13), pp. 1325–1334, 2017.

[137] J. C. Vickerman and I. S. Gilmore, Surface Analysis - The Principal Techniques: Second Edition. John Wiley & Sons, 2009.

[138] H. Huang et al., “Water soluble corrosion inhibitors for copper in 3.5 wt% sodium chloride solution,” Corros. Sci., vol. 123, pp. 339–350, 2017.

[139] G. Xue, X. Y. Huang, J. Dong, and J. Zhang, “The formation of an effective anti-corrosion film on copper surfaces from 2-mercaptobenzimidazole solution,” J. Electroanal. Chem., vol. 310, no. 1–2, pp. 139–148, 1991.

[140] J. Coates, “Interpretation of Infrared Spectra, A Practical Approach,” in Encyclopedia of Analytical Chemistry, 2006.

[141] C. N. R. Rao and R. Venkataraghavan, “The C=S stretching frequency and the ‘-N-C=S bands’ in the infrared,” Spectrochim. Acta, vol. 45, pp. 299–305, 1962.

[142] E. Pretsch, T. Clerc, J. Seibl, and W. Simon, Tabellen zur Strukturaufklärung organischer Verbindungen mit spektroskopischen Methoden, 3rd ed. New York: Springer-Verlag Berlin Heidelberg GmbH, 1986.

[143] G. R. Form, E. S. Raper, and T. C. Downie, “The crystal and molecular structure of 2-mercaptobenzimidazole,” Acta Crystallogr. Sect. B Struct. Crystallogr. Cryst. Chem., no. 32, pp. 345–348, 1976.

[144] S. Suresh, K. Jayamoorthy, P. Saravanan, and S. Karthikeyan, “Switch-Off fluorescence of 5-amino-2-mercapto benzimidazole with Ag3O4 nanoparticles: Experimental and theoretical investigations,” Sensors Actuators, B Chem., vol. 225, pp. 463–468, 2016.

[145] “Sigma Aldrich USA, IR Spectrum Table by Frequency Range,” 2020. [Online]. Available: https://www.sigmaaldrich.com/technical-documents/articles/biology/ir-spectrum-table.html. [Accessed: 13-Jan-2020].

[146] Z. Chen, L. Huang, G. Zhang, Y. Qiu, and X. Guo, “Benzotriazole as a volatile corrosion inhibitor during the early stage of copper corrosion under adsorbed thin electrolyte layers,” Corros. Sci., vol. 65, pp. 214–222, 2012.

[147] V. Brusic et al., “Copper Corrosion With and Without Inhibitors,” J. Electrochem. Soc., vol. 138, no. 8, p. 2253, 1991.

[148] I. C. G. Ogle and G. W. Poling, “Corrosion inhibition of copper with benzotriazole,” Can. Metall. Q., vol. 14, no. 1, pp. 37–46, 1975.

[149] B. Nowack, “Environmental chemistry of phosphonates,” Water Res., vol. 37, pp. 2533–2546, 2003.

[150] A. Paszternák, A. Pilbáth, Z. Keresztes, I. Felhősi, J. Telegdi, and E. Kálmán, “Atomic force microscopy studies of alkyl-phosphonate SAMs on mica,” Mater. Sci. Forum, no. 589, pp. 257–262, 2008.

[151] E. Hoque, J. A. Derose, P. Hoffmann, B. Bhushan, and H. J. Mathieu, “Alkylperfluorosilane self-assembled monolayers on aluminum: A comparison with alkylphosphonate self-assembled monolayers,” J. Phys. Chem. C, vol. 111, no. 10, pp. 3956–3962, 2007.

[152] B. Heggen, S. Roy, and F. Muller-Plathe, “Ab initio calculations of the condensation of phosphonic acid and methylphosphonic acid: Chemical properties of potential electrolyte materials for fuel cell applications,” J. Phys. Chem. C, vol. 112(36), pp. 14209–14215, 2008.

[153] M. Handke, C. Paluszkiewicz, and W. Wyrwa, “Fourier transform IR spectroscopical investigation of the anodic oxide films on aluminum. Part. 1. Structural features during oxide films formation,” Mater. Chem., vol. 5(3), pp. 199–212, 1980.

[154] K. Popov, H. Rönkkömäki, and L. H. . Lajunen, “Critical evaluation of stability constants of phosphonic acids (IUPAC Technical Report),” Pure Appl. Chem., vol. 73, pp. 1641–1677, 2001.

[155] M. Metikoš-Huković, R. Babić, and A. Marinović, “Spectrochemical characterization of benzotriazole on copper,” J. Electrochem. Soc., vol. 145, no. 12, p. 4045, 1998.

[156] Y. I. Kuznetsov and L. P. Kazansky, “Physicochemical aspects of metal protection by azoles as corrosion inhibitors,” Russ. Chem. Rev., vol. 77, no. 3, pp. 219–232, 2008.

[157] A. Kokalj, N. Kovačević, S. Peljhan, M. Finšgar, A. Lesar, and I. Milošev, “Triazole, benzotriazole, and naphthotriazole as copper corrosion inhibitors: I. Molecular electronic and adsorption properties,” ChemPhysChem, vol. 12, no. 8, pp. 3547–3555, 2011.

[158] X. Wu, F. Wiame, V. Maurice, and P. Marcus, “2-mercaptobenzimidazole films formed at ultra-low pressure on copper: adsorption, thermal stability and corrosion inhibition performance,” Appl. Surf. Sci., vol. 146814, 2020.

[159] A. Kokalj et al., “Simplistic correlations between molecular electronic properties and inhibition efficiencies: Do they really exist?,” Corros. Sci., vol. 108856, 2021.

[160] M. M. Solomon and S. A. Umoren, “Electrochemical and gravimetric measurements of inhibition of aluminum corrosion by poly (methacrylic acid) in H2SO4 solution and synergistic effect of iodide ions,” Meas. J. Int. Meas. Confed., vol. 76, pp. 104–116, 2015.

[161] M. G. Hosseini, H. Tavakoli, and T. Shahrabi, “Synergism in copper corrosion inhibition by sodium dodecylbenzenesulphonate and 2-mercaptobenzoimidazole,” J. Appl. Electrochem., vol. 38, no. 11, pp. 1629–1636, 2008.

[162] O. Geuli and D. Mandler, “The synergistic effect of benzotriazole and trimethylsiloxysilicate towards corrosion protection of printed Cu-based electronics,” Corros. Sci., vol. 143, pp. 329–336, 2018.

[163] F. X. Perrin and J. Pagetti, “Characterization and mechanism of direct film formation on a Cu electrode through electro-oxidation of 2-mercaptobenzimidazole,” Corros. Sci., vol. 40, no. 10, pp. 1647–1662, 1998.

[164] S. L. Cohen, V. A. Brusic, F. B. Kaufman, G. S. Frankel, S. Motakef, and B. Rush, “X-ray photoelectron spectroscopy and ellipsometry studies of the electrochemically controlled adsorption of benzotriazole on copper surfaces,” J. Vac. Sci. Technol. A Vacuum, Surfaces, Film., vol. 8, no. 3, pp. 2417–2424, 1990.

[165] Physical Electronics, “ToF-SIMS,” 2020. [Online]. Available: https://www.phi.com/surface-analysis-techniques/tof-sims.html.

[166] M. R. Linford, “An Introduction to Time-of-Flight Secondary Ion Mass Spectrometry (ToF-SIMS),” Vac. Technol. Coat., pp. 30–35, 2014.

[167] M. A. Quraishi, D. S. Chauhan, and V. S. Saji, Heterocyclic Organic Corrosion Inhibitors: Principles and Applications. Elsevier, 2020.

[168] J. Kovač, “Surface characterization of polymers by XPS and SIMS techniques,” Mater. Tehnol., vol. 45, no. 3, pp. 191–197, 2011.

[169] J. T. Francis, H. Y. Nie, N. S. McIntyre, and D. Briggs, “ToF-SIMS investigation of octadecylphosphonic acid monolayers on a mica substrate,” Langmuir, vol. 22, no. 22, pp. 9244–9250, 2006.

[170] J. Crousier, L. Pardessus, and J. P. Crousier, “Voltammetry study of copper in chloride solution,” Electrochim. Acta, vol. 33, no. 8, pp. 1039–1042, 1988.

[171] M. R. Vogt, R. J. Nichols, O. M. Magnussen, and R. J. Behm, “Benzotriazole adsorption and inhibition of Cu(100) corrosion in HCl: A combined in situ STM and in situ FTIR spectroscopy study,” J. Phys. Chem. B, vol. 102, no. 30, pp. 5859–5865, 1998.

[172] A. D. Modestov, G. D. Zhou, H. H. Ge, and B. H. Loo, “A study by voltammetry and the photocurrent response method of copper electrode behavior in acidic and alkaline solutions containing chloride ions,” J. Electroanal. Chem., vol. 380, no. 1–2, pp. 63–68, 1995.

[173] R. M. Souto, S. González, R. C. Salvarezza, and A. J. Arvia, “Kinetics of copper passivation and pitting corrosion in Na2SO4 containing dilute NaOH aqueous solution,” Electrochim. Acta, vol. 39, no. 17, pp. 2619–2628, 1994.

[174] R. Woods, G. A. Hope, and K. Watling, “SERS spectroelectrochemical investigation of the interaction of 2-mercaptobenzothiazole with copper, silver and gold surfaces,” J. Appl. Electrochem., vol. 30, no. 11, pp. 1209–1222, 2000.

[175] B. Assouli, Z. A. Chikh, H. Idrissi, and A. Srhiri, “Electrosynthesis of adherent poly (2-mercaptobenzimidazole) films on brass prepared in nonaqueous solvents,” Polymer (Guildf)., vol. 42, no. 6, pp. 2449–2454, 2001.

[176] N. Shukla, S. K. Tripathi, A. Banarjee, A. S. V. Ramana, N. S. Rajput, and V. N. Kulkarni, “Study of temperature rise during focused Ga ion beam irradiation using nanothermo-probe,” Appl. Surf. Sci., vol. 256, no. 2, pp. 475–479, 2009.

[177] X. Wu, F. Wiame, V. Maurice, and P. Marcus, “Moiré Structure of the 2-Mercaptobenzothiazole Corrosion Inhibitor Adsorbed on a (111)-Oriented Copper Surface,” J. Phys. Chem. C, vol. 124, no. 29, pp. 15995–16001, 2020.

[178] J. B. Cotton and I. R. Scholes, “Benzotriazole and related compounds as corrosion inhibitors for copper,” Br. Corros. J., vol. 2, no. 1, pp. 1–5, 1967.

[179] H. Shi, E. H. Han, F. Liu, T. Wei, Z. Zhu, and D. Xu, “Study of corrosion inhibition of coupled Al2Cu-Al and Al3Fe-Al by cerium cinnamate using scanning vibrating electrode technique and scanning ion-selective electrode technique,” Corros. Sci., vol. 98, 2015.

[180] L. B. Coelho, M. Mouanga, M. E. Druart, I. Recloux, D. Cossement, and M. G. Olivier, “A SVET study of the inhibitive effects of benzotriazole and cerium chloride solely and combined on an aluminium/copper galvanic coupling model,” Corros. Sci., vol. 110, 2016.

[181] J. Izquierdo, L. Nagy, J. J. Santana, G. Nagy, and R. M. Souto, “A novel microelectrochemical strategy for the study of corrosion inhibitors employing the scanning vibrating electrode technique and dual potentiometric/amperometric operation in scanning electrochemical microscopy: Application to the study of the cathodic inhibition by benzotriazole of the galvanic corrosion of copper coupled to iron,” Electrochim. Acta, vol. 58, no. 1, 2011.

[182] R. M. Souto, Y. González-García, A. C. Bastos, and A. M. Simões, “Investigating corrosion processes in the micrometric range: A SVET study of the galvanic corrosion of zinc coupled with iron,” Corros. Sci., vol. 49, no. 12, 2007.

[183] A. M. Simões, A. C. Bastos, M. G. Ferreira, Y. González-García, S. González, and R. M. Souto, “Use of SVET and SECM to study the galvanic corrosion of an iron-zinc cell,” Corros. Sci., vol. 49, no. 2, 2007.

[184] S. Y. Yu, W. E. O’Grady, D. E. Ramaker, and P. M. Natishan, “Chloride Ingress into Aluminum Prior to Pitting Corrosion An Investigation by XANES and XPS,” J. Electrochem. Soc., vol. 147, no. 8, 2000.

[185] P. Marcus, V. Maurice, and H. H. Strehblow, “Localized corrosion (pitting): A model of passivity breakdown including the role of the oxide layer nanostructure,” Corros. Sci., vol. 50, no. 9, 2008.

[186] G. T. Burstein, C. Liu, R. M. Souto, and S. P. Vines, “Origins of pitting corrosion,” in Corrosion Engineering Science and Technology, 2004, vol. 39, no. 1.

[187] T. R. Beck, “Salt film formation during corrosion of aluminum,” Electrochim. Acta, vol. 29, no. 4, 1984.

[188] G. S. Frankel, “The growth of 2-D pits in thin film aluminum,” Corros. Sci., vol. 30, no. 12, 1990.

[189] M. Curioni and F. Scenini, “The Mechanism of Hydrogen Evolution during Anodic Polarization of Aluminium,” Electrochim. Acta, vol. 180, 2015.

[190] J. P. Popić, M. Avramov-Ivić, and D. M. Dražić, “Ring detection of hydrogen evolution on a rotating disc-ring electrode,” J. Serbian Chem. Soc., vol. 61, no. 12, 1996.

[191] G. S. Frankel, S. Fajardo, and B. M. Lynch, “Introductory lecture on corrosion chemistry: A focus on anodic hydrogen evolution on Al and Mg,” Faraday Discussions, vol. 180. 2015.

[192] A. J. Bard and M. V. Mirkin, Scanning electrochemical microscopy, 2nd ed. New York: CRS Press, 2001.

[193] D. Polcari, P. Dauphin-Ducharme, and J. Mauzeroll, “Scanning Electrochemical Microscopy: A Comprehensive Review of Experimental Parameters from 1989 to 2015,” Chemical Reviews, vol. 116, no. 22. 2016.

[194] C. B. Bargeron and R. C. Benson, “Analysis of the Gases Evolved during the Pitting Corrosion of Aluminum in Various Electrolytes,” J. Electrochem. Soc., vol. 127, no. 11, 1980.

[195] D. M. Dražić and J. Popić, “Hydrogen evolution on aluminium in chloride solutions,” J. Electroanal. Chem., vol. 357, no. 1–2, 1993.

[196] C. Laurent, F. Scenini, T. Monetta, F. Bellucci, and M. Curioni, “The contribution of hydrogen evolution processes during corrosion of aluminium and aluminium alloys investigated by potentiodynamic polarisation coupled with real-time hydrogen measurement,” npj Mater. Degrad., vol. 1, no. 1, 2017.

[197] J. Izquierdo, A. Eifert, C. Kranz, and R. M. Souto, “In situ investigation of copper corrosion in acidic chloride solution using atomic force—scanning electrochemical microscopy,” Electrochim. Acta, vol. 247, 2017.

[198] S. V. Lamaka, M. L. Zheludkevich, K. A. Yasakau, M. F. Montemor, and M. G. S. Ferreira, “High effective organic corrosion inhibitors for 2024 aluminium alloy,” Electrochim. Acta, vol. 52(25), pp. 7231–7247, 2007.

[199] Y. González-García, S. J. García, A. E. Hughes, and J. M. C. Mol, “A combined redox-competition and negative-feedback SECM study of self-healing anticorrosive coatings,” Electrochem. commun., vol. 13, no. 10, 2011.

[200] L. Zhang, J. Gao, L. N. W. Damoah, and D. G. Robertson, “Removal of iron from aluminum: A review,” Mineral Processing and Extractive Metallurgy Review, vol. 33, no. 2. 2012.

Bibliography

Publications Related to the Thesis

Journal Articles

1. D.K. Kozlica, A. Kokalj and I. Milošev, “Synergistic effect of 2-mercaptobenzimidazole and octylphosphonic acid as corrosion inhibitors for copper and aluminium–An electrochemical, XPS, FTIR and DFT study,” *Corrosion Science*, 182, p.109082, 2021.
2. D.K. Kozlica, J. Ekar, J. Kovač and I. Milošev, “Roles of Chloride Ions in the Formation of Corrosion Protective Films on Copper,” *Journal of The Electrochemical Society*, 168(3), p.031504, 2021.

Conference Paper

1. D.K. Kozlica and I. Milošev, “The influence of surface preparation on efficiency of mercapto and phosphonic inhibitors adsorbed on aluminium and copper metal,” *7th Regional Symposium on Electrochemistry – South East Europe*,” Split, Croatia, 2019.
2. D.K. Kozlica, A. Kokalj and I. Milošev, “Efficiency of mercapto and phosphonic inhibitors for copper and aluminum as a function of surface preparation, “ *The Annual Congress of the European Federation of Corrosion*, Seville, Spain, 2019.